Szkoła Główna Gospodarstwa Wiejskiego
w Warszawie
Instytut Medycyny Weterynaryjnej

mgr inż. Michalina Maria Bartak

Mechanizmy neuropatogenezy oraz neurotropizmu MHV (Mouse Hepatitis Virus) oraz SDAV (Sialodacryoadenitis Virus) na modelu *in vitro* hodowli pierwotnej mysich komórek centralnego układu nerwowego – astrocytów, neuronów oraz mikrogleju

Mechanisms of neuropathogenesis and neurotropism of MHV (Mouse Hepatitis Virus) and SDAV (Sialodacryoadenitis Virus) in an *in vitro* primary culture model of mouse central nervous system cells - astrocytes, neurons, and microglia

Rozprawa doktorska

Doctoral thesis

Rozprawa doktorska wykonana pod kierunkiem:
dr hab. Joanny Cymerys-Bulenda, prof. SGGW
Instytut Medycyny Weterynaryjnej
Katedra Nauk Przedklinicznych

Warszawa 2025

Oświadczenie promotora rozprawy doktorskiej

Oświadczam, że niniejsza rozprawa została przygotowana pod moim kierunkiem i stwierdzam, że spełnia warunki do przedstawienia jej w postępowaniu o nadanie stopnia naukowego doktora.

Data 05.06.2025 Czytelny podpis promotora Joanna Cymerys-Bulenda

Oświadczenie autora rozprawy doktorskiej

Świadom/a odpowiedzialności prawnej, w tym odpowiedzialności karnej za złożenie fałszywego oświadczenia, oświadczam, że niniejsza rozprawa doktorska została napisana przez mnie samodzielnie i nie zawiera treści uzyskanych w sposób niezgodny z obowiązującymi przepisami prawa, w szczególności z ustawą z dnia 4 lutego 1994 r. o prawie autorskim i prawach pokrewnych (tj. z dnia 28 października 2022 r., Dz.U. z 2022 r. poz. 2509 ze zm.)

Oświadczam, że przedstawiona rozprawa nie była wcześniej podstawą żadnej procedury związanej z uzyskaniem stopnia naukowego doktora.

Oświadczam ponadto, że niniejsza wersja rozprawy jest identyczna z załączoną wersją elektroniczną.

Przyjmuję do wiadomości, że rozprawa doktorska poddana zostanie procedurze antyplagiatowej.

Data 04.06.2025 Czytelny podpis autora rozprawy Michalina Bartak

Pragnę złożyć serdeczne podziękowania, mojej promotor, Pani ***dr hab. Joannie Cymerys prof. SGGW*** *za opiekę, wyrozumiałość, krytyczny głos i ogromne wsparcie w przygotowywaniu pracy doktorskiej oraz za wprowadzenie w świat wirusologii (i nie tylko) przez dzielenie się cenną wiedzą, doświadczeniem, umocnieniem wiary w siebie i swoje przekonania od pierwszych naukowych kroków.*

Szczególne wyrazy wdzięczności składam Panu ***dr Marcinowi Chodkowskiemu,*** *dzięki któremu wkroczyłam na drogę naukową powiązaną z wirusologią. Dodatkowo dziękuję za pomoc w pracach laboratoryjnych i planowaniu doświadczeń oraz za naukowe wsparcie.*

Bardzo dziękuje doktorantce, ***mgr inż. Weronice D. Krahel****, która wspomagała mnie podczas przebiegu doktoratu, zarówno w pomocy w doświadczeniach jak i w rozweselaniu codziennego życia laboratoryjnego.*

Serdecznie dziękuję Panu ***prof. dr hab. Marcinowi Bańburze,*** *za przybliżenie niezmiernie ciekawych zagadnień wirusologicznych oraz pomoc w redagowaniu pracy doktorskiej.*

Dziękuję wszystkim pracownikom, koleżankom i kolegom, z Katedry Nauk Przedklinicznych Instytutu Medycyny Weterynaryjnej SGGW za cenne uwagi, pomoc w doświadczeniach laboratoryjnych, życzliwość i przyjazną atmosferę.

Szczególne podziękowania kieruję mojej najbliżej rodzinie, a w szczególności ***Mamie, Babci i Tacie****, za wiarę i wsparcie w realizowaniu moich życiowych celów. Dziękuję moim* ***drogim przyjaciołom i miłości mojego życia*** *za trwanie przy mnie i wspieranie w dążeniu do spełniania marzeń.*

Pragnę również podziękować wszystkim, którzy przyczynili się, świadomie lub nie, do spełnienia moich pragnień i marzeń...

Spis treści

Streszczenie

Koronawirusy mogą stanowić poważne zagrożenie dla zdrowia publicznego, czego przykładem jest miniona pandemia COVID-19 oraz rosnąca liczba przypadków tzw. długiego COVID i towarzyszących im powikłań neurologicznych. Mechanizmy neurotropizmu koronawirusów i neuropatogenezy w obrębie ośrodkowego układu nerwowego (OUN) pozostają, jednak, nie do końca poznane. Częste mutacje w obrębie genomu koronawirusów, szczególnie w podjednostce białka S, wpływają na zmianę tropizmu i ich transmisję międzygatunkową, co podkreśla potrzebę prowadzenia dalszych badań nad ich patogennością. Neurotropowy szczep JHM mysiego wirusa zapalenia wątroby (MHV-JHM) oraz „zapomniany" szczurzy wirus sialodacryoadenitis (SDAV) stanowią dobre modele badawcze umożlwiające realizację założonych celów prezentowanej rozprawy doktorskiej. Celem rozprawy doktorskiej było zbadanie mechanizmów interakcji MHV-JHM oraz SDAV z komórkami OUN – neuronów, mikrogleju i astrocytów, poprzez: (i) określenie efektów zakażenia komórek, poprzez ustalenie rodzaju i czasu pojawienia się efektu cytopatycznego; (ii) zbadanie roli cytoszkieletu neuronów; (iii) określenie roli VCP podczas replikacji i uwalniania wirionów potomnych z neuronów; (iv) określenie profilu cytokin i chemokin produkowanych przez astrocyty i mikroglej w odpowiedzi na zakażenie (v) ocenę wpływu zakażenia na produkcję reaktywnych form tlenu i żywotność komórek. Do realizacji postawionych założeń badawczych użyto klasycznych i nowoczesnych technik wykorzystywanych w wirusologii. Obserwacja zmian morfologicznych cytoszkieletu neuronów (filamenty aktynowe, mikrotubule) po zakażeniu MHV-JHM została przeprowadzona przy użyciu mikroskopii konfokalnej, a wpływ inhibitorów cytoszkieletu (cytochalazyna D, latrunkulina A, noskapina i nokodazol) na replikację wirusa został oceniony techniką RT-qPCR. Rolę białka zawierającego walozynę (VCP) w cyklu replikacyjnym SDAV w neuronach zbadano wykorzystując wysokoprzepustową mikroskopię konfokalną (Operetta® CLS™ Revvity™, Array Scan XTI ThermoFisher™), technikę western blot, obrazowanie przyżyciowe komórek (JuLI™Br NanoEnTek) oraz traktowanie neuronów inhibitorem Eeyarestatyną I (EerI). Odpowiedź komórkową i produkcję reaktywnych form tlenu (ROS) przez mikroglej i astrocyty zbadano za pomocą cytometrii przepływowej, mikroskopii konfokalnej, panelu immunologicznego (Luminex™ xMAP technology) do analizy 48 cytokin i chemokin oraz klasycznego testu ELISA. Przeprowadzone badania jakościowe i ilościowe pozwoliły na zaobserwowanie istotnych wyników. Replikacja MHV-JHM w neuronach pierwotnych była efektywna i prowadziła do zmian morfologicznych zaobserwowanych jako kondensacja filamentów aktynowych w postaci pierścieni podbłonowych, licznych struktur nanorurek (TNT) oraz struktur mikrotubularnych cystern zlokalizowanych w neurytach. Analiza RT-qPCR wykazała, że inhibitory noskapina i nokodazol znacząco ograniczają replikację wirusa w neuronach. Po raz pierwszy wykazano, że SDAV produktywnie replikuje się w neuronach mysich

in vitro, prezentując trzy różne CPE. Poziom VCP był istotnie podwyższony podczas zakażenia, a zastosowanie inhibitora EerI w stężeniu 5 μM/mL w systemie postinkubacji skutkowało statystycznie istotnym obniżeniem miana SDAV oraz widocznym nagromadzeniem antygenu wirusowego w okolicy podbłonowej współwystępującego z antygenem VCP. Miesięczna obserwacja pierwotnej hodowli mikrogleju i astrocytów zakażonej SDAV i MHV-JHM wykazała, że zakażenie wzmagało apoptozę w ciągu pierwszych 2 godzin po zakażeniu a efekt ten utrzymywał się do 672 godzin po zakażeniu. Zakażenie MHV-JHM powodowało najwyższy wzrost poziomu ROS we wczesnych godzinach po zakażeniu, natomiast zakażenie SDAV - w późniejszych etapach replikacji. Podczas analizy profilu produkowanych cytokin i chemokin zauważono zmiany w produkcji cytokin i chemokin IL-6, IL-18, IL-33, MCP-1, MIP-1 beta i MIP-2 alfa po zakażeniu MHV-JHM. Natomiast zakażenie SDAV zwiększyło produkcję IL-1 alfa, IL-6, IL-10, IL-18, IL-19, IL-23, IL-28, IL-33, MCP-1, MCP-3, MIP-1 alfa, MIP-1 beta, MIP-2 alfa, TNF alfa. Podsumowując wyniki przedstawione w niniejszej rozprawie doktorskiej wykazano, że zarówno MHV-JHM, jak i SDAV produktywnie replikują się w pierwotnych hodowlach neuronów, mikrogleju i astrocytów, bez konieczności wcześniejszej adaptacji. Po zakażeniu MHV-JHM, filamenty aktynowe są wykorzystywane do składania i uwalniania wirionów potomnych, podczas gdy mikrotubule uczestniczą w transporcie wewnątrzkomórkowym. Dodatkowo, zakażenie MHV-JHM promuje powstawanie nanorurek (TNT) łączących sąsiednie neurony, co prawdopodobnie stanowi mechanizm rozprzestrzeniania się wirusa w ośrodkowym układzie nerwowym z pominięciem odpowiedzi komórkowej na zakażenie. Podczas replikacji SDAV, VCP jest niezbędne do składania i uwalniania wirionów potomnych z neuronów. Zakażenie obydwoma wirusami wywołało podwyższoną produkcję ROS utrzymującą się przez cały miesiąc trwania zakażenia. Zarówno mikroglej, jak i astrocyty aktywnie produkowały cytokiny i chemokiny prozapalne, jednocześnie hamując produkcję czynników przeciwzapalnych. Długotrwale zaburzona odpowiedź immunologiczna może przyczyniać się do przewlekłych uszkodzeń OUN obserwowanych podczas zakażeń koronawirusowych.

Słowa kluczowe: neuropatogeneza, neurodegeneracja, OUN, koronawirus, MHV-JHM, SDAV

Abstract

Coronaviruses might pose a serious threat to public health, as was demonstrated by the past COVID-19 pandemic and the increasing number of long COVID cases and accompanying neurological complications. The mechanisms of neurotropism and neuropathogenesis of coronaviruses within the central nervous system (CNS) remain, however, insufficiently understood. Frequent mutations within the coronavirus genome, particularly in the S-protein subunit, alter tropism and their interspecies transmission, highlighting the need for further research concerning their pathogenesis. The neurotropic JHM strain of Mouse Hepatitis Virus (MHV-JHM) and the 'forgotten' Rat Sialodacryoadenitis Virus (SDAV) provide a good research model to achieve the set objectives of the presented dissertation. The aim of the dissertation was to investigate the mechanisms of MHV-JHM and SDAV interactions with CNS cells - neurons, microglia and astrocytes, by: (i) characterising the effects of cell infection, by determining the type and timing of the appearance of the cytopathic effect; (ii) investigating the role of the neuronal cytoskeleton; (iii) determining the role of VCP during replication and release of progeny virions from neurons; (iv) determining the profile of cytokines and chemokines produced by astrocytes and microglia in response to infection (v) assessing the effect of infection on reactive oxygen species production and cell viability. Classical and modern techniques used in virology were applied to achieve the set research objectives. The observation of morphological changes in the cytoskeleton of neurons (actin filaments, microtubules) after MHV-JHM infection was carried out using confocal microscopy, and the effect of cytoskeleton inhibitors (cytochalasin D, latrunculin A, noscapine and nocodazole) on virus replication was assessed using RT-qPCR. The role of valosin-containing protein (VCP) in the SDAV replication cycle in neurons was investigated using high-throughput confocal microscopy (Operetta® CLS™ Revvity™, Array Scan XTI ThermoFisher™), western blot technique, cell live imaging (JuLI™Br NanoEnTek) and treatment of neurons with the inhibitor Eeyarestatin I (EerI). The cellular response and production of reactive oxygen species (ROS) by microglia and astrocytes were examined by flow cytometry, confocal microscopy, an immunoassay panel (Luminex™ xMAP technology) for the analysis of 48 cytokines and chemokines and a classical ELISA. The qualitative and quantitative studies carried out allowed significant results to be observed. MHV-JHM replication in primary neurons was productive and led to morphological changes observed as condensation of actin filaments in the form of submembrane rings,

numerous tunnelling nanotube (TNT) structures and microtubular cisternae structures located in neurites. RT-qPCR analysis showed that the inhibitors noscapine and nocodazole significantly hinder virus replication in neurons. For the first time, SDAV was shown to replicate productively in mouse neurons *in vitro*, presenting three different CPE. VCP levels were significantly elevated during infection, and treatment with the EerI inhibitor at 5 μM/mL in the post-incubation system resulted in a statistically significant reduction in SDAV titres and accumulation of viral antigen in the submembranous region co-occurring with VCP antigen. Monthly observation of primary cultures of microglia and astrocytes infected with SDAV and MHV-JHM showed that infection increased apoptosis within the first 2 hours post-infection and this effect persisted until 672 hours post-infection. MHV-JHM infection caused the highest increase in ROS levels in the early hours after infection, while SDAV infection caused the highest increase in ROS levels in the later stages of replication. When the profile of cytokines and chemokines produced was analysed, changes in the production of the cytokines and chemokines IL-6, IL-18, IL-33, MCP-1, MIP-1 beta and MIP-2 alpha were noted after MHV-JHM infection. In contrast, SDAV infection increased the production of IL-1 alpha, IL-6, IL-10, IL-18, IL-19, IL-23, IL-28, IL-33, MCP-1, MCP-3, MIP-1 alpha, MIP-1 beta, MIP-2 alpha, and TNF alpha. In summary, the results presented in this dissertation demonstrate that both MHV-JHM and SDAV replicate productively in primary cultures of neurons, microglia and astrocytes, without the need for prior adaptation. Upon MHV-JHM infection, actin filaments are used to assemble and release progeny virions, while microtubules are involved in intracellular transport. In addition, MHV-JHM infection promotes the formation of tunnelling nanotubes (TNTs) connecting neighbouring neurons, which is likely to be a mechanism for virus spread in the central nervous system bypassing the cellular response to infection. During SDAV replication, VCP is essential for the assembly and release of virions from neurons. Infection with both viruses resulted in elevated ROS production sustained throughout the month-long infection. Both microglia and astrocytes actively produced pro-inflammatory cytokines and chemokines, while limiting the production of anti-inflammatory factors. A long-term impairment of the immune response may contribute to the chronic central nervous system (CNS) damage observed during coronaviral infections.

Keywords: neuropathogenesis, neurodegeneration, CNS, coronavirus, MHV-JHM, SDAV

1. Wykaz publikacji będących podstawą rozprawy doktorskiej

Niniejsza rozprawa doktorska składa się na zbiór czterech opublikowanych i powiązanych tematycznie artykułów naukowych.

Punktacja została podana na podstawie *Journal Citation Reports* (Clarivate Analytics, 20 Czerwca 2024) oraz wykazów czasopism naukowych i recenzowanych materiałów z konferencji międzynarodowych (Komunikaty Ministra Nauki z dnia 1 grudnia 2021 r., 17 lipca 2023 r., 05 stycznia 2024 r.).

1. **Bartak, M.,** Słońska, A., Bańbura, M. W., Cymerys, J. (2021). SDAV, the Rat Coronavirus-How Much Do We Know about It in the Light of Potential Zoonoses. Viruses, 13(10), 1995. https://doi.org/10.3390/v13101995 **(IF_{2021}: 5,818; pkt. $MNiSW_{2021}$: 100)**
2. **Bartak, M.,** Bąska, P., Chodkowski, M., Tymińska, B., Bańbura, M. W., i Cymerys, J. (2024). Neurons cytoskeletal architecture remodeling during the replication cycle of mouse coronavirus MHV-JHM: a morphological in vitro study. BMC veterinary research, 20(1), 18. https://doi.org/10.1186/s12917-023-03813-y **(IF_{2023}: 2,3; pkt. $MNiSW_{2023}$: 140)**
3. **Bartak, M.,** Krahel, W. D., Chodkowski, M., Grel, H., Walczak, J., Pallepati, A., Komorowski, M., i Cymerys, J. (2024). ATPase Valosin-Containing Protein (VCP) Is Involved During the Replication and Egress of Sialodacryoadenitis Virus (SDAV) in Neurons. International journal of molecular sciences, 25(21), 11633. https://doi.org/10.3390/ijms252111633 **(IF_{2023}: 4,9 pkt. $MNiSW_{2023}$: 140)**
4. **Bartak, M.,** Krahel, W. D., Gregorczyk-Zboroch, K., Chodkowski, M., Potârniche, A. V., Długosz, E., Krzyżowska, M., i Cymerys, J. (2025). Cytokine Profile Analysis During Sialodacryoadenitis Virus and Mouse Hepatitis Virus JHM Strain Infection in Primary Mixed Microglia and Astrocyte Culture-Preliminary Research. Cells, 14(9), 637. https://doi.org/10.3390/cells14090637 **(IF_{2023}: 5,1; pkt. $MNiSW_{2023}$: 140)**

Sumaryczny IF= **18,12**

Sumaryczna liczba pkt. MNSiW= **520**

2. Wykaz skrótów

ACE2	enzym przekształcający angiotensynę 2 (ang. angiotensin converting enzyme 2)
AF	filamenty aktynowe (ang. actin filaments)
AG	aparat Golgiego (ang. Golgi apparatus)
BCoV	koronawirus bydlęcy (ang. bovine coronavirus)
CAND	zespół zaburzeń neurokognitywnych związanych z COVID-19 (ang. coronavirus associated neurocognitive disorder)
CCoV	psi koronawirus (ang. canin coronavirus)
CD11b	klaster różnicowania 11b (ang. cluster of differentiation 11b)
Ceacam-1	cząsteczka adhezji komórkowej 1 (ang. carcinoembryonic antigen-related cell adhesion molecule 1)
ChRCoV HKU24	chiński koronawirus szczura domowego (ang. China Rattus Coronavirus HKU24)
COVID19	choroba wywołana przez SARS-CoV-2 (ang. coronavirus disease 2019)
CRS	zespół wyrzutu cytokin (ang. cytokine release syndrome)
EHV-1	koński herpeswirus typu I (ang. equine herpesvirus type I)
FCoV	koci koronawirus (ang. feline coronavirus)
FFU/ml	jednostki tworzące ognisko (ang. fluorescence focal forming unit)
FITC	izotiocyjanan 5 fluorosceiny (ang. fluorescein 5(6)-isothiocyanate)
GAPDH	dehydrogenaza 3-fosforanu gliceraldehydu (ang. glyceraldehyde 3-phosphate dehydrogenase)
GBS	zespół Guillaina-Barrégo (ang. Guillain-Barré syndrome)
GFAP	kwaśne białko włókienkowe gleju (ang. glial fibrillary acidic protein)
HCoV	ludzki koronawirus (ang. human coronavirus)

HCoV-229E	ludzki koronawirus szczep 229E
HCoV-HKU1	ludzki koronawirus szczep HKU1
HCoV-NL63	ludzki koronawirus szczep NL63
HCoV-OC43	ludzki koronawirus szczep OC43
HHV 1	ludzki herpeswirus typu 1 (ang. human herpesvirus type 1)
HHV-2	ludzki herpeswirus typu 2 (ang. human herpervirus type 2)
IF	filamenty pośrednie (ang. intermediate filaments)
IFN	interferon
IL	interleukina (ang. interleukin)
JP	jodek propidyny (ang. propidium iodide)
Kpz	kilo par zasad
M1	współczynniki Mander'a 1 (ang. parameter Mander's 1)
M2	współczynniki Mander'a 2 (ang. parameter Mander' s2)
mAb	przeciwciało monoklonalne (ang. monoclonal antibody)
MAPK	kinaza białkowa aktywowana mitogenem (ang. mitogen-activated protein kinase)
MERS-CoV	koronawirus bliskowschodniego zespołu niewydolności oddechowej (ang. Middle East respiratory syndrom coronavirus)
MHV	mysi koronawirus zapalenia wątroby (ang. mouse hepatitis virus)
MHV-59	mysi koronawirus zapalenia wątroby szczep 59
MT	mikrotubule (ang. microtubules)
MVH-JHM	mysi koronawirus zapalenia wątroby szczep JHM
NeuN	jądrowe białko neuronalne (ang. neuronal nuclear protein)
NF-κB	jądrowy czynnik transkrypcyjny NF kappa B (ang. nuclear factor kappa-light-chain-enhancer of activated B cells)
NFC	grupa nitrofuranowa (ang. nitrofuran group)

NLRP3	białko NOD 3 - podobne, zawierające domenę pirynową (ang. NOD-like receptor family, pyrin domain containing 3)
NRF2	jądrowy czynnik erytroidalny 2 (ang. nuclear factor erythroid 2-related factor 2 gene)
ORF-6	otwarta ramka odczytu 6 (ang. open reading frame 6)
OUN	ośrodkowy układ nerwowy
PASC	zespół następstw zdrowotnych po przechorowaniu COVID-19 (ang. postacute sequal of COVID-19)
PCC	współczynnik korelacji Pearson'a (ang. Pearson correlation coefficient)
PHEV	wirus epidemicznej biegunki świń (ang. porcine epidemic diarrhea virus)
PRC	szczurzy koronawirus Parker'a (ang. Parker's rat coronavirus)
Rbd	domena wiążąca receptor (ang. receptor binding domain)
RCoV	szczurzy koronawirus (ang. rat coronavirus)
RCV-BCMM	szczurzy koronawirus szczep BCMM
RCV-CARS	szczurzy koronawirus szczep CARS
RCV-NJ	szczurzy koronawirus szczep NJ
RCV-W	szczurzy koronawirus szczep W
Rh-BatCoV HKU2	koronawirus nietoperzy *Rhinolophus* HKU2
ROS	reaktywne formy tlenu (ang. reactive oxide species)
RT qPCR	PCR w czasie rzeczywistym z reakcją odwrotnej transkrypcji (ang. quantitative reverse transcription polymerase chain reaction)
SADS	zespół ostrej biegunki świń (ang. swine acute diarrhea syndrome)
SARS- CoV-2	koronawirus ciężkiego ostrego zespołu oddechowego 2 (ang. severe acute respiratory syndrome coronavirus 2)
SARS-CoV	koronawirus ciężkiego ostrego zespołu oddechowego

SDAV	szczurzy koronawirus zapalenia gruczołów ślinowych i węzłów chłonnych (ang. sialodacryoadenitis virus)
Tau	jednostka związana z tubuliną (ang. tubulin associated unit)
TNT	nanorurki (ang. tunneling nanotubes)
USUV	wirus Usutu (ang. Usutu virus)
VCP/p97	białko zawierające walozynę (ang. valosin containing protein)
VZV	wirus krowianki (ang. variocella zoster virus)
WGA	aglutynina kiełków pszenicy (ang. wheat germ agglutinin)
XTT	test oceny cytotoksyczności
ZIKV	wirus Zika (ang. Zika virus)

3. Wstęp i uzasadnienie podjęcia tematu

Rodzina *Coronaviridae* należy do rzędu *Nidovirales.* Składa się ona z dwóch podrodzin: *Letovirinae* i *Orthocoronavirinae*. Na podstawie badań genetycznych i serologicznych do *Orthocoronavirinae* zalicza się cztery rodzaje: alfa-, beta-, gamma- i deltakoronawirusy. Do rodzaju betakoronawirusów należy wirus mysiego zapalenia wątroby (MHV, ang. mouse hepatits virus) oraz szczurzy koronawirus zapalenia gruczołów ślinowych i węzłów chłonnych (SDAV, ang. sialodacryoadenitis virus), podobnie jak SARS-CoV i SARS-CoV-2 (Walker i in., 2020). Wiriony koronawirusów są pleomorficzne lub kuliste, o średnicy 80-220 nm. Pokrywa je otoczka, a na ich powierzchni występuje charakterystyczna 'korona' zbudowana z peplomerów (Fehr i Perlman, 2015; Kanso i in., 2020). Genom składa się z pojedynczej cząsteczki liniowego, jednoniciowego RNA o dodatniej polarności i wielkości od 25 do 31 kpz. Proces replikacji zachodzi w cytoplazmie. Koronawirusy zawierają cztery główne białka strukturalne, którymi są: białko kolca (S), białko otoczki (E), białko błonowe (M), nukleoproteina (N). U niektórych betakoronawirusów, takich jak np. MHV, występuje piąte białko - esteraza hemaglutyniny (HE) (B. Chen i in., 2025; Kazi i in., 2005; Langereis i in., 2012; Mallick i Duttaroy, 2021). Wirusy te zakażają głównie ptaki i ssaki, powodując liczne choroby układu oddechowego, nerwowego, narządów wewnętrznych czy układu pokarmowego. Do chorób wywoływanych przez koronawirusy zwierzęce należą m.in.: zakaźne zapalenie oskrzeli u ptaków; zakaźne zapalenie otrzewnej kotów; epidemiczna biegunka świń, czy wirusowe zapalenie żołądka i jelit u bydła. Najbardziej interesujące, z medycznego punktu widzenia, są wirusy grup alfa oraz beta, do których należą wszystkie znane gatunki zakażające ludzi (odpowiednio do rodzajów alfa-koronawirusów: HCoV-229E i HCoV-NL63 oraz beta- koronawirusów: HCoV-OC43, HCoV-HKU1, SARS-CoV i SARS-CoV-2)(Haake i in., 2020; Ji, 2021; Kenney i in., 2021).

Obraz ludzkich koronawirusów jako stosunkowo niegroźnych patogenów zmienił się wraz z pojawieniem się w 2002 roku w chińskiej prowincji Guangdong nowego gatunku ludzkiego koronawirusa – SARS-CoV (Drosten i in., 2003; Ksiazek i in., 2003). Został on nazwany od nazwy zespołu chorobowego wirusem SARS (ang. severe acute respiratory syndrome). Wysoka śmiertelność (~ 10%) oraz bardzo wysoka zaraźliwość patogenu doprowadziły do znaczącego wzrostu zainteresowania podrodziną *Coronavirinae*. Liczne prace pokazały, że istnieje olbrzymia grupa wirusów zwierzęcych,

które potencjalnie mogą przekroczyć barierę gatunkową (H. Wang i in., 2007). W związku z tym nie było zaskoczeniem, że w 2012 roku pojawił się kolejny odzwierzęcy koronawirus zakażający ludzi – MERS-CoV (ang. Middle East respiratory syndrome coronavirus) (Hijawi i in., 2013; Zaki i in., 2012). Warto jednak zauważyć, iż początkowy zapał naukowców osłabł po stwierdzeniu, że zakażenia koronawirusem SARS ograniczone były do jednego sezonu. Prace nad nowymi lekami przeciwwirusowymi i szczepionkami nie zostały niejednokrotnie doprowadzone nawet do etapu badań przedklinicznych i po dekadzie badań można stwierdzić, że nie opracowano żadnych nowych form terapii (Chiou i in., 2005; Gomersall i in., 2004; Pearson, 2005; Z. Yang i in., 2005). Cenę tego zaniedbania populacja na całym świecie zapłaciła w 2020 roku. Ten rok stał się datą rozpoczynającą pandemię nowego wirusa SARS-CoV-2, który w następstwie rozprzestrzeniania się powodował (i wciąż powoduje) chorobę COVID-19 u ludzi. Nowy koronawirus SARS-CoV-2, wywołujący ostry zespół oddechowy, został po raz pierwszy zidentyfikowany w grudniu 2019 r. w Chinach (Zhu i in., 2020). Od wybuchu pandemii różne źródła szczegółowo opisywały objawy i skutki zakażenia, koncentrując się głównie na powikłaniach oddechowych (V'kovski i in., 2021). Badacze początkowo dołożyli wszelkich starań do stworzenia szczepionki, która mogłaby ograniczyć zastraszającą liczbę ofiar śmiertelnych SARS-CoV-2 (Krammer, 2020; Lamb, 2021; Sahin i in., 2021). Z ogromnym sukcesem stworzono szczepionki oparte na technologii mRNA (np. Moderna, Pfizer-BioNTech) oraz wektorowe (np. AstraZeneca, Johnson&Johnson). Dzięki nim, między grudniem 2020 r. a marcem 2023 r., w 34 z 54 państw/terenów uwzględnionych w analizie szczepionek przeciwko COVID-19 zmniejszono liczbę zgonów ogółem o 59% (zakres 17-82%), co szacuje się na około 1 do 6 milionów uratowanych istnień ludzkich wśród osób w wieku 25 lat lub starszych (96% w wieku 60 lat lub starszych, a 52% w wieku 80 lat lub starszych; pierwsze dawki przypominające uratowały 51% istnień ludzkich, a 60% uratowano w okresie dominacji wariantu Omicron) (Meslé i in., 2024; Thibault Fiolet i in., 2021).

Pomimo tak wielkiego sukcesu, stopniowo pojawiało się coraz więcej doniesień o ogólnoustrojowym działaniu wirusa, w szczególności na układ nerwowy u pacjentów po przebytym zakażeniu. Częstymi neurologicznymi objawami zakażenia SARS-CoV-2 są bóle głowy oraz zanik węchu i smaku. Mniej powszechne objawy, które notowano to: drgawki, udar i pojedyncze przypadki zespół Guillaina-Barrégo (GBS, ostre zapalenie demielinizacyjne ze współistniejącą aksonalną neuropatią ruchową) (Kujawska i in.,

2023; Mendonça Filho i in., 2023; Robert Weissert, 2023; Whittaker i in., 2020). Diagnozowane coraz częściej, długotrwałe powikłania neurologiczne jako efekt zakażenia SARS-CoV-2, obligowały do zintensyfikowania badań nad neurotropizmem i neuropatogennoscią koronawirusów. W efekcie opisano nowy zbiór objawów chorobowych określany zbiorczo jako zespół długiego COVID-19 (ang. long COVID-19 syndrome) lub PASC (ang. post-acute sequelae of COVID-19). Termin ten odnosi się do objawów klinicznych (najczęściej wymienianych: zmęczenie, osłabienie, dyspenia, „mgła mózgowa", ansomia, dysgeuzja, zawroty głowy, bóle mięśni i stawów), które rozwijają się w trakcie lub po zakażeniu COVID-19 i trwają przez co najmniej 12 tygodni. W sumie opisano ponad 200 różnych kombinacji objawów, których pacjenci mogą doświadczać (Jarrott i in., 2022; Krahel i in., 2024; Merhavy i in., 2024). Ze względu na brak specyficznych testów dla tego zespołu, długi COVID jest obecnie diagnozowany na podstawie wywiadu i badania zdrowia fizycznego (Meo i in., 2025). Z tego powodu trudno jest odróżnić długi COVID od wtórnego zakażenia SARS-CoV-2 lub aktywacji wirusów pozostających w stanie latencji, takich jak wirus opryszczki (HHV-1, ang. human herpesvirus type 1) czy wirus ospy wietrznej (VZV, ang. varicella zoster virus) (Barton i in., 2007; Mayla i in., 2025; Tome i in., 2025). Z tego samego powodu zaburzeń neurokognitywnych związanych z COVID (CAND, ang. coronavirus associated neurocognitive disorder) nie można łatwo oddzielić od innych zaburzeń poznawczych, zarówno nowych, jak i wcześniej występujących u pacjentów (Panagea i in., 2025; Watson i in., 2013). W tym celu, niezbędne wydawało się być stworzenie nowych modeli *in vitro*, odpowiednich do badania molekularnych mechanizmów neuropatogenności koronawirusów.

Warto wskazać, iż jednym z lepiej poznanych przedstawicieli *Coronaviridae* jest mysi wirus zapalenia wątroby. Szczepy MHV charakteryzują się szerokim tropizmem, a pojedyncze izolaty wywołują zakażenia układu oddechowego, pokarmowego lub nerwowego (Weiss i Leibowitz, 2011). Najchętniej badanymi są szczepy neurotropowe ze względu na ich zdolność do wywoływania ostrego zapalenia mózgu oraz rdzenia kręgowego, z lub bez przewlekłej demielinizacji aksonalnej (Bender i Weiss, 2010). W kontekście pandemii wywołanej przez innego przedstawiciela betakoronawirusów – SARS-CoV-2, MHV okazuje się być doskonałym modelem do badania patogenezy, w tym tropizmu i wirulencji, jak również odpowiedzi immunologicznej gospodarza na zakażenie (MHV był już wcześniej stosowany jako model dla SARS-CoV) (Matthews i

in., 2002; Sanclemente-Alaman i in., 2020). Ponadto, z uwagi na fakt, że zakażenie SARS-CoV-2 powoduje objawy neurologiczne, w tym znaczne uszkodzenia ośrodkowego układu nerwowego (OUN), szczepy MHV-A59 i MHV-JHM mogą być wykorzystane jako model do zbadania mechanizmów wnikania wirusa do OUN i wynikającej z tego odpowiedzi immunologicznej gospodarza. Najważniejsze podobieństwa między zakażeniem MHV u myszy a zakażeniem SARS-CoV-2 u ludzi obejmują: ich powinowactwo do opuszki węchowej (MHV-A59) i nabłonek pęcherzyków płucnych (MHV-1), rozprzestrzenianie się do mózgu powodujące objawy neurologiczne (MHV-A59, MHV-JHM), rozwój mikro zakrzepów w wątrobie (MHV) lub w mózgu (SARS-CoV-2) oraz zdolność do modyfikacji odpowiedzi immunologicznej (Boylan i in., 2023; Körner i in., 2020). Mając na względzie wyżej wymienione cechy mysiego koronawirusa oraz jego znaczne podobieństwo do SARS-CoV-2 oraz SARS-CoV można wnioskować, że stanowi on bardzo dobry model badawczy do projektowania nowych środków leczniczych, ochrony osobistej czy poznawania szlaków molekularnych interakcji wirus-komórka *in vitro*. Dodatkowo uzyskane wyniki badań prezentowanych w niniejszej rozprawie można ze znacznym prawdopodobieństwem zastosować w celu poszerzania wiedzy do prewencji powikłań po zakażeniu SARS-CoV-2. Co więcej, w kontekście badań nad MHV-JHM, nie ma wyczerpujących doniesień na temat znaczenia cytoszkieletu komórkowego w zakażeniach przebiegających w OUN, a w szczególności tych poruszających temat regulacji motoryki cytoszkieletu podczas wnikania wirusa do komórki oraz uwalniania wirionów potomnych. Brakuje również informacji na temat wykorzystania i udziału filamentów aktynowych, mikrotubul czy neurofilamentów pośrednich w przebiegu zakażenia MHV-JHM (Wen i in., 2021).

Drugim koronawirusem, który został wykorzystany jako model badawczy, to szczurzy koronawirus – SDAV. Wirus ten jest czynnikiem etiologicznym wywołującym częste zakażenia wśród szczurów laboratoryjnych (Bhatt i in., 1977; Jacoby, 1986; Maru i Sato, 1982). Objawy kliniczne zakażenia obejmują zapalenie ślinianek i gardła wraz z obrzękiem, światłowstręt oraz zmniejszoną płodność, a nawet encefalopatię (Kojima i in., 1983; Percy i in., 1991). Należy podkreślić, że SDAV i inne gatunki szczurzych koronawirusów należą do tego samego rodzaju, co wysoce epidemiczne/pandemiczne i najbardziej patogenne koronawirusy człowieka, takie jak SARS-CoV, MERS-CoV czy SARS-CoV-2. Wszystkie znane koronawirusy szczurów należą do rodzaju beta. Betakoronawirusy obejmują pięć podrodzajów: *Embecovirus, Hibecovirus,*

Merbecovirus, Nobecovirus i Sarbecovirus. Gatunki podrodzaju *Embecovirus* zakażające szczury to SDAV, PRC (szczurzy koronawirus Parker'a), RCV-BCMM (szczurzy koronawirus szczep BCMM), RCV-W (szczurzy koronawirus szczep W), RCV-NJ (szczurzy koronawirus szczep NJ), RCV-CARS (szczurzy koronawirus szczep CARS) i nowy ChRCoV HKU24 (chiński koronawirus szczura domowego) (Walker i in., 2020). Biorąc pod uwagę analizę proteomiczną sekwencji białka kolca (S), które charakteryzuje się wysoką zmiennością, występuje 86,3% podobieństwa do sekwencji izolowanych od MHV-JHM, 65% do HCoV-HKU1 i HCoV-OC43 oraz 40,3% do MERS-CoV i 37,7% do SARS-CoV-2 (UniProt Blast). Doniesienia te potwierdzają słuszność wyboru tego szczepu do badań nad neuropatogennością koronawirusów oraz pogłębienia wiedzy na temat tego gatunku, którego użycie w badaniach zostało istotnie ostatnio zaniedbane.

Znaczna większość danych literaturowych o SDAV pochodzi z lat 80. i 90. Jedynie nieliczne badania zostały opublikowane we wczesnych latach 2000 (na podstawie: pubmed.ncbi.nlm.nih.gov). Zaskakująco ich tematyka nie jest związana z neuropatogenezą. Tym samym brak jest informacji na ten temat w kontekście zakażenia szczurzym koronawirusem. Warto tutaj podkreślić fakt, iż głównym gospodarzem zakażenia jest szczur (Compton, 2021; Jacoby, 1986). Szczury zamieszkują duże aglomeracje miejskie, powodując znaczne zagrożenie epidemiczne. W przeciwieństwie do najczęściej wskazywanego rezerwuaru i wektora SARS-CoV-2 - nietoperza, szczury występują licznie na całym świecie, a nie jedynie w rejonach tropikalnych czy subtropikalnych (Zhang i in., 2021). Fakt ułatwionej zdolności koronawirusów do przekraczania bariery gatunkowej oraz obecności gospodarza powszechnie występującego w bliskim otoczeniu człowieka podkreśla konieczność prowadzenia dalszych badań nad charakterystyką zakażeń wywołanych przez SDAV. Szczegółowa analiza dostępnej na ten czas literatury opisującej SDAV została zamieszczona w artykule przeglądowym stanowiącym pierwszą publikację wchodzącą w skład cyklu prezentowanej rozprawy doktorskiej (Bartak i in., 2021).

Zaproponowany model *in vitro*, który został specjalnie wystandaryzowany, zaprojektowany i z sukcesem używany przez zespół Cymerys i wsp. (2010-2020) (Cymerys, Chodkowski, i in., 2019; Cymerys i in., 2010, 2013, 2020; Cymerys, Kowalczyk, i in., 2019) pozwoli uzupełnić wiedzę na temat interakcji betakoronawirusów z komórkami OUN, tym samym umożliwi zbadanie roli cytoszkieletu (neuronów, astrocytów) i odpowiedzi prozapalnej na zakażenie wirusem (mikroglej, astrocyty).

Co więcej, myszy szczepu BALB/c (H-2^d), z których zostanie pozyskana hodowla pierwotna, od lat stosowane są jako laboratoryjne zwierzęta modelowe. Dodatkowo wykazują one wrażliwość na zakażenie MHV-JHM jak i SDAV (Kojima i in., 1980; Matthews i in., 2002; Percy i in., 1986). Warto dodać, iż w pracach nad neuropatogennością wirusów, w szczególności koronawirusów, prowadzonych *in vitro* niezwykle rzadko wykorzystywane są pierwotne komórki nerwowe.

Podsumowując braki literaturowe dotyczące zagadnienia zakażeń ośrodkowego układu nerwowego przez wspomniane gatunki koronawirusów oraz wysoki potencjał zoonotyczny SDAV, postanowiono podjąć się wyzwania poszerzenia wiedzy w tym zakresie, wykorzystując model hodowli pierwotnej *in vitro* komórek OUN.

4. Cel, zakres pracy i hipotezy badawcze

W rozprawie przedstawiono następujące **cele badawcze**:

1. Zbadanie mechanizmów interakcji MHV-JHM i SDAV z komórkami OUN *in vitro:*
   i. Określenie efektów zakażenia neuronów, mikrogleju i astrocytów, poprzez ustalenie rodzaju i czasu pojawienia się efektu cytopatycznego.
   ii. Rola cytoszkieletu komórek nerwowych podczas przebiegu zakażenia MHV-JHM.
   iii. Charakterystyka uwalniania wirionów potomnych SDAV z komórek nerwowych.
2. Określenie profilu cytokin wydzielanych przez komórki astrocytów i mikrogleju podczas zakażenia MHV-JHM i SDAV.
3. Wpływ zakażenia MHV-JHM oraz SDAV na produkcję reaktywnych form tlenu i żywotność astrocytów i mikrogleju.

W związku z tym sformułowano **hipotezę badawczą,** która zakłada, że **(i)** cytoszkielet komórek nerwowych jest niezbędny do replikacji koronawirusów w OUN **(ii)** zmiana ekspresji białek komórkowych takich jak VCP, jest niezbędna podczas replikacji i uwalniania z komórki **(iii)** zakażeniu towarzyszy produkcja cytokin prozapalnych i przeciwzapalnych, których poziom może być zależny od intensywności i czasu trwania zakażenia **(iv)** długotrwałe zakażenie mikrogleju i astrocytów prowadzi do zwiększenia produkcji reaktywnych from tlenu i zmiany żywotności tych komórek.

Zakres pracy doktorskiej obejmuje następujące zadania badawcze:

1. Namnożenie MHV-JHM i SDAV oraz określenie miana zakaźnego wirusów – odpowiednio $TCID_{50}$ i PFU/mL, na modelu pierwotnej hodowli mysich neuronów, astrocytów i mikrogleju *in vitro*.
2. Wykonanie testów cytotoksyczności w celu ustalenia stosowanych stężeń inhibitorów i cytostatyków do określenia udziału cytoszkieletu w zakażeniu oraz mechanizmu uwalniania wirionów potomnych.
3. Ocena wpływu zakażenia MHV-JHM i SDAV na komórki OUN poprzez przyżyciową obserwację hodowli i analizę preparatów mikroskopowych, określając efekt cytopatyczny (CPE).

4. Określenie wpływu zakażenia MHV-JHM na cytoszkielet (mikrotubule, filamenty aktynowe) komórek nerwowych *in vitro* oraz zbadanie udziału poszczególnych jego elementów podczas replikacji MHV-JHM przez zastosowanie odpowiednich inhibitorów – nokodazolu, noskapiny, palitakselu, latrunkuliny A, cytochalazyny D, zaburzających synergię cytoszkieletu.
5. Określenie sposobu uwalniania wirionów potomnych z komórek nerwowych w zakażeniu SDAV poprzez zbadanie roli białka zawierającego walozynę (VCP, ang. valosin-containing protein) i zastosowanie inhibitora udziału VCP w procesie degradacji białek zależnego od retikulum endoplazmatycznego (ERAD) w systemie pre- i postinkubacji.
6. Oznaczenie profilu cytokin produkowanych w przebiegu zakażenia długoterminowego MHV i SDAV. Określenie poziomu reaktywnych form tlenu (ROS) i ocena procesu apoptozy astrocytów i mikrogleju po zakażeniu.

5. Materiały i metody badań

Przedstawiona sekcja została opisana w sposób syntetyczny i zgodny z zadaniami badawczymi, gdyż szczegółowy opis metod i materiałów został zawarty w artykułach składających się na dysertację. Każda z metod wraz z materiałami została podzielona na etapy, które odbywały się w czasie pracy nad poszczególnymi publikacjami:

Pierwszym etapem badań było określenie efektów zakażenia komórek OUN *in vitro.* Hodowla pierwotna do zbadania zakażenia o etiologii koronawirusowej została pozyskana z embrionów mysich (stadium rozwoju E17) (neurony) oraz osesków (mikroglej i astrocyty) myszy szczepu BALB/c (H-2^d). Procedurę wykonano zgodnie z opracowaniem zespołu Cymerys i wsp.(Cymerys, Chodkowski, i in., 2019; Cymerys i in., 2010, 2012, 2014, 2020; Cymerys, Kowalczyk, i in., 2019), który badał EHV-1, HSV-1 oraz HSV-2. Dla potwierdzenia uzyskania odpowiedniego stosunku komórkowego oraz do oceny morfologii komórek za każdym razem przeprowadzono analizę jakościową metodami immunofluorescencji bezpośredniej z zastosowaniem markerów NeuN dla neuronów, GFAP dla astrocytów i CD11b dla mikrogleju.

Wirusami użytymi w badaniach były MHV-JHM oraz SDAV szczep 682. Koronawirus mysi, szczep neurotropowy MHV-JHM (VR-76513™, ATCC®) namnożono w linii komórkowej mysich hepatocytów (NCTC, CCL-9.1™, ATCC®). Medianę dawki zakaźnej hodowli tkankowej ($TCID_{50}$) ustalono przy użyciu metody Spearmana-Kärber (Kärber, 1931). Wszystkie badania przeprowadzono z użyciem wirusa na poziomie drugiego pasażu i miana $10^{7,8}$ $TCID_{50}$/mL. Drugi wykorzystany koronawirus, Sialodacryoadenitis szczep 682 (dalej wspominany jako SDAV), uzyskany został dzięki uprzejmości prof. Susan Compton z Uniwersytetu w Yale w Stanach Zjednoczonych i namnożony w komórkach nabłonka płuca szczura (L-2, CCL-149™, ATCC®). Miano ustalono metodą Gaertnera (Gaertner i in., 1993). Wszystkie badania przeprowadzono z użyciem wirusa na poziomie trzeciego pasażu i miana $10^{6,8}$ PFU/mL. Przygotowane zawiesiny wirusowe przechowywano w temperaturze -80°C do momentu wykorzystania w badaniach.

Zakażenie hodowli komórkowych zawiesiną MHV-JHM lub SDAV przeprowadzono z godzinną adsorbcją wirusa. Kolejno zawiesinę odciągano i dodawano świeży płyn hodowlany przeznaczony dla odpowiedniej hodowli komórkowej. Zakażone hodowle komórkowe inkubowano w warunkach i w czasie zgodnych z potrzebami

każdego z doświadczeń. Do obserwacji efektu zakażenia (ocena CPE, ang. cytopathic effect) hodowli pierwotnej mysich neuronów, astrocytów i mikrogleju wirusem MHV-JHM lub SDAV wykorzystywano system do przyżyciowej obserwacji komórek Juli™Br (Real-time cell growth analysis system; NanoEnTek Inc). Umożliwia on monitorowanie w czasie rzeczywistym zmian zachodzących w hodowli, bez narażania na zmianę warunków mogących powodować zaburzenia w ocenie poziomu pokrycia hodowli i żywotności komórek. Dodatkowo stosowano technikę barwienia immunofluorescencjnego antygenu wirusowego i białek komórkowych oraz obrazowania za pomocą mikroskopii konfokalnej klasycznej i zautomatyzowanej wysokoprzepustowej.

Drugi etap badań został poświęcony określeniu wpływu zakażenia MHV-JHM na poszczególne elementy cytoszkieletu neuronów hodowanych *in vitro*. W celu określenia roli danej struktury cytoszkieletu oraz jej udziału w replikacji użyto inhibitorów, które zakłócały prawidłowe funkcjonowanie badanych elementów cytoszkieletu. Były to toksyny produkowane m.in. przez bakterie lub grzyby. Do filamentów aktynowych użyto inhibitorów: latrunkulina A (Sigma Aldrich®) oraz cytochalazyna D (Sigma Aldrich®), a do mikrotubuli: nokodazol (Sigma Aldrich®), noskapina (ThermoFisher®), paklitaksel (ThermoFisher®) oraz iwermektyna (Sigma Aldrich®). Pierwotne hodowle neuronów, po zróżnicowaniu (dzień 14) i na odpowiednim poziomie pokrycia hodowli (min. 70%), były poddawane pre- i postinkubacji inhibitorami (nokodazolem 30µM/mL; cytochalazyną D 10µM/mL; latrunkuliną A 10µM/mL; noskapiną 75µM/mL; palitakselem 10µM/mL. Podczas metody preinkubacji, komórki inkubowano przez 1 godzinę z pożądanym inhibitorem w temperaturze 37°C, 5% CO_2, a następnie zakażano. Po zakażeniu płyn hodowlany zastąpiono świeżym. W metodzie postinkubacji komórki zakażano MHV-JHM przez 1 godzinę w temperaturze 37°C, 5% CO_2. Następnie komórki pozostawiano do inkubacji w świeżym płynie hodowlanym zawierającym wymienione inhibitory (Ryc. 1). W przypadku analizy jakościowej efekt oceniano za pomocą mikroskopii konfokalnej (ocena morfologiczna zmian w cytoszkielecie komórkowym po zakażeniu MHV-JHM) oraz ilościowo przy pomocy techniki RT-qPCR (startery zostały uwzględnione w Tabeli 1) (poziom replikacji MHV-JHM przed użyciem inhibitorów i po traktowaniu komórek). Aby upewnić się, że obserwowany efekt nie wynika z oddziaływania cytotoksycznego inhibitorów, żywotność komórek określono testem XTT (Roche, Cell Proliferation Kit II).

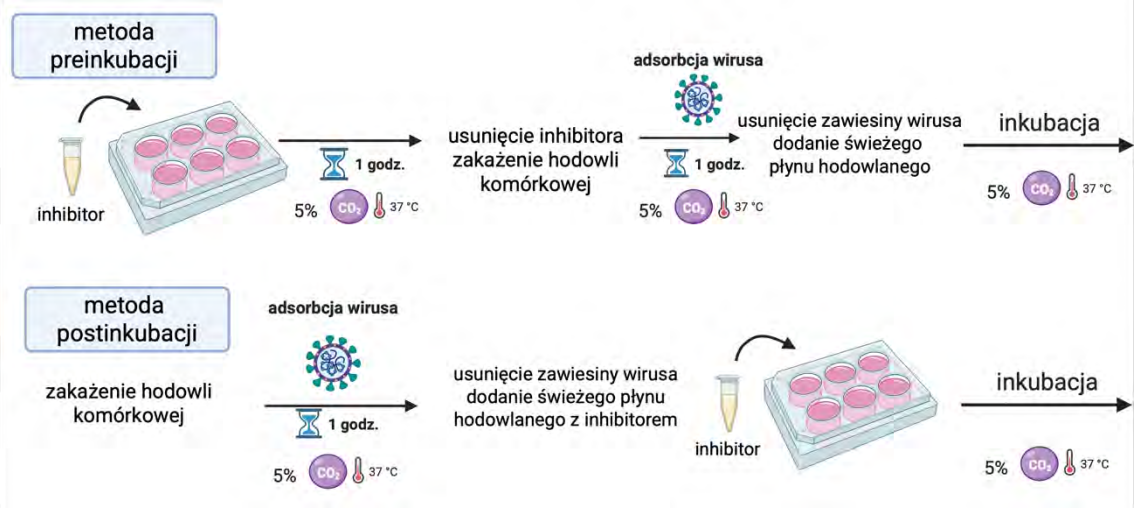

Rycina 1. Schemat przedstawiający metodę pre- oraz postinkubacji z inhibitorami komórkowymi.

Tabela 1. Startery i sekwencja sondy wykorzystane do RT-qPCR.

Starter	**Sekwencja**	**AC_000192.1 zakres regionu**	**Długość produktu**
MHV_L_full	TTGGCTTGTGAGTGACGCCTG	28 571 – 28 591	806 pz
MHV_R_full	GCGCATACACGCAATTGAACAT	39 376 - 29 355	
MHV_L_v2	GTATGGTATGTGGGGCAGATTA	28 906 – 28 927	88 pz
MHV_R_v2	GTTTAATAGACGCAAGGAAGGC	28 993- 28 972	
Probe 5` 6-FAM 3` TAMRA	AGTCGCAGTGTGTTTGATGGTCACC	28 935 – 28 959	Nie dotyczy

Trzeci etap badań dotyczył scharakteryzowania procesu uwalniania wirionów potomnych SDAV z neuronów hodowanych *in vitro*. Do realizacji tego etapu posłużyło istotne w procesie replikacji i uwalniania wirionów potomnych z endosomów VCP (Q. Wang i in., 2010). Dodatkowo sprawdzono wpływ inhibitora, Eeyarestatyny I (EerI), oddziałującego na VCP na szlaku ERAD (w stężeniu 5 µM/mL i 25 µM/mL ustalonym w teście XTT (Roche, Cell Proliferation Kit II, w systemie wyżej opisanej pre- i postinkubacji (Ryc.1)) na wydajność uwalniania wirionów potomnych z komórki. Analiza jakościowa zakażenia została oceniona za pomocą mikroskopii konfokalnej (analiza morfologiczna komórek po zakażeniu SDAV oraz odziaływania z VCP) i

przyżyciowego systemu monitoringu hodowli komórkowej (ocena morfologiczna i żywotności komórek pierwotnych neuronów po miesiącu od zakażenia SDAV), oraz ilościowo przy pomocy techniki analizy wysoko przepustowej z wykorzystaniem mikroskopów Operetta® CLS™ (Revvity™) oraz Array Scan XTI (ThermoFisher™). Do analizy użyto programu HCS studio software (wersja 2.0) do wyznaczenia obszarów z pożądaną immunofluorescencją (w tym jednostek tworzących ognisko FFU/mL) oraz Harmony software (wersja 4.9) do wyliczenia ilość antygenu wirusowego SDAV i antygenu VCP przed użyciem inhibitorów i po traktowaniu komórek (określona jako średnia fluorescencja zliczana ze wszystkich komórek w dołku hodowlanym lub ilości punktów korespondujących z sygnałem odpowiedniego antygenu na pojedynczą komórkę).

Ostatni **czwarty etap badań** został poświęcony odpowiedzi komórkowej, a w szczególności wyrzutowi cytokin stanowiących główny element neuropatogenezy chorób o etiologii wirusowej. Astrocyty, najliczniejsze komórki w OUN, są heterogeniczne i wielofunkcyjne, a niedawno odkryto, że są częścią glejowego układu limfatycznego (glimfatycznego) OUN, podobnie jak mikroglej (Domingues i in., 2016). W tym etapie zbadany został wpływ zakażenia MHV-JHM i SDAV na mikroglej i astrocyty hodowane *in vitro* poprzez analizę produkcji ROS, cytokin i chemokin oraz śmierci komórek, w przebiegu miesięcznego zakażenia. W tym celu wykorzystano metody jakościowe - mikroskopię konfokalną (analiza morfologii pierwotnej hodowli i określenie fenotypu przy użyciu markerów dla komórek OUN – GFAP dla astrocytów, NeuN dla neuronów i CD11b dla mikrogleju oraz ocena produkcji ROS po zakażeniu MHV-JHM i SDAV) oraz metody ilościowe - cytometrię przepływową (ocena fenotypu pierwotnej hodowli komórkowej w 7 i 14 dniu hodowli oraz ocena żywotności, śmierci komórki i wytwarzanych ROS po miesiącu od zakażenia), wysokoprzepustowy test immunologiczny (ProcartaPlex™ Mouse Immune Monitoring Panel, 48plex, ThermoFisher™) dla 48 cytokin i chemokin odczytany przy pomocy systemu Luminex® (Tabela 2) oraz klasyczny test ELISA dla wybranych cytokin (IL-4, IL-5, IL-6, IL-10 IL-17, TNF alfa, Mouse DuoSet®, RiD Systems) z płynu pobranego znad hodowli podczas miesięcznego zakażenia mikrogleju i astrocytów.

Tabela 2. Lista 48 białek składających się na zestaw ProcartPlex™ Mouse Immune Monitoring Panel (Thermofisher™).

Typ	Lista
Cytokiny	BAFF, G-CSF (CSF-3), GM-CSF, IFN alfa, IFN gamma, IL-1 alfa, IL-1 beta, IL-2, IL-3, IL-4, IL-5, IL-6, IL-7, IL-9, IL-10, IL-12p70, IL-13, IL-15/IL-15R, IL-17A (CTLA-8), IL-18, IL-19, IL-22, IL-23, IL-25 (IL-17E), IL-27, IL-28, IL-31, IL-33, LIF18, M-CSF, RANKL, TNF alfa
Chemokiny	ENA-78 (CXCL5), Eotaxin (CCL11), GRO alfa (CXCL1), IP-10 (CXCL10), MCP-1 (CCL2), MCP-3 (CCL7), MIP-1 alfa (CCL3), MIP-1 beta (CCL4), MIP-2, RANTES (CCL5)
Czynniki/ regulatory wzrostu	Betacelulina (BTC), Leptin, VEGF-A
Receptory	IL-2R, IL-7R alfa, IL-33R (ST2)

Analiza statystyczna i graficzne opracowanie wyników

W każdym, z prezentowanych artykułów oryginalnych wyniki zostały poddane analizie statystycznej jednoczynnikową lub dwuczynnikową analizą wariancji (ANOVA) z testem post-hoc (Tukey lub Dunnet) oraz przy użyciu testów nieparametrycznych Kruskal–Wallis i Friedman z testem post–hoc (Dunn) lub niesparowanym testem t studenta z wykorzystaniem granicznej wartości p i korekty wielokrotnych porównań Šídák-Bonerroni. Analizy zostały wykonane przy pomocy programu GraphPad™ (wersja, 9.4.0 (453), GraphPad Software Inc.). Każdy z eksperymentów był wykonany przynajmniej w trzech powtórzeniach biologicznych i technicznych. Wyniki uzyskane dla komórek zakażonych były porównywane do komórek niezakażonych, podobnie, jeśli komórki były traktowane związkami wpływającymi na replikację wirusów, zmiany porównywano między grupami traktowanymi i nietraktowanymi. Różnice statystyczne uważano za wysoce istotne przy $p \leq 0{,}001$, za istotne dla $p \leq 0{,}05$ i $p \leq 0{,}01$ oraz jako nieistotne dla $p \geq 0{,}05$.

Tabela 3. Zestawienie wykorzystanych przeciwciał i barwników użytych do badań w prezentowanych trzech publikacjach oryginalnych.

Nazwa	**Struktura barwiona/marker**	**Producent**	**Stężenie**
I rzędowe mAb mysie anty– SARS-CoV/SARS-CoV-2 Spike Protein S2 (1A9) II rzędowe Ab kozie anty–mysie Alexa Fluor 488	wirus, białko kolca (podjednostka S2)	ThermoFisher™	I i II rzędowe Ab 1:250
I rzędowe mAb mysie anty–SARS/SARS-CoV-2 N protein II rzędowe Ab: a) kozie anty–mysie AlexaFluor™ 488 b) kozie anty–mysie TexasRed	wirus, białko nukleokapsydu (N)	ThermoFisher™	I rzędowe Ab 1:200 II rzędowe Ab a) 1:500 b) 1:1000
mAb mysie anty-GFAP – Alexa Fluor 488 (koniugat)	astrocyty	ThermoFisher™	1:100
mAb mysie anty-CD11b – APC (koniugat)	mikroglej	ThermoFisher™	1:100
I rzędowe mAb mysie anty-CNP II rzędowe Ab kozie anty-mysie Alexa Fluor 647	oligodendrocyty	ThermoFisher™	I rzędowe Ab 1:100 II rzędowe Ab 1:250
I rzędowe mAb mysie anty-NeuN II rzędowe Ab kozie anty-mysie Alexa Fluor 647	neurony	ThermoFisher™	I rzędowe Ab 1:100 II rzędowe Ab 1:250
Falloidyna – TRITC (koniugat)	F-aktyna	Sigma-Aldrich	500 µg/mL
I rzędowe mAb królicze anty–beta-tubulin III II rzędowe Ab kozie anty-królicze Texas Red	beta-tubulina III	Sigma Aldrich	I rzędowe Ab 1:200 II rzędowe Ab 1:2000
I rzędowe mAb królicze anty-VCP II rzędowe Ab kozie anty-królicze Texas Red™-X	VCP	ThermoFisher™	I rzędowe 1:500 IF 1:1000 WB II rzędowe 1:500
I rzędowe mAb mysie anty-GAPDH II rzędowe królicze anty-mysie-HRP (koniugat)	GAPDH	ThermoFisher™	I i II rzędowe Ab 1:5000 WB
Aglutynina kiełków pszenicy -wheat germ agglutinin (WGA) – Alexa Fluor™ 647 (koniugat)	reszty N-acetylo-D-glukozaminy i kwasu sialowego (błony komórkowe)	ThermoFisher™	10µg/mL
Hoechst 33258	jądro komórkowe	ThermoFisher™	1µg/mL

6. Najważniejsze wyniki badań

6.1. **Publikacja I**

<u>Bartak, M.,</u> Bąska, P., Chodkowski, M., Tymińska, B., Bańbura, M. W., i Cymerys, J. (2024). Neurons cytoskeletal architecture remodeling during the replication cycle of mouse coronavirus MHV-JHM: a morphological in vitro study. BMC veterinary research, 20(1), 18. https://doi.org/10.1186/s12917-023-03813-y

W pierwszym artykule oryginalnym zrealizowane zostały pierwsze cztery zadania badawcze dotyczące MHV-JHM. Celem badania była charakterystyka morfologiczna mikrofilamentów aktynowych i mikrotubul oraz sprawdzenie wpływu wybranych związków chemicznych zaburzających układ cytoszkieletu komórkowego na zakażenie MHV-JHM w pierwotnych neuronach pochodzących od myszy Balb/c(H-d^2). Obserwacja morfologii (mikroskopia konfokalna, przyżyciowa ocena żywotności neuronów) została poprzedzona analizą ilościową (RT-qPCR) weryfikującą poziom replikacji wirusa (ilość kopii/µg RNA) przed i po potraktowaniu komórek inhibitorami wpływającymi na dystrybucję filamentów aktynowych i mikrotubul.

Wyniki badań związanych z filamentami aktynowi oraz ich udziałem w zakażeniu MHV-JHM potwierdziły nieprzewidywalną naturę rodziny *Coronaviridae*. W początkowej fazie zakażenia zaobserwowano dynamiczną reorganizację F-aktyny (filamenty aktynowe), która częściowo ułatwiała wniknięcie wirionów MHV-JHM do ciała neuronu (somy) (Publikacja I, Ryc. 4, 5, 6). W 2 godz. p.z., zaobserwowano kondensację filamentów aktynowych w postaci pierścieni podbłonowych (Publikacja I, Ryc. 5A, a" zielony grot strzałki; Ryc. 6A, biała gwiazdka) i jej rozluźnienia w strefie okołojądrowej (Publikacja I, Ryc. 5A, a”, biała gwiazdka; Ryc. 6A, żółta strzałka). Zauważalne były również liczne antygeny wirusowe w długich wypustkach zwanych filopodiami (Ryc. 5A, a’’, biały grot strzałki) oraz nagromadzenie się antygenu wirusowego w obszarze okołojądrowym (Publikacja I, Ryc. 5A, a’, żółty kwadrat, zielony grot strzałki). Liczne zmiany w morfologii komórek zostały zaobserwowane po 24 godz. p.z, po pełnym cyklu replikacyjnym wirusa. Neurony pierwotne po zakażeniu MHV-JHM tworzyły liczne połączenia międzykomórkowe w postaci podłużnych filamentów aktynowych, służących prawdopodobnie do transportu cząstek wirusowych (Publikacja I, Ryc. 5B, b’, białe groty strzałek). Co więcej, dostrzeżono liczne struktury nanorurek (TNT, ang. tunneling nanotubes), w których obserwowano antygeny MHV-JHM, przez cały okres zakażenia (Publikacja I, Ryc. 5B, b” zielone groty strzałek, żółty kwadrat).

Można było wyróżnić struktury cienkich mostów i grubszych połączeń TNT (Publikacja I, Ryc. 5B, b', b'', białe groty strzałek) Co ciekawe, największa liczba tych struktur aktynowych pojawiła się po 168 godz. p.z. (Publikacja I, Ryc. 5E, e'', biały grot strzałki, żółty kwadrat). Inne zaobserwowane zmiany morfologiczne obejmowały: zmniejszenie liczby długich wypustek na rzecz krótkich (Publikacja I, Ryc. 5C, c', c'', białe gwiazdki) i tworzące się obwodowe włókna naprężeniowe w postaci silnie skondensowanych włókien F-aktyny po 48 godz. p.z. (Publikacja I, Ryc. 5C, c', c'', żółte groty strzałek) oraz defragmentacja sieci włókien aktynowych z występującą silnie skondensowaną F-aktyną w miejscach dużego nagromadzeniem antygenu wirusowego, obecnego w regionie okołojądrowym po 72 godz. p.z. (Publikacja I, Ryc. 5D, d', d''). Prawidłowa dynamika struktury filamentów aktynowych została przywrócona po 168 godz. p.z. (Publikacja I, Ryc. 5E). Zaobserwowano w tym czasie ciekawe struktury wskazujące na efekt cytopatyczny w postaci tak zwanej „sieci pajęczej" (Publikacja I, Ryc. 5E, e', żółty kwadrat), w których nie doszło do depolimeryzacji aktyny oraz klasycznych syncytiów (Publikacja I, Ryc. 5E, e'', żółty grot strzałki). Znaczna liczba struktur TNT, łączyła ze sobą dwie odległe komórki nerwowe służąc jako swoista droga dla przemieszczającego się antygenu wirusowego (Publikacja I, Ryc. 7A, a'', białe strzałki). Analiza kolokalizacji ilościowej antygenu wirusowego i struktury TNT podczas całego zakażenia wykazała wysokie wartości (PCC = 0,73 ± 0,18; M1 = M2 = 0,93), podkreślając istotność tej struktury w przebiegu zakażenia MHV-JHM (Publikacja I, Ryc. 8).

Analogicznie przeprowadzono analizę ilościową RT-qPCR, aby potwierdzić rolę cytoszkieletu aktynowego w zakażeniu MHV-JHM z użyciem inhibitorów – cytochalazyny D i latrunkuliny A (Publikacja I, Ryc.11). Te dwa inhibitory, zmieniające polimeryzację aktyny, nie wpłynęły na wydajność wnikania wirusa do komórki (po 2 godz. p.z.), oraz efektywność replikacji MHV-JHM w 24 godz. p.z. w porównaniu do komórek zakażonych nietraktowanych. W późniejszych etapach zakażenia – po 72 godz. p.z., efekt obniżający wydajność replikacji MHV-JHM był widoczny przez spadek o trzy logarytmy liczby kopi wirusa po zastosowaniu cytochalazyny D w postinkubacji ($6{,}1x10^4$) i latrunkuliny A w preinkubacji ($8x10^4$), w porównaniu do kontroli nietraktowanej ($1{,}2x10^7$).

Analizując wyniki badań dotyczących udziału mikrotubul w zakażeniu MHV-JHM w neuronach, dowiedziono, że odgrywają one niezwykle istotną rolę podczas zakażenia. Interpretacja zdjęć z mikroskopu konfokalnego pozwoliła dostrzec

przemieszczające się wiriony (antygen białka nukleokapsydu) między neuronami w długich wypustkach aksonalnych i neurytach, już po 2 godz. p.z. (Publikacja I, Ryc.10A, zielone groty strzałek i żółty prostokąt). Co ciekawe, w 48 godz. p.z. (Publikacja I, Ryc. 10C, c', c'' żółty kwadrat, żółte i białe groty strzałek) i w 72 godz. p.z. (Publikacja I, Ryc. 10D, d'' żółte i zielone groty strzałek) obecność MHV-JHM wyraźnie wpłynęła na zaburzenie układu mikrotubul, prowadząc do ich depolimeryzacji, degradacji komórek i tworzenia syncytiów (Publikacja I, Ryc.10C, c'', c'', żółty kwadrat, białe groty strzałek). Pomimo tych zmian, komórki nadal były zdolne do transportu wirionów potomnych. Neurony wciąż wytwarzały długie wypustki, a wiriony gromadziły się w charakterystycznych strukturach cystern zlokalizowanych w neurytach (Publikacja I, Ryc. 10D, d'', fioletowe groty strzałek). W czasie 168 godz. p.z. antygen wirusowy wciąż był obecny w dużych ilościach i współwystępował ze strukturami mikrotubul, które pozostały nienaruszone, a komórki nie uległy degradacji (Publikacja I, Ryc. 10E, e', e''), w porównaniu do komórek niezakażonych (Publikacja I, Ryc. 8).

Wyniki otrzymane z analizy obrazów z mikroskopu konfokalnego zostały potwierdzone przez RT-qPCR, podobnie jak w przypadku analizy cytoszkieletu aktynowego. Po pre- i postinkubacji z czynnikiem depolimeryzującym mikrotubule – nokodazolem, czynnikiem stabilizującym – noskapiną oraz paklitakselem, zaobserwowano znaczne ograniczenie poziomu replikacji MHV-JHM (Publikacja I, Ryc.11). Najbardziej obiecujące wyniki uzyskano podczas postinkubacji z noskapiną w 72 godz. p.z., gdzie nastąpił spadek o cztery logarytmy ($7{,}6x10^3$), w porównaniu do kontroli nietraktowanej zakażonej ($1{,}2x10^7$) oraz stosując preinkubację z nokodazolem ($2{,}3x10^4$) w 168 godz. p.z., gdzie nastąpił spadek o sześć logarytmów, w porównaniu do kontroli pozytywnej (10^{10}).

Podsumowując, badanie potwierdziło, że MHV-JHM w czasie tygodniowego zakażenia nie powoduje degradacji komórek pierwotnej hodowli neuronów mysich, i wpływa na strukturę cytoszkieletu od momentu wniknięcia wirusa aż do uwolnienia wirionów potomnych (Publikacja I, Ryc. 3). Struktury TNT, są wykorzystywane podczas transportu między-komórkowego MHV-JHM, unikającego uaktywnienia odpowiedzi komórkowej. Dzięki zastosowaniu inhibitorów aktyny stwierdzono, że cytoszkielet aktynowy odgrywa istotniejszą rolę przy składaniu i wychodzeniu wirionów potomnych z neuronów. Natomiast mikrotubule pełnią główną rolę w wewnątrzkomórkowym transporcie wirionów MHV-JHM do miejsca replikacji, a następnie między komórkami.

Odkrycie to zostało potwierdzone dzięki zastosowaniu inhibitorów noskapiny i nokodazolu, które skutecznie zmniejszyły replikację MHV-JHM w neuronach.

6.2. **Publikacja II**

<u>Bartak, M.</u>, Krahel, W. D., Chodkowski, M., Grel, H., Walczak, J., Pallepati, A., Komorowski, M., i Cymerys, J. (2024). ATPase Valosin-Containing Protein (VCP) Is Involved During the Replication and Egress of Sialodacryoadenitis Virus (SDAV) in Neurons. International journal of molecular sciences, 25(21), 11633. https://doi.org/10.3390/ijms252111633

W drugim artykule oryginalnym zrealizowane zostały pierwsze trzy zadania badawcze dotyczące SDAV oraz zadanie piąte. W celu ustalenia, w jaki sposób SDAV uzyskuje dostęp do neuronów i jak następnie je opuszcza, skupiono się na małej cząsteczce, ATPazie, białku zawierającym walozynę (VCP, ang. valosin containing protein). VCP jest znane ze swojej funkcji w proteasomalnej degradacji białek, w tym białek pochodzenia wirusowego, za pośrednictwem ubikwityny. Do sprawdzenia hipotezy o potencjalnym wpływie VCP na replikację i uwalnianie się wirionów potomnych SDAV, zastosowano wysokoprzepustową mikroskopię konfokalną (Operetta® CLS™ i Array Scan XTI HCS). Określono miano wirusa (FFU/mL), ilość antygenów wirusowych (średnia fluorescencji oraz liczba punktów sygnału fluorescencyjnego antygenu wirusowego na komórkę) oraz ilość białka VCP (średnia fluorescencji oraz liczba punktów sygnału fluorescencyjnego antygenu VCP na komórkę). W celu ustalenia względnej produkcji VCP zastosowano również analizę Western blot. Przeprowadzono obrazowanie w czasie rzeczywistym komórek zakażonych SDAV (JuliBR™) i analizę morfologii komórek w mikroskopie konfokalnym.

Jako pierwszą przeprowadzono analizę przyżyciową hodowli pierwotnych neuronów, która umożliwiła potwierdzenie zakażenia SDAV i produktywną replikację bez konieczności adaptacji. Jest to pierwsza tego typu obserwacja zakażonych przez SDAV mysich neuronów pierwotnych *in vitro*. Obecność wirusa wykryto w postaci syncytialnego, ogniskowego oraz rozproszonego efektu cytopatycznego (Publikacja II, Ryc. 1A, czerwone strzałki). Wartość miana wirusa była wysoka i osiągała wartość PFU = 10^6 oraz log10 FFU/mL = 2,193 ± 0,15 (Publikacja II, Ryc. 2A, B). Istotnym jest, że obserwację zakażonej pierwotnej hodowli neuronów prowadzono przez miesiąc (672 godziny), w czasie którego nie zanotowano drastycznego obniżenia żywotności neuronów, a pierwszy, syncytialny efekt cytopatyczny, pojawił się po 276 godz. p.z. Drugi efekt replikacji SDAV w neuronach - efekt cytopatyczny ogniskowy, odnotowano po 454 godz. p.z., przy jednoczesnym obniżeniu pokrycia hodowli neuronów do 83% w porównaniu do punktu początkowego monitorowania żywotności (97,66%) (Publikacja

II, Ryc. 1A,B, czerwone strzałki). Hodowla neuronów po 628 godz. p.z., utrzymała pokrycie na poziomie 23,9%. Po 672 godz. p.z. nastąpił nagły spadek do poziomu 6%, natomiast nadal widoczne były neurony, charakteryzujące się poprawną morfologią. (Publikacja II, Ryc. 1A, B, pomarańczowa strzałka). Po ustaleniu wykorzystywanego miana wirusowego przeprowadzono ilościową ocenę replikacji SDAV w neuronach w ciągu 24 godzin z uwzględnieniem czasów od 0 do 4 godzin dla prześledzenia kinetyki transportu wirusa do komórek. Zastosowano wysokoprzepustową mikroskopię konfokalną i pomiar średniej intensywności fluorescencji odpowiadającej znakowanemu białku nukleokapsydu (N) SDAV (Rycina 3A, B). Analiza wykazała, że w porównaniu z komórkami ocenianymi w 0 godz. p.z. (czas po adsorpcji wirusa do komórki) zaobserwowano wysoce istotny statystycznie (*** $p \leq 0,001$) wzrost średniej intensywności fluorescencji po 24 godz. p.z. (n=400), potwierdzający skuteczne wniknięcie SDAV do neuronów oraz zakończenie pełnego cyklu replikacyjnego wirusa (Publikacja II, Ryc. 3B). Analiza morfologiczna zdjęć z mikroskopu konfokalnego, po 24 godz. p.z., umożliwiła obserwację antygenu wirusowego zlokalizowanego w okolicy podbłonowej neuronów oraz przemieszczającego się wzdłuż neurytów do sąsiednich komórek (Publikacja II, Ryc. 4C, a, białe strzałki).

Kolejnym etapem tego badania było sprawdzenie roli VCP w replikacji SDAV, co rozpoczęto od określenia jego poziomu (intensywność fluorescencji) w zakażonych komórkach pierwotnych neuronach, przez 24 godziny w odniesieniu do komórek niezakażonych (Publikacja II, Ryc. 5A, B). Zaobserwowano wysoce istotny statystycznie (** $p \leq 0,01$) wzrost średniej intensywności fluorescencji odpowiadającej VCP po 24 godz. p.z., co może sugerować zwiększoną produkcję tego białka w neuronach w wyniku zakażenia SDAV (Publikacja II, Ryc. 5B). Podobną zależność zauważono po analizie morfologicznej zdjęć konfokalnych, gdzie intensywna fluorescencja odpowiadająca sygnałowi białka VCP współwystępowała z sygnałem emitowanym przez białko wirusowe w obszarze okołojądrowym (Publikacja II, Ryc. 4C, żółta strzałka). Przeprowadzona analizę Western blot potwierdziła zmianę w ilości VCP podczas 24-godzinnego zakażenia. Odnotowano istotny statystycznie (* $p \leq 0,05$) wzrost względnej produkcji VCP w komórkach zakażonych (12 ± 1,1), w porównaniu do komórek kontrolnych niezakażonych (9 ± 0,98) (Publikacja II, Ryc. 7C, D).

Następnie, po zaobserwowaniu tej zależności, istotne było sprawdzenie roli VCP w procesie replikacji SDAV, ze szczególnym uwzględnieniem etapu jego zaangażowania podczas wewnątrzkomórkowej syntezie wirionów potomnych. W tym celu zastosowano inhibitor VCP – Eeyarestatynę I (EerI), w systemie pre- i postinkubacji (Ryc.1). Relatywny poziom produkcji białka po inkubacji z EerI spadł, istotnie statystycznie ($p < 0,05$), w obu metodach inkubacji, w porównaniu do pozytywnej zakażonej kontroli (preinkubacja z EerI o stężeniu 5 μM/mL (10 ± 1,1 vs. 12 ± 1,1), 25 μM/mL (9 ± 0,95 vs. 12 ± 1,1) i postinkubacja z 5 μM/mL (8,7 ± 0,4 vs. 12 ± 1,1) i 25 μM/mL (5 ± 1,0 vs. 12 ± 1,1)) (Publikacja II, Ryc. 7C, D). Ilościowa analiza wysokoprzepustowej mikroskopii konfokalnej (Operetta® CLS™) ujawniła wysoce istotny statystycznie *(*** $p \leq 0,001$*) wzrost poziomu VCP w grupie kontrolnej zakażonej, nietraktowanej inhibitorem EerI, po 24 godz. p.z. w porównaniu do komórek kontrolnych niezakażonych (29,96 ± 9,35 vs. 9,52 ± 6,1) (Publikacja II, Ryc. 8C). Istotny statystycznie spadek (** $p \leq 0,05$) w porównaniu do kontroli pozytywnej wystąpił jedynie po postinkubacji z 5 μM/mL EerI po zakażeniu (29,96 ± 9,35 vs. 14,61 ± 4,19) (Publikacja II, Ryc. 8C). W pozostałych warunkach inkubacji nie zaobserwowano istotnych zmian poziomu produkcji VCP, co może wynikać z działania EerI, jego powinowactwa do retikulum endoplazmatycznego oraz braku możliwości oddziaływania z VCP zlokalizowanymi w innych organellach lub cytoplazmie. W kontekście analizy ilości sygnału korespondującego z białkiem N SDAV po traktowaniu EerI zaobserwowano wysoce istotny statystycznie (** $p \leq 0,01$) spadek liczby punktów sygnału na komórkę w metodzie preinkubacji 25 μM/mL (69,07 ± 12,5) EerI oraz postinkubacji z 5 μM/mL (63,17 ± 11,5) EerI, w porównaniu do kontroli pozytywnej (zakażonej, nietraktowanej) (153,87 ± 26,7) (Publikacja II, Ryc. 8B). Wskazuje to na prawdopodobny udział VCP w późniejszym etapie replikacji – podczas uwalniania strukturalnych białek wirusowych z retikulum endoplazmatycznego. Interesującą obserwacją, potwierdzającą rolę VCP w późnych etapach replikacji wirusa było nagromadzenie sygnału antygenu wirusowego w obszarze pod błonowym neuronu po postinkubacji z 5 μM/mL EerI (Publikacja II, Ryc. 6B, b', d'), białe strzałki). Co ciekawe, podczas morfologicznej analizy zdjęć z mikroskopu konfokalnego, nie wykryto obecności antygenu wirusowego w wypustkach komórkowych, jak to miało miejsce w nietraktowanych komórkach zakażonych (Publikacja II, Ryc. 4C, białe strzałki). Tym samym wydajniejszy efekt hamujący składania wirionów potomnych wystąpił podczas stosowania metody postinkubacji z inhibitorem EerI (Publikacja II, Ryc. 6, 7, 8, 9).

Ostatni etap badania stanowił potwierdzenie skuteczności metody postinkubacji z EerI i obniżenia efektywności replikacji SDAV. W tym celu początkowo wyznaczono miano SDAV, po inkubacji z inhibitorem EerI w stężeniach 5 μM/mL i 25 μM/mL, a następnie wykorzystano zebrany po 24 godz. p.z. płyn hodowlany znad komórek, aby sprawdzić, czy hamowanie VCP przez EerI wpływa na uwalnianie wirionów potomnych SDAV z neuronów (Publikacja II, Ryc. 9A, B). Analiza potwierdziła hipotezę, wskazując, że powtórne mianowanie wykazało wysoce istotne statystycznie (*** $p \leq 0{,}001$) zmniejszenie miana wirusa. Zastosowanie EerI w stężeniu5 μM/mL spowodowało spadek log10 FFU/mL o 0,840 logarytmu w rozcieńczeniu 10^{-3} (1,96 ± 0,53 nietraktowane do 1,12 ± 0,41 traktowanego 5 μM/mL EerI) (Publikacja II, Ryc. 9B, d').

6.3. **Publikacja III**

<u>Bartak, M.,</u> Krahel, W. D., Gregorczyk-Zboroch, K., Chodkowski, M., Potârniche, A. V., Długosz, E., Krzyżowska, M., i Cymerys, J. (2025). Cytokine Profile Analysis During Sialodacryoadenitis Virus and Mouse Hepatitis Virus JHM Strain Infection in Primary Mixed Microglia and Astrocyte Culture-Preliminary Research. Cells, 14(9), 637. https://doi.org/10.3390/cells14090637

Trzecia praca oryginalna, składająca się na cykl rozprawy, stanowi wypełnienie ostatniego zadania badawczego, ale również swoiste porównanie natury obu wirusów będących przedmiotem tej dysertacji. Celem niniejszego badania było sprawdzenie wpływu dwóch zwierzęcych betakoronawirusów - Mouse Hepatitis Virus (MHV) i Rat Sialodacryoadenitis Virus (SDAV) na mikroglej i astrocyty hodowane *in vitro*, ze szczególnym uwzględnieniem analizy poziomów produkcji cytokin i chemokin wydzielanych przez te komórki w odpowiedzi na zakażenie. Szczep JHM mysiego koronawirusa jest neuropatogenny, natomiast SDAV charakteryzuje się wysokim potencjałem zoonotycznym i neurotropowym, który został potwierdzony w opisywanej dysertacji.

Pierwszym etapem badania było sprawdzenie zdolności SDAV do zakażenia mikrogleju i astrocytów. Obserwacja wybarwionych immunofluorescencyjnie preparatów w mikroskopie konfokalnym potwierdziła obecność antygenu wirusowego SDAV i MHV-JHM, zarówno w astrocytach jak i mikrogleju (Publikacja III, Ryc. 1A). Jednocześnie sprawdzono również zdolność MHV-JHM do zakażenia tych samych komórek. W tym przypadku udało się również zauważyć charakterystyczny dla MHV-JHM efekt cytopatyczny w postaci syncytium po 72 godz. p.z (Publikacja III, Ryc. 1 B, biały kwadrat).

Docelowe badanie było prowadzone przez miesiąc, dlatego ważnym etapem było sprawdzenie żywotności komórek (określenie poziomu apoptozy/nekrozy) po zakażeniu SDAV i MHV-JHM. Oba wirusy indukowały apoptozę w mikrogleju i astrocytach, co potwierdziła analiza z użyciem techniki cytometrii przepływowej i znakowania komórek anneksyną V-FITC oraz jodkiem propidyny (JP) (Publikacja III, Ryc. 2A, B). Barwienie to pozwoliło określić komórki znajdujące się w stanie wczesnej apoptozy (anneksyna V-FITC+/JP-), późnej apoptozy (anneksyna V-FITC+/JP+), czy nekrozy (anneksyna V-FITC-/JP+), lub nieapoptotycznym (anneksyna V-FITC-/JP-). MHV-JHM wywoływał wczesną apoptozę już w ciągu 2 godz. p.z., utrzymując podwyższony poziom przez cały miesięczny okres zakażenia (Publikacja III, Ryc. 2A). Komórki zakażone SDAV

wykazywały podobną wczesną odpowiedź apoptotyczną, przy istotnym wzroście późnej apoptozy w 48 i 168 godz. p.z. (Publikacja III, Ryc. 2B). Warto podkreślić, że komórki nekrotyczne występowały w nieznacznej liczbie po zakażeniu SDAV, w przeciwieństwie do niewielkiego wzrostu obserwowanego po miesiącu zakażenia MHV-JHM (Publikacja III, Ryc. 2A, B).

Kolejny etap badań stanowiła analiza ilości wytwarzanych reaktywnych form tlenu (ROS). W tym celu wykorzystano barwienie immunofluorescencyjne z użyciem barwnika CellROX Green. Kontrolę negatywną stanowiły komórki nie zakażone a pozytywną komórki traktowane nadtlenkiem wodoru (H_2O_2). Badania wykazały szybki i istotny wzrost produkcji ROS w odpowiedzi na zakażenie zarówno MHV-JHM, jak i SDAV, co potwierdzono cytometrią przepływową (% wydzielanych ROS) oraz analizą zdjęć konfokalnych (poziom całkowitej fluorescencji w komórce, CTCF) (Publikacja III, Ryc.3, 4). Zakażenie MHV-JHM indukowało istotny wzrost poziomu ROS już po 2 godz. p.z., który utrzymywał się na wyższym poziomie niż w komórkach kontrolnych niezakażonych, przez co najmniej tydzień (Publikacja III, Ryc. 3A, B). Zakażenie SDAV prowadziło do produkcji ROS, już po 2 godzinach od zakażenia i utrzymywania podwyższonego poziomu ROS przez cały okres zakażenia (do 1 miesiąca), w porównaniu do kontroli (Publikacja III, Ryc. 4A, B). Analiza zdjęć konfokalnych wykazała obecność ROS w zakażonych komórkach, a analiza ilościowa ujawniła wysoce istotny wzrost poziomu CTCF. Po zakażeniu MHV-JHM najwyższą fluorescencję ROS obserwowano po 72 godzinach, natomiast w przypadku SDAV – po 96 godzinach od momentu zakażenia (Publikacja III, Ryc. 3C, D, 4C, D). Poziom fluorescencji ROS w komórkach zakażonych MHV-JHM, po 72 godzinach oraz SDAV, po 96 i 168 godzinach był porównywalny lub wyższy niż w dodatniej kontroli niezakażonej, traktowanej H_2O_2 (Publikacja III, Ryc. 3D, 4D). Utrzymująca się produkcja ROS sugeruje przedłużający się stan stresu oksydacyjnego w zakażonym mikrogleju i astrocytach, co może nasilać stan neurozapalny i przyczyniać się do rozwoju zapalenia mózgu (encefalopatii).

Ostatni etap badań stanowiło określenie profilu cytokin i chemokin wydzielanych przez mikroglej i astrocyty w odpowiedzi na zakażenie SDAV i MHV, podczas miesięcznej inkubacji z wirusem (672 godziny). Przeanalizowano 48 cytokin, chemokin oraz innych białek istotnych w odpowiedzi zapalnej ośrodkowego układu nerwowego. Użyta metoda (ProcartaPlex™ Mouse Immune Monitoring Panel; system Luminex) bazuje na konwencjonalnym teście ELISA w formacie wysokoprzepustowym – każda metalowa

kulka opłaszczona jest czterdziestoma ośmioma przeciwciałami specyficznymi dla każdego z analitów (Publikacja III, Ryc. 5, 6, 7). Kontrolę stanowił płyn zebrany znad hodowli niezakażonej. Wyniki wykazały, że we wczesnych etapach zakażenia (od 2 godz. p.z.) SDAV indukuje w mikrogleju i astrocytach znacznie szerszy profil cytokin i chemokin, w porównaniu do MHV-JHM (Publikacja III, Ryc. 6A, 7A). Wykazano, że zakażenie SDAV prowadzi do istotnego statystycznie wzrostu poziomu takich cytokin jak: BTC, G-CSF, IFN alfa, IFN gamma, IL-1 alfa, IL-1 beta, IL-3, IL-6, IL-7, IL-10, IL-13, IL-15, IL-23, IL-28, IL-33, leptyna, MCP-3, RANKL oraz VEGF-A. W późniejszej fazie replikacji (od 72 godz. p.z.) zakażenie oboma wirusami promowało znaczny wzrost poziomu cytokin i chemokin, przy czym zakażenie SDAV skutkowało w utrzymaniu wyższego poziomu cytokin w porównaniu do MHV-JHM (Publikacja III, Ryc. 6D–G, 7D–G). Po miesiącu od zakażenia MHV-JHM, najbardziej znaczący wzrost stężenia białek zaobserwowano w przypadku ENA-78, G-CSF, GM-CSF, IL-6, IL-33, MIP-2 alfa oraz VEGF-A (Publikacja III, Ryc. 6G). Warto podkreślić, że w tym czasie po zakażeniu z SDAV indukowane były cytokiny takie jak IL-1 alfa, IL-10, IL-19, IL-23 oraz IL-28, które nie były istotnie podwyższone w zakażeniu MHV-JHM (Publikacja III, Ryc. 7G). W kontekście produkcji chemokin, oba wirusy indukowały istotny wzrost kluczowych chemokin, takich jak IP-10, RANTES, MIP-2 alfa, ENA-78, MCP-1 alfa i RANKL dla MHV-JHM oraz Eotaxin, ENA-78, Gro alfa, IP-10, RANTES, RANKL, MCP-3 i MIP-1 alfa dla SDAV. Wysoki poziom IL-6 prawdopodobnie indukował produkcję IL-10 oraz VEGF-A, co mogło sprzyjać regeneracji komórek na wczesnym i późnym etapie zakażenia (Publikacja III, Ryc. 6, 7, 8). Ograniczona indukcja cytokin przeciwzapalnych, takich jak IL-4 i IL-10, w wyniku zakażenia koronawirusem może stanowić potencjalne wyjaśnienie nasilonej odpowiedzi zapalnej obserwowanej podczas tzw. „burzy cytokinowej”.

.

7. Dyskusja

Koronawirusy stały się zagrożeniem dla ludzkości od wybuchu epidemii SARS w 2003 roku (Matejuk i Ransohoff, 2020). Tematem wciąż wzbudzającym emocje wśród badaczy i epidemiologów jest fakt, że wszystkie zakażenia o etiologii koronawirusowej ludzi są wynikiem przekroczenia bariery międzygatunkowej ludzie-zwierzęta (Ye i in., 2020). W czasach, kiedy jeszcze nie przewidywano, że ewolucja tego patogenu potoczy się w stronę globalnej pandemii COVID-19, pierwsze wzmianki o pokonaniu bariery gatunkowej przez koronawirusa i zakażeniu człowieka miały miejsce w 1975 roku na Bałkanach (Apostolov i in., 1975). Na łamach Lancet opisano patologiczne segmentalne i ogniskowe zmiany stwierdzone w kłębuszkach i kanalikach nerkowych w pooperacyjnych próbkach biopsji nerek od siedmiu pacjentów z klinicznie potwierdzoną endemiczną (bałkańską) nefropatią. Nefropatia bałkańska występowała prawie wyłącznie u osób, które miały bliski kontakt ze zwierzętami gospodarskimi - świniami. Dalsza analiza potwierdziła obecność koronawirusów w próbkach, które zostały wyizolowane od świń, co potwierdziło związek zakażenia koronawirusem odzwierzęcym i powiązaną z tym endemiczną nefropatią u ludzi (Apostolov i in., 1975). Ponad 60% chorób zakaźnych u ludzi jest wywoływanych przez patogeny współdzielone z dzikimi lub domowymi zwierzętami. Organizmy wywołujące choroby odzwierzęce obejmują te, które występują endemicznie w populacjach ludzkich lub enzootycznie w populacjach zwierząt, z częstym przenoszeniem międzygatunkowym na ludzi (Karesh i in., 2012). Rosnąca w ostatnim czasie liczba nowych gatunków koronawirusów jest niepokojąca ze względu na bliskie podobieństwo genetyczne między koronawirusami, których gospodarze są daleko spokrewnionymi zwierzętami. Takie skoki międzygatunkowe mogą powodować niekontrolowane wybuchy chorób odzwierzęcych. Przykłady obejmują: (i) FCoV i CCoV w grupie alfakoronawirusów; (ii) MHV, SDAV, inne gatunki RCoV, HCoV-OC43, BCoV i PHEV; SARS-CoV-1, SARS-COV-2 i MERS-CoV w grupie betakoronawirusów; (iii) IBV, TCoV, oraz nowe gatunki ptasich koronawirusów w grupie gammakoronawirusów (Dhama i in., 2020; Woo i in., 2009). Nie tak dawno, w 2018 r., naukowcy opisali i zdiagnozowali przyczynę śmierci około 25 000 świń (w 2016 roku) z powodu zespołu ostrej biegunki świń (SADS) w południowych Chinach. Czynnikiem etiologicznym SADS okazał się koronawirus HKU-2, którego nosicielem jest nietoperz podkowcowaty (*Rhinolophus*) (Gong i in., 2017; Zhou i in., 2018). Nietoperze podkowcowate są wyjątkowym i efektywnym rezerwuarem, tzw. „naczyniem

mieszającym" do przekraczania bariery międzygatunkowej dla koronawirusów z rodzaju alfa i beta, (Latinne i in., 2024).

W przypadku gryzoni, odnotowano, że 13 z 79 dzikich szczurów wędrownych (*Rattus norvegicus*) wytworzyło przeciwciała przeciwko SARS-CoV-2 (IgG- lub IgM-pozytywne), a u części osobników potwierdzono trwające zakażenie (RT-qPCR). Badanie zostało przeprowadzone w Nowym Jorku na populacji miejskich szczurów a wyniki zrodziły obawy o możliwości utworzenia nowego rezerwuaru zwierzęcego i ryzyka wtórnej zoonozy (Y. Wang i in., 2023). Podobne badanie przeprowadzono pod kątem wirusa SDAV jako modelu transmisji SARS-COV-2 między dzikimi szczurami, w wyniku, którego odkryto, że dalsze rozprzestrzenianie wirusa było możliwe przez seropozytywne, wcześniej zakażone lub zaszczepione osobniki (Zeiss i in., 2021). W innym badaniu dowiedziono, że dziko żyjące myszy (*Mus musculus*) nie były wrażliwe na zakażenie SARS-CoV-2. Jedynie w warunkach laboratoryjnych poprzez zwiększenie powinowactwa wiązania wirusowej domeny receptorowej (RBD ang. receptor binding domain) do mysiego wariantu receptora ACE-2 (mACE2) oraz jedynie w przypadku użycia wariantu SARS-CoV-2 B.1.351(wariant brytyjski, Alfa) możliwe (Pan i in., 2021). Biorąc pod uwagę możliwość koronawirusów do skoków międzygatunkowych, dzięki możliwości adaptacji strukturalnej do receptorów gospodarza (m.in. modyfikacje RBD, zmienność podjednostki S2 białka kolca), persystencji zakażenia oraz wysokiej zakaźności, wyniki zamieszczone w tej pracy stanowią poszerzenie stanu wiedzy na temat betakoronawirusów gryzoni – MHV-JHM oraz SDAV w kontekście koncepcji jednego zdrowia (ang. One Health Approach) oraz modelu neurozakażenia.

Coraz bardziej niepokojące wydają się być częstsze zakażenia ośrodkowego układu nerwowego o etiologii koronawirusowej jak np. wspomniany wcześniej zespół długiego COVID-19 (Panagea i in., 2025) lub niedawno udokumentowany przypadek zakażenia persystentnego SARS-CoV-2 u 92 letniej pacjentki (Valkov i in., 2024). W opublikowanych badaniach z wykorzystaniem MHV-JHM oraz SDAV udowodniono, że oba wirusy w hodowlach pierwotnych neuronów oraz mikrogleju i astrocytów ulegają replikacji przez miesiąc od zakażenia, nie doprowadzając do całkowitego zniszczenia komórek w hodowli (Publikacja I, II, III). Nasuwa się pytanie, jakie mechanizmy molekularne *in vitro* wpływają na ułatwioną neurozjadliwość i zachowanie gospodarza we względnie dobrym stanie? Pierwszą odpowiedzią mogą być mechanizmy związane z wnikaniem wirusa i transportem białek wirusowych do miejsca replikacji.

Jak powszechnie wiadomo, jednym z pierwszych ważnych etapów jest zlokalizowanie receptora komórkowego gospodarza i przyłączenie się odpowiednich białek powierzchniowych wirusa. W przypadku koronawirusów jest to głownie strukturalne, fuzyjne, białko kolca (S), a u niektórych betakoronawirusów jak, MHV i SDAV dodatkowo, białko esterazy hemaglutyniny (HE). Białka te również stanowią o zmienności wirulencji, tropizmie komórkowym a nawet zakresie gospodarza (Y. Wang i in., 2020). Skupiając się na dwóch wspomnianych gatunkach, receptorem o najwyższym powinowactwie wiązania z MHV-JHM jest Ceacam1a, a w przypadku SDAV są to reszty kwasu sialowego powierzchniowych glikoprotein i glikolipidów (Gagneten i in., 1996). Dotychczas nie wyodrębniono konkretnego receptora w przypadku SDAV. Pomimo, że w tej pracy nie przedstawiono wyników dotyczących powyższego zagadnienia, są one zawarte i analizowane w otrzymanym przeze mnie grancie (Preludium20, nr. 2021/41/N/NZ6/04383) dotyczącym „zapomnianego" szczurzego koronawirusa SDAV i wpływu zakażenia na OUN. W procesie wnikania wirusa do komórki oraz późniejszego transportu białek wirusowych uczestniczą elementy cytoszkieletu komórkowego (filamenty aktynowe (AF), mikrotubule (MT) i filamenty pośrednie (IF)). W kontekście wnikania wirusów do komórki najważniejszą rolę odgrywają struktury MT, ponieważ są one zaangażowane we wsteczny transport cząstek wirusa, zwłaszcza w strefie okołojądrowej, oraz AF, które są zaangażowane w ruch w regionie podbłonowym, transport międzykomórkowy, wejście i wyjście wirionów (Wen i in., 2021). W I publikacji badawczej składającej się na cykl rozprawy doktorskiej udowodniono, że AF pełnią istotną rolę w procesie transportu wirionów potomnych MHV-JHM, między komórkami (w strukturach TNT) oraz aktywnie uczestniczą w uwalnianiu wirionów potomnych z neuronów. Podobne zjawisko, określone jako tzw. „serfowanie antygenu wirusowego" zostało opisane u innych przedstawicieli RNA wirusów takich jak wirus Coxaskie i ludzki papillomawirus typu 16 (HPV-16) (Huang i in., 2007; Schelhaas i in., 2008)) oraz u DNA wirusów np.: herpeswirusów (HHV-1, HHV-2, EHV-1) i adenowirusów (Bartak i in., 2022; Cymerys i in., 2013; Dixit i in., 2008; Meier i Greber, 2004; Słońska i in., 2021). W późniejszych etapach zakażenia, filamenty aktynowe promują wydostawanie się wirusa poprzez zagęszczanie i odbudowę struktur włókien naprężeniowych oraz tworzenie licznych TNT (168 godz. p.z). Takie zjawisko zostało wcześniej opisane podczas zakażenia innymi koronawirusami - IBV (wirus zakaźnego zapalenia oskrzeli) i SARS-CoV. Mechanizm ten jest niezbędny

podczas składania wirionów potomnych i ich uwalniania z komórki (Ng i in., 2004; J. Wang i in., 2009).

Jak wynika z przeprowadzonych badań, mikrotubule wydają się być kluczową strukturą komórkową uczestniczącą w transporcie wewnątrzkomórkowym MHV-JHM do miejsca replikacji. W przypadku większości wirusów RNA wczesne etapy wnikania do komórki następują względnie szybko, a replikacja rozpoczyna się wkrótce po wejściu do cytoplazmy. Jednak nawet w przypadku tych wirusów MT odgrywają ważną rolę w szlaku endocytarnym i wydostawaniu się nowych wirionów po ukończeniu cyklu replikacyjnego (Naghavi i Walsh, 2017). Podobne wyniki uzyskano podczas zakażenia MHV-JHM komórek pierwotnych neuronów hipokampa szczura i w komórek OBL-21 (hodowle opuszki węchowej myszy CD.1) (Pasick i Dales, 1994). Co więcej związek między wysokim neurotropizmem i rolą MT można upatrywać w szczególnej interakcji między białkiem tau (ang. tubulin associated unit) a białkiem nukleokapsydu MHV-JHM. Komplementarność aminokwasowa obu białek pokrywała się w 44% podobieństwa i 22% identyczności w strukturze (Kalicharran i Dales, 1995; Pasick i Dales, 1994).

Pozostając przy zagadnieniu transportu wirusa do miejsca replikacji i wyjścia z komórki, w drugiej publikacji badano białko zawierające walozynę (VCP) i jego rolę w replikacji SDAV. Udział białka VCP w zakażeniach wirusowych jest tematem niezwykle ciekawym i dotychczas poznanym dla pikornawirusów (Arita i in., 2012; T. Wang i in., 2017; Wu i in., 2016), flawiwirusów (Phongphaew i in., 2017; Yi i in., 2016; Yi i Yuan, 2017) i koronawirusów (IBV, HCoV 229E, HCoV OC43) (Cheng i in., 2021; Wong i in., 2015), jako czynnik o działaniu pro- i antywirusowym. W przeciwieństwie do wcześniejszych nieudanych prób zakażenia mysich komórek nerwowych *in vitro* (Bhatt i in., 1972), udało się doprowadzić do zakażenia pierwotnych neuronów mysich uzyskanych z myszy Balb/c bez konieczności adaptacji wirusa, z widocznym efektem replikacji w postaci ogniskowego i syncytialnego CPE. Efekt cytopatyczny SDAV w neuronach dostrzeżono po 276 godz. p.z. Natomiast w badaniach na linii komórkowej LBC (komórki płuca szczura) CPE pojawia się po 48 godz. p.z., w postaci ognisk litycznych (Hirano, 1990). Potencjalnym wytłumaczeniem dla pojawienia się efektu syncytialnego po zakażeniu SDAV może być działanie białka kolca (S), które jest znane ze swoich właściwości fuzogennych, a szczególnie podjednostki S2, która destabilizuje błony komórkowe inicjując tym samym ich łączenie (Buchrieser i in., 2020; Mihaescu i in., 2024). Inne wytłumaczenie może łączyć się z zaobserwowanym przy zakażeniu

MHV-2 mechanizmem tworzenia się syncytiów w wyniku fragmentacji i rearanżacji aparatu Golgiego (AG), bez konieczności udziału białka kolca (Lavi i in., 1996). Wynikiem wspierającym to wnioskowanie, może być brak tworzących się syncytiów i ognisk litycznych, po miesiącu od zakażenia neuronów SDAV, po zastosowaniu inhibitora EerI, który pośrednio wpływa na działanie aparatu Golgiego.

Zakażenie SDAV prowadziło również do wzrostu ilości VCP w neuronach, już po 24 godz. p.z, co może wskazywać, że SDAV indukuje produkcję tego białka w neuronach. Wytłumaczeniem tego zjawiska może być związane z wymaganym przez koronawirusy odpowiednim środowiskiem do replikacji, które jest tworzone przez DMV, które pochodzą od EDEMosomów (pęcherzyków powstających z błony retikulum endoplazmatycznego, zawierających regulatory szlaku ERAD). Szczególnie podczas zakażenia betakoronawirusami, komórka intensyfikuje tworzenie EDEMosomów, aby zapobiegać wzmożonemu gromadzeniu się białek wirusowych w retikulum endoplazmatyczne, a w konsekwencji prowadzić do zwiększenia aktywności ERAD i wpływać na uwalnianie białek strukturalnych wirusa (Movaqar i in., 2021; Noack i in., 2014; Reggiori i in., 2010, 2011). Co ciekawe zupełnie odwrotny efekt, obniżenie produkcji VCP, wynikało z zakażenia monocytów człowieka przez SARS-CoV i HCoV-229E (Hu i in., 2012). Więcej odpowiedzi przyniosło zastosowanie inhibitora VCP, EerI. EerI jest substancją, która wykazuje powinowactwo do retikulum endoplazmatycznego ze względu na swoją domenę aromatyczną. Wykazano, że EerI oddziałuje z VCP zlokalizowanym w retikulum endoplazmatycznym poprzez grupę zawierającą nitrofuran (NFC). VCP obecny w tym obszarze jest częścią ERAD, szlaku związanego z degradacją białek (Q. Wang i in., 2010; Yi i Yuan, 2017). W przeprowadzonym badaniu nie obserwowano wpływu inhibitora na zahamowanie wnikania SDAV do neuronów oraz produkcji samego VCP. Może to być spowodowane działaniem EerI, jego powinowactwem do retikulum endoplazmatycznego i niezdolnością do interakcji z VCP zlokalizowanymi w innych organellach lub w cytoplazmie (Tabata i in., 2021). Tej hipotezie przychyla się również obserwacja obniżonej ilości antygenu wirusowego w komórkowych wypustkach oraz duża ilość antygenu wirusowego w regionie podbłonowym po postinkubacji z EerI, w przeciwieństwie do pozytywnej kontroli. Można spekulować, że zachodzi tutaj zjawisko tzw. „homeostazy białek wirusowych", które kontroluje ilość składowanych białek strukturalnych SDAV w zakażonych neuronach przez system ERAD modulowany

przez inhibitor EerI (Tabata i in., 2021). Inne badania wykazały, że podawanie ksantohumolu lub eeyarestatyny I spowodowało obniżenie miana wirusa Zika (ZIKV) i wirusa Usutu (USUV) w zakażonych komórkach. Odkrycie to jest zgodne z kluczową rolą VCP podczas wewnątrzkomórkowych etapów cyklu replikacji wirusa (Rodrigo i in., 2022). W przypadku SDAV nie zaobserwowano istotnego ograniczenia miana wirusa po ponownym zakażeniu hodowli płynem zebranym znad komórek traktowanych inhibitorem EerI (obniżenie o 0.84 logarytmu). Jednak miesięczna obserwacja przyżyciowa tej hodowli wykazała brak prezentowanego przez SDAV efektu cytopatycznego i nienaruszoną morfologię neuronów, co może być dowodem na działanie ograniczające nie tyle replikację, ale również składanie wirionów potomnych SDAV. Można również spekulować, że poprawna homeostaza proteolityczna wpływa na ograniczenie uwalniania wirusów z neuronów (Chu i in., 2023).

Odpowiadając na postawione powyżej pytanie, neurotropizm SDAV i MHV-JHM, zmiany w cytoszkielecie oraz zachwianie proteostazy w neuronach, potencjalnie skutkujące wystąpieniem stresu siateczki endoplazmatycznej może prowadzić do neurodegeneracji spowodowanej wytwarzaniem neurotoksyn przez obecny w komórkach OUN stres oksydacyjny i wyrzut czynników prozapalnych (Damon J. DiSabato i in., 2016). W związku z tym, kolejnym celem badawczym było sprawdzenie jak zakażenie MHV-JHM i SDAV wpływa na komórki odpowiedzialne za ochronę neuronów – mikroglej i astrocyty. Pierwszą ważną obserwacją opisaną w publikacji III, była utrzymująca się miesiąc po zakażeniu, na bardzo wysokim poziomie, ilość reaktywnych form tlenu (ROS). Ciągła produkcja ROS sugeruje przedłużony stan stresu oksydacyjnego w zakażonym mikrogleju i astrocytach, co potencjalnie wpływa na zaostrzenie neurozapalenia i pojawienie się objawów encefalopatii (Reshi i in., 2014). W przypadku SARS-CoV-2 spekuluje się, że utrzymujący się wysoki poziom ROS związany jest pośrednio lub całkowicie z aktywacją NF-κB i inflamasomu NLRP3, dążąc do wyrzutu cytokin i wystąpienia niewydolności oddechowej (Mehta i in., 2020). W innych badaniach nad SARS-CoV-2 i ramką odczytu ORF6, stwierdzono, że w ludzkich komórkach nerki (HEK-293T) i płuca (A549) człowieka, zakażenie moduluje wewnątrzkomórkową równowagę redoks, wpływając na szlak sygnałowy jądrowego czynnika erytroidalnego 2 (NRF2) i kinazy aktywowanej mitogenami p39 (MAPK), a produkcja białka wt-ORF6 negatywnie wpływa na homeostazę redoks komórek, prowadząc do wzrostu produkcji ROS, wraz ze spadkiem produkcji białka NRF2

i ekspresji kontrolowanych przez niego genów. Uruchomienie tego mechanizmu prowadziło do wzrostu replikacji SARS-CoV-2 (De Angelis i in., 2023).

W trzecim artykule cyklu opisany został panel 48 cytokin, chemokin i innych czynników wydzielanych w odpowiedzi na zakażenie. Wykazano, że zakażenie SDAV prezentuje znacznie bardziej rozbudowaną odpowiedź komórkową i statystycznie istotny wzrost liczby cytokin i chemokin niż MHV-JHM. W szczególności we wczesnym okresie zakażenia SDAV znacznie wzbudziło produkcję BTC, G-CSF, IFN alfa, IFN gamma, IL-1 alfa, IL-1 beta, IL-3, IL-6, IL-7, IL-10, IL-13, IL-15, IL-23, IL-28, IL-33, Leptyny, MCP-3, RANKL, i VEGF-A. Warto zauważyć, że zakażenie SDAV po miesiącu indukowało cytokiny, takie jak IL-1 alfa, IL-10, IL-19, IL-23 i IL-28, które nie były znacząco podwyższone w zakażeniu MHV-JHM. Natomiast zakażenie MHV-JHM wpływało na wzrost ENA-78, G-CSF, GM-CSF, IL-6, IL-33, MIP-2 alfa, and VEGF-A. Za teorią o wystąpieniu wyrzutu cytokin (termin burzy cytokinowej jest pomijany celowo, gdyż badania były prowadzone na hodowli komórkowej) przemawiają wyniki badania nad SARS-CoV-2, które wykazały, że związana z COVID-19 burza cytokinowa (CS) charakteryzuje się podwyższonym poziomem IL-1 beta, IL-6, CXCL10, TNF alfa, IFN gamma, MIP 1 alfa i 1 beta, a także MCP-1, GM-CSF, VEGF i IL-10 (Dharra i in., 2023). Podobnie badania przeprowadzone na astrocytach typu I zakażonych MHV-A59 ujawniły wzrost produkcji cytokin - IL-1 alfa, IL-1 beta, IL-2, IL-15, IL-13, IL-17, wszystkich trzech interferonów i TNF alfa. Co ciekawe zakażenie MHV-A59 wpłynęło na obniżenie produkcji cytokin przeciwzapalnych - IL-4 i IL-10, może stanowić potencjalne wyjaśnienie zwiększonej odpowiedzi zapalnej obserwowanej podczas „burzy cytokinowej" (Lavi i Cong, 2020). Podobny wzorzec podwyższonej produkcji prozapalnych i obniżenia poziomu cytokin przeciwzapalnych zaobserwowano w prezentowanych badaniach, zarówno w przypadku MHV-JHM, jak i SDAV. Tym samym można domniemać, że w pierwotnej hodowli mikrogleju i astrocytów doszło do wystąpienia zespołu wyrzutu cytokin (CRS), który wpłynął na zmianę fenotypu astrocytów i mikrogleju na formy reaktywne (A2 i M2). Dokładna analiza tego zjawiska nie została przeprowadzona w tej publikacji, niemniej jednak warto dodać, że fenotypu komórek glejowych może zmienić się w wyniku zakażenia wirusowego w aktywowane astrocyty i mikroglej, które mogą być neurotoksyczne (fenotyp A1 astrocytów i fenotyp M1 komórek mikrogleju) lub neuroprotekcyjne (fenotyp A2 astrocytów i fenotyp M2 komórek mikrogleju) (Kwon i Koh, 2020). Towarzyszy temu wydzielanie IL-1 alfa, IL-1

beta, IL-6 i TNF oraz CCL-2, CX3CL1, CXCL10, GM-CSF i IL-1, co w efekcie może doprowadzić do neurozapalenia a nastepnie neurodegeneracji (Colonna i Butovsky, 2017; Ding i in., 2021).

Trwający stan prozapalnych w zakażeniu MHV-JHM i SDAV był również wzmocniony indukcją produkcji kluczowych chemokin związanych z odpowiedzią przeciwwirusową. Obejmowały one IP-10, RANTES, MIP-2 alfa, ENA-78, MCP-1 alfa i RANKL dla MHV-JHM oraz eotaksynę, ENA-78, Gro alfa, IP-10, RANTES, RANKL, MCP-3 i MIP-1 alfa dla SDAV. Wysokie wartości chemokin są często skorelowane z ciężkością przebiegu choroby wirusowej. Wysokie wartości IP-10, MCP-1 I MIP-2 alfa są złym prognostykiem w rokowaniach pacjenta podczas COVID-19 (Y. Chen i in., 2020). Co ciekawe, IP-10 wpływa również na regulowanie produkcji innych cytokin czy chemokin takich jak: MCP-3, MCP-1, MIP1 alpha, RANTES, MIP-2 alpha, GRO alpha, IL-7, IL-6, and IFN gamma (Y. Chen i in., 2020; Gudowska-Sawczuk i Mroczko, 2022; Madhurantakam i in., 2023; Y. Yang i in., 2020). Taką zależność można również zauważyć w odniesieniu do MHV-JHM, jak i SDAV. Jedyne porównanie, które zostało opisane w przypadku zakażenia SDAV to badanie przeprowadzone przez Miura i wsp. (2007), które wykazało, że komórki pęcherzyków płucnych typu I zakażone PRC (szczurzy koronawirus Parker'a) i SDAV indukowały produkcję chemokin CINC-2 (GRO), CINC-3 (MIP-2), LIX (ENA-78), MIP-3 alfa i fraktalkiny zarówno 6 godzin, jak i 24 godziny po zakażeniu (Miura i in., 2007). W innym badaniu dotyczącym SDAV, zidentyfikowano chemokiny MCP-1, LIX (ENA-78) i IP-10, których poziom wzrósł znacząco po 12 dniach od zakażenia (Funk i in., 2009).

8. Podsumowanie i Wnioski

Wyniki przedstawione w niniejszej rozprawie stanowią istotny wkład w rozwój nauki w dziedzinie weterynarii oraz w realizację koncepcji „Jednego Zdrowia". Jedną z zasad tej koncepcji jest zapobieganie chorobom odzwierzęcym, co jest obecnie poważnym wyzwaniem na całym świecie w zakresie chorób o etiologii wirusowej (Rajeev i in., 2020). Warto również przypomnieć jak bliskie jest podobieństwo sekwencji białka kolca SDAV do MHV-JHM (86,3%), HCoV-HKU1, HCoV-OC43 (65%) MERS-CoV (40,6%), oraz SARS-CoV-2 (37,7%). Wyniki zaprezentowane w tej rozprawie doktorskiej, dotyczące SDAV są najnowszymi doniesieniami na temat zakażenia w OUN.

Postawione hipotezy okazały się być poprawne: **(i)** cytoszkielet komórek nerwowych jest niezbędny do replikacji koronawirusów neurotropowych. Zmiany jego struktury zachodzą na każdym etapie zakażenia wirusowego, a zastosowanie czynnika destabilizującego elementy cytoszkieletu wpływa istotnie na zahamowanie wydajności replikacji MHV-JHM, **(ii)** Inne struktury komórkowe, aparat Golgiego oraz retikulum endoplazmatyczne i obecne w strukturach ERAD VCP, są powiązane z replikacją SDAV w OUN modulując mechanizmy neuropatogenności oraz neurotropizmu betakoronawirusów, **(iii)** zakażeniu SDAV i MHV-JHM towarzyszy produkcja cytokin prozapalnych z równoczesnym hamowaniem cytokin przeciwzapalnych ulegająca zmianom podczas miesięcznego zakażenia, a **(iv)** długotrwałe zakażenie mikrogleju i astrocytów prowadziło do zwiększenia produkcji reaktywnych from tlenu i zmiany żywotności tych komórek. Pytania, na które nie udało się odpowiedzieć w pełni lub tylko częściowo będą kontynuowane w ramach grantu Preludium 20 i innych przyszłych projektów.

Wnioski jakie wyciągnięto podczas badań przeprowadzonych w ramach prezentowanego doktoratu to:

1. MHV-JHM oraz SDAV replikują się produktywnie w hodowli pierwotnej neuronów, mikrogleju i astrocytów bez konieczności adaptacji.
2. Cytoszkielet aktynowy neuronów jest wykorzystywany do składania i uwalniania wirionów potomnych MHV-JHM, zaś mikrotubule używane są w procesie transportu wewnątrzkomórkowego.
3. Zakażenie MHV-JHM w pierwotnych neuronach indukuje tworzenie długich połączeń międzykomórkowych (TNT) służących do rozprzestrzeniania zakażenia między komórkami z pominięciem aktywacji układu immunologicznego.

4. W procesie składania i uwalniania wirionów potomnych SDAV z neuronów istotną rolę pełni białko zawierające walozynę (VCP).
5. Produkcja cytokin i chemokin prozapalnych w mikrogleju i astrocytach oraz ograniczenie wytwarzania cytokin przeciwzapalnych podczas zakażenia MHV-JHM i SDAV może sugerować wystąpienie syndromu wyrzutu cytokin (CRS).
6. Utrzymujący się w przebiegu miesięcznego zakażenia MHV-JHM i SDAV wysoki poziom reaktywnych form tlenu (ROS) prawdopodobnie wpływa na zaostrzenie neurozapalenia.

Bibliografia

1. Apostolov, K., Spasic, P., i Bojanic, N. (1975). Evidence Of a Viral Ætiology In Endemic (Balkan) Nephropathy. *The Lancet*, *306*(7948), 1271–1273. https://doi.org/10.1016/S0140-6736(75)90609-1
2. Arita, M., Wakita, T., i Shimizu, H. (2012). Valosin-Containing Protein (VCP/p97) Is Required for Poliovirus Replication and Is Involved in Cellular Protein Secretion Pathway in Poliovirus Infection. *Journal of Virology*, *86*(10), 5541–5553. https://doi.org/10.1128/JVI.00114-12
3. Bartak, M., Chodkowski, M., Słońska, A., Grodzik, M., Szczepaniak, J., Bańbura, M. W., i Cymerys, J. (2022). Equid Alphaherpesvirus 1 Modulates Actin Cytoskeleton and Inhibits Migration of Glioblastoma Multiforme Cell Line A172. *Pathogens*, *11*(4), Article 4. https://doi.org/10.3390/pathogens11040400
4. Bartak, M., Słońska, A., Bańbura, M. W., i Cymerys, J. (2021). SDAV, the Rat Coronavirus—How Much Do We Know about It in the Light of Potential Zoonoses. *Viruses*, *13*(10), Article 10. https://doi.org/10.3390/v13101995
5. Barton, E. S., White, D. W., Cathelyn, J. S., Brett-McClellan, K. A., Engle, M., Diamond, M. S., Miller, V. L., i Virgin, H. W. (2007). Herpesvirus latency confers symbiotic protection from bacterial infection. *Nature*, *447*(7142), 326–329. https://doi.org/10.1038/nature05762
6. Bender, S. J., i Weiss, S. R. (2010). Pathogenesis of Murine Coronavirus in the Central Nervous System. *Journal of Neuroimmune Pharmacology*, *5*(3), 336–354. https://doi.org/10.1007/s11481-010-9202-2
7. Bhatt, P. N., Jacoby, R. O., i Jonas, A. M. (1977). Respiratory infection in mice with sialodacryoadenitis virus, a coronavirus of rats. *Infection and Immunity*, *18*(3), 823–827. https://doi.org/10.1128/iai.18.3.823-827.1977
8. Bhatt, P. N., Percy, D. H., i Jonas, A. M. (1972). Characterization of the Virus of Sialodacryoadenitis of Rats: A Member of the Coronavirus Group. *The Journal of Infectious Diseases*, *126*(2), 123–130. https://doi.org/10.1093/infdis/126.2.123
9. Boylan, B. T., Hwang, M., i Bergmann, C. C. (2023). The Impact of Innate Components on Viral Pathogenesis in the Neurotropic Coronavirus Encephalomyelitis Mouse Model. *Viruses*, *15*(12), Article 12. https://doi.org/10.3390/v15122400
10. Buchrieser, J., Dufloo, J., Hubert, M., Monel, B., Planas, D., Rajah, M. M., Planchais, C., Porrot, F., Guivel-Benhassine, F., Van der Werf, S., Casartelli, N., Mouquet, H., Bruel, T., i Schwartz, O. (2020). Syncytia formation by SARS-CoV-2-infected cells. *The EMBO Journal*, *39*(23), e106267. https://doi.org/10.15252/embj.2020106267

11. Chen, B., Farzan, M., i Choe, H. (2025). SARS-CoV-2 spike protein: Structure, viral entry and variants. *Nature Reviews Microbiology*, 1–14. https://doi.org/10.1038/s41579-025-01185-8
12. Chen, Y., Wang, J., Liu, C., Su, L., Zhang, D., Fan, J., Yang, Y., Xiao, M., Xie, J., Xu, Y., Li, Y., i Zhang, S. (2020). IP-10 and MCP-1 as biomarkers associated with disease severity of COVID-19. *Molecular Medicine*, *26*(1), 97. https://doi.org/10.1186/s10020-020-00230-x
13. Cheng, K.-W., Li, S., Wang, F., Ruiz-Lopez, N. M., Houerbi, N., i Chou, T.-F. (2021). Impacts of p97 on Proteome Changes in Human Cells during Coronaviral Replication. *Cells*, *10*(11), Article 11. https://doi.org/10.3390/cells10112953
14. Chiou, H.-E., Liu, C.-L., Buttrey, M. J., Kuo, H.-P., Liu, H.-W., Kuo, H.-T., i Lu, Y.-T. (2005). Adverse Effects of Ribavirin and Outcome in Severe Acute Respiratory Syndrome. *Chest*, *128*(1), 263–272. https://doi.org/10.1378/chest.128.1.263
15. Chu, S., Xie, X., Payan, C., i Stochaj, U. (2023). Valosin containing protein (VCP): Initiator, modifier, and potential drug target for neurodegenerative diseases. *Molecular Neurodegeneration*, *18*(1), 52. https://doi.org/10.1186/s13024-023-00639-y
16. Colonna, M., i Butovsky, O. (2017). Microglia Function in the Central Nervous System During Health and Neurodegeneration. *Annual Review of Immunology*, *35*(Volume 35, 2017), 441–468. https://doi.org/10.1146/annurev-immunol-051116-052358
17. Compton, S. R. (2021). Overview of Coronaviruses in Veterinary Medicine. *Comparative Medicine*, *71*(5), 333–341. https://doi.org/10.30802/AALAS-CM-21-000007
18. Cymerys, J., Chodkowski, M., Słońska, A., Krzyżowska, M., i Bańbura, M. W. (2019). Disturbances of mitochondrial dynamics in cultured neurons infected with human herpesvirus type 1 and type 2. *Journal of Neurovirology*, *25*(6), 765. https://doi.org/10.1007/s13365-019-00762-x
19. Cymerys, J., Dzieciątkowski, T., Golke, A., Słońska, A., Majewska, A., Krzyżowska, M., i Bańbura, M. W. (2013). Primary cultures of murine neurons for studying herpes simplex virus 1 infection and its inhibition by antivirals. *Acta Virologica*, *57*(3), 339–345.
20. Cymerys, J., Dzieciątkowski, T., Słońska, A., Bierła, J., Tucholska, A., Chmielewska, A., Golke, A., i Bańbura, M. (2010). Equine herpesvirus type 1 (EHV-1) replication in primary murine neurons culture. *Polish Journal of Veterinary Sciences*, *13*(4). https://doi.org/10.2478/v10181-010-0022-3
21. Cymerys, J., Kowalczyk, A., Mikołajewicz, K., Słońska, A., i Krzyżowska, M. (2019). Nitric Oxide Influences HSV-1-Induced Neuroinflammation. *Oxidative Medicine and Cellular Longevity*, *2019*, 2302835. https://doi.org/10.1155/2019/2302835

22. Cymerys, J., Miszczak, D., Słońska, A., Golke, A., i Bańbura, M. W. (2014). Autophagy in cultured murine neurons infected with equid herpesvirus 1. *Acta Virologica*, *58*(3), 292–295. https://doi.org/10.4149/av_2014_03_292
23. Cymerys, J., Słońska, A., Chodkowski, M., Golke, A., Krzyżowska, M., i Bańbura, M. W. (2020). Neuropathogenic and non-neuropathogenic EHV-1 strains induce the accumulation of hyperphosphorylated Tau in primary murine neurons. *Acta Virologica*, *64*(4), 490–495. https://doi.org/10.4149/av_2020_407
24. Cymerys, J., Słońska, A., Godlewski, M. M., Golke, A., Tucholska, A., Chmielewska, A., i Bańbura, M. W. (2012). Apoptotic and necrotic changes in cultured murine neurons infected with equid herpesvirus 1. *Acta Virologica*, *56*(1), 39–48. https://doi.org/10.4149/av_2012_01_39
25. Damon J. DiSabato, DiSabato, D. J., Ning Quan, Quan, N., Jonathan P. Godbout, i Godbout, J. P. (2016). Neuroinflammation: The devil is in the details. *Journal of Neurochemistry*, *139*, 136–153. https://doi.org/10.1111/jnc.13607
26. De Angelis, M., Anichini, G., Palamara, A. T., Nencioni, L., i Gori Savellini, G. (2023). Dysregulation of intracellular redox homeostasis by the SARS-CoV-2 ORF6 protein. *Virology Journal*, *20*(1), 239. https://doi.org/10.1186/s12985-023-02208-7
27. Dhama, K., Patel, S. K., Sharun, K., Pathak, M., Tiwari, R., Yatoo, M. I., Malik, Y. S., Sah, R., Rabaan, A. A., Panwar, P. K., Singh, K. P., Michalak, I., Chaicumpa, W., Martinez-Pulgarin, D. F., Bonilla-Aldana, D. K., i Rodriguez-Morales, A. J. (2020). SARS-CoV-2 jumping the species barrier: Zoonotic lessons from SARS, MERS and recent advances to combat this pandemic virus. *Travel Medicine and Infectious Disease*, *37*, 101830. https://doi.org/10.1016/j.tmaid.2020.101830
28. Dharra, R., Kumar Sharma, A., i Datta, S. (2023). Emerging aspects of cytokine storm in COVID-19: The role of proinflammatory cytokines and therapeutic prospects. *Cytokine*, *169*, 156287. https://doi.org/10.1016/j.cyto.2023.156287
29. Ding, Z.-B., Song, L.-J., Wang, Q., Kumar, G., Yan, Y.-Q., i Ma, C.-G. (2021). Astrocytes: A double-edged sword in neurodegenerative diseases. *Neural Regeneration Research*, *16*(9), 1702. https://doi.org/10.4103/1673-5374.306064
30. Dixit, R., Tiwari, V., i Shukla, D. (2008). Herpes simplex virus type 1 induces filopodia in differentiated P19 neural cells to facilitate viral spread. *Neuroscience Letters*, *440*(2), 113–118. https://doi.org/10.1016/j.neulet.2008.05.031
31. Domingues, H. S., Portugal, C. C., Socodato, R., i Relvas, J. B. (2016). Corrigendum: Oligodendrocyte, Astrocyte and Microglia Crosstalk in Myelin Development, Damage, and Repair. *Frontiers in Cell and Developmental Biology*, *4*. https://doi.org/10.3389/fcell.2016.00079

32. Drosten, C., Günther, S., Preiser, W., Werf, S. van der, Brodt, H.-R., Becker, S., Rabenau, H., Panning, M., Kolesnikova, L., Fouchier, R. A. M., Berger, A., Burguière, A.-M., Cinatl, J., Eickmann, M., Escriou, N., Grywna, K., Kramme, S., Manuguerra, J.-C., Müller, S., … Doerr, H. W. (2003). Identification of a Novel Coronavirus in Patients with Severe Acute Respiratory Syndrome. *New England Journal of Medicine*, *348*(20), 1967–1976. https://doi.org/10.1056/NEJMoa030747
33. Fehr, A. R., i Perlman, S. (2015). Coronaviruses: An Overview of Their Replication and Pathogenesis. W H. J. Maier, E. Bickerton, i P. Britton (Red.), *Coronaviruses* (T. 1282, s. 1–23). Springer New York. https://doi.org/10.1007/978-1-4939-2438-7_1
34. Funk, C. J., Manzer, R., Miura, T. A., Groshong, S. D., Ito, Y., Travanty, E. A., Leete, J., Holmes, K. V., i Mason, R. J. (2009). Rat respiratory coronavirus infection: Replication in airway and alveolar epithelial cells and the innate immune response. *The Journal of General Virology*, *90*(Pt 12), 2956–2964. https://doi.org/10.1099/vir.0.014282-0
35. Gaertner, D. J., Winograd, D. F., Compton, S. R., Paturzo, F. X., i Smith, A. L. (1993). Development and optimization of plaque assays for rat coronaviruses. *Journal of Virological Methods*, *43*(1), 53–64. https://doi.org/10.1016/0166-0934(93)90089-A
36. Gagneten, S., Scanga, C. A., Dveksler, G. S., Beauchemin, N., Percy, D., i Holmes, K. V. (1996). Attachment glycoproteins and receptor specificity of rat coronaviruses. *Laboratory Animal Science*, *46*(2), 159–166.
37. Gomersall, C. D., Kargel, M. J., i Lapinsky, S. E. (2004). Pro/con clinical debate: Steroids are a key component in the treatment of SARS. *Critical Care*, *8*(2), 105–107. https://doi.org/10.1186/cc2452
38. Gong, L., Li, J., Zhou, Q., Xu, Z., Chen, L., Zhang, Y., Xue, C., Wen, Z., i Cao, Y. (2017). A New Bat-HKU2-like Coronavirus in Swine, China, 2017. *Emerging Infectious Diseases*, *23*(9), 1607–1609. https://doi.org/10.3201/eid2309.170915
39. Gudowska-Sawczuk, M., i Mroczko, B. (2022). What Is Currently Known about the Role of CXCL10 in SARS-CoV-2 Infection? *International Journal of Molecular Sciences*, *23*(7), Article 7. https://doi.org/10.3390/ijms23073673
40. Haake, C., Cook, S., Pusterla, N., i Murphy, B. (2020). Coronavirus Infections in Companion Animals: Virology, Epidemiology, Clinical and Pathologic Features. *Viruses*, *12*(9), 1023. https://doi.org/10.3390/v12091023
41. Hijawi, B., Abdallat, M., Sayaydeh, A., Alqasrawi, S., Haddadin, A., Jaarour, N., Alsheikh, S., i Alsanouri, T. (2013). Novel coronavirus infections in Jordan, April 2012: Epidemiological findings from a retrospective investigation. *Eastern Mediterranean Health Journal = La Revue De Sante De La Mediterranee Orientale = Al-Majallah Al-Sihhiyah Li-Sharq Al-Mutawassit*, *19 Suppl 1*, S12-18.

42. Hirano, N. (1990). Plaque assay and propagation in rat cell line LBC cells of rat coronavirus and 5 strains of sialodacryoadenitis virus. *Zentralblatt Fur Veterinarmedizin. Reihe B. Journal of Veterinary Medicine. Series B*, *37*(2), 91–96. https://doi.org/10.1111/j.1439-0450.1990.tb01031.x
43. Hu, W., Yen, Y.-T., Singh, S., Kao, C.-L., i Wu-Hsieh, B. A. (2012). SARS-CoV Regulates Immune Function-Related Gene Expression in Human Monocytic Cells. *Viral Immunology*, *25*(4), 277–288. https://doi.org/10.1089/vim.2011.0099
44. Huang, K.-C., Yasruel, Z., Guérin, C., Holland, P. C., i Nalbantoglu, J. (2007). Interaction of the Coxsackie and adenovirus receptor (CAR) with the cytoskeleton: Binding to actin. *FEBS Letters*, *581*(14), 2702–2708. https://doi.org/10.1016/j.febslet.2007.05.019
45. Jacoby, R. O. (1986). RAT CORONAVIRUS. *Viral and Mycoplasmal of Laboratory Rodents*, 625–638. https://doi.org/10.1016/B978-0-12-095785-9.50034-2
46. Jarrott, B., Head, R., Pringle, K. G., Lumbers, E. R., i Martin, J. H. (2022). "LONG COVID"—A hypothesis for understanding the biological basis and pharmacological treatment strategy. *Pharmacology Research i Perspectives*, *10*(1), e00911. https://doi.org/10.1002/prp2.911
47. Ji, W. (2021). Coronaviruses: What Should We Know About the Characteristics of Viruses? W N. Rezaei (Red.), *Coronavirus Disease—COVID-19* (s. 23–39). Springer International Publishing. https://doi.org/10.1007/978-3-030-63761-3_2
48. Kalicharran, K., i Dales, S. (1995). Involvement of Microtubules and the Microtubule-Associated Protein TAU in Trafficking of JHM Virus and Components within Neurons. W P. J. Talbot i G. A. Levy (Red.), *Corona- and Related Viruses: Current Concepts in Molecular Biology and Pathogenesis* (s. 57–61). Springer US. https://doi.org/10.1007/978-1-4615-1899-0_8
49. Kanso, M. A., Piette, J. H., Hanna, J. A., i Giacomin, A. J. (2020). Coronavirus rotational diffusivity. *Physics of Fluids (Woodbury, N.Y.: 1994)*, *32*(11), 113101. https://doi.org/10.1063/5.0031875
50. Kärber, G. (1931). Beitrag zur kollektiven Behandlung pharmakologischer Reihenversuche. *Naunyn-Schmiedebergs Archiv für Experimentelle Pathologie und Pharmakologie*, *162*(4), 480–483. https://doi.org/10.1007/BF01863914
51. Karesh, W. B., Dobson, A., Lloyd-Smith, J. O., Lubroth, J., Dixon, M. A., Bennett, M., Aldrich, S., Harrington, T., Formenty, P., Loh, E. H., Machalaba, C. C., Thomas, M. J., i Heymann, D. L. (2012). Ecology of zoonoses: Natural and unnatural histories. *Lancet (London, England)*, *380*(9857), 1936–1945. https://doi.org/10.1016/S0140-6736(12)61678-X

52. Kazi, L., Lissenberg, A., Watson, R., de Groot, R. J., i Weiss, S. R. (2005). Expression of hemagglutinin esterase protein from recombinant mouse hepatitis virus enhances neurovirulence. *Journal of Virology*, *79*(24), 15064–15073. https://doi.org/10.1128/JVI.79.24.15064-15073.2005
53. Kenney, S. P., Wang, Q., Vlasova, A., Jung, K., i Saif, L. (2021). Naturally Occurring Animal Coronaviruses as Models for Studying Highly Pathogenic Human Coronaviral Disease. *Veterinary Pathology*, *58*(3), 438–452. https://doi.org/10.1177/0300985820980842
54. Kojima, A., Fujinami, F., Doi, K., Yasoshima, A., i Okaniwa, A. (1980). Isolation and properties of sialodacryoadenitis virus of rats. *Jikken Dobutsu. Experimental Animals*, *29*(4), 409–418. https://doi.org/10.1538/expanim1978.29.4_409
55. Kojima, A., Takada, H., Yamanaka, H., Okaniwa, A., Doi, K., i Yasoshima, A. (1983). Pathology of sialodacryoadenitis virus infection in newborn mice. *Nihon Juigaku Zasshi. The Japanese Journal of Veterinary Science*, *45*(3), 297–304. https://doi.org/10.1292/jvms1939.45.297
56. Körner, R., Majjouti, M., Alcazar, M., i Mahabir, E. (2020). Of Mice and Men: The Coronavirus MHV and Mouse Models as a Translational Approach to Understand SARS-CoV-2. *Viruses*, *12*(8), 880. https://doi.org/10.3390/v12080880
57. Krahel, W. D., Bartak, M., i Cymerys, J. (2024). Acute and long-term SARS-CoV-2 infection and neurodegeneration processes—Circulus vitiosus. *Acta Virologica*, *68*, 12765. https://doi.org/10.3389/av.2024.12765
58. Krammer, F. (2020). SARS-CoV-2 vaccines in development. *Nature*, *586*(7830), 516–527. https://doi.org/10.1038/s41586-020-2798-3
59. Ksiazek, T. G., Erdman, D., Goldsmith, C. S., Zaki, S. R., Peret, T., Emery, S., Tong, S., Urbani, C., Comer, J. A., Lim, W., Rollin, P. E., Dowell, S. F., Ling, A.-E., Humphrey, C. D., Shieh, W.-J., Guarner, J., Paddock, C. D., Rota, P., Fields, B., … null, null. (2003). A Novel Coronavirus Associated with Severe Acute Respiratory Syndrome. *New England Journal of Medicine*, *348*(20), 1953–1966. https://doi.org/10.1056/NEJMoa030781
60. Kujawska, M., Mostafavi, E., i Kaushik, A. (2023). SARS-CoV-2 getting into the brain; neurological phenotype of COVID-19, and management by nano-biotechnology. *Neural Regeneration Research*, *18*(3), 519. https://doi.org/10.4103/1673-5374.346486
61. Kwon, H. S., i Koh, S.-H. (2020). Neuroinflammation in neurodegenerative disorders: The roles of microglia and astrocytes. *Translational Neurodegeneration*, *9*(1), 42. https://doi.org/10.1186/s40035-020-00221-2
62. Lamb, Y. N. (2021). BNT162b2 mRNA COVID-19 Vaccine: First Approval. *Drugs*, *81*(4), 495–501. https://doi.org/10.1007/s40265-021-01480-7

63. Langereis, M. A., Zeng, Q., Heesters, B. A., Huizinga, E. G., i de Groot, R. J. (2012). The murine coronavirus hemagglutinin-esterase receptor-binding site: A major shift in ligand specificity through modest changes in architecture. *PLoS Pathogens*, *8*(1), e1002492. https://doi.org/10.1371/journal.ppat.1002492

64. Latinne, A., Hu, B., Olival, K. J., Zhu, G., Zhang, L.-B., Li, H., Chmura, A. A., Field, H. E., Zambrana-Torrelio, C., Epstein, J. H., Li, B., Zhang, W., Wang, L.-F., Shi, Z.-L., i Daszak, P. (2024). Origin and cross-species transmission of bat coronaviruses in China. *Nature Communications*, *15*(1), 10705. https://doi.org/10.1038/s41467-024-55384-7

65. Lavi, E., i Cong, L. (2020). Type I astrocytes and microglia induce a cytokine response in an encephalitic murine coronavirus infection. *Experimental and Molecular Pathology*, *115*, 104474. https://doi.org/10.1016/j.yexmp.2020.104474

66. Lavi, E., Wang, Q., Weiss, S. R., i Gonatas, N. K. (1996). Syncytia Formation Induced by Coronavirus Infection Is Associated with Fragmentation and Rearrangement of the Golgi Apparatus. *Virology*, *221*(2), 325–334. https://doi.org/10.1006/viro.1996.0382

67. Madhurantakam, S., Lee, Z. J., Naqvi, A., i Prasad, S. (2023). Importance of IP-10 as a biomarker of host immune response: Critical perspective as a target for biosensing. *Current Research in Biotechnology*, *5*, 100130. https://doi.org/10.1016/j.crbiot.2023.100130

68. Mallick, R., i Duttaroy, A. K. (2021). Origin and Structural Biology of Novel Coronavirus (SARS-CoV-2). W A. A. A. Asea i P. Kaur (Red.), *Coronavirus Therapeutics – Volume I: Basic Science and Therapy Development* (s. 1–13). Springer International Publishing. https://doi.org/10.1007/978-3-030-85109-5_1

69. Maru, M., i Sato, K. (1982). Characterization of a coronavirus isolated from rats with sialoadenitis. *Archives of Virology*, *73*(1), 33–43. https://doi.org/10.1007/BF01341725

70. Matthews, A., Weiss, S., i Paterson, Y. (2002). Murine hepatitis virus—A model for virus-induced CNS demyelination. *Journal of Neurovirology*, *8*(2), 76–85. https://doi.org/10.1080/13550280290049534

71. Mayla, A. M., Mohamed, W. S., Zekri, A.-R. N., Gouda, N. A., Lotfy, M. M., Seadawy, M. G., Elgohary, M. A.-S., i Abdallah, Z. F. (2025). Co-infections and Reactivation of some Herpesviruses (HHV) and Measles Virus (MeV) in Egyptian Cancer Patients infected with Severe Acute Respiratory Syndrome Coronavirus 2 (SARS-CoV-2). *Journal of the Egyptian National Cancer Institute*, *37*(1), 19. https://doi.org/10.1186/s43046-025-00275-1

72. Mehta, P., McAuley, D. F., Brown, M., Sanchez, E., Tattersall, R. S., i Manson, J. J. (2020). COVID-19: Consider cytokine storm syndromes and immunosuppression. *Lancet (London, England)*, *395*(10229), 1033–1034. https://doi.org/10.1016/S0140-6736(20)30628-0

73. Meier, O., i Greber, U. F. (2004). Adenovirus endocytosis. *The Journal of Gene Medicine*, *6 Suppl 1*, S152-163. https://doi.org/10.1002/jgm.553
74. Mendonça Filho, V. C. M., de Oliveira, A. G., Maia, I. de F. V. C., de Falcone, A. C. M., Betini, B. G., Rezende, L. B., i Magri Alves, F. H. (2023). COVID-19 in the nervous system: Physiopathology and neurological manifestations. *Arquivos de Neuro-Psiquiatria*, *81*(8), 756–763. https://doi.org/10.1055/s-0043-1769123
75. Meo, M. O. S., AlHusseini, N., Ibrahim, D. I., Meo, M. Z. S., Ahsan, F., Tamim, H., i Sajid, M. R. (2025). Clinical manifestations of Long-COVID: An observational perspective. *Frontiers in Medicine*, *12*. https://doi.org/10.3389/fmed.2025.1523817
76. Merhavy, Z. I., Junor, T., Gonzalez, A., Filippis, S. M. D., Oveisitork, S., Rivera, E., Ndukwu, I., i Bhatara, K. (2024). Long COVID: A Comprehensive Overview of the Signs and Symptoms across Multiple Organ Systems. *Korean Journal of Family Medicine*, *45*(6), 305–316. https://doi.org/10.4082/kjfm.24.0085
77. Meslé, M. M. I., Brown, J., Mook, P., Katz, M. A., Hagan, J., Pastore, R., Benka, B., Redlberger-Fritz, M., Bossuyt, N., Stouten, V., Vernemmen, C., Constantinou, E., Maly, M., Kynčl, J., Sanca, O., Krause, T. G., Vestergaard, L. S., Leino, T., Poukka, E., … WHO European Respiratory Surveillance Network. (2024). Estimated number of lives directly saved by COVID-19 vaccination programmes in the WHO European Region from December, 2020, to March, 2023: A retrospective surveillance study. *The Lancet. Respiratory Medicine*, *12*(9), 714–727. https://doi.org/10.1016/S2213-2600(24)00179-6
78. Mihaescu, G., Chifiriuc, M. C., Filip, R., Bleotu, C., Ditu, L. M., Constantin, M., Cristian, R.-E., Grigore, R., Bertesteanu, S. V., Bertesteanu, G., i Vrancianu, C. O. (2024). Role of interferons in the antiviral battle: From virus-host crosstalk to prophylactic and therapeutic potential in SARS-CoV-2 infection. *Frontiers in Immunology*, *14*. https://doi.org/10.3389/fimmu.2023.1273604
79. Miura, T. A., Wang, J., Holmes, K. V., i Mason, R. J. (2007). Rat coronaviruses infect rat alveolar type I epithelial cells and induce expression of CXC chemokines. *Virology*, *369*(2), 288–298. https://doi.org/10.1016/j.virol.2007.07.030
80. Movaqar, A., Yaghoubi, A., Rezaee, S. R., Jamehdar, S. A., i Soleimanpour, S. (2021). Coronaviruses construct an interconnection way with ERAD and autophagy. *Future Microbiology*, *16*(14), 1135–1151. https://doi.org/10.2217/fmb-2021-0044
81. Naghavi, M. H., i Walsh, D. (2017). Microtubule Regulation and Function during Virus Infection. *Journal of Virology*, *91*(16), e00538-17. https://doi.org/10.1128/JVI.00538-17
82. Ng, M. L., Lee, J. W. M., Leong, M. L. N., Ling, A.-E., Tan, H.-C., i Ooi, E. E. (2004). Topographic Changes in SARS Coronavirus–infected Cells at Late Stages of Infection.

Emerging Infectious Diseases, *10*(11), 1907–1914. https://doi.org/10.3201/eid1011.040195

83. Noack, J., Bernasconi, R., i Molinari, M. (2014). How viruses hijack the ERAD tuning machinery. *Journal of Virology*, *88*(18), 10272–10275. https://doi.org/10.1128/JVI.00801-14
84. Pan, T., Chen, R., He, X., Yuan, Y., Deng, X., Li, R., Yan, H., Yan, S., Liu, J., Zhang, Y., Zhang, X., Yu, F., Zhou, M., Ke, C., Ma, X., i Zhang, H. (2021). Infection of wild-type mice by SARS-CoV-2 B.1.351 variant indicates a possible novel cross-species transmission route. *Signal Transduction and Targeted Therapy*, *6*(1), 1–12. https://doi.org/10.1038/s41392-021-00848-1
85. Panagea, E., Messinis, L., Petri, M. C., Liampas, I., Anyfantis, E., Nasios, G., Patrikelis, P., i Kosmidis, M. (2025). Neurocognitive Impairment in Long COVID: A Systematic Review. *Archives of Clinical Neuropsychology*, *40*(1), 125–149. https://doi.org/10.1093/arclin/acae042
86. Pasick, J., i Dales, S. (1994). MHV-JHM Infections of Rodent Neuronal Cells: Replication and Trafficking of Structural Proteins and Progeny Virions. W H. Laude i J.-F. Vautherot (Red.), *Coronaviruses* (T. 342, s. 319–325). Springer US. https://doi.org/10.1007/978-1-4615-2996-5_49
87. Pearson, H. (2005). Caution raised over SARS vaccine. *Nature*. https://doi.org/10.1038/news050110-3
88. Percy, D. H., Lynch, J. A., i Descôteaux, J.-P. (1986). Central Nervous System Lesions in Suckling Mice and Rats Inoculated Intranasally with Sialodacryoadenitis Virus. *Veterinary Pathology*, *23*(1), 42–49. https://doi.org/10.1177/030098588602300107
89. Percy, D. H., Williams, K. L., i Paturzo, F. X. (1991). A comparison of the sensitivity and specificity of sialodacryoadenitis virus, Parker's rat coronavirus, and mouse hepatitis virus-infected cells as a source of antigen for the detection of antibody to rat coronaviruses. *Archives of Virology*, *119*(3–4), 175–180. https://doi.org/10.1007/BF01310668
90. Phongphaew, W., Kobayashi, S., Sasaki, M., Carr, M., Hall, W. W., Orba, Y., i Sawa, H. (2017). Valosin-containing protein (VCP/p97) plays a role in the replication of West Nile virus. *Virus Research*, *228*, 114–123. https://doi.org/10.1016/j.virusres.2016.11.029
91. Rajeev, R., Prathiviraj, R., Kiran, G. S., i Selvin, J. (2020). Zoonotic evolution and implications of microbiome in viral transmission and infection. *Virus Research*, *290*, 198175. https://doi.org/10.1016/j.virusres.2020.198175

92. Reggiori, F., de Haan, C. A. M., i Molinari, M. (2011). Unconventional Use of LC3 by Coronaviruses through the Alleged Subversion of the ERAD Tuning Pathway. *Viruses*, *3*(9), 1610–1623. https://doi.org/10.3390/v3091610
93. Reggiori, F., Monastyrska, I., Verheije, M. H., Calì, T., Ulasli, M., Bianchi, S., Bernasconi, R., de Haan, C. A. M., i Molinari, M. (2010). Coronaviruses Hijack the LC3-I-positive EDEMosomes, ER-derived vesicles exporting short-lived ERAD regulators, for replication. *Cell Host i Microbe*, *7*(6), 500–508. https://doi.org/10.1016/j.chom.2010.05.013
94. Reshi, M. L., Su, Y.-C., i Hong, J.-R. (2014). RNA Viruses: ROS-Mediated Cell Death. *International Journal of Cell Biology*, *2014*, 467452. https://doi.org/10.1155/2014/467452
95. Robert Weissert. (2023). Nervous system-related tropism of SARS-CoV-2 and autoimmunity in COVID-19 infection. *European journal of immunology*. https://doi.org/10.1002/eji.202250230
96. Rodrigo, I., Ballesta, C., Nunes, E. B., Pérez, P., García-Arriaza, J., i Arias, A. (2022). Eeyarestatin I, an inhibitor of the valosin-containing protein, exhibits potent virucidal activity against the flaviviruses. *Antiviral Research*, *207*, 105416. https://doi.org/10.1016/j.antiviral.2022.105416
97. Sahin, U., Muik, A., Vogler, I., Derhovanessian, E., Kranz, L. M., Vormehr, M., Quandt, J., Bidmon, N., Ulges, A., Baum, A., Pascal, K. E., Maurus, D., Brachtendorf, S., Lörks, V., Sikorski, J., Koch, P., Hilker, R., Becker, D., Eller, A.-K., … Türeci, Ö. (2021). BNT162b2 vaccine induces neutralizing antibodies and poly-specific T cells in humans. *Nature*, *595*(7868), 572–577. https://doi.org/10.1038/s41586-021-03653-6
98. Sanclemente-Alaman, I., Moreno-Jiménez, L., Benito-Martín, M. S., Canales-Aguirre, A., Matías-Guiu, J. A., Matías-Guiu, J., i Gómez-Pinedo, U. (2020). Experimental Models for the Study of Central Nervous System Infection by SARS-CoV-2. *Frontiers in Immunology*, *11*, 2163. https://doi.org/10.3389/fimmu.2020.02163
99. Schelhaas, M., Ewers, H., Rajamäki, M.-L., Day, P. M., Schiller, J. T., i Helenius, A. (2008). Human Papillomavirus Type 16 Entry: Retrograde Cell Surface Transport along Actin-Rich Protrusions. *PLOS Pathogens*, *4*(9), e1000148. https://doi.org/10.1371/journal.ppat.1000148
100. Słońska, A., Cymerys, J., Chodkowski, M., Bąska, P., Krzyżowska, M., i Bańbura, M. W. (2021). Human herpesvirus type 2 infection of primary murine astrocytes causes disruption of the mitochondrial network and remodeling of the actin cytoskeleton: An in vitro morphological study. *Archives of Virology*, *166*(5), 1371–1383. https://doi.org/10.1007/s00705-021-05025-x

101. Tabata, K., Arakawa, M., Ishida, K., Kobayashi, M., Nara, A., Sugimoto, T., Okada, T., Mori, K., i Morita, E. (2021). Endoplasmic Reticulum-Associated Degradation Controls Virus Protein Homeostasis, Which Is Required for Flavivirus Propagation. *Journal of Virology*, *95*(15), 10.1128/jvi.02234-20. https://doi.org/10.1128/jvi.02234-20
102. Thibault Fiolet, Fiolet, T., Yousra Kherabi, Kherabi, Y., MacDonald, C.-J., Conor-James MacDonald, MacDonald, C.-J., Ghosn, J., Jade Ghosn, Jade Ghosn, Nathan Peiffer-Smadja, i Peiffer-Smadja, N. (2021). Comparing COVID-19 vaccines for their characteristics, efficacy and effectiveness against SARS-CoV-2 and variants of concern: A narrative review. *Clinical Microbiology and Infection*. https://doi.org/10.1016/j.cmi.2021.10.005
103. Tome, R., Arima, S., Akamine, M., Hashioka, H., Arakaki, W., Kami, W., Nabeya, D., Ideguchi, S., Nakamura, H., Kinjo, T., Nakamatsu, M., Furugen, M., Miyagi, K., Haranaga, S., i Yamamoto, K. (2025). Varicella-zoster virus reactivation with severe pneumonia following convalescence from coronavirus disease: A case report and literature review. *Internal Medicine (Tokyo, Japan)*. https://doi.org/10.2169/internalmedicine.4932-24
104. Valkov, T., Argirova, R., i Dimitrov, G. (2024). SARS-CoV-2 Infection of the Central Nervous System: A Case Report. *Viruses*, *16*(12), 1962. https://doi.org/10.3390/v16121962
105. V'kovski, P., Kratzel, A., Steiner, S., Stalder, H., i Thiel, V. (2021). Coronavirus biology and replication: Implications for SARS-CoV-2. *Nature Reviews. Microbiology*, *19*(3), 155–170. https://doi.org/10.1038/s41579-020-00468-6
106. Walker, P. J., Siddell, S. G., Lefkowitz, E. J., Mushegian, A. R., Adriaenssens, E. M., Dempsey, D. M., Dutilh, B. E., Harrach, B., Harrison, R. L., Hendrickson, R. C., Junglen, S., Knowles, N. J., Kropinski, A. M., Krupovic, M., Kuhn, J. H., Nibert, M., Orton, R. J., Rubino, L., Sabanadzovic, S., … Davison, A. J. (2020). Changes to virus taxonomy and the Statutes ratified by the International Committee on Taxonomy of Viruses (2020). *Archives of Virology*, *165*(11), 2737–2748. https://doi.org/10.1007/s00705-020-04752-x
107. Wang, H., Rao, S., i Jiang, C. (2007). Molecular pathogenesis of severe acute respiratory syndrome. *Microbes and Infection*, *9*(1), 119–126. https://doi.org/10.1016/j.micinf.2006.06.012
108. Wang, J., Fang, S., Xiao, H., Chen, B., Tam, J. P., i Liu, D. X. (2009). Interaction of the Coronavirus Infectious Bronchitis Virus Membrane Protein with β-Actin and Its Implication in Virion Assembly and Budding. *PLoS ONE*, *4*(3), e4908. https://doi.org/10.1371/journal.pone.0004908

109. Wang, Q., Shinkre, B. A., Lee, J., Weniger, M. A., Liu, Y., Chen, W., Wiestner, A., Trenkle, W. C., i Ye, Y. (2010). The ERAD Inhibitor Eeyarestatin I Is a Bifunctional Compound with a Membrane-Binding Domain and a p97/VCP Inhibitory Group. *PLOS ONE*, *5*(11), e15479. https://doi.org/10.1371/journal.pone.0015479
110. Wang, T., Wang, B., Huang, H., Zhang, C., Zhu, Y., Pei, B., Cheng, C., Sun, L., Wang, J., Jin, Q., i Zhao, Z. (2017). Enterovirus 71 protease 2Apro and 3Cpro differentially inhibit the cellular endoplasmic reticulum-associated degradation (ERAD) pathway via distinct mechanisms, and enterovirus 71 hijacks ERAD component p97 to promote its replication. *PLoS Pathogens*, *13*(10), e1006674. https://doi.org/10.1371/journal.ppat.1006674
111. Wang, Y., Grunewald, M., i Perlman, S. (2020). Coronaviruses: An Updated Overview of Their Replication and Pathogenesis. W H. J. Maier i E. Bickerton (Red.), *Coronaviruses: Methods and Protocols* (s. 1–29). Springer US. https://doi.org/10.1007/978-1-0716-0900-2_1
112. Wang, Y., Lenoch, J., Kohler, D., DeLiberto, T. J., Tang, C. Y., Li, T., Tao, Y. J., Guan, M., Compton, S., Zeiss, C., Hang, J., i Wan, X.-F. (2023). SARS-CoV-2 Exposure in Norway Rats (Rattus norvegicus) from New York City. *mBio*, *14*(2), e03621-22. https://doi.org/10.1128/mbio.03621-22
113. Watson, A. M. M., Prasad, K. M., Klei, L., Wood, J. A., Yolken, R. H., Gur, R. C., Bradford, L. D., Calkins, M. E., Richard, J., Edwards, N., Savage, R. M., Allen, T. B., Kwentus, J., McEvoy, J. P., Santos, A. B., Wiener, H. W., Go, R. C. P., Perry, R. T., Nasrallah, H. A., … Nimgaonkar, V. L. (2013). Persistent infection with neurotropic herpes viruses and cognitive impairment. *Psychological Medicine*, *43*(5), 1023–1031. https://doi.org/10.1017/S003329171200195X
114. Weiss, S. R., i Leibowitz, J. L. (2011). Coronavirus Pathogenesis. W *Advances in Virus Research* (T. 81, s. 85–164). Elsevier. https://doi.org/10.1016/B978-0-12-385885-6.00009-2
115. Wen, Z., Zhang, Y., Lin, Z., Shi, K., i Jiu, Y. (2021). Cytoskeleton—A crucial key in host cell for coronavirus infection. *Journal of Molecular Cell Biology*, *12*(12), 968–979. https://doi.org/10.1093/jmcb/mjaa042
116. Whittaker, A., Anson, M., i Harky, A. (2020). Neurological Manifestations of COVID-19: A systematic review and current update. *Acta Neurologica Scandinavica*, *142*(1), 14–22. https://doi.org/10.1111/ane.13266
117. Wong, H. H., Kumar, P., Tay, F. P. L., Moreau, D., Liu, D. X., i Bard, F. (2015). Genome-Wide Screen Reveals Valosin-Containing Protein Requirement for Coronavirus Exit from Endosomes. *Journal of Virology*, *89*(21), 11116–11128. https://doi.org/10.1128/JVI.01360-15

118. Woo, P. C. Y., Lau, S. K. P., Huang, Y., i Yuen, K.-Y. (2009). Coronavirus Diversity, Phylogeny and Interspecies Jumping. *Experimental Biology and Medicine*, *234*(10), 1117–1127. https://doi.org/10.3181/0903-MR-94

119. Wu, K. X., Phuektes, P., Kumar, P., Goh, G. Y. L., Moreau, D., Chow, V. T. K., Bard, F., i Chu, J. J. H. (2016). Human genome-wide RNAi screen reveals host factors required for enterovirus 71 replication. *Nature Communications*, *7*, 13150. https://doi.org/10.1038/ncomms13150

120. Yang, Y., Shen, C., Li, J., Yuan, J., Wei, J., Huang, F., Wang, F., Li, G., Li, Y., Xing, L., Peng, L., Yang, M., Cao, M., Zheng, H., Wu, W., Zou, R., Li, D., Xu, Z., Wang, H., … Liu, Y. (2020). Plasma IP-10 and MCP-3 levels are highly associated with disease severity and predict the progression of COVID-19. *Journal of Allergy and Clinical Immunology*, *146*(1), 119-127.e4. https://doi.org/10.1016/j.jaci.2020.04.027

121. Yang, Z., Werner, H. C., Kong, W., Leung, K., Traggiai, E., Lanzavecchia, A., i Nabel, G. J. (2005). Evasion of antibody neutralization in emerging severe acute respiratory syndrome coronaviruses. *Proceedings of the National Academy of Sciences*, *102*(3), 797–801. https://doi.org/10.1073/pnas.0409065102

122. Ye, Z.-W., Yuan, S., Yuen, K.-S., Fung, S.-Y., Chan, C.-P., i Jin, D.-Y. (2020). Zoonotic origins of human coronaviruses. *International Journal of Biological Sciences*, *16*(10), 1686–1697. https://doi.org/10.7150/ijbs.45472

123. Yi, Z., Fang, C., Zou, J., Xu, J., Song, W., Du, X., Pan, T., Lu, H., i Yuan, Z. (2016). Affinity Purification of the Hepatitis C Virus Replicase Identifies Valosin-Containing Protein, a Member of the ATPases Associated with Diverse Cellular Activities Family, as an Active Virus Replication Modulator. *Journal of Virology*, *90*(21), 9953–9966. https://doi.org/10.1128/JVI.01140-16

124. Yi, Z., i Yuan, Z. (2017). Aggregation of a hepatitis C virus replicase module induced by ablation of p97/VCP. *Journal of General Virology*, *98*(7), 1667–1678. https://doi.org/10.1099/jgv.0.000828

125. Zaki, A. M., Boheemen, S. van, Bestebroer, T. M., Osterhaus, A. D. M. E., i Fouchier, R. A. M. (2012). Isolation of a Novel Coronavirus from a Man with Pneumonia in Saudi Arabia. *New England Journal of Medicine*, *367*(19), 1814–1820. https://doi.org/10.1056/NEJMoa1211721

126. Zeiss, C. J., Asher, J. L., Vander Wyk, B., Allore, H. G., i Compton, S. R. (2021). Modeling SARS-CoV-2 propagation using rat coronavirus-associated shedding and transmission. *PloS One*, *16*(11), e0260038. https://doi.org/10.1371/journal.pone.0260038

127. Zhang, G., Li, B., Yoo, D., Qin, T., Zhang, X., Jia, Y., i Cui, S. (2021). Animal coronaviruses and SARS-CoV-2. *Transboundary and Emerging Diseases*, *68*(3), 1097–1110. https://doi.org/10.1111/tbed.13791
128. Zhou, P., Fan, H., Lan, T., Yang, X.-L., Shi, W.-F., Zhang, W., Zhu, Y., Zhang, Y.-W., Xie, Q.-M., Mani, S., Zheng, X.-S., Li, B., Li, J.-M., Guo, H., Pei, G.-Q., An, X.-P., Chen, J.-W., Zhou, L., Mai, K.-J., … Ma, J.-Y. (2018). Fatal swine acute diarrhoea syndrome caused by an HKU2-related coronavirus of bat origin. *Nature*, *556*(7700), 255–258. https://doi.org/10.1038/s41586-018-0010-9
129. Zhu, N., Zhang, D., Wang, W., Li, X., Yang, B., Song, J., Zhao, X., Huang, B., Shi, W., Lu, R., Niu, P., Zhan, F., Ma, X., Wang, D., Xu, W., Wu, G., Gao, G. F., i Tan, W. (2020). A Novel Coronavirus from Patients with Pneumonia in China, 2019. *New England Journal of Medicine*, *382*(8), 727–733. https://doi.org/10.1056/NEJMoa2001017

Strony internetowe:

https://www.uniprot.org/uniprotkb/Q9IKD1/entry (data dostępu 10.05.25)
https://pubmed.ncbi.nlm.nih.gov (data dostępu 10.05.25)

Kopie publikacji składających się na rozprawę doktorską wraz z oświadczeniami współautorów

viruses

Review

SDAV, the Rat Coronavirus—How Much Do We Know about It in the Light of Potential Zoonoses

Michalina Bartak *, Anna Słońska, Marcin W Bańbura and Joanna Cymerys *

Division of Microbiology, Department of Preclinical Sciences, Institute of Veterinary Medicine, Warsaw University of Life Sciences—SGGW, Ciszewskiego 8, 02-786 Warsaw, Poland; anna_slonska@sggw.edu.pl (A.S.); marcin_banbura@sggw.edu.pl (M.W.B.)

* Correspondence: michalina_bartak@sggw.edu.pl (M.B.); joanna_cymerys@sggw.edu.pl (J.C.)

Abstract: Sialodacryoadenitis virus (SDAV) is known to be an etiological agent, causing infections in laboratory rats. Until now, its role has only been considered in studies on respiratory and salivary gland infections. The scant literature data, consisting mainly of papers from the last century, do not sufficiently address the topic of SDAV infections. The ongoing pandemic has demonstrated, once again, the role of the *Coronaviridae* family as extremely dangerous etiological agents of human zoonoses. The ability of coronaviruses to cross the species barrier and change to hosts commonly found in close proximity to humans highlights the need to characterize SDAV infections. The main host of the infection is the rat, as mentioned above. Rats inhabit large urban agglomerations, carrying a vast epidemic threat. Of the 2277 existing rodent species, 217 are reservoirs for 66 zoonotic diseases caused by viruses, bacteria, fungi, and protozoa. This review provides insight into the current state of knowledge of SDAV characteristics and its likely zoonotic potential.

Keywords: SDAV; rat infections; coronaviruses; zoonoses

Citation: Bartak, M.; Słońska, A.; Bańbura, M.W.; Cymerys, J. SDAV, the Rat Coronavirus—How Much Do We Know about It in the Light of Potential Zoonoses. *Viruses* **2021**, *13*, 1995. https://doi.org/10.3390/v13101995

Academic Editor: Tohru Suzuki

Received: 25 August 2021
Accepted: 1 October 2021
Published: 4 October 2021

1. Introduction

Recently, research interest has turned to animals known to be sources of zoonoses, including primates and other companion animals [1]. The outbreak of the new coronaviral pandemic in 2020 multiplied the quantity of research concerning animals, such as horseshoe bats (*Rhinolophus* spp.), fruit bats (*Rousettus aegyptiacus*), bank voles (*Myodes glareolus*), and raccoons, as well as cats, dogs, ferrets, mink, and other livestock such as pigs and cows. Most of the studies were performed to evaluate if these animals are capable of ACE2 expression, the major SARS-CoV-2 human cell entry receptor [2–6].

The majority of articles have been oriented on bats, but there is a need to focus on rodents, primarily rats. Rodents have been recognized as reservoirs or carriers for several zoonotic viruses, causing, for example, hemorrhagic fever with renal syndrome, Omsk hemorrhagic fever, Apoi virus disease, lymphocytic choriomeningitis virus (LCMV), Western equine encephalitis, and hepatitis E cowpox [7,8]. Notably, *Rattus* spp. thrive in urban areas and are so well-adapted to close cohabitation with people that they are rarely found in habitats devoid of humans. Rats can be found in almost every corner of every city on Earth, and humans are more likely to interact with them than any other wildlife species [9].

Considering this, in the present review, we will describe the current state of knowledge on Sialodacryoadenitis virus (SDAV), its characteristics and potential zoonotic threat.

2. Rat Coronaviruses: The Origin

2.1. Discovery

The first report on the new member of the coronavirus family appeared in the 1960s, as the laboratory rats had been experiencing destructive sialoadenitis, dacryoadenitis, and transmission disease of the lower respiratory tract [10–13]. After an outbreak in laboratory rats, possibly antigenically related to mouse hepatitis virus (MHV), agents were found in rat sera

by the team of Hartley in 1964 [14,15]. This discovery was confirmed by Jonas et al. in their study of a pathogenic agent, then recognized as virus-like particles in an electron-microscopic examination of the infected salivary glands of rats [10]. Further studies conducted by the team of Parker, led to the isolation of Parker's rat coronavirus (RCV-P) from the lungs of asymptomatic rats [16]. A second newly recognized strain causing sialoadacryoadenitis (SDA) was also antigenically related to MHV and the rat coronavirus of Parker [17]. Subsequent studies evaluated several other strains such as Japanese isolates, causative agent of rat Sialoadenitis (CARS) [18,19]; and U.S. isolates RCV-BCMM, RCV-W [20], and RCV-NJ [21].

2.2. Sialodacryoadenitis Virus: Transmission, Clinical Signs of Infection, and Diagnosis

Experimental studies demonstrated that RCoVs (rat coronaviruses) can remain infectious when dried on solid surfaces [22]. Spread of the infection is relatively easy and can occur by direct contact with infected individuals or by aerosol. There is no evidence for intrauterine transmission. Morbidity frequently reaches 100% among conventionally housed rats [23].

Rat coronaviruses can cause two types of infection: asymptomatic or symptomatic, with tissue tropism to salivary glands, lacrimal glands, Harderian glands, and respiratory epithelium. Moreover, there are two models of infection. The first type develops in breeding colonies (virus present endemically), where an epizootic develops in young non-immune individuals who develop conjunctivitis lasting up to a week [24]. The second type is associated with the sudden onset of episcleritis in naive rats from weaning to adulthood. Within this clinical picture, the symptoms persist for up to 2 weeks and, as with the herpes virus, complications may lead to keratitis and megaloglobus. Other frequently observed signs of SDAV infection include edema of the submaxillary salivary glands, nasal, and ocular discharge (characteristically porphyrin stained), lacrimation, photophobia, corneal opacities, corneal ulcers, and cervical swelling due to inflammation. Moreover, ancillary effects may include transient anorexia and weight loss and disruption of estrus [25–29].

SDAV and other RCoVs are today detectable by immunohistochemical techniques and serological tests, e.g., multiplex fluorescent immunoassay (MFI) with IFA confirmation, ELISA. Prior to seroconversion, especially in the case of an outbreak, histological examination of the Harderian glands and the submaxillary and parotid salivary glands may be necessary [30]. In addition, molecular diagnostic RT-PCR for the M gene (membrane glycoprotein gene), N gene (nucleocapsid gene), and *pol* gene are performed from a fragment of infected tissue, feces, or oral or cage swabs to confirm the initial diagnosis [31–33]. Individuals that are diagnosed as positive are quarantined or eliminated. Quarantine also includes animal rooms, which should be disconnected from use for at least 5–8 weeks. Since SDAV is highly contagious, personnel handling quarantined animals may become an important risk factor for transmission, because virus particles can be transmitted on protective clothing [23].

3. Characteristics

3.1. The General Classification

Coronaviruses, along with toroviruses, roniviruses, arteriviruses, and mesoniviruses, belong to the order *Nidovirales* ('nido' means 'nest'), so named because of the nested subgenomic RNAs generated during the replication cycle [34]. The *Nidovirales* order exhibits enveloped, non-segmented positive-sense RNA viruses. The characteristic features include a highly conserved genomic organization, expression of non-structural protein (NSPs) genes by ribosomal frameshifting, and several unique, non-conventional enzymatic activities encoded within the large replicase. The viruses with the largest capacity to cause epidemics and pandemics among the eight suborders of the order *Nidovirales* are the *Cornidovirineae*. In the *Cornidovirineae* suborder there is one family, *Coronaviridae,* divided into two subfamilies: *Letovirinae* and *Orthocoronavirinae* [35].

The *Coronaviridae* family comprises the largest RNA viruses, in terms of genome length (~30,000 nucleotides) and virion size (spherical, 80–180 nm in diameter). They infect birds and mammals, causing numerous diseases of the respiratory system, nervous system, internal organs, or digestive system. The *Orthocoronavirinae* subfamily is further

divided into four genera: Alpha-(14 subgenera and 19 species), Beta-(5 subgenera and 14 species), Delta-(3 subgenera and 7 species), and Gamma-(3 subgenera and 5 species) coronaviruses [36]. From a medical point of view, the most interesting are viruses of the Alpha and Beta genera, which contain human-infecting viruses (alpha-coronaviruses: HCoV-229E and HCoV-NL63, and beta-coronaviruses: HCoV-OC43, HCoV-HKU1, and SARS-CoV, MERS-CoV, and SARS-CoV-2). There are currently seven known human coronaviruses, almost all of them are zoonotic in origin and capable of breaking the species barrier. Of the animal coronaviruses (CoVs), alphacoronaviruses and betacoronaviruses infect only bats and other mammals, while gammacoronaviruses and deltacoronaviruses infect birds, and some of them can also infect marine mammals [37]. Among the most common are PEDV, porcine epidemic diarrhea virus; TGEV, transmissible gastroenteritis coronavirus; FCoV, feline coronavirus; MHV, mouse hepatitis virus; FIPV, feline infectious peritonitis virus; and IBV, infectious bronchitis virus (chicken). CoVs cause a wide variety of diseases in animals, and their ability to be rapidly transmitted among livestock and companion animals led to significant research on these viruses in the second half of the 20th century [38] (Figure 1).

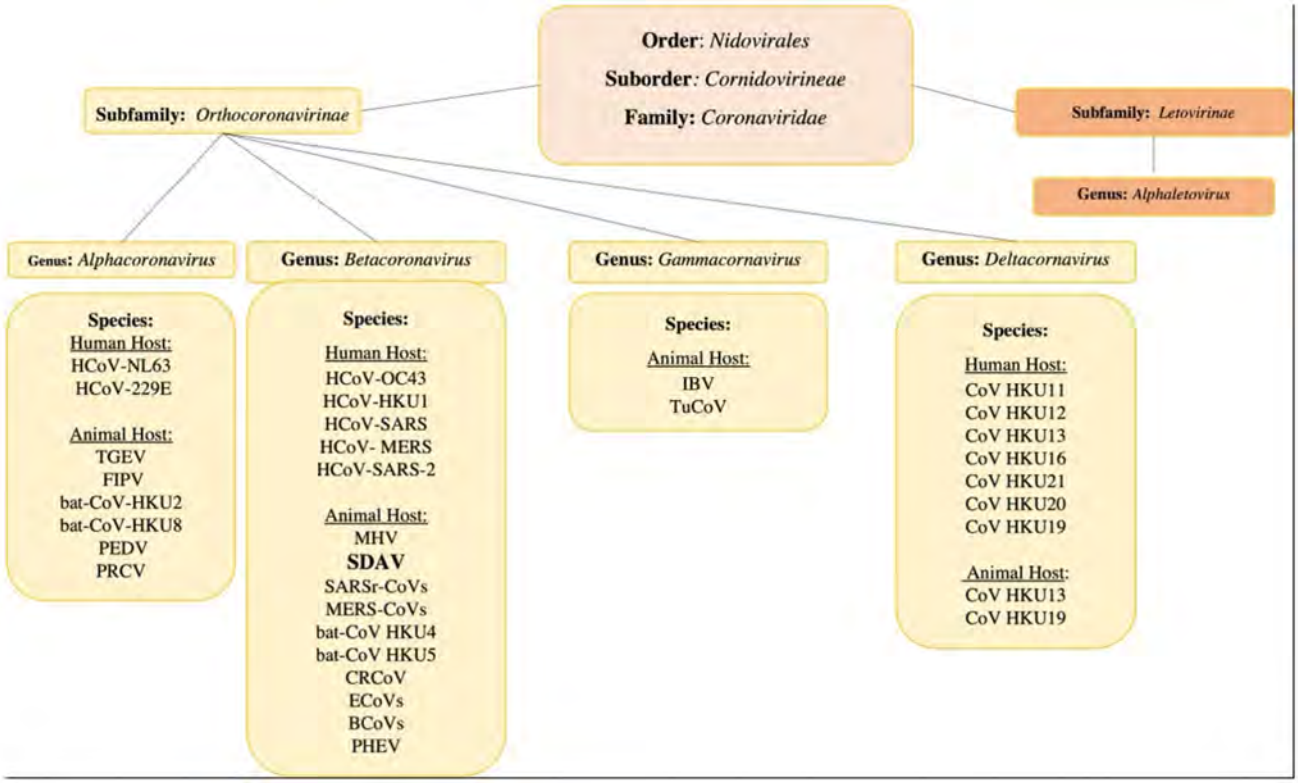

Figure 1. Taxonomy graph of the *Coronaviridae* family. Own work based on ICTV 2020 [36]. Abbreviations: alpha-coronaviruses: HCoV-NL63 (human coronavirus NL63), HCoV-229E (human coronavirus 229E), TGEV (transmissible gastroenteritis coronavirus), FIPV (feline infectious peritonitis virus), bat-CoV-HKU2 (Rhinolophus bat coronavirus HKU2), bat-CoV-HKU8 (Rhinolophus bat coronavirus HKU8), PEDV (porcine epidemic diarrheal virus), PRCV (porcine respiratory coronavirus); Betacoronaviruses: HCoV-OC43 (human coronavirus OC43), HCoV-HKU1 (human coronavirus HKU1), SARS (severe acute respiratory syndrome coronavirus), MERS (Middle East respiratory syndrome coronavirus), SARS-CoV-2 (Severe acute respiratory syndrome coronavirus -2), MHV (mouse hepatitis virus), SDAV (sialodacryoadenitis virus), bat-CoV- HKU4 (Tylonycteris bat coronavirus HKU4), bat-CoV-HKU5 (Pipistrellus bat coronavirus HKU5), CRCoV (canine respiratory coronaviruses), ECoVs (equine coronaviruses), BCoVs (bovine coronaviruses), PHEV (porcine haemagglutinating encephalomyelitis virus); Gammacoronaviruses: IBV (infectious bronchitis virus), TuCoV (turkey coronaviruses); Deltacoronaviruses: CoV HKU11 (bulbul CoV HKU11), CoV HKU12 (thrush CoV HKU12), CoV HKU 13 (munia CoV HKU13), CoV HKU16 (white-eye CoV HKU16), CoV HKU19 (night heron CoV HKU19), CoV HKU20 (wigeon CoV HKU20), CoV HKU21 (moorhen CoV HKU21).

3.2. The Rat Coronaviruses

To date, all known rat coronaviruses belong to the Beta genus. Betacoronaviruses contain five subgenera: *Embecovirus*, *Hibecovirus*, *Merbecovirus*, *Nobecovirus*, and *Sarbecovirus*. Members of the subgenera *Embecovirus* include SDAV, PRCV, RCV-BCMM, RCV-W, RCV-NJ, RCV-CARS, and novel ChRCoV (China Rattus Coronavirus) HKU24 [36,39]. The ChRCoV isolated from Norway rats in China represents the murine origin of *Betacoronavirus* 1. The significance of this discovery lies in the fact that it is a distinct species and not derived from either an avian or bat host, forming the basis of a new lineage of A Beta-CoV (A βCoVs), of which rodents are the principal host. ChRCoV HKU24 represents the murine lineage of Betacoronaviruses 1, with the possibility of interspecies transmission from rodents to other mammals. This transmission occurred before the appearance of the human HCoV coronavirus OC43 in the late 19th century [40]. It is also important to point out that the SDAV and other species of the rat coronaviruses belong to the same genus as the highly epidemic/pandemic and most pathogenic CoVs for humans, such as SARS-CoV, MERS-CoV, SARS-CoV-2, and others [37] (Figure 2).

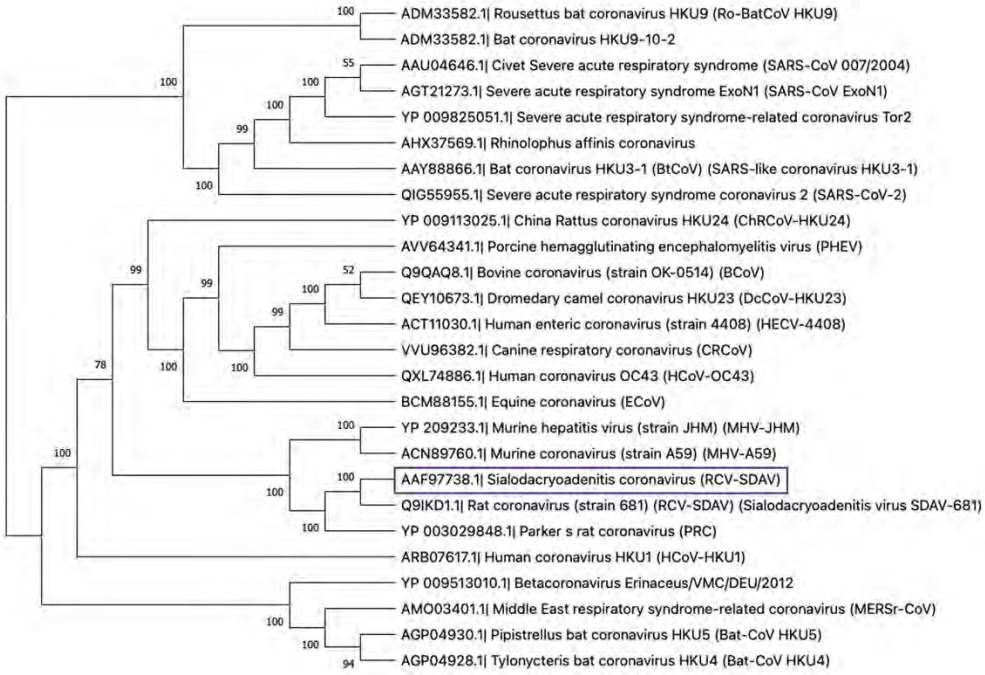

Figure 2. The neighbor-joining tree involves 26 amino acid sequences of spike glycoprotein of betacoronaviruses. The tree was constructed using the p-distance model and 1000 bootstraps in the MEGA X. 10.2.6. The SDAV is indicated in purple.

3.3. Virion Structure and Biological Functions of Proteins

The architecture of a SDAV virion, as in all coronaviruses, is spherical with a diameter ranging from 80 to 180 nm, as confirmed by tomography and cryo-electron microscopy [10]. It consists of a genomic core made up of non-segmented, positive sense, ssRNA stabilized by a nucleocapsid protein and surrounded by a viral membrane envelope. The most characteristic feature of all coronaviruses is the presence of tentacle-shaped spikes, emanating from the surface of the virion and giving it the appearance of a corona, hence the name. CoVs have a helically symmetric nucleocapsid, which is rare among positive sense RNA viruses and much more common in negative sense RNA viruses [41–43]. As Barker et al. (1994) and Yoo et al. (2000) described, SDAV contains four major coronaviral structural proteins and one present only in a few species of CoVs. These are the spike (S), membrane (M), envelope (E), nucleocapsid (N) proteins, and hemagglutinin esterase (HE), all of which are encoded at the 3′ end of the viral genome [42,43] (Figure 3).

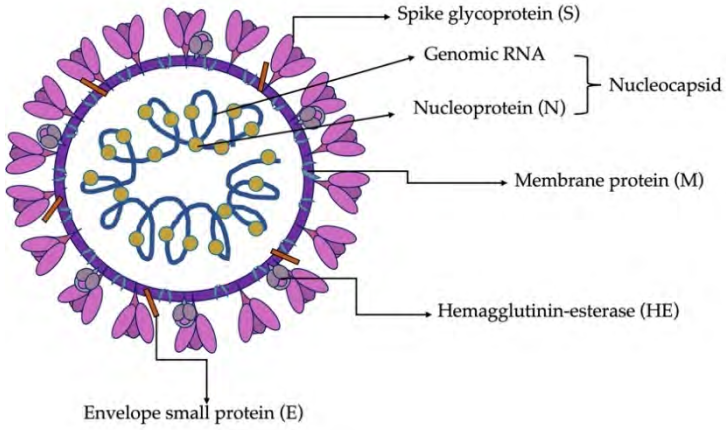

Figure 3. Schematic structure of SDAV virion. Own work based on [42–44].

The homotrimer protein S is the main molecule that binds the virus to the cell surface and is responsible for membrane fusion and entry of the viral genome into the cell. Consequently, it is responsible for SDAV infection, and its gene regions are highly variable and heterogeneous, which determines the change of virulence and tissue tropism. The S protein of SDAV is type I transmembrane N-linked glycosylated protein (149.6 kD), consisting of 1357 amino acids. It is cleaved by host proteases (TMPRESS2, furin) into two subunits: the S1 and S2 [45–48]. Comparing its sequence to MHV-A59 and MHV-JHM, it has relatively low similarity (76.6%), which comes from additional sequences in the N-terminal half of the S-protein gene of SDAV [43]. Numerous studies have shown that changes in the genes encoding the S protein or related factors can alter CoV virulence, tissue tropism, host range, or host immune response [49].

The second crucial structural protein of SDAV is protein M, a monomer composed of three hydrophobic domains strongly linked to the viral envelope [50]. The M protein of SDAV is 228 aa and 26 kD in size [43]. It has a short N-terminal ectodomain (extracellular domain), modified by glycosylation and C-terminal endodomain situated in the interior of the virion or on the cytoplasmic site of the intracellular membrane [41,51]. The role of protein M is to promote membrane curvature by adapting the membrane region for virion assembly and the uptake of structural protein residues. However, its role in folding virus-like-particles (VLPs), requires the participation and simultaneous expression of protein E. In addition, the M protein participates in the interaction with RNA, by carrying the genomic packaging signal [52].

Small membrane protein (E), made of 88 aa and 10.1 kD, is classified as a homopentamer and is present in small amounts in the virion [53]. It cooperates with protein M during morphogenesis and virion assembly. It also interacts as a viroporin in the host membrane to form pentameric protein-lipid pores that allow ion transport [54].

The nucleocapsid protein (N), the only one present in the helical nucleocapsid, has a size of 454 aa and 49.4 kD and is almost 97% similar to the MHV N protein [55]. Its role is to engage in the replication process by forming homodimers and homo-oligomers, by binding genomic RNA and packaging it, thus forming nucleocapsid. It is also responsible for inhibiting the translation process in the host cell ribosomes. In addition, it collaborates with proteins M and E in the folding and budding process of the newly assembled virions [56]. In other murine coronavirus, such as MHV-JHM, the nucleocapsid protein has been confirmed to be an important enhancer and determinant of neurovirulence [57].

The fifth major structural protein, haemagglutinin esterase (HE), anchored to the viral membrane envelope of SDAV, can bind sialic acid residues on surface glycoproteins and glycolipids. It has acetyl esterase activity and is a homodimer of a size of 439 aa and 49kD [43]. The HE lectin domain contributes to virion attachment and simultaneously enhances sialate-O-acetylesterase activity toward clustered sialoglycotopes. The SDAV HE is highly conserved compared to the MHVs. The HE protein is only present in some

embecoviruses (MHV and other rodent CoVs, BCoV, HCoV-OC43, HKU1) [58,59]. It has been postulated that HE is an essential protein for viruses within the betacoronavirus-1 species, including bovine coronavirus (BCoV) and HCoV-OC43 [60–62], but for MHV-JHM, MHV-S, and MHV-DVIM it is a non-essential protein [63–65]. Its role is more like an additional/supporting binding molecule, an addition to spike protein [66].

3.4. Cell Infection and Virus Replication

In rats and mice, SDAV can infect a wide range of cell types, such as the epithelial cells of respiratory airways, mononuclear cells in lymphoid organs, or CNS cells (neurons and astroglia) [19,67,68]. Entry receptor of SDAV has not yet been conclusively confirmed [69]. Unlike closely related viruses (MHV-JHM, MHV-S), SDAV and other RCoVs do not enter cells via CEACAM1 (carcinoembryonic antigen-related cell adhesion molecule 1) receptor or its isoforms [70].

What further distinguishes SDAV, and the other embecoviruses mentioned in Table 1, from other coronaviruses are two surface proteins that allow attachment to the host cell [71–78]. An essential clue in the context of the mechanism of SDAV entry into the cell and binding to the cell receptor was described by Gagneten et al. (1996) [70]. Among other results, the paper showed that only Parker RCV (RCV-P) expresses the haemagglutinin-esterase glycoprotein, which has acetyl-esterase activity. Therefore, SDAV, unlike RCV-P, exhibits the ability to bind to host cell receptors via S glycoprotein. In contrast, RCV-P can bind to the host cell via both haemagglutinin-esterase glycoprotein and spike protein [70]. However, further studies have not been carried out to determine the mechanism of SDAV entry. SDAV probably utilizes the mechanism used by human Betacoronaviruses-1 HKU1 and OC43 and binds via a spike protein to sugar-based receptor-determinates 4-O-acetylated sialic acids (4-O-Ac-Sias) attached as terminal residues to glycan chains on glycoproteins and lipids (forming glycoconjugates) [79]. Whereas HE, a sialate-O-esterase with a specific lectin domain attached to 4-O-Ac-Sia, acts as a receptor-destructive enzyme [44,78]. The hemagglutinin esterase protein promotes virus spread and entry in vivo by facilitating reversible virion attachment to O-acetylated sialic acids [80,81]. In the case of another representative of the embecoviruses, bovine coronavirus, HE activity at the end of replication results in the destruction of intracellular and surface receptors, facilitating the release of progeny virions from the infected cell [44].

After viral S and HE protrusions bind to glycan glycoconjugate receptors on the host cell membrane, fusion with the membrane of endocytic vesicles and virus entry into host cells occurs [49,79]. Most CoVs' spike proteins are cleaved; however, there are coronaviruses (FIPV, BCoV, MHV-Y, MHV-2) that fuse with cells without cleavage of S protein. In the case of SDAV, S protein undergoes proteolytic cleavage to two subunits: S1 and S2. The interesting fact is that the cleavage recognition sequence (HRARR) is identical to that of MHV-Y, which is not cleaved [43,82]. In fact, the cleavage of the spike (S) protein occurs at two different points of the infection cycle in CoVs. The first, usually induced by furin, results in the separation of the receptor-binding domain (RBD) from the fusion protein S. Following binding of the virion to the receptor, a second proteolytic cut by TMPRRS2 protease, cathepsin, or another occurs. This allows the S2' fusion peptide to be exposed, thus, it fuses the viral envelope with the cellular membrane, ultimately introducing RNA into the cytoplasm [83]. This process occurs directly on the plasma membrane or via endosomal vesicles and is always triggered by receptor binding [84]. However, this mechanism differs between coronaviruses species and strains and also depends on cell type. The MHV-JHM strain is capable of fusion at neutral pH but was also found in endosomal vesicles (by endosomal pathway) [85]. Recent studies have shown that MHV-JHM uses either the endosomal or the non-endosomal pathway, depending on the cell type. After fusion of the viral envelope with the endosome membrane, the viral genome is released into the cytoplasm. It has been shown that for MHV-4, the fusion is dependent on low pH, which is necessary to mature vesicles to late endosomes and subsequently set up an infection [85,86].

The next step of viral replication is translation of the replicase gene from virion genomic RNA. In the case of SDAV, the complete replicase gene sequence is thought to be as yet undiscovered [43]. However, the region of the replicase gene was described by Stephensen et al., 1999, while developing a consensus PCR assay for coronaviruses [87]. Two overlapping open reading frames (ORF) encode replicase genes: *repl1a* and *rep1b*, which express large polyproteins: pp1a and pp1ab. For these two polyproteins to be expressed, the virus uses a slippery sequence (5′-UUUAAAC-3′) and a pseudoknot RNA, which causes a ribosomal frameshift from *rep1a* to *rep1b* ORF (-1 frameshift). This process lasts until the unwinding of the RNA pseudoknot and the encountering of the *rep1a* stop codon, or pseudoknot blocks the ribosome from further elongation resulting in a stop at the slippery sequence, causing a -1 frameshift before extended translation into *rep1b*, which produced pp1ab polyprotein [88]. These polyproteins pp1a and pp1ab are co-translationally and post-translationally processed into the individual non-structural proteins (nsps). Pp1a and pp1ab contain the nsp 1–11 and 1–16, respectively, forming the viral replication and transcription complex. Proteolytic cleavage of these polyproteins into sixteen nsps is possible by two cysteine papain-like protease (PLP1, PLP2) and chymotrypsin-like protease. These non-structural proteins are then assembled into replicase-transcriptase complex (RTC) and dedicated to viral RNA synthesis [89–91]. With the formation of RTC and an environment suitable for RNA synthesis, the process of viral RNA replication and transcription of subgenomic mRNAs begins. The created microenvironment consists of viral replication organelles of characteristic perinuclear double-membrane vesicles (DMVs), convoluted membranes (CMs), and small open double-membrane spherules (DMSs) [69]. The whole replication process is initiated by synthesizing a full-length negative-sense genomic RNA, the template for producing a new positive-sense genomic RNA. Therefore, the generated fragments are then used for translation to produce more nsps and RTCs or packaged into new progeny virions. Notably, the transcription process of coronaviruses is a discontinuous viral transcription that involves the production of a set of nested 3′- and 5′-terminal subgenomic RNAs (sgRNAs) [92]. During negative-strand RNA synthesis, the RTC interrupts transcription against a transcriptional regulatory sequence (TRS) at the 3′ end and restarts upon encountering a TRS-L leader sequence at the 5′ end. The initiated re-synthesis of RNA in the TRS-L region results in the final negative-strand sgRNA formation, by attaching a copy of the negative-strand leader sequence to the nascent RNA strand. These strands are used as templates for the production of the characteristic nested subgenomic positive sense mRNA. The sgmRNA positive sense is successively used for the translation of structural and accessory proteins (spike protein (S), envelope protein (E), membrane protein (M), nucleocapsid protein (N), and hemagglutinin esterase (HE)) [93–95]. These proteins are transported to the endoplasmic reticulum and then to the ERGIC compartment (endoplasmic reticulum-Golgi intermediate compartment), where after the entry of viral RNA, the formation of mature virions occurs. The virions are transported in secretory vesicles to the vicinity of the cell membrane, where their exocytosis occurs, as with most coronaviruses (Figure 4). For SDAV, the mechanism of egress has not been clearly described, but for MHV, it is known to utilize the lysosomal trafficking pathway with antigen presentation. Intriguingly, some of the produced and unused S-proteins are transported to the surface of the cell membrane, allowing the connection of several neighboring cells, and thus easier propagation of the infection without going into the extracellular space and alarming the immune system [96–98].

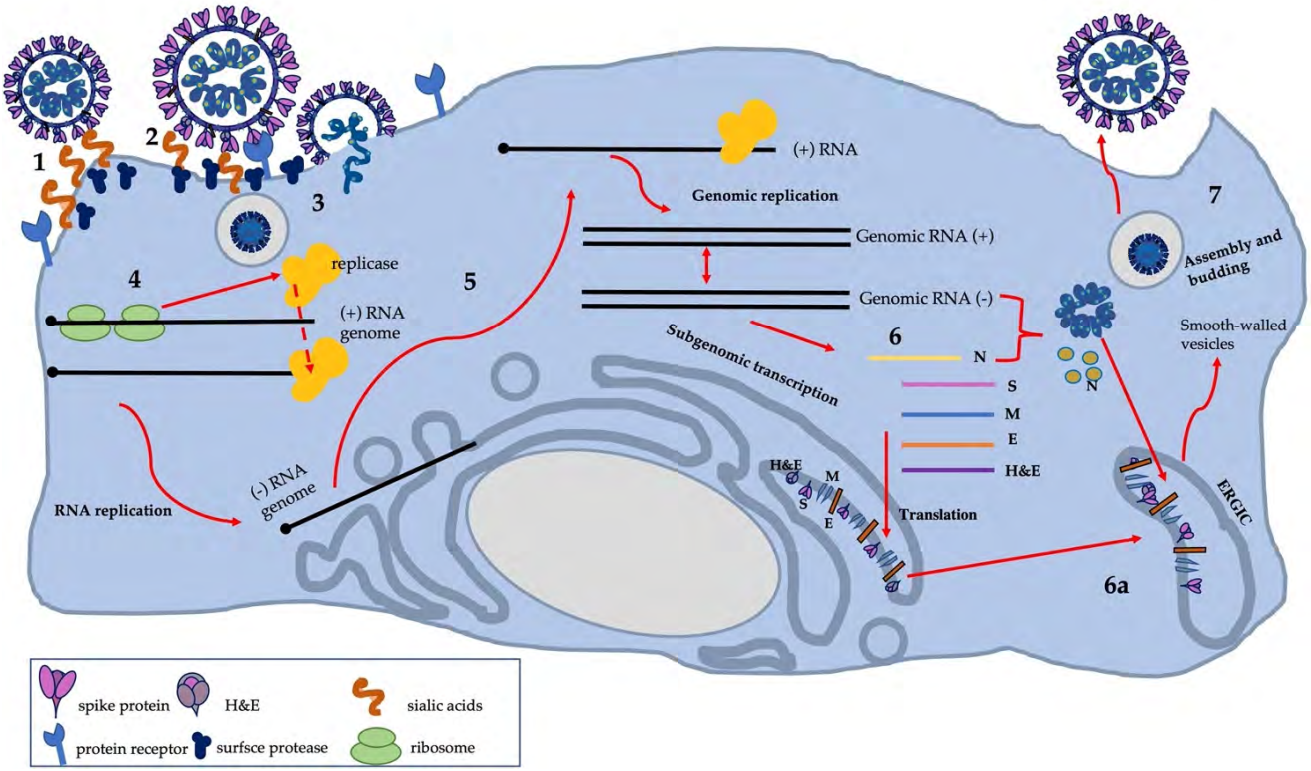

Figure 4. The scheme of SDAV replication: own work based on available knowledge. (1) SDAV HE probably mediates weak interactions with abundant host cell surface sialates, keeping the virus concentrated on cells before connecting S protein with the still unknown cell receptor. (2) S-glycoproteins then bind to protein receptors and are proteolytically activated (by cutting with specific proteases: TMPRESS2 or furin) into two subunits, S1 and S2, to conformations that induce membrane fusion. (3) Virus–cell fusion involves S binding to sialic acids. The likely route of entry into the cell is cell–virus fusion associated with S-protein connections to sialic acids. Connections to host cell receptors may not be required for this process, thus allowing distribution, beginning with the binding of viral protein S (RBD/S1) on the host cell receptor, driving a conformational change in the S2 subunit and facilitating its fusion with the plasma membrane and ultimately the release of viral genome (+ ssRNA) into the cytoplasm. However, the route by which SDAV enters the cell is still unknown and also can be mediated by acidified endosomes. (4) Promptly, the translation produces nonstructural pp1a and pp1ab co-terminal polyproteins (pp1a and pp1ab) that are proteolytically cleaved and assembled into a functional replicase–transcriptase complex: RTC. (5) Viral RNA synthesis produces copies of gRNA, as well as a nested set of sgRNA. This is possible by discontinuous transcription of a negative-sense RNA intermediate. (6) Following replication and sgRNA synthesis, various structural and accessory proteins are translated into the endoplasmic reticulum (ER) and (6a) then assembled as virion in the endoplasmic reticulum-Golgi intermediate component (ERGIC), along with viral genomes encapsulated by N protein budded into membranes of the ERGIC. (7) Then, virions are transported in vesicles and exit cells via exocytosis.

Table 1. Examples of viruses expressing the O-acetylesterases. Based on [44,99].

Family	Genus	Species	Substrate *
Coronaviridae	Coronavirus	Human coronavirus OC43 Bovine coronavirus Hemagglutinating encephalomyelitis virus	Neu5,9Ac$_2$
		Mouse hepatitis virus	Neu4,5Ac$_2$
		Puffinosis coronavirus	Neu4,5Ac$_2$
		Sialodacryoadenitis virus	Neu4,5Ac$_2$
	Torovirus	Porcine torovirus Bovine torovirus	n.d.

Table 1. *Cont.*

Family	Genus	Species	Substrate *
Orthomyxoviridae	Isavirus	Infectious salmon anemia virus	Neu4,5Ac$_2$
	Influenza C virus	Influenza C virus	Neu5,9Ac$_2$ (α2-8-linked, GL)
	Influenza D virus	Influenza D virus	Neu5,9Ac$_2$

* Abbrevations: Neu5,9Ac2 (*5-N-acetyl-9-O-acetyl neuraminic acid*); Neu4,5Ac2 (N-Acetyl-4-O-acetylneuraminic acid); *GL* (*glycolipids*).

3.5. Genomic Structure and Gene Functions

Until the 2000s, little was known about SDAV structural proteins. The only knowledge available was based on serological tests, without a concrete distinction between specific proteins. However, the first trial was attempted in 1993 by Kunita et al., on obtaining the complete nucleotide sequence of the N gene of SDAV-681 and establishing its similarity to other coronaviruses [55]. Additionally, it was known that antibodies specific for the structural proteins (spike protein, nucleocapsid protein, and membrane protein) of MHV, could recognize SDAV and PRCV using the immunoblot technique [42]. The next attempt was made in 2000 to characterize the remaining structural proteins and genome structure of SDAV by the team of Yoo et al. [43]. They sequenced the 3′ terminal 9.8 kb of the SDAV genomic RNA. During the research, using specially designed primers based on several coronaviral sequences, it was possible to generate seven cDNA fragments by RT-PCR cDNA cloning, which represented the 3′ terminal of the genome [43]. By amplifying various fragments, they confirmed the coding sequences for S, M, and N structural proteins and non-structural proteins, NS2 and HE gene in nine major open reading frames (ORFs), as is shown in the Figure 5. The coding sequence for 12.6k (ORF5a, non-structural protein), M (membrane-associated protein), and 7b (ORF7b, small internal ORF) is present in the +1 frame. The encoding sequence for polymerase 1b is present in the +2 frame, as well as genes for 15k (15k nonstructural protein), S (spike protein), and sM (small membrane protein). The other sequence for NS2 (nonstructural protein NS2), HE (hemagglutinin-esterase) and N (nucleocapsid protein) is placed in +3 frame. The NS2 gene absent in the MHV-JHM Wb1 variant is present in SDAV. In contrast to the HE gene region of MHV-JHM; MHV-4; MHV-DIVM, the SDAV HE nucleotides are highly conserved and exhibit low (58%) homology with other coronaviruses (BCV or OC43) but maintain a relatively high MHV amino acid identity (91%). In contrast to a previous statement in research by Gangneten et al., 1990, the HE protein is expressed by SDAV and maintained as in BCV, HCoV OC43, MHV-JHM, MHV-4, MHV-DVIM, and human Influenza type C [70]. Moreover, in small internal ORF (ORF7b) and the untranslated 3′ region (UTR), 298 encoding amino acids with a polyadenylated tail have been recognized. Additionally, each protein gene identified a short intergenic consensus sequence [43].

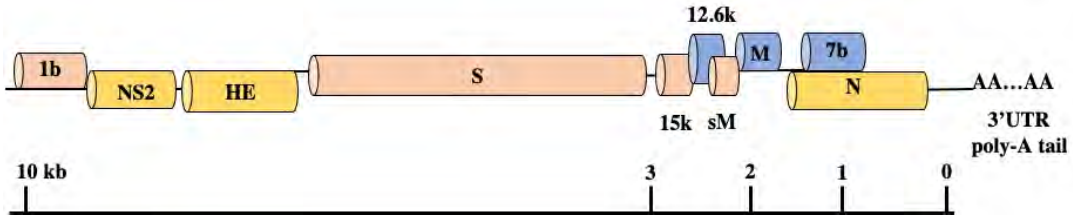

Figure 5. Genome structure and ORFs in the 3′ end 9.8 kb of SDAV viral genome. Own work based on [43].

In 2002, the method of detecting rodent coronaviruses, including SDAV, was improved by fluorogenic RT-PCR, known as Real-Time PCR/TaqMan PCR. Besselsen and colleagues designed a novel reverse transcriptase PCR procedure using an internal fluorogenic hybridization probe to detect MHV and RCVs. The reaction utilized selected fragments from a genome segment of M protein highly conserved among all coronaviruses [33]. This method

improved detection and in vitro quantitative analysis assays for SDAV research; previously invented by Yoo et al., 2000 [43].

3.6. SDAV Propagation and Role of In Vitro Studies

Until recently, SDAV had been mainly used in the evaluation of alveolar epithelial cell response to infection. The team of Miura et al. (2007) detected the ability of uninfected alveolar type I epithelial cells to produce chemokines as a response to IL-1 produced by SDAV/RCoV-P-infected cells and leading to pulmonary inflammation [100]. Further research by Funk et al. (2009) provided insight into SDAV-infection induced chemokine expression in alveolar type I, type II, and airway epithelial cells. They confirmed the importance of SDAV as a model for the early events of innate immune response to respiratory CoVs infections of natural hosts, and they also detected that type I epithelial cells stand as a primary target of SDAV infection and the crucial role of CXC chemokine expression following infection and innate immune response cell influx [68].

As currently known, SDAV in vitro propagation is possible in established cell lines, such as murine fibroblasts L-2(Percy) cells, subclone L2P-41.a, LBC cells, RCV-9, and in primary rat kidney cell cultures (RKCC). In other frequently used cell lines (VERO, Hep-2, NTCT 1469, BHK-21), infection is not possible [15,28,70,101–104]. For purification and plaque assay, L-2cells, L2P-41.a, and LBC are often used [100,101]. The virus samples can be stored at −60 °C for 7 years, but according to research by Jacoby et al. (1975), they can become less infectious when stored at −20 °C [11,105].

4. Conclusions

Despite many commonalities with zoonotic coronaviruses of the genus Betacoronaviruses, there is a notable lack of interest in rat coronavirus SDAV. When considering SDAV in the context of a potential zoonosis, and not just an enzootic laboratory threat, the insufficient knowledge of the entire replication cycle after entry into the organism must be taken into consideration. Information on the entry receptor and the surface interaction with the host cell is still unclear. Indeed, on the basis of the information presented in this review, it is tempting to speculate that most of the processes are identical or very similar to other representatives of embecoronaviruses and betacoronaviruses. However, the high capacity of this family for transient mutations in the hypervariable region of the main structural glycoprotein, the S-spike protein, may lead to another crossing of the inter-species barrier, as happened in 2019 in Wuhan with Sars-CoV-2 [38]. Information about the possible SDAV infection of mice was confirmed in the 1970s by the teams of Parker (1970) and Bhatt (1972) [16,17]. The growing number of new coronaviruses recently is worrying, due to the close relationship between coronaviruses and distantly related animals. Such interspecies jumps can cause uncontrolled outbreaks of zoonoses. Examples include: (i) FCoV and CCoV in the alphacoronaviruses group; (ii) MHV and the aforementioned SDAV; other RCoVs or HCoV -OC43, BCoV and PHEV; SARS -CoV-1, SARS-COV-2, and MERS-CoV in the betacoronaviruses group; (iii) IBV, TCoV, Asian leopard cat coronavirus and new avian coronaviruses in the gammacoronaviruses group [38,106,107].

Symptomatic SDAV infection is currently relatively easy to control under laboratory conditions [108]. When infection occurs and it is confirmed by PCR tests, infected animals can be eliminated. However, mild or asymptomatic infections can become a problem, providing ideal conditions for the virus to mutate. Poorly maintained hygienic conditions in mouse or rat cages and inadequate management of potentially infectious waste could contribute significantly to undesired SDAV transmission. This problem was highlighted in a work of de Bruin et al. (2016). A systematic review revealed that through the transfer of soiled bedding (mainly spread by the oral and fecal route), infection is effectively transmitted in cases of mouse hepatitis virus (MHV), mouse parvovirus (MPV), and Theiler's mouse encephalomyelitis virus (TMEV). Unfortunately, in the context of SDAV infection or other infectious agents (minute virus of mice (MVM), Sendai virus (SeV), murine rotavirus (EDIM)), insufficient data are available for evaluation [108].

At this time, only studies on respiratory infections caused by SDAV have been described. More studies should be conducted to identify the mechanism of virus–cell interaction on different cell models. In vitro CNS-SDAV model studies are still lacking, and based on recent studies concerning SARS-CoV-2, it appears that this virus (SDAV) may cause significant changes in the central nervous system, as in other CoVs [18,67,109].

Based on actual knowledge and general properties of coronaviruses a main question can be asked. If SDAV a possible threat to humans? Considering the algorithm and risk of zoonotic potential designed by Palmer et al. in 2005, there are three crucial stages in the transmission of a pathogen, which comprise the levels of potential risk [110]. The risk of cross species transmission and exposure of humans to an infected host is relatively substantial. The high capacity of coronaviruses to mutate within the genome, especially the S-protein subunit (spike), leads to rapid adaptation and transmission among multiple hosts. The facts of the facilitated potential of coronaviruses to cross the inter-species barrier and being a host commonly found near humans highlights the need for further research into the characterization of SDAV infections.

Author Contributions: M.B. conceptualized the review, prepared the original draft, table, and figures; A.S. and M.W.B. revised the manuscript; J.C. conceptualized the review, revised, and edited the manuscript. All authors have read and agreed to the published version of the manuscript.

Funding: This research received no external funding.

Conflicts of Interest: The authors declare no conflict of interest.

References

1. Mallapaty, S. The search for animals harbouring coronavirus-and why it matters. *Nature* **2021**, *591*, 26–28. [CrossRef]
2. Shi, J.; Wen, Z.; Zhong, G.; Yang, H.; Wang, C.; Huang, B.; Liu, R.; He, X.; Shuai, L.; Sun, Z.; et al. Susceptibility of ferrets, cats, dogs, and other domesticated animals to SARS-coronavirus 2. *Science* **2020**, *368*, 1016–1020. [CrossRef]
3. Schlottau, K.; Rissmann, M.; Graaf, A.; Schön, J.; Sehl, J.; Wylezich, C.; Höper, D.; Mettenleiter, T.C.; Balkema-Buschmann, A.; Harder, T.; et al. SARS-CoV-2 in fruit bats, ferrets, pigs, and chickens: An experimental transmission study. *Lancet Microbe* **2020**, *1*, 218–225. [CrossRef]
4. Seyran, M.; Takayama, K.; Uversky, V.N.; Lundstrom, K.; Palù, G.; Sherchan, S.P.; Attrish, D.; Rezaei, N.; Aljabali, A.; Ghosh, S.; et al. The structural basis of accelerated host cell entry by SARS-CoV-2†. *FEBS J.* **2020**, *288*, 5010–5020. [CrossRef] [PubMed]
5. Abdel-Moneim, A.S.; Abdelwhab, E.M. Evidence for SARS-CoV-2 Infection of Animal Hosts. *Pathogens* **2020**, *9*, 529. [CrossRef] [PubMed]
6. Yan, H.; Jiao, H.; Liu, Q.; Zhang, Z.; Xiong, Q.; Wang, B.J.; Wang, X.; Guo, M.; Wang, L.F.; Lan, K.; et al. ACE2 receptor usage reveals variation in susceptibility to SARS-CoV and SARS-CoV-2 infection among bat species. *Nat. Ecol. Evol.* **2021**, *5*, 600–608. [CrossRef]
7. Meerburg, G.B.; Singleton, R.G.; Kijlstra, A. Rodent-borne diseases and their risks for public health. *Crit. Rev. Micro.* **2009**, *35*, 221–270. [CrossRef]
8. Alvarez-Munoz, S.; Upegui-Porras, N.; Gomez, A.P.; Ramirez-Nieto, G. Key Factors That Enable the Pandemic Potential of RNA Viruses and Inter-Species Transmission: A Systematic Review. *Viruses* **2021**, *13*, 537. [CrossRef]
9. Han, B.A.; Schmidt, J.P.; Bowden, S.E.; Drake, J.M. Rodent reservoirs of future zoonotic diseases. *Proc. Natl. Acad. Sci. USA* **2015**, *112*, 7039–7044. [CrossRef]
10. Jonas, A.M.; Craft, J.; Black, L.; Bhatt, P.N.; Hilding, D. Sialodacryoadenitis in the rat. A light and electron microscopic study. *Arch. Pathol.* **1969**, *88*, 613–622.
11. Jacoby, R.O.; Bhatt, P.N.; Jonas, A.M. Pathogenesis of sialodacryoadenitis in gnotobiotic rats. *Vet. Pathol.* **1975**, *12*, 196–209. [CrossRef] [PubMed]
12. Percy, D.H.; Hanna, P.E.; Paturzo, F.; Bhatt, P.N. Comparison of strain susceptibility to experimental sialodacryoadenitis in rats. *Lab. Anim. Sci.* **1984**, *34*, 255–260. [PubMed]
13. Wojcinski, Z.W.; Percy, D.H. Sialodacryoadenitis virus-associated lesions in the lower respiratory tract of rats. *Vet. Pathol.* **1986**, *23*, 278–286. [CrossRef] [PubMed]
14. Hartley, J.W.; Rowe, W.P.; Bloom, J.J.; Turner, H.C. Antibodies to mouse hepatitis virus in human sera. *Proc. Soc. Exp. Biol. Med.* **1964**, *115*, 414–418. [CrossRef] [PubMed]
15. Anonymous. *Coronaviruses*; Nature: London, UK, 1968; pp. 220–650.
16. Parker, J.C.; Cross, S.S.; Rowe, W.P. Rat coronavirus (RCV): A prevalent, naturally occurring pneumotropic virus of rats. *Arch. Gesamte Virusforsch.* **1970**, *31*, 293–302. [CrossRef]
17. Bhatt, P.N.; Percy, D.H.; Jonas, A.M. Characterization of the virus of sialodacryoadenitis of rats: A member of the coronvarivus group. *J. Infect. Dis.* **1972**, *126*, 123–130. [CrossRef]

18. Kojima, A.; Fujimani, F.; Doi, K.; Yasoshima, A.; Okaniwa, A. Isolation and properties of sialodacryoadenitis virus of rats. *Exp. Anim.* **1980**, *29*, 409–418. [CrossRef] [PubMed]
19. Maru, M.; Sato, K. Characterization of a coronavirus isolated from rats with sialodacryoadenitis. *Arch. Virol.* **1982**, *73*, 33–43. [CrossRef]
20. Compton, S.R.; Smith, A.L.; Gaertner, D.J. Comparison of the pathogenicity in rats of rat coronaviruses of different neutralization groups. *Lab. Anim. Sci.* **1999**, *49*, 514–518.
21. Compton, S.R.; Vivas-Gonzales, B.E.; Macy, J.D. Reverse transcriptase chain reaction-based diagnosis and molecular characterization of a new rat coronavirus strain. *Lab. Anim. Sci.* **1999**, *49*, 506–513.
22. Gaertner, D.J.; Compton, S.R.; Winograd, D.F. Environmental stability of rat coronaviruses (RCVs). *Lab. Anim. Sci.* **1993**, *43*, 403–404.
23. La Regina, M.; Woods, L.; Klender, P.; Gaertner, D.J.; Paturzo, F.X. Transmission of sialodacryoadenitis virus (SDAV) from infected rats to rats and mice through handling, close contact, and soiled bedding. *Lab. Anim. Sci.* **1992**, *42*, 344–346.
24. Bhatt, P.N.; Jacoby, R.O. Epizootiological observations of natural and experimental infection with sialodacryoadenitis virus in rats. *Lab. Anim. Sci.* **1985**, *35*, 129–134.
25. Percy, D.H.; Bond, S.J.; Paturzo, F.X.; Bhatt, P.N. Duration of protection from reinfection following exposure to sialodacryoadenitis virus in Wistar rats. *Lab. Anim. Sci.* **1990**, *40*, 144–149. [PubMed]
26. Weir, E.C.; Jacoby, R.O.; Paturzo, E.X.; Johnson, E.A. Infection of SDAV-immune rats with SDAV and rat coronavirus. *Lab. Anim. Sci.* **1990**, *40*, 363–366. [PubMed]
27. Percy, D.H.; Williams, K.L.; Croy, B.A. Experimental sialodacryoadenitis virus infection in severe combined immunodeficient mice. *Can. J. Vet. Res.* **1991**, *55*, 89–90. [PubMed]
28. Percy, D.H.; Scott, R.A. Coronavirus infection in the laboratory rat: Immunization trials using attenuated virus replicated in L-2 cells. *Can. J. Vet. Res.* **1991**, *55*, 60–66. [PubMed]
29. Sato, T.; Meguid, M.M.; Quinn, R.H.; Zhang, L.; Chen, C. Feeding behavior during sialodacryoadenitis viral infection in rats. *Physiol. Behav.* **2001**, *72*, 721–726. [CrossRef]
30. Barthold, S.W.; Griffey, S.M.; Percy, D.H. *Rat, Pathology of Laboratory Rodents and Rabbits*, 4th ed.; John Wiley & Sons, Inc: Hoboken, NJ, USA, 2016; pp. 119–172.
31. Smith, A.L.; Winograd, D.F. Two enzyme immunoassays for the detection of antibody to rodent coronaviruses. *J. Virol. Methods* **1986**, *14*, 335–343. [CrossRef]
32. Homberger, F.R.; Smith, A.L.; Barthold, S.W. Detection of rodent coronaviruses in tissues and cell cultures by using polymerase chain reaction. *J. Clin. Microbiol.* **1991**, *29*, 2789–2793. [CrossRef]
33. Besselsen, D.G.; Wagner, A.M.; Loganbill, J.K. Detection of rodent coronaviruses by use of fluorogenic reverse transcriptase-polymerase chain reaction analysis. *Comp. Med.* **2002**, *52*, 111–116.
34. Gorbalenya, A.E.; Enjuanes, L.; Ziebuhr, J.; Snijder, E.J. Nidovirales: Evolving the largest RNA virus genome. *Virol. Res.* **2006**, *117*, 17–37. [CrossRef] [PubMed]
35. Bukhari, K.; Mulley, G.; Gulyaeva, A.A.; Zhao, L.Y.; Shu, G.C.; Jiang, J.P.; Neuman, B.W. Description and initial characterization of metatranscriptomic nidovirus-like genomes from the proposed new family Abyssoviridae, and from a sister group to the Coronavirinae, the proposed genus Alphaletovirus. *Virol. J.* **2018**, *524*, 160–171. [CrossRef] [PubMed]
36. Walker, P.J.; Siddell, S.G.; Lefkowitz, E.J.; Mushegian, A.R.; Adriaenssens, E.M.; Dempsey, D.M.; Dutilh, B.E.; Harrach, B.; Harrison, R.L.; Hendrickson, R.C.; et al. Changes to virus taxonomy and the Statutes ratified by the International Committee on Taxonomy of Viruses (2020). *Arch. Virol.* **2020**, *165*, 2737–2748. [CrossRef] [PubMed]
37. Zhou, Z.; Qiu, Y.; Ge, X. The taxonomy, host range and pathogenicity of coronaviruses and other viruses in the *Nidovirales* order. *Anim. Dis.* **2021**, *1*, 1–28. [CrossRef]
38. Cui, J.; Li, F.; Shi, Z.L. Origin and evolution of pathogenic coronaviruses. *Nat. Revs. Microbiol.* **2019**, *17*, 181–192. [CrossRef]
39. Wu, Z.; Lu, L.; Du, J.; Yang, L.; Ren, X.; Liu, B.; Jiang, J.; Yang, J.; Dong, J.; Sun, L.; et al. Comparative analysis of rodent and small mammal viromes to better understand the wildlife origin of emerging infectious diseases. *Microbiome* **2018**, *6*, 178. [CrossRef]
40. Lau, S.K.P.; Woo, P.C.Y.; Li, K.S.M.; Tsang, A.K.L.; Fan, R.Y.Y.; Luk, H.K.H.; Cai, J.-P.; Chan, K.-H.; Zheng, B.-J.; Wang, M.; et al. Discovery of a novel coronavirus, China Rattus coronavirus HKU24, from Norway rats supports the murine origin of Betacoronavirus 1 and has implications for the ancestor of Betacoronavirus lineage A. *J. Virol.* **2015**, *89*, 3076–3092. [CrossRef]
41. Wang, Y.; Grunewald, M.; Perlman, S. Coronaviruses: An Updated Overview of Their Replication and Pathogenesis. *Methods Mol. Biol.* **2020**, *2203*, 1–29. [CrossRef]
42. Barker, M.G.; Percy, D.H.; Hovland, D.J.; MacInnes, J.I. Preliminary characterization of the structural proteins of the coronaviruses, sialodacryoadenitis virus and Parker's rat coronavirus. *Can. J. Vet. Res.* **1994**, *58*, 99–103.
43. Yoo, D.; Pei, Y.; Christie, N.; Cooper, M. Primary structure of the sialodacryoadenitis virus genome: Sequence of the structural-protein region and its application for differential diagnosis. *Clin. Diag. Lab. Immunol.* **2000**, *7*, 568–573. [CrossRef]
44. Strasser, P.; Unger, U.; Strobl, B.; Vilas, U.; Vlasak, R. Recombinant viral sialate-O-acetylesterases. *Glyc. J.* **2004**, *20*, 551–561. [CrossRef]
45. Compton, S.R.; Kunita, S. Characterization of the S protein of enterotropic murine coronavirus strain-Y. *Adv. Exp. Med. Biol.* **1995**, *380*, 23–28. [CrossRef]
46. Raamsman, M.J.; Locker, J.K.; de Hooge, A.; de Vries, A.A.; Griffiths, G.; Vennema, H.; Rottier, P.J. Characterization of the coronavirus mouse hepatitis virus strain A59 small membrane protein E. *J. Virol.* **2000**, *74*, 2333–2342. [CrossRef]

47. Yadav, R.; Chaudhary, J.K.; Jain, N.; Chaudhary, P.K.; Khanra, S.; Dhamija, P.; Sharma, A.; Kumar, A.; Handu, S. Role of Structural and Non-Structural Proteins and Therapeutic Targets of SARS-CoV-2 for COVID-19. *Cells* **2021**, *10*, 821. [CrossRef] [PubMed]
48. Fung, T.S.; Liu, X.D. Similarities and Dissimilarities of COVID-19 and Other Coronavirus Diseases. *Annu. Rev. Microbiol.* **2021**, *75*, 1–29. [CrossRef] [PubMed]
49. V'kovski, P.; Kratzel, A.; Steiner, S.; Stalder, H.; Thiel, V. Coronavirus biology and replication: Implications for SARS-CoV-2. *Nat. Rev. Microbiol.* **2021**, *19*, 155–170. [CrossRef] [PubMed]
50. Hogue, B.G.; Machamer, C.E. Coronavirus structural proteins and virus assembly. In *Nidoviruses*; Perlman, S., Ed.; ASM Press: Washington, DC, USA, 2007; pp. 179–200.
51. Neuman, B.W.; Kiss, G.; Kunding, A.H.; Bhella, D.M.; Baksh, F.M.; Connelly, S.; Droese, B.; Klaus, J.P.; Makino, S.; Sawicki, S.G.; et al. A structural analysis of M protein in coronavirus assembly and morphology. *J. Struct. Biol.* **2011**, *174*, 11–22. [CrossRef] [PubMed]
52. Narayanan, K.; Chen, C.J.; Maeda, J.; Makino, S. Nucleocapsid-independent specific viral RNA packaging via viral envelope protein and viral RNA signal. *J. Virol.* **2003**, *77*, 2922–2927. [CrossRef]
53. Masters, P.S. The molecular biology of coronaviruses. *Adv. Virus Res.* **2006**, *66*, 193–292.
54. Wilson, L.; McKinlay, C.; Gage, P.; Ewart, G. SARS coronavirus E protein forms cation- selective ion channels. *Virology* **2004**, *330*, 322–331. [CrossRef]
55. Kunita, S.; Mori, M.; Terada, E. Sequence analysis of the nucleocapsid protein gene of rat coronavirus SDAV-681. *Virology* **1993**, *193*, 520–523. [CrossRef] [PubMed]
56. Payne, S. *In Viruses: From Understanding to Investigation*, 1st ed.; Payne, S., Ed.; Academic Press: New York, NY, USA, 2017; Volume 1, pp. 149–158. [CrossRef]
57. Cowley, T.J.; Long, S.Y.; Weiss, S.R. The murine coronavirus nucleocapsid gene is a determinant of virulence. *J. Virol.* **2010**, *84*, 1752–1763. [CrossRef] [PubMed]
58. Lang, Y.; Li, W.; Li, Z.; Koerhuis, D.; van den Burg, A.; Rozemuller, E.; Bosch, B.J.; van Kuppeveld, F.; Boons, G.J.; Huizinga, E.G.; et al. Coronavirus hemagglutinin-esterase and spike proteins coevolve for functional balance and optimal virion avidity. *Proc. Nat. Acad. Sci. USA* **2020**, *117*, 25759–25770. [CrossRef] [PubMed]
59. Klausegger, A.; Strobl, B.; Regl, G.; Kaser, A.; Luytjes, W.; Vlasak, R. Identification of a coronavirus hemagglutinin-esterase with a substrate specificity different from those of influenza C virus and bovine coronavirus. *J. Virol.* **1999**, *73*, 3737–3743. [CrossRef]
60. Kienzle, T.E.; Abraham, S.; Hogue, B.G.; Brian, D.A. Structure and orientation of expressed bovine coronavirus hemagglutinin-esterase protein. *J. Virol.* **1990**, *64*, 1834–1838. [CrossRef]
61. Vlasak, R.; Luytjes, W.; Spaan, W.; Palese, P. Human and bovine coronaviruses recognize sialic acid-containing receptors similar to those of influenza C viruses. *Proc. Natl. Acad. Sci. USA* **1988**, *85*, 4526–4529. [CrossRef]
62. Vlasak, R.; Luytjes, W.; Leider, J.; Spaan, W.; Palese, P. The E3 protein of bovine coronavirus is a receptor-destroying enzyme with acetylesterase activity. *J. Virol.* **1988**, *62*, 4686–4690. [CrossRef]
63. Yokomori, K.; Banner, L.R.; Lai, M.M. Heterogeneity of gene expression of the hemagglutinin-esterase (HE) protein of murine coronaviruses. *Virology* **1991**, *183*, 647–657. [CrossRef]
64. Yokomori, K.; Baker, S.C.; Stohlman, S.A.; Lai, M.M. Hemagglutinin-esterase-specific monoclonal antibodies alter the neuropathogenicity of mouse hepatitis virus. *J. Virol.* **1992**, *66*, 2865–2874. [CrossRef]
65. Yokomori, K.; Asanaka, M.; Stohlman, S.A.; Makino, S.; Shubin, R.A.; Gilmore, W.; Weiner, L.P.; Wang, F.I.; Lai, M.M. Neuropathogenicity of mouse hepatitis virus JHM isolates differing in hemagglutinin-esterase protein expression. *J. Neurovirol.* **1995**, *1*, 330–339. [CrossRef]
66. Weiss, S.R.; Leibowitz, J.L. Coronavirus pathogenesis. *Adv. Virus Res.* **2011**, *81*, 85–164. [CrossRef]
67. Percy, D.H.; Lynch, J.A.; Descôteaux, J.P. Central nervous system lesions in suckling mice and rats inoculated intranasally with sialodacryoadenitis virus. *Vet. Pathol.* **1986**, *23*, 42–49. [CrossRef]
68. Funk, C.J.; Manzer, R.; Miura, T.A.; Groshong, S.D.; Ito, Y.; Travanty, E.A.; Leete, J.; Holmes, K.V.; Mason, R.J. Rat respiratory coronavirus infection: Replication in airway and alveolar epithelial cells and the innate immune response. *J. Gen. Virol.* **2009**, *90*, 2956–2964. [CrossRef]
69. Perlman, S.; Netland, J. Coronaviruses post-SARS: Update on replication and pathogenesis. *Nat. Rev. Microbiol.* **2009**, *7*, 439–450. [CrossRef] [PubMed]
70. Gagneten, S.; Scanga, C.A.; Dveksler, G.S.; Beauchemin, N.; Percy, D.; Holmes, K.V. Attachment glycoproteins and receptor specificity of rat coronaviruses. *Lab. Anim. Sci.* **1996**, *46*, 159–166.
71. King, B.; Potts, B.J.; Brian, D.A. Bovine coronavirus hemagglutinin protein. *Virus Res.* **1985**, *2*, 53–59. [CrossRef]
72. Williams, R.K.; Jiang, G.S.; Holmes, K.V. Receptor for mouse hepatitis virus is a member of the carcinoembryonic antigen family of glycoproteins. *Proc. Nat. Acad. Sci. USA* **1991**, *88*, 5533–5536. [CrossRef] [PubMed]
73. Regl, G.; Kaser, A.; Iwersen, M.; Schmid, H.; Kohla, G.; Strobl, B.; Vilas, U.; Schauer, R.; Vlasak, R. The hemagglutinin-esterase of mouse hepatitis virus strain S is a sialate-4-O-acetylesterase. *J. Virol.* **1999**, *73*, 4721–4727. [CrossRef] [PubMed]
74. Wurzer, W.J.; Obojes, K.; Vlasak, R. The sialate-4-O-acetylesterases of coronaviruses related to mouse hepatitis virus: A proposal to reorganize group 2 Coronaviridae. *J. Gen. Virol.* **2002**, *83*, 395–402. [CrossRef] [PubMed]

75. Smits, S.L.; Gerwig, G.J.; van Vliet, A.L.; Lissenberg, A.; Briza, P.; Kamerling, J.P.; Vlask, R.; de Groot, R.J. Nidovirus sialate-O-acetylesterases: Evolution and substrate specificity of corona- and toroviral receptor-destroying enzymes. *J. Biol. Chem.* **2005**, *280*, 6933–6941. [CrossRef] [PubMed]
76. Langereis, M.A.; van Vliet, A.L.; Boot, W.; de Groot, R.J. Attachment of mouse hepatitis virus to O-acetylated sialic acid is mediated by hemagglutinin-esterase and not by the spike protein. *J. Virol.* **2010**, *84*, 8970–8974. [CrossRef]
77. Langereis, M.A.; Zeng, Q.; Heesters, B.A.; Huizinga, E.G.; de Groot, R.J. The murine coronavirus hemagglutinin-esterase receptor-binding site: A major shift in ligand specificity through modest changes in architecture. *PLoS Pathog.* **2012**, *8*, 1002492. [CrossRef]
78. Bakkers, M.J.; Zeng, Q.; Feitsma, L.J.; Hulswit, R.J.; Li, Z.; Westerbeke, A.; van Kuppeveld, F.J.; Boons, G.J.; Langereis, M.A.; Huizinga, E.G.; et al. Coronavirus receptor switch explained from the stereochemistry of protein-carbohydrate interactions and a single mutation. *Proc. Natl. Acad. Sci. USA* **2016**, *113*, 3111–3119. [CrossRef] [PubMed]
79. Hulswit, R.J.G.; Lang, Y.; Bakkers, M.J.G.; Li, W.; Li, Z.; Schouten, A.; Ophorst, B.; van Kuppeveld, F.J.M.; Boons, G.J.; Bosch, B.J.; et al. Human coronaviruses OC43 and HKU1 bind to 9-O-acetylated sialic acids via a conserved receptor-binding site in spike protein domain A. *Proc. Natl. Acad. Sci. USA* **2019**, *116*, 2681–2690. [CrossRef] [PubMed]
80. Lissenberg, A.; Vrolijk, M.M.; van Vliet, A.L.; Langereis, M.A.; de Groot-Mijnes, J.D.; Rottier, P.J.; de Groot, R.J. Luxury at a cost? Recombinant mouse hepatitis viruses expressing the accessory hemagglutinin esterase protein display reduced fitness in vitro. *J. Virol.* **2005**, *79*, 15054–15063. [CrossRef] [PubMed]
81. Olofsson, S.; Bergström, T. Glycoconjugate glycans as viral receptors. *Ann. Med.* **2005**, *37*, 154–172. [CrossRef] [PubMed]
82. Hingley, S.T.; Leparc-Goffart, I.; Weiss, S.R. The spike protein of murine coronavirus mouse hepatitis virus strain A59 is not cleaved in primary glial cells and primary hepatocytes. *J. Virol.* **1998**, *72*, 1606–1609. [CrossRef]
83. White, J.M.; Whittaker, G.R. Fusion of Enveloped Viruses in Endosomes. *Traffic* **2016**, *7*, 593–614. [CrossRef]
84. Matsuyama, S.; Taguchi, F. Receptor-induced conformational changes of murine coronavirus spike protein. *J. Virol.* **2002**, *76*, 11819–11826. [CrossRef]
85. Nash, T.C.; Buchmeier, M.J. Entry of mouse hepatitis virus into cells by endosomal and nonendosomal pathways. *Virology* **1997**, *233*, 1–8. [CrossRef] [PubMed]
86. Burkard, C.; Verheije, M.H.; Wicht, O.; van Kasteren, S.I.; van Kuppeveld, F.J.; Haagmans, B.L.; Pelkmans, L.; Rottier, P.J.; Bosch, B.J.; de Haan, C.A. Coronavirus cell entry occurs through the endo-/lysosomal pathway in a proteolysis-dependent manner. *PLoS Pathog.* **2014**, *10*, 1004502. [CrossRef] [PubMed]
87. Stephensen, C.B.; Casebolt, D.B.; Gangopadhyay, N.N. Phylogenetic analysis of a highly conserved region of the polymerase gene from 11 coronaviruses and development of a consensus polymerase chain reaction assay. *Virus Res.* **1999**, *60*, 181–189. [CrossRef]
88. Denison, M.R.; Perlman, S. Translation and processing of mouse hepatitis virus virion RNA in a cell-free system. *J. Virol.* **1986**, *60*, 12–18. [CrossRef]
89. Kanjanahaluethai, A.; Chen, Z.; Jukneliene, D.; Baker, S.C. Membrane topology of murine coronavirus replicase nonstructural protein 3. *Virology* **2007**, *361*, 391–401. [CrossRef]
90. Oostra, M.; Hagemeijer, M.C.; van Gent, M.; Bekker, C.P.; te Lintelo, E.G.; Rottier, P.J.; de Haan, C.A. Topology and membrane anchoring of the coronavirus replication complex: Not all hydrophobic domains of nsp3 and nsp6 are membrane spanning. *J. Virol.* **2008**, *82*, 12392–12405. [CrossRef]
91. Neuman, B.W.; Chamberlain, P.; Bowden, F.; Joseph, J. Atlas of coronavirus replicase structure. *Virus Res.* **2014**, *194*, 49–66. [CrossRef]
92. Sawicki, S.G.; Sawicki, D.L. Coronaviruses use discontinuous extension for synthesis of subgenome-length negative strands. *Adv. Exp. Med. Biol.* **1995**, *380*, 499–506.
93. Sola, I.; Almazán, F.; Zúñiga, S.; Enjuanes, L. Continuous and discontinuous RNA synthesis in coronaviruses. *Annu. Rev. Virol.* **2015**, *2*, 265–288. [CrossRef]
94. Di, H.; McIntyre, A.A.; Brinton, M.A. New insights about the regulation of Nidovirus subgenomic mRNA synthesis. *Virology* **2008**, *517*, 38–43. [CrossRef] [PubMed]
95. Viehweger, A.; Krautwurst, S.; Lamkiewicz, K.; Madhugiri, R.; Ziebuhr, J.; Hölzer, M.; Marz, M. Direct RNA nanopore sequencing of full-length coronavirus genomes provides novel insights into structural variants and enables modification analysis. *Gen. Res.* **2019**, *29*, 1545–1554. [CrossRef] [PubMed]
96. Stertz, S.; Reichelt, M.; Spiegel, M.; Kuri, T.; Martínez-Sobrido, L.; García-Sastre, A.; Weber, F.; Kochs, G. The intracellular sites of early replication and budding of SARS-coronavirus. *Virology* **2007**, *361*, 304–315. [CrossRef] [PubMed]
97. De Haan, C.A.; Rottier, P.J. Molecular interactions in the assembly of coronaviruses. *Adv. Vir. Res.* **2005**, *64*, 165–230. [CrossRef]
98. Fehr, A.R.; Perlman, S. Coronaviruses: An overview of their replication and pathogenesis. *Meth. Mol. Biol.* **2015**, *1282*, 1–23. [CrossRef]
99. Visser, E.A.; Moons, S.J.; Timmermans, S.; de Jong, H.; Boltje, T.J.; Büll, C. Sialic acid O-acetylation: From biosynthesis to roles in health and disease. *J. Biol. Chem.* **2021**, *297*, 100906. [CrossRef]
100. Miura, T.A.; Wang, J.; Holmes, K.V.; Mason, R.J. Rat coronaviruses infect rat alveolar type I epithelial cells and induce expression of CXC chemokines. *Virology* **2007**, *369*, 288–298. [CrossRef]
101. Gaertner, D.J.; Compton, S.R.; Winograd, D.F.; Smith, A.L. Growth characteristics and protein profiles of prototype and wild-type rat coronavirus isolates grown in a cloned subline of mouse fibroblasts (L2p.176 cells). *Virus Res.* **1996**, *41*, 55–68. [CrossRef]

102. Percy, D.; Bond, S.; MacInnes, J. Replication of sialodacryoadenitis virus in mouse L-2 cells. *Arch. Virol.* **1989**, *104*, 323–333. [CrossRef]
103. Hirano, N.; Suzuki, Y.; Ono, K.; Murakami, T.; Fujiwara, K. Growth of rat sialodacryoadenitis viruses in LBC cell culture. *Jap. J. Vet. Sci.* **1986**, *48*, 193–195. [CrossRef]
104. Ohsawa, K.; Watanabe, Y.; Takakura, A.; Itoh, T.; Sato, H. Replication of rat coronaviruses in intestinal cell line, RCN-9, derived from F344 rats. *J. Exp. Anim.* **1996**, *45*, 389–393. [CrossRef] [PubMed]
105. Macy, J.D.; Compton, S.R. Viral diseases. In *Laboratory Rat*, 3rd ed.; Suckow, M.A., Hankenson, F.C., Wilson, R.P., Foley, P.L., Eds.; Academic Press: Washington, DC, USA, 2020; Chapter 131; pp. 541–568. ISBN 9780128143384. [CrossRef]
106. Woo, P.C.Y.; Lau, S.K.P.; Huang, Y.; Yuen, K.-Y. Coronavirus Diversity, Phylogeny and Interspecies Jumping. *Exp. Biol. Med.* **2009**, *234*, 1117–1127. [CrossRef] [PubMed]
107. Dhama, K.; Patel, S.K.; Sharun, K.; Pathak, M.; Tiwari, R.; Yatoo, M.I.; Malik, Y.S.; Sah, R.; Rabaan, A.A.; Panwar, P.K.; et al. SARS-CoV-2 jumping the species barrier: Zoonotic lessons from SARS, MERS and recent advances to combat this pandemic virus. *Travel Med. Infect. Dis.* **2020**, *37*, 101830. [CrossRef] [PubMed]
108. de Bruin, W.C.; van de Ven, E.M.; Hooijmans, C.R. Efficacy of Soiled Bedding Transfer for Transmission of Mouse and Rat Infections to Sentinels: A Systematic Review. *PLoS ONE* **2016**, *11*, e0158410. [CrossRef]
109. Mishra, R.; Banerjea, A.C. Neurological Damage by Coronaviruses: A Catastrophe in the Queue! *Front. Immunol.* **2020**, *11*, 565521. [CrossRef] [PubMed]
110. Palmer, S.; Brown, D.; Morgan, D. Early qualitative risk assessment of the emerging zoonotic potential of animal diseases. *BMJ* **2005**, *331*, 1256–1260. [CrossRef] [PubMed]

BMC Veterinary Research

RESEARCH

Open Access

Neurons cytoskeletal architecture remodeling during the replication cycle of mouse coronavirus MHV-JHM: a morphological in vitro study

Michalina Bartak[1*], Piotr Bąska[2], Marcin Chodkowski[3], Beata Tymińska[1], Marcin W. Bańbura[1] and Joanna Cymerys[1*]

Abstract

Nowadays, the population is still struggling with a post-COVID19 syndrome known as long COVID, including a broad spectrum of neurological problems. There is an urgent need for a better understanding and exploration of the mechanisms of coronavirus neurotropism. For this purpose, the neurotropic strain of mouse hepatitis virus (MHV-JHM) originating from the beta-coronavirus genus, the same as severe acute respiratory syndrome coronavirus 2 (SARS-CoV-2), has been used. The role of the cytoskeleton during virus replication in neurons in vitro was determined to understand the mechanisms of MHV-JHM neuroinfection. We have described for the first time the changes of actin filaments during MHV-JHM infection. We also observed productive replication of MHV-JHM in neurons during 168 h p.i. and syncytial cytopathic effect. We discovered that the MHV-JHM strain modulated neuronal cytoskeleton during infection, which were manifested by: (i) condensation of actin filaments in the cortical layer of the cytoplasm, (ii) formation of microtubule cisternae structures containing viral antigen targeting viral replication site (iii) formation of tunneling nanotubes used by MHV-JHM for intercellular transport. Additionally, we demonstrated that the use of cytoskeletal inhibitors have reduced virus replication in neurons, especially noscapine and nocodazole, the microtubule shortening factors.

Keywords MHV-JHM, Neurons, Microtubules, Actin filaments, Neurotropism

Introduction

One of the most tricky and unpredictable family of viruses, *Coronavirideae*, again has forced scientists to investigate crucial stages of viral replication [1]. During the replication cycle, the cytoskeleton plays an essential role and takes part in infection. In healthy, uninfected cells, these dynamic arrays and their associated motor proteins are responsible for the processes of proliferation, migration, differentiation, apoptosis, and intake and transport of cargo by the cell [2]. The cell's scaffold comprises actin filaments (AFs), microtubules (MTs), and intermediate filaments (IFs). In the context of pathogen invasion, the most crucial role is played by the structures,

*Correspondence:
Michalina Bartak
michalina_bartak@sggw.edu.pl
Joanna Cymerys
joanna_cymerys@sggw.edu.pl
[1] Division of Microbiology, Department of Preclinical Sciences, Institute of Veterinary Medicine, Warsaw University of Life Sciences, Ciszewskiego 8 St., Warsaw 02-786, Poland
[2] Division of Pharmacology and Toxicology, Department of Preclinical Sciences, Institute of Veterinary Medicine, Warsaw University of Life Sciences—SGGW, Ciszewskiego 8 St., Warsaw 02-786, Poland
[3] Laboratory of Nanobiology and Biomaterials, Military Institute of Hygiene and Epidemiology, Kozielska 4 St., Warsaw 01-063, Poland

MTs, as they are involved in the retrograde transport of viral particles, especially in the perinuclear zone, and AFs involved in the movement in the sub-membrane region, cell to cell transport, the entry and egress of virions [3]. Actin is the most abundant protein in eukaryotes. It forms a monomeric and spherical form called globular actin (G-actin), not found outside of myosin, and polymerized in the form of filaments (F-actin) [4]. Actin filaments are prominently accumulated in the sub-membranous region of the cell at its periphery (cell cortex AF). They are capable of forming shorter protrusions such as lamellipodia, membrane ruffle, bladders, and long ones such as filopodia, microvilli, or podosomes (looser bundles) and organized in parallel stress fibers (tightly packed bundles) [4, 5]. Actin filaments also form tubular F-actin-rich structures called TNTs (tunneling nanotubes). They connect the cytoplasm of neighboring and/or distant cells by mediating efficient intercellular communication. They are a kind of long cytoplasmic bridges with the ability to maintain homeostasis in the physiological processes of the cell. Unfortunately, viral particles and other pathogens use these formations at early or late stages of the life cycle, promoting viral spread. The usage of TNTs has been documented for a diverse group of viruses such as retroviruses, vaccinia virus, influenza A virus, human metapneumovirus, human herpes virus type I, and severe acute respiratory syndrome coronavirus 2 to promote viral entry, virus trafficking, and cell-to-cell spread. Especially neuron-neuron transfer of pathological Tau protein assemblies and prion-like proteins in neurodegenerative diseases [6–9].

Microtubules are ultrathin structures, unbranched cylinders made of alpha and beta-tubulin heterodimers that form the wall of protofilaments. In all eukaryotes, they are responsible for essential functions in the cell: segregation of chromosomes into daughter cells at cell division as a significant component of the mitotic spindle, for transport of vesicles and organelles within the cytoplasm, the highly asymmetric morphology of neurons and, together with MTs and IFs, for maintaining the dynamic spatial organization of the cytoplasm in the cell [4, 10–12]. Microtubules are distributed in the cytoplasm in the form of evenly spaced clusters. They form the axons and dendrites of neurocytes, the cytoplasmic protrusions of cells, e.g., fibroblasts, and the pseudopodia in protozoa. Nerve cells are particularly rich in microtubule bundles of the interphase cytoplasm. The structure of the cytoskeleton in neurons is extremely dynamic and is involved in axon transport and proliferation. Microtubules originate at sites called microtubule organization centers (MTOCs), including centrosomes. These structures are where the beginning of microtubule construction occurs. These centers are common organelles present in the perinuclear region, as well as Golgi Apart (GA). MTOCs are suspected of determining the proper location of GAs [4, 13]. Significant is the fact of interaction of microtubules with actin filaments which is possible due to the presence of MAP (microtubule associated proteins) molecules. The level of its phosphorylation influences the formation of branched structures of the cytoskeleton and 3D networks [14]. Moreover, the role of these connections and the MAP molecule is significant in viral infection. Many viruses have encoded their own MAPs to manipulate MT networks directly. These are human immunodeficiency virus type 1, Kaposi's sarcoma-associated herpesvirus, Epstein-Barr virus, African swine fever virus, human herpes virus type 1, murine norovirus, murine coronavirus [15–23].

As early as 1970, it was discovered by electron microscopy that viral particles localize within cytoskeletal elements, and the effect on cross-linking architecture negatively affects viral replication [24]. Why is it important to know about the changes occurring in the cytoskeleton of cells? Especially in the context of cells of the nervous system, the dysfunction that occurs, the distortion of the architecture of the cytoskeleton leads to severe diseases, including neurodegenerative diseases such as Alzheimer, Parkinson, amyotrophic lateral sclerosis, tauopathies, Huntington's disease, and Charcot Marie tooth disease [25–27]. The situation is more serious when changes in the cytoskeleton are induced by neurotropic viruses such as some coronaviruses, including the titular MHV-JHM and another well-known beta-coronavirus representative, SARS-CoV-2. Since 2020 cases of common neurological symptoms have been reported, including loss of smell and taste. Less common symptoms were seizures, stroke, and isolated cases of Guillain-Barre syndrome (GBS, acute demyelinating inflammation with coexisting axonal motor neuropathy) [28–30]. According to a recent study, long-term effects caused by SARS-CoV-2 infection include a significant decrease in the brain's gray matter, changes in markers of damage to tissue connected to the primary olfactory cortex, and a significant reduction in overall brain volume in affected patients [31].

Diagnosed, with increasing frequency, long-term neurological complications due to SARS-CoV-2 infection oblige scientists to intensify research on the neurotropism and neuropathogenicity of coronaviruses. For this purpose, it seems necessary to create new in vitro models suitable for studying the molecular mechanisms of coronavirus neuropathogenicity. One of the coronaviruses that has already contributed to neurodegeneration research is mouse hepatitis virus, specifically the JHM strain (MHV-JHM) [32–34]. A broad spectrum of tissue tropism characterizes MHV strains, and single isolates

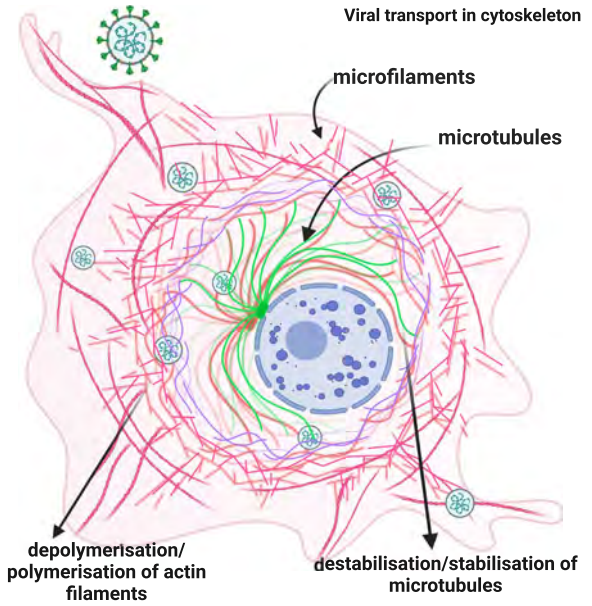

Fig. 1 Schematic presentation of MHV-JHM entry and transport. Possible events occurring during virion transport in the cytoskeleton. Own work created with Biorender

cause respiratory, gastrointestinal, or CNS diseases [35]. The pulmonary (polytropic) strains of MHV: MHV-1, MHV-2, MHV-3, MHV-JHM (MHV-4), MHV-A59, and MHV-S, replicate initially in the respiratory and olfactory epithelium of the nasal cavity, then develop viremia and spread to the lungs, liver, bone marrow, brain, lymphoid tissue, and reproductive organs. Enterotropic strains, such as MHV-D, MHV-DVIM, MHV-Y, and MHV-RI, mainly infect the gut and can spread to the liver, lymphoid tissue, and spleen [36–38]. Neurotropic strains are the most studied due to their ability to cause acute encephalomyelitis with or without chronic axonal demyelination [34, 37, 39].

Considering various virus-cytoskeleton relationships presented above and the still unknown facts about the interaction of coronaviruses with cytoskeletal structures (especially in nerve cells), we have attempted to characterize the morphological characteristics of microfilaments and microtubules and to check the effect of selected chemicals affecting the disruption of cytoskeletal distribution on the efficiency of MHV-JHM infection in primary neuron cells derived from Balb/c(H-d^2) mice (Fig. 1).

Methods

Primary neuronal cell culture

Balb/c(H-2^d) mice were used to establish the primary culture of murine neurons using the method by Cymerys et al. [40]. Balb/c mice aged 6–8 weeks were purchased from Animal House of Mossakowski Medical Research Institute Polish Academy of Sciences (Warsaw) and were handled in accordance with the guidelines regarding the use and care of laboratory animals. All actions involving live animals were performed according to Polish Local Ethics Committee guidelines and conformed to applicable international standards. Pregnant female mice (16–19 days post mating) were sacrificed in general anesthesia induced with 2%-3% isoflurane in an induction chamber (MiniVac Complete Anesthesia Systems, Harvard Apparatus). After sedation mice were sacrificed by cervical dislocation. Fetuses were removed and decapitated for brain collection. Then isolated cerebral hemispheres from fetal' brains were washed three times in cold HBSS solution (10× Hanks Buffer; Life Technologies Waltham MA, USA) and treated with 2,5% EDTA-free trypsin solution at 37°C in 5% CO_2 for 15 min. Again, cells were washed three times in a warm HBSS solution after incubation and mechanically homogenized using a pipette. After suspending and counting, cells were plated onto poly-L-lysine or poly-D-lysine with laminin-coated coverslips for immunofluorescent staining and without for RT-qPCR replication analysis at a density of 5×10^4 neurons per well (3.6 cm^2). Primary murine neurons were cultured in B-27 Neuron Plating Medium, consisting of the neurobasal medium, B-27 supplement, 200 mmol/l of glutamine, 10 mmol/l of glutamate, and penicillin/streptomycin antibiotics (1%) with 5% supplement of fetal bovine (5%) and 5% equine serum (5%) (Gibco Life Technologies, Waltham MA, USA). To avoid propagation of non-neural cells, cultures were maintained in a growth medium supplemented with 10 μM cytosine β-D-arabinofuranoside (after 3 days for 24 h) (Sigma-Aldrich, Darmstadt, Germany). Subsequently, the medium was removed and replaced with Neuron Feeding Medium (B-27 Neuron Plating Medium without glutamate; Life Technologies Waltham MA, USA). In such conditions, neurons were maintained for the next 8 days prior to analysis, infection, and treatments with inhibitors at 37°C with 5% CO_2.

MHV-JHM maintenance

Mouse coronavirus (MHV, mouse hepatitis virus), neuropathological strain MHV-JHM [ATCC-VR-76513] was propagated and in mouse hepatocyte cell line [NCTC, ATCC-CCL-9.1]. The median tissue culture infectious dose ($TCID_{50}$) was calculated using the Spearman-Kärber method [41]. Aliquots were stored at -70°C. All studies were conducted with the virus stock at the second passage level and titer of $10^{7.8}$ $TCID_{50}$/mL.

Primary cell culture infection

Primary neuronal cell cultures were infected with MHV-JHM strain (MOI = 1.25) for 60 min at 37°C. After

incubation, the inoculum was removed, washed with PBS, and a fresh culture medium was added. Subsequently, infected cells were incubated for 2, 24, 48, 72, and 168 h at 37°C with 5% CO_2.

Inhibitors and cell viability assay (XTT)

Mouse hepatocytes (ATCC-CCL-9.1) were cultured in a 96-well plate at 10,000 cells/well and incubated until fully confluent (24 h) at 37°C and a 5% CO_2-enriched atmosphere. After full confluence was achieved, the culture fluid was aspirated, and a suspension of each serine protease and cytoskeletal inhibitors (Table 1) were added at a volume of 100 µl per well. The cultures were incubated for 24 h at 37°C and in an atmosphere enriched with 5% CO_2. After incubation, 50 µl of XTT labeling mixture (Roche, The Cell Proliferation Kit II (XTT), Darmstadt, Germany) was added to each well. After a 4-h incubation (37°C, 5% CO_2), a reading was taken at $\lambda = 450$ nm, subtracting the background measured at 600 nm. Individual assays were performed in 3 replicates, and the average absorbance value for each dilution was calculated, followed by the calculation of the percentage of viable cells compared to the positive control (assuming 100% viable cells for the absorbance value of the positive control).

Immunofluorescence staining and imaging

The immunofluorescence method was used to visualize cell structures and viral antigen. After incubation in desired infection time, primary neuronal cell cultures were washed twice in PBS (Sigma-Aldrich, Darmstadt, Germany), then fixed in 4% PFA (paraformaldehyde, ThermoFisher, Waltham MA, USA) for 30 min. After fixation, the cells were washed twice with PBS solution and further incubated with 0.5% Tween/PBS solution for 10 min at room temperature. Following, the cells were washed twice with PBS solution. The F-actin filaments were stained with 50 µL of TRITC-labelled phalloidin conjugate (500 µg/mL; Sigma-Aldrich) and incubated for 60 min in a wet chamber. Likewise, microtubules were stained for 60 min in a wet chamber with indirect immunofluorescence with Anti-β-Tubulin III antibody produced in rabbit (dilution 1:200, Sigma Aldrich, Darmstadt, Germany) and then visualized with a secondary antibody, Texas Red goat anti-rabbit IgG (dilution 1:2000, Sigma- Aldrich, Darmstadt, Germany) for 60 min. The presence of viral antigen was determined by indirect immunofluorescence, using SARS-CoV/SARS-CoV-2 Spike Protein S2 Monoclonal Antibody (1A9) (ThermoFisher, Waltham MA, USA, dilution 1:250) incubated overnight at 4°C. To visualize the viral antigen, Alexa Fluor 488 anti-mouse IgG was used for 60 min, RT. Additionally, cell nuclei were stained with Hoechst 33258 (ThermoFisher, Waltham MA, USA) for 2 min, RT. Afterward, coverslips were mounted on microscope slides using ProLong Gold Antifade Mounting Medium (ThermoFisher, Waltham MA, USA). Images were acquired in a confocal microscope (Fluoview FV10i, Olympus, Warsaw, Poland), saved in 24-bit.tiff format, and analyzed using FV10i software (Olympus), ImageJ2 (NIH Image, version 1.53q, Bethesda, MD, USA), and Adobe Photoshop CS6 software (Adobe Systems Incorporated, ver. 23.4.1, San Jose, CA, USA).

Cell treatment method with cytoskeleton-interfering inhibitor drugs

Primary neuron cells after maturation (day 14) and at proper confluence level (min 70%) were pretreated or post-treated with nocodazole 30µM/mL; cytochalasin D

Table 1 Inhibitors of cell cytoskeleton used in the study

Substance	Form	Therapeutic effect/treatment
Nocodazole	benzimidazole substituted at position 2 by a (methoxycarbonyl) amino group and at position 5 by a 2-thienoyl group	antineoplastic agent, a tubulin modulator, an antimitotic, and a microtubule-destabilizing agent and an inhibitor of various cancer-related kinases.
Noscapine	phthalide isoquinoline alkaloid from *Papaver somniferum*	analgesic, antitussive, disruption of the dynamics of microtubule assembly, the inhibition of mitosis and tumor cell death, noscapine does not affect microtubule polymerization, antiviral activity by inhibition of Mpro protease.
Paclitaxel	a tetracyclic diterpenoid from the bark of the *Taxus brevifolia*	a mitotic inhibitor used in cancer chemotherapy, an antineoplastic agent, a microtubule-stabilizing agent, and an antineoplastic agent.
Latrunculin A	16-membered bicyclic lactone attached to the rare 2-thiazolidinone moiety from *Latrunculia magnifica*	impacts actin polymerization, microfilament organization, and microfilament-mediated processes.
Cytochalasin D	cell-permeable fungal toxin; from *Zygosporium mansonii*	potent inhibitor of actin polymerization; disrupts actin microfilaments; activates the p53-dependent pathways; inhibits smooth muscle contraction.

10μM/mL; latrunculin A 10μM/mL; noscapine 75μM/mL; Taxol 10μM/mL, all dissolved in DMSO 1%. During the pre-treatment method, cells were incubated for 1 h with the desired drug at 37°C, 5% CO_2 cells, then infected with MHV-JHM. After infection, the medium was replaced with a fresh culture medium. In the post-treatment method, cells were infected with MHV-JHM for 1 h at 37°C, 5% Co_2. Then the cells were washed and left for incubation in a fresh medium containing the listed drugs. Primary neuronal cell cultures were further incubated for 2, 24, 48, 72, and 168 h. Cellular and supernatant fractions from appropriate periods were collected in RLT buffer (Qiagen, Germantown, MD, USA), stored at -20°C, and later used for RNA isolation and reverse transcription quantitative real-time PCR (RT-qPCR) analysis.

RNA isolation and reverse transcription quantitative real-time PCR (RT-qPCR)

Primer design and construction of standard for RT-qPCR

RNA from infected and control cells was isolated using RNeasy Mini Kit (Qiagen, Germantown, MD, USA) followed by cDNA 1st synthesis using random hexamer primer (RevertAid First Strand cDNA Synthesis Kit, ThermoFisher). Product spanning a particular region of the MHV genome (Gen Bank No. AC_000192.1) was amplified using MHV_L_full and MHV_R_full primers (Table 2), followed by electrophoresis and gel extraction. The extracted DNA fragment was used for reamplification and cloned in E. coli using pGEM®-T Easy Vector System (Promega), and recombinant plasmid pGEM-T/MHV_1 was achieved. RT-qPCR (in the total volume of 12 μl) with primers MHV_L_v2 (0.9 μM), MHV_R_v2 (0.9 μM), and probe (0.2 μM) (Table 2) was performed on cDNA from both infected and control cells, as well as on plasmid pGEM-T/MHV_1 construct using TaqMan™ Gene Expression Master Mix (ThermoFisher, Waltham MA, USA). The PCR was performed as follows 50°C – 2 min, 95°C- 10 min, 45 × (95°C – 15 s, 60°C – 1 min).

Measurement of MHV copies in samples using RT-qPCR

RNA was isolated from cells using RNeasy Mini Kit (Qiagen, Germantown, MD, USA), followed by RNA concentration measurement using Synergy H1 Microplate Reader (BioTeK) and cDNA 1st synthesis using random hexamer primers (RevertAid First Strand cDNA Synthesis Kit, ThermoFisher, Waltham MA, USA). The cDNA was diluted 40 × in water. In parallel control buffer (CON_buf) was prepared by mixing all necessary reagents for RT reaction except from RNA, dNTPs, and random hexamer primer: 14 μl of water, 4 μl of reaction buffer (5 × concentrated), 1 μl of RNA inhibitor and 1 μl of Reverse Transcriptase (RevertAid First Strand cDNA Synthesis Kit, ThermoFisher, Waltham MA, USA) were mixed and incubated 25°C – 5 min, 42°C - 60 min and 70°C – 5 min. The mixture was diluted 40 x, and CON_buf was achieved. The RT-qPCR was performed in 12 μl prepared as follows: 6 μl of 2 × TaqMan™ Gene Expression Master Mix (ThermoFisher, Waltham MA, USA), 2.16 μl of primers mix MHV_L_v2 and MHV_R_v2 (5 μM each), 1.2 μl of probe (2 μM) and 0.64 μl of water were mixed resulting in mixture volume of 10 μl. The mixture was added to the plate wells, and 2 μl of 40 × cDNA was added as matrices. To achieve a standard curve, pGEM-T/MHV_1 was diluted in CON_buf to achieve 1E8, 1E7, 1E6, 1E5, 1E4, 1E3, 1E2 and 33 copies per 2 μl and used as matrices for RT-qPCR. The PCR was performed as follows: 50°C – 2 min, 95°C - 10 min, 45 × (95°C – 15 s, 60° C – 1 min). Additionally, each plate contained a sample with cDNA from infected and control cells serving as positive and negative controls, respectively. Each reaction was performed in triplicate in MicroAmp™ Optical 96-Well Reaction Plate with Barcode using a thermocycler.

Real-time cell growth analise JuLi™Br

To determine the cellular growth and morphology of primary neurons infected with MHV-JHM, the JuLI™Br Live Cell—system for bright-field analysis (NanoEnTek, Seoul, Korea 2015) was used. When cultured neurons reached about 80% confluency, cells were infected with MHV-JHM as previously described. Images were captured for 168 h with 30 min intervals. The results were obtained and analyzed using JuLI™Br PC software. Uninfected cells were used as a negative control. All images were captured at a × 40 magnification.

Table 2 Description of primers used during RT-qPCR

Primer	Sequence	AC_000192.1 covering region	Product length
MHV_L_full	TTGGCTTGTGAGTGACGCCTG	28 571 – 28 591	806 bp
MHV_R_full	GCGCATACACGCAATTGAACAT	39 376 - 29 355	
MHV_L_v2	GTATGGTATGTGGGGCAGATTA	28 906 – 28 927	88 bp
MHV_R_v2	GTTTAATAGACGCAAGGAAGGC	28 993- 28 972	
Probe 5` 6-FAM 3` TAMRA	AGTCGCAGTGTGTTTGATGGTCACC	28 935 – 28 959	Not applicable

Statistical analysis

The results were statistically evaluated by one-way or two-way analysis of variation (ANOVA) using the Tukey multiple comparisons test or multiple unpaired t test using threshold p value with the Šídák-Bonerroni multiple comparisons correction method. All experiments were done at least in triplicate. These analyses were performed using GraphPad Prism™ version 9.4.0 (453) for macOS software (GraphPad Software Inc., San Diego, CA, USA). Statistical differences were interpreted as significant at $p \leq 0.05$, highly significant at $p \leq 0.01$, extremely significant at $p \leq 0.001$, and insignificant at $p > 0.05$.

To analyze the colocalization of the fluorescence signal derived from TNTs and the viral antigen during the study, a minimum 100 confocal images were used. Images were analyzed using the Fiji BIOP JACoP plugin. The parameters analyzed were two channels, green fluorescence corresponding to the viral antigen and red fluorescence for the F-actin. The quantitative interpretation of pixel correlation coefficients in the form of threshold parameters of Pearson's correlation coefficient (PCC) and Manders' correlation coefficient (M1 and M2) of global statistical analysis were considered for statistical analysis, considering pixel intensity distributions from fluorogram plots [42]. The degrees of correlation were indicated as perfect for values near ± 1; strong for values between ± 0.50 and ± 1; medium for values between ± 0.30 and ± 0.49, and low for values below + 0.29.

Results

MHV-JHM productively replicates in neurons

The number of copies of viral RNA were determined from the suspension of cells and media from each time post-infection (Fig. 2). In the positive control of neuron cells infected with MHV-JHM, the number of copies per µg RNA has been increasing logarithmically. At the start, after 2 h p.i., the virus copies were at 5.30×10^6 per µg RNA. Then, 24 h p.i. values increased to 1.03×10^8 copies/µg RNA when the complete replication cycle occurred. At 48 h p.i., values decreased by two logarithms (5.60×10^6) and gradually raised, reaching its peak – 6.48×10^9 at 168 h p.i. On the other hand, the morphological analysis done with JuLi™Br live imaging showed that neurons infected with MHV-JHM did not drastically change the confluence of the culture nor the appearance of cells (Fig. 3). During the 168 h of infection, the lower density of cell culture was observed, but the ability to form long protrusions or neuritis were present until the assay's end. Therefore, there was no visible CPE, and cells did not undergo lysis. The confluence level had been raised until 96 h post infection (92.55%) and started to drop after 120 h p.i., reaching the final confluence of 64.06% at 168 h p.i. (Fig. 3, graph).

MHV-JHM controls the dynamic processes of the actin cytoskeleton

The effect of MHV-JHM on the cytoskeletal structure of primary cultured mouse neurons manifested in the form of changes in the distribution of filaments.

The first changes could be seen as early as 2 h p.i., where, compared to the control (Fig. 4) even arrangement of stress filaments (Fig. 5A, a',a" yellow arrowheads), excessive condensation of actin in the submembranous region (Fig. 5A,a" green arrowhead; Fig. 6A, white asterisk) and its thinning in the zone close to the cell nucleus (Fig. 5A,a", white asterisk; Fig. 6A, yellow arrow) were noted. Also, the presence of penetrating/moving viral antigens in the long filopodia (Fig. 5A,a", white arrowhead) and the accumulation of virion antigen was captured in the perinuclear area, which is the site of target replication in the cytoplasm (Fig. 5A,a', yellow box, green arrowhead).

The changes have worsened at 24 h p.i. When productive replication occurred, neurons formed many intercellular connections in the form of longitudinal actin filaments - tunnelling nanotubes, to transport viral particles to neighbour cells (Fig. 5B, b' white arrowheads). It is possible to distinguish the formation of thin TNT bridges and long thicker ones (Fig. 5B, b',b" white arrowheads). In the area marked by the yellow box, the progeny virions were present, moving across the bridge from one cell to another (Fig. 5B, b" green arrowheads). Peripheral stress fibres in the form of highly condensed structures were still visible (Fig. 5B, b', b" yellow arrowheads), and a large amount of viral antigen localized in the perinuclear region (Fig. 5B, b', yellow box, green arrowhead) with a much-diluted structure was still clearly visible.

Interesting morphological changes begin to occur on the second day after infection, where neurons clearly have lost their ability to form long protrusions (Fig. 5C, c',c"). Instead, shorter filopodia appeared (Fig. 5C, c',c" white asterisk). Also, the structure of the stress fibres has again become highly polarized fibres in which the viral antigen was present (Fig. 5C, c',c" green arrowheads and yellow arrowheads).

Complete rearrangement and loss of the proper structure of actin filaments and their local defragmentation occurred at 72 h p.i. (Fig. 5D, d',d"). The viral antigen was predominantly present in the perinuclear space where the actin structure has been polymerized (Fig. 5D, d' yellow boxes green arrowheads).

Interestingly, 1 week after infection, the structure of the actin cytoskeleton has restored. (Fig. 5E, e',e"). Stress fibres (Fig. 5E, e' yellow arrowheads), TNTs (Fig. 5E,e",

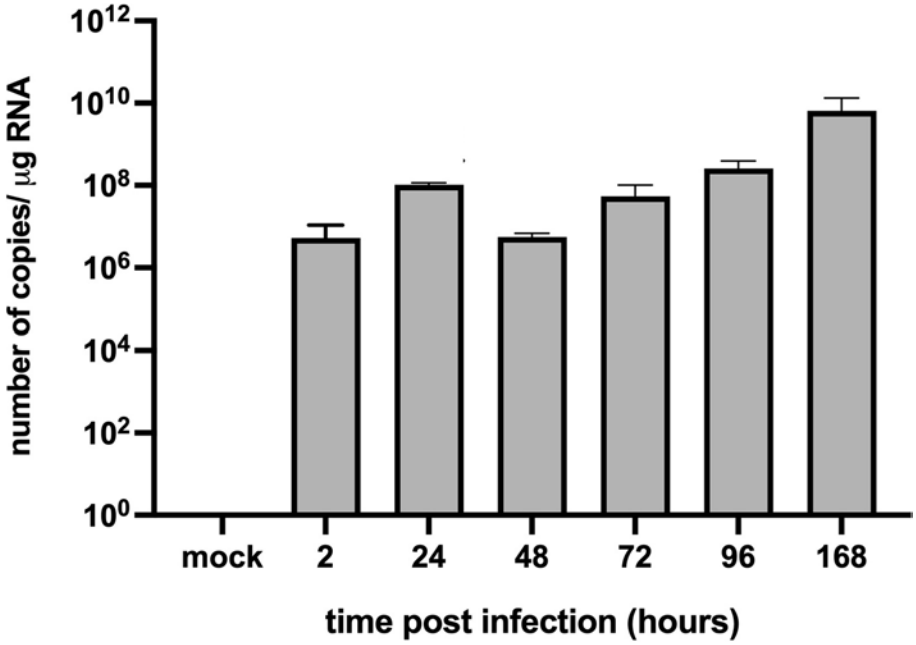

Fig. 2 RT-qPCR analysis of MHV-JHM viral RNA copies per µg during 168 h p.i. in murine neurons

yellow box, white arrowhead), and lamellipodia (Fig. 5E, e' yellow box, white asterisk) could be distinguished. However, further examples of the cytopathic effect in the form of spiderweb-like structure (Fig. 5E, e' yellow box) and cell syncytia (Fig. 5E, e" yellow arrowhead) appeared. The moving viral antigen have been still present in the actin protrusions (Fig. 5E, e" yellow box, green arrowhead). These actin structures were noticeable throughout the infection cycle but were best and most visible 1 week after infection. Such as numerous long actin protrusions and nanotubes in which the moving viral antigen was present (Fig. 7A,B,C; white arrow). A tunneling nanotubule connected two nerve cells transmitting virions between them (Fig. 7A a"; white arrow). The quantification colocalization analysis of viral antigen and TNTs structure throughout the infection exhibited strong values (PCC = 0.73 ± 0.18; M1 = M2 = 0.93) (Fig. 8). Moreover, interesting spiderweb-like structures appeared with local highly polarized filaments and complete absence or depolarization (Figs. 6B and 7C; green boxes and yellow arrows).

Another interesting phenomenon was also observed. The formation of actin structures, highly polarized filaments forming a circle, was noted during infection at early and late time post infection (Fig. 6A,B). At 2 h p.i., the filaments were polarized in the perinuclear and submembrane area (Fig. 6A, white asterisk; yellow arrows) while at 168 h p.i., a significant condensation of polarized actin filaments were visible, forming a ring-like form in submembrane area (Fig. 6B, white asterisk, yellow arrow). In these structures, high number of viral particles were noted (Fig. 6A,B; green arrows).

MHV-JHM modulates microtubule structure and uses during transport

Microtubules are less involved in virus entry into the cell. In contrast, MTs in neurons facilitate viral transport along the neuron's cell body and axonal terminals. This can be seen as early as 2 h p.i. as viral particles were moving 'surfing' inside MTs (Fig. 10Aa"). In the box highlighted in yellow, attention was drawn to the accumulation of viral antigen in the perinuclear space and its presence in the neurite (Fig. 10Aa", yellow box, and green arrowheads). Also, viral antigen was visible in perinuclear area (Fig. 9Aa", yellow box, and green arrowheads).

Progressive accumulation of viral antigen was observed after the first day after infection. On images, it was manifested as yellow fluorescence present mainly in the soma region (Fig. 10Bb', yellow box, green arrowhead). The dots of green fluorescence present in numerous dendrites likely represented progeny virions moving between neurons (Fig. 10Bb', yellow box, green arrowheads). Early syncytium formation was also detected after 24 h p.i. (Fig. 10Bb", green and white arrowhead).

Compared to control (Fig. 9), microtubule architecture changes occurred after 48 h p.i. Microtubules radiated toward the forming syncytium (Fig. 10Cc',c", yellow

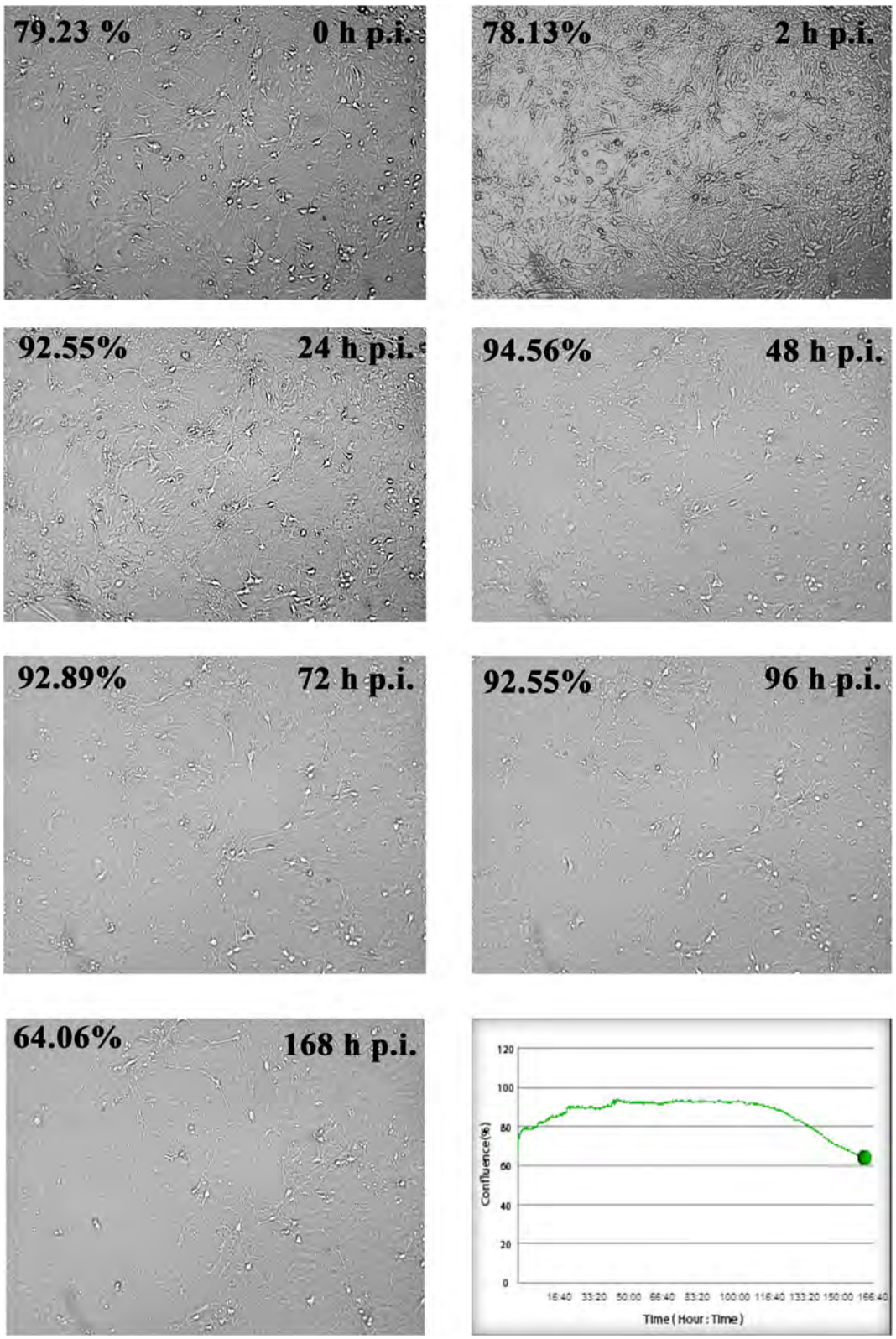

Fig. 3 Real-time cell growth analysis of MHV-JHM infected primary murine neurons performed by using live image move analyser JuLi™Br. Cultures were observed from initial seeding for 168 h. The generated graph shows the percentage of cells' confluence level [%] during complete analysis [hours]. All images were recorded every 5 min and analysed monolayer confluence. Objective magnification × 40

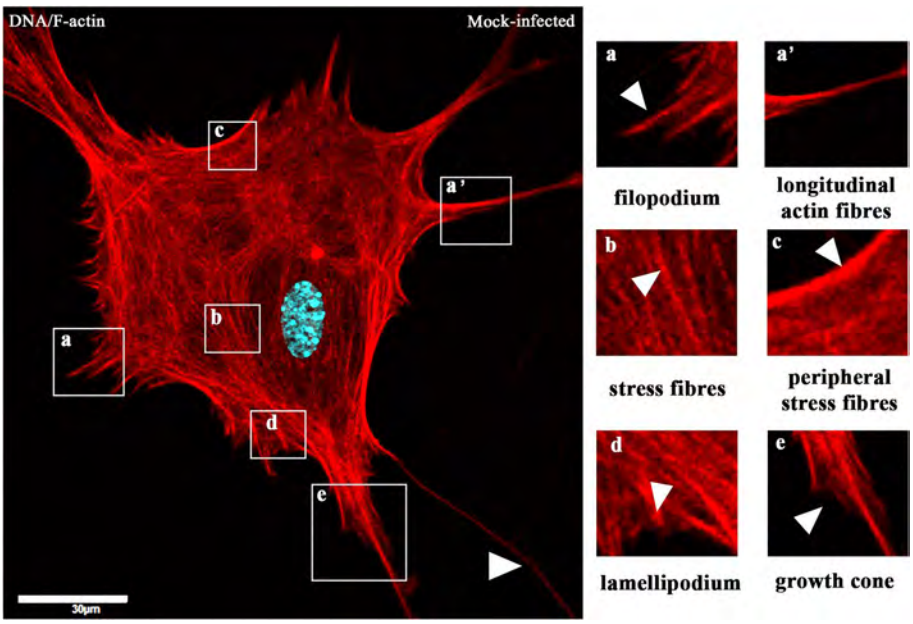

Fig. 4 Actin cytoskeleton network morphology of non-infected primary murine neurons. Various forms of actin fibres structures were presented and highlighted by white arrowheads: tunnelling nanotube (main image), filopodium (a) and longitudinal actin fibres (a'), stress fibres (b), peripheral stress fibres (c), lamellipodium (d), and growth cone (e). Indirect and direct immunofluorescence staining; merge images: actin filaments – red; cell nuclei – blue. Microscope magnification 60x, scale 20 μm

square, yellow arrowheads, white arrowhead) were noted. On the first image, a loss of dendrites, axons and a pronounced rounding of the neuron cell were seen (Fig. 10Cc'). In places, as captured in the second photo, a long protrusion is present in which the progeny virion was moving (Fig. 10Cc", yellow arrowhead, green arrowheads).

On the other hand, on the third day after infection, a restoration of the neurons' ability to form protrusions was observed (Fig. 10Dd',d", yellow arrowheads). However, compared to control (Fig. 9), the structure of MTs became depolymerized, facilitating the distribution of viral proteins (Fig. 10Dd',d", yellow arrowheads). The second picture showed strong condensation of microtubules at the site of viral antigen and formation of bulges in dendrites - a possible site of release of progeny virus (Fig. 10D,d", yellow square, green arrowheads). Syncytia at 72 h p.i. were still present with a clear ring of viral antigen around fused cell nuclei (Fig. 10D,d", yellow squares, white arrowheads).

Interestingly similar to what was described for actin filaments, 1 week after infection, there was no loss of cellular protrusions, microtubule structure was similar to that present in control (Fig. 8) with well-defined polymerization (Fig. 10E,e", yellow arrowheads). Viral antigen was still present and expressed by bright fluorescence in each neuronal cell (Fig. 10E,e' green arrowhead; e" green arrowhead, yellow box, green arrowhead), especially in the perinuclear space of the soma (Fig. 10E,e' yellow box; e" green arrowhead). The cultured primary murine neurons were not degraded after 168 h p.i. MHV-JHM.

Effect of specific cytoskeleton inhibitors on MHV-JHM replication

Reverse transcriptase real-time PCR was applied to detect viral RNA in neuronal cells pre-treated and post-treated with actin and microtubule inhibitors to determine their effect on virus replication. The following substances were used: cytochalasin D 10uM/mL; latrunculin A 10uM/mL; paclitaxel 10uM/mL nocodazole 30uM/mL; noscapine 75uM/mL. Both treatment methods had a significant effect on replication. Starting from 2 h p.i. there were visibly higher levels of viral RNA copies than in control untreated cells (2.02×10^5) (Fig. 11A). After 24 h p.i., the viral copies decreased by at least 2 logarithms. The actin cytoskeleton inhibitors – cytochalasin D and latrunculin A had a similar effect on replication inhibition, but post-treatment method had better results. Compared to the positive control, viral RNA copies were at a level of 10^8, whereas after applying actin depolymerization agents, latrunculin A and cytochalasin D, the values had reached level of copies 10^7 in pre-treatment and 10^5 in post-treatment. Cytochalasin (pre-treatment 7.47×10^7; post-treatment 4.04×10^6), latrunculin A (pre-treatment 1.38×10^8; post-treatment 1.25×10^6). Approximate values were detected for microtubule destabilization agents

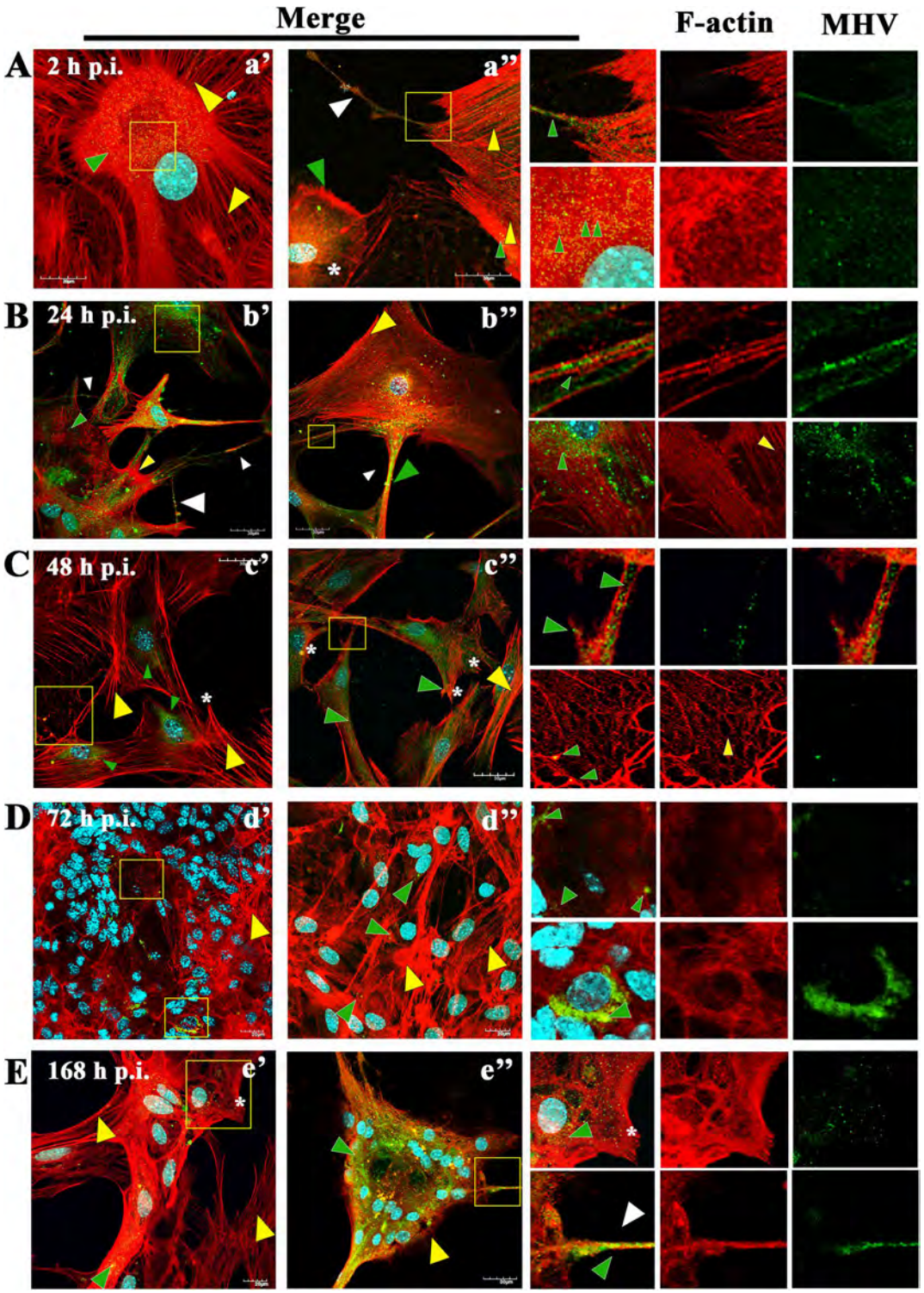

Fig. 5 Primary culture of murine neurons infected with MHV-JHM virus. Representative confocal images of neurons obtained at 2 (A,a',a''), 24 (B,b',b''), 48 (C,c',c''), 72 (D,d',d''), and 168 h p.i (E,e',e''). Green arrowheads point to the presence of viral antigens in actin structures. Yellow arrowheads show areas of changes in f-actin filaments resulting from MHV-JHM infection. White arrowheads point to tunnelling nanotube (TNTs) structures. White asterisk show lamellipodia. Yellow boxes indicate the overlapping presence of actin filaments fluorescence with viral antigen and magnified area. Indirect and direct immunofluorescence staining; merge images: actin filaments - red; cell nuclei - blue; viral antigen - green. Microscope magnification 60x, scale 20 µm

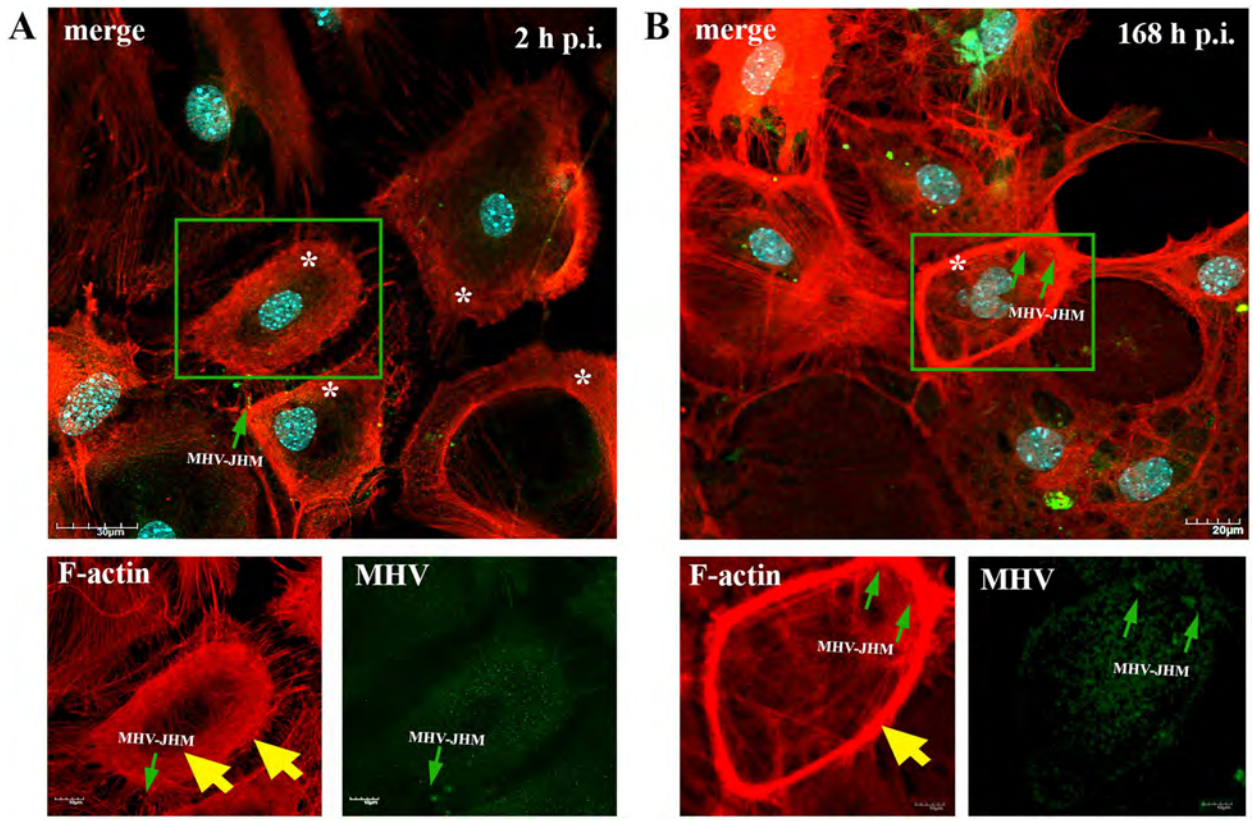

Fig. 6 Primary culture of murine neurons infected with MHV-JHM virus. Representative confocal images of neurons obtained at 2 h p.i. (**A**) and 168 h p.i (**B**). White asterisk represents the occurrence of a F-actin ring structures – juxtanuclear ring (**A**) and submembranous ring (**B**); green boxes show magnified areas; green arrows indicate viral antigen; double yellow arrows show juxtanuclear ring and single yellow arrow points submembrane ring. Indirect and direct immunofluorescence staining; merge images: actin filaments - red; cell nuclei - blue; viral antigen - green. Microscope magnification 60x, scale 20 μm and 10 μm

(Fig. 11B). In 48 h p.i. there was no spectacular effect both from actin and microtubular inhibitors. Overall positive control viral RNA copies were at a relatively high level of 10^8 (1.13×10^8) logarithm. After incubation best results were obtained for latrunculin A post-treatment (2.45×10^6) (Fig. 11C). On the contrary, 72 h p.i. with extreme significance, microtubule shortening noscapine, post-treatment (7.6×10^3), decreased viral replication by 4 logarithms compared to untreated control (1.2×10^7). Similar results were obtained with post-treatment actin depolymerizing cytochalasin D (6.1×10^4). Other pair of actin and microtubule inhibitors, latrunculin A, and paclitaxel, arrested viral replication on levels of 8.0×10^4 pre-treatment, 1.6×10^5, and 1.7×10^5 pre-treatment, 5.9×10^6 post-treatment as followed (Fig. 11D). Overall, the viral replication levels drop happened at 168 h p.i. where levels decreased by 6 logarithms after usage of post-treatment (6.3×10^4) and pre-treatment (2.3×10^4) incubation with nocodazole. Control untreated cells, infected with MHV-JHM (168 h p.i.), have reached value of 10^{10}. Other microtubule inhibitors - noscapine and post-treatment actin depolymerization substations cytochalasin D, and latrunculin A have blocked replication by 2/3 logarithm (Fig. 11E).

Discussion

Several works have examined and confirmed the cell's cytoskeleton's significant role in the virus entry into the cell and in the further stage of the replication cycle, culminating in the assembly and release of progeny virions. Much is already discovered in the context of coronaviruses, but unknown areas still leave doubts. We have delved into this topic, not least because of the increasingly reported cases of long-Covid in the CNS [43–45]. As is well known, MHV, especially neurotropic strains, e.g., JHM, A549, are well suited as models for SARS-CoV-2 [34]. Moreover, morphological, and molecular analysis of the effect of MHV-JHM infection on the cytoskeleton of primary neurons adds to the knowledge of beta-coronaviruses. Our study confirmed that MHV-JHM in 1 week infection period does not destroy neuronal cells and manipulate the cytoskeleton from entry

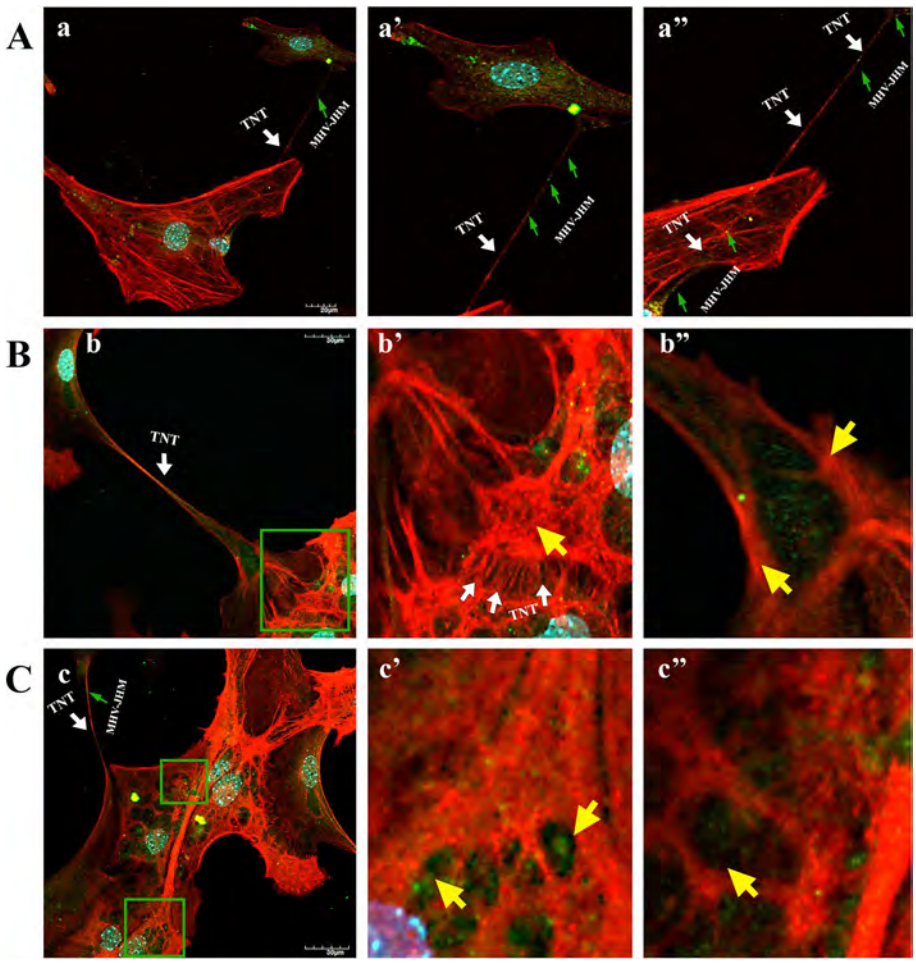

Fig. 7 Primary culture of murine neurons infected with MHV-JHM after 168 h p.i.. Representative confocal images of specific filamentous actin structures – tunnelling nanotubes (TNTs) (a,a',a",b,b',c; white arrows); depolymerised (b' yellow arrow) and highly polymerised rings structures (b" yellow arrows) spider-web-like actin structures (c',c" yellow arrows). Green boxes indicate magnified area. Indirect and direct immunofluorescence staining; merge images: actin filaments - red; cell nuclei - blue; viral antigen - green. Microscope magnification 60x, scale 30 µm and 20 µm

until viral shedding. What is more important MHV-JHM uses tunnelling nanotubules as a cell-to-cell transport route avoiding immune response and direct receptor binding.

During neuroinfection, the cytoskeleton plays a very significant role. In our study, we presented a morphological and quantitative analysis verifying the level of viral replication after treating cells with substances that affect the distribution of actin filaments and microtubules. There is little information available on the utilization of the neural cell cytoskeleton by MHV-JHM. The available literature has focused more on the role of microtubules during intracellular transport than actin filaments. Microtubules have been shown to play an important role in intraneuronal transport in primary culture cells of rat hippocampal neurons and OBL-21 cells (olfactory bulb cultures of CD.1 mouse) [46]. Moreover, the team of Pasick et al. 1994 and Kalicharran and Dales, 1995 proved that there is a special interaction between Tau protein and MHV-JHM nucleocapsid protein [23, 46]. The amino acid complementarity of the two proteins overlapped at 44% similarity and 22% identity in structure. This homology probably influences such high neuropathogenicity and tropism of the virus through the interaction of MTs with MHV-JHM N protein. Some α-coronaviruses like TGEV (transmissible gastroenteritis coronavirus), HCoV-NL63 (human coronavirus NL63), and HCoV-229E (human coronavirus 229E) were proven to interact with their S and M proteins directly or indirectly with tubulin [47]. In our study, we confirmed the dominant role of microtubules during MHV-JHM infection. We already observed at 24 h p.i. moving viral particles between neurons in long axonal protuberances and neurites (Fig. 10B, green arrowheads and yellow boxes). On the other hand, at 2 h p.i. (Fig. 10A, a" yellow box) and 72 h p.i. (Fig. 10D, d" yellow and green arrowheads), MHV-JHM disrupted

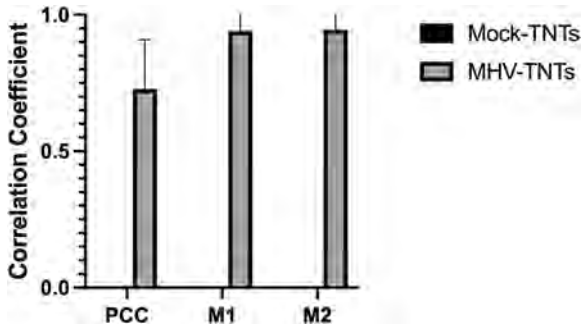

Fig. 8 Colocalization analysis of viral antigen present inside tunnelling nanotubule structures. Histograms compared correlations of TNTs with MHV-JHM antigen from the 2 h p.i. until 168 h p.i with uninfected cells (mock-infected) showing Pearson's correlation coefficient (PCC) and Meander's coefficients (M1 and M2) from ≥ 100 cells (data represented as mean ± SEM from TNTs structurers). The degrees of correlation were indicated as perfect for values near ± 1; strong for values between ± 0.50 and ± 1; medium for values between ± 0.30 and ± 0.49, and low for values below + 0.29. Obtained with JACoP BIOP analysis

microtubules' architecture, leading to their depolymerization, cell degradation, and syncytia formation (Fig. 10C, D yellow arrowheads). However, some cells were still able to transport progeny virions (Fig. 10C, D green arrowheads). Neurites did not disappear, and virions accumulated in characteristic cisternae (Fig. 10D, purple arrowheads). At 168 h p.i., the viral antigen was still present in large amounts and colocalized with the structures of the microtubule, which were intact, and the cells were not degraded (Fig. 10E). Similar results were obtained by Pasick et al. where viral antigen were present in large amounts after 48 h p.i. Virions located in a linear position were moving along axons and have formed microtubules into cisternae structures [46]. On the other hand, a study by Biswas and Sarma [48], using demyelinating strains of MHV - RSA59 and non-demyelinating RSMHV2 in the infection of Neuro2a cells, showed that viral transport took place in axonal terminals as early as 4h 15 min p.i. in the case of RSA59 and RSMHV2 in

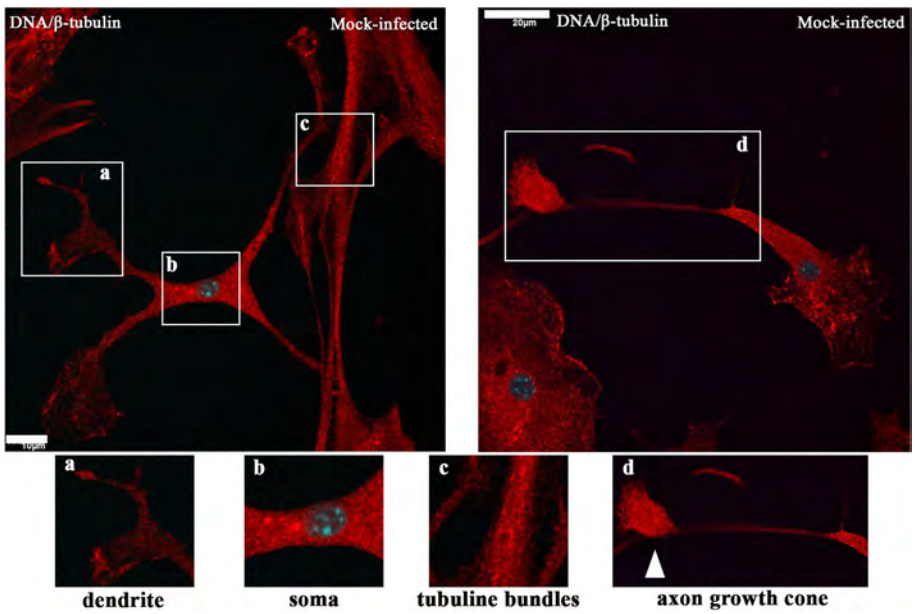

Fig. 9 Microtubule network morphology of non-infected primary murine neurons. Various forms of β-tubulin rich structures were presented and highlighted by white boxes: dendrite (a), soma (b), tubulin bundles (c), and axon growth cone (d). Indirect and direct immunofluorescence staining; merge images: β-tubulin- red; cell nuclei – blue. Microscope magnification 60x, scale 10 µm

(See figure on next page.)

Fig. 10 Primary culture of murine neurons infected with MHV-JHM virus. Representative confocal images of neurons obtained at 2 (A,a',a''), 24 (B,b',b''), 48 (C,c',c''), 72 (D,d',d''), and 168 (E,e',e'') hours post infection. Green arrowheads point the presence of viral antigens in actin structures; Yellow arrowheads show areas of changes in β-tubulin resulting from MHV-JHM infection. White arrowheads point to syncytia formation. Purple arrowheads indicate cisternae microtubule structures. Yellow boxes indicate the overlapping presence of β-tubulin fluorescence with viral antigen. Indirect and direct immunofluorescence staining; merge images: β-tubulin - red; cell nuclei - blue; viral antigen - green. Microscope magnification 60x, scale 20 µm

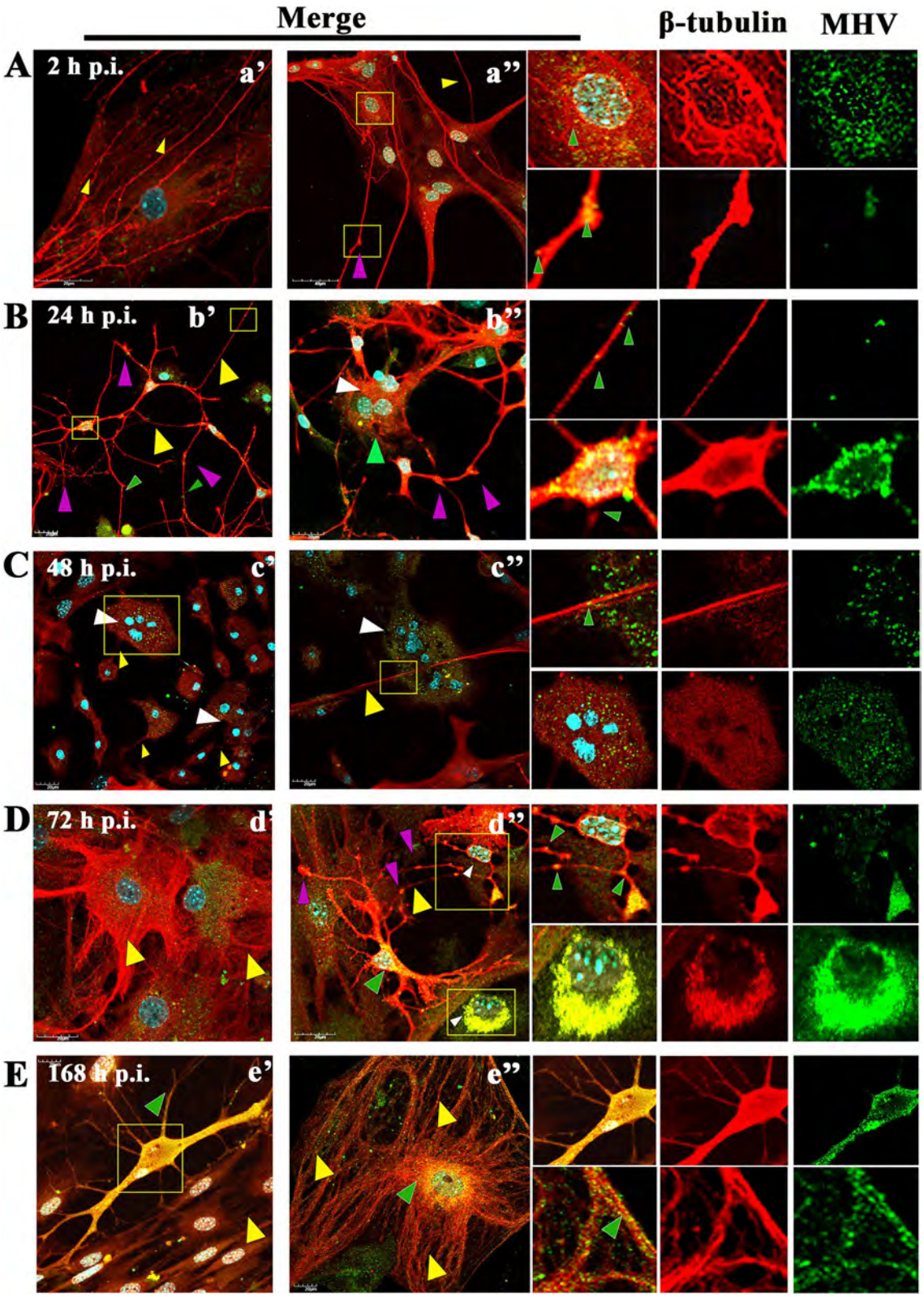

Fig. 10 (See legend on previous page.)

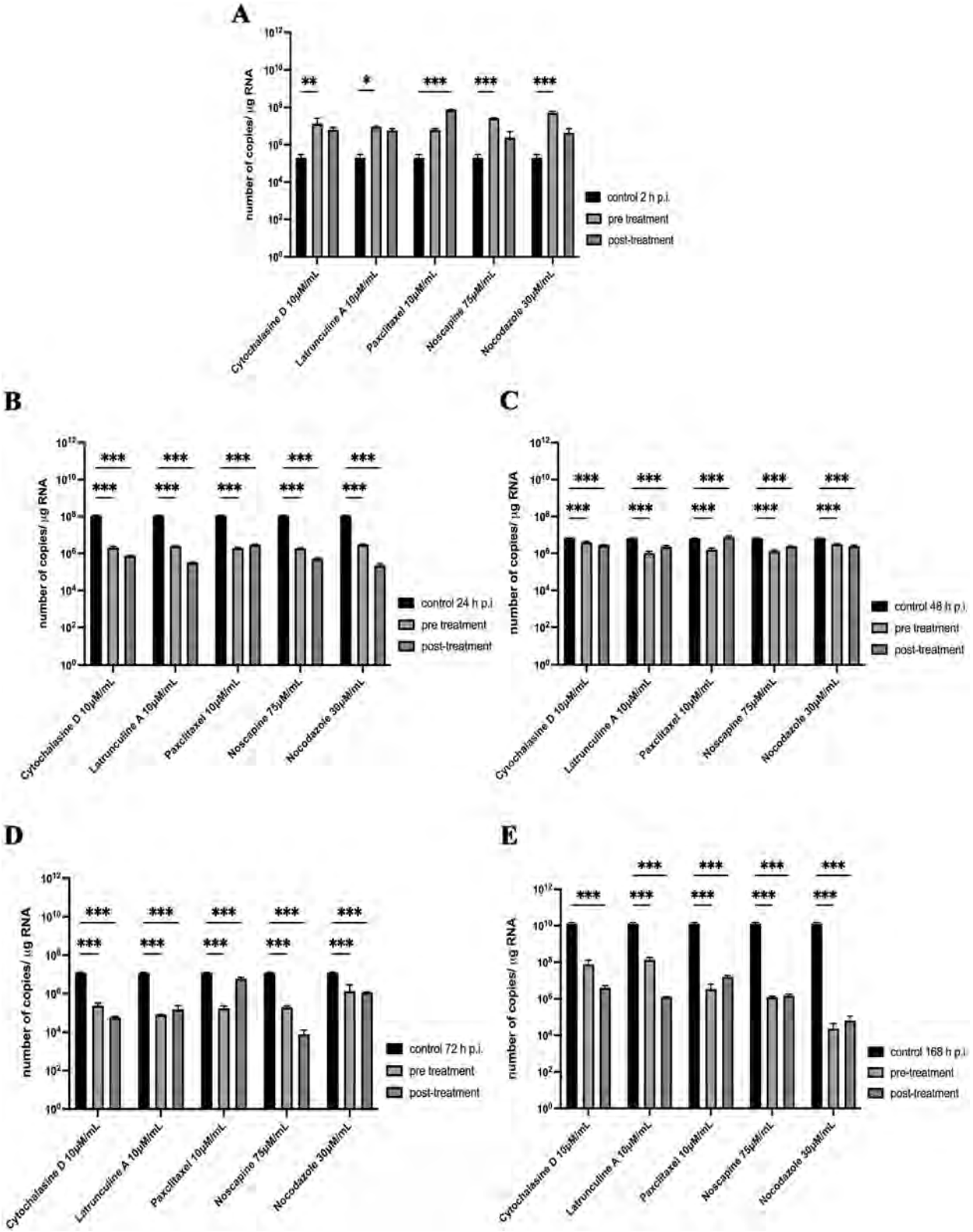

Fig. 11 The effect of pre-treatment and post-treatment incubation with cytoskeletal inhibitors on MHV-JHM replication in primary murine neurons culture. Presented time points: 2 h (**A**), 24 h (**B**), 48 h (**C**), 72 h (**D**), 168 h (**E**). Viral RNA was quantified by RT real-time PCR. Data are presented as the mean ± standard deviation (SD) ($n = 3$). Two-way Anova tests were used to analyse statistical significance compared with the untreated control: *, significant ($P \leq 0.05$); **, highly significant ($P \leq 0.01$); and ***, extremely significant ($P \leq 0.001$)

general, up to 36 h p.i. when the cells lysed. Syncytia were present as early as 9 h p.i. in Neuro2a cells upon RSA59 infection [48]. We also detected syncytium formation by MHV-JHM after 24 h p.i. as a cytopathic effect in primary murine neurons (Fig. 10B, b", white arrowhead), contrary to the previous finding by Bender et al. [49]. Thus, it proves that direct cell-to-cell spread in neurons may be the top way of virion spread because of its efficiency and no engagement with cell-membrane-specific receptors [50, 51]. Also, after a week of infection, we observed the renovation of the cytoskeletal structure of neurons and an increase in proliferation. Generally, infection with MHV may lead to Tau phosphorylation by glycogen synthase kinase-3β-dependent mechanism, which disrupts MT stabilizing ability causing brain damage but not neurons death [52, 53]. The results were observed by analysis of confocal microscopy images were confirmed by RT-qPCR. After pre-, and post-treating with microtubules depolymerizing agent – nocodazole, a stabilizing agent – noscapine, and paclitaxel, we have observed successful limitation in MHV-JHM replication (Fig. 11). This indicates that disrupted MTs distribution, mostly in late hours post infection (a significant number of RNA copies decreased at 72 h p.i.) had a highly statistical effect on the virus's ability to replicate in primary murine neurons. The best results were obtained by noscapine 72 h p.i. post-infection treatment by three logarithms drops and nocodazole pre-treatment by six logarithms drop (Fig. 11). In other viruses, the replication of sindbis virus, vesicular stomatitis virus, and human herpes virus type I, was quantified by the titre (plaque forming units/ml; pfu/ml) produced in cells treated with three anti-microtubule drugs (colchicine, noscapine, or paclitaxel) and none of these drugs affected the replication [54]. In the case of MHV-A59 and MHV-2 treatment with colchicine, vinblastine did not affect fusogenic properties and thus replication in 36 h p.i. in Neuro2a cells and fibroblasts [48, 55].

To our knowledge, no publications considered changes in actin filament during MHV-JHM infection in neurons. We have observed dynamic rearrangement of F-actin which led to facilitated MHV-JHM entry into the soma (Fig. 5). It is well known that microfilaments participate in virion surfing after the virus binds to a target cell [54]. In our study, as early as 2 h post infection, the filament condensation in the form of submembranous rings were seen (Fig. 5A,a" green arrowhead; Fig. 6). These structures, which can be sites of viral entry, were also present after IPEC-J2 cells infection with PEDV (Porcine epidemic diarrhoea virus) and TGEV (Transmissible gastroenteritis coronavirus) [56]. The first changes appeared 2 h p.i., where excessive condensation of actin in the submembranous region and its thinning in the zone close to the cell nucleus (Fig. 9A, green arrows) were noted. We also captured the penetrating/moving viral antigens in the long filopodial protuberance (Fig. 9A, white arrowhead) and the accumulation of virion antigen in the perinuclear area. The changes worsened at 24 h p.i. when productive replication occurred. Neurons formed numerous intercellular connections in the form of longitudinal actin filaments, probably forming tunnelling nanotubes for transporting viral particles. The use of TNTs and their important involvement in intercellular transport during SARS-CoV-2 infection has recently been discovered. The enhanced ability to form TNTs and the movement of viral antigen within the bridges were investigated on a coculture model of African green monkey kidney Vero E6 cell and human neuroblastoma (SH-SY5Y) cells [57]. In our study conducted on primary murine neurons, numerous TNT structures were seen and the movement of MHV-JHM antigen within TNTs throughout the infection period were noted. Interestingly, the largest number of this actin structures appeared after 168 h p.i. which may be an important sign especially in the treatment or research for the pathology of long-COVID and the changes that coronaviruses cause in the central nervous system.

Peripheral stress fibres in the form of highly condensed fibres were visible, and a large amount of viral antigen localized in the perinuclear region (Fig. 9B, white arrowheads) with a much-diluted structure was still clearly visible. Like in microtubule structure, proper actin filaments dynamics were restored after 168 h p.i. (Fig. 9E). During later hours post infection, characteristic juxtanuclear rings were observed. Again, in PEDV and TGEV infected IPEC-J2 cells, juxtanuclear rings support viral genome replication and protein synthesis [56]. Actin filaments also promote viral egress by thickening and restoring stress fibres structures, as we noted. Such phenomenon occurred during IBV (Infectious Bronchitis Virus) and SARS-CoV infection and proved essential during virus budding and assembly of viral particles [31, 58, 59]. To confirm the role of the actin cytoskeleton in MHV-JHM infection, we have used cytochalasin D and Latrunculin A treatment (Fig. 11). These two actin polymerization inhibitors did not influence the entry of the virus, thus the replication ability of MHV-JHM after 2 h p.i., but in later stages of replication, the inhibitory effect was visible by three logarithms decreased after 168 h p.i. In a study by Yeung 2021, BafA1 and cytochalasin D, which impair endosomal acidification and endosomal-lysosomal system, respectively, were proven to inhibit the infection of the SARS-CoV-2 virus [60].

In conclusion, here, we showed that neuronal actin cytoskeleton is likely used during MHV-JHM infection, which we confirmed by morphological analysis. Its role is not essential in the process of viral penetration but crucial in cell-to-cell transport of progeny virions. This type of viral transport permits infected cells to hide from immune system response and allows more effective viral spreading. Our studies show that the primary role in the intracellular transport of MHV-JHM virions to the site of replication and then between cells is played by microtubules. This finding was confirmed after using noscapine and nocodazole inhibitors, which effectively reduced MHV-JHM replication in neurons.

Acknowledgements
Not applicable.

Authors' contributions
Conceptualization, M.B., and J.C.; methodology, M.B., J.C., P.B., M.C.; software, M.B.,P.B.; validation, P.B., J.C., M.B.; formal analysis, M.B, J.C., P.B.; investigation, M.B., J.C., P.B.; resources, M.C., M.W.B; data curation, M.B., P.B.; writing—original draft preparation, M.B.; writing—review and editing, M.B., P.B., J.C., M.C., B.T.; visualization, M.B., M.C.; supervision, J.C., M.W.B., project administration, M.B., J.C.; funding acquisition, M.B.

Funding
This research was funded by grant number 2021/41/N/NZ6/04383 (to MB) from National Science Centre in Cracow, Poland. The publication was financed by Science development fund of the Warsaw University of Life Sciences - SGGW.

Availability of data and materials
The datasets used and/or analysed during the current study are included in this publication.

Declarations

Ethics approval and consent to participate
This type of research does not require permission from the ethics committee. Relevant documents have been included. The Ethics review board II Local Committee for Ethics in Animal Research of Warsaw University of Life Sciences - SGGW considers that this type of project does not fall under the legislation for the protection of animals used for scientific purposes, national decree-law (Dz. U. 2015 poz. 266 and 2010-63-EU directive). Moreover, the research team members have training issued by Polish Laboratory Animal Science Association (PolLASA) in animal handling, planning experiments, performing procedures, and killing animals.

Consent for publication
Not applicable.

Competing interests
The authors declare no competing interests.

Received: 7 February 2023 Accepted: 10 November 2023
Published online: 09 January 2024

References

1. Zhang XY, Huang HJ, Zhuang DL, Nasser MI, Yang MH, Zhu P, et al. Biological, clinical and epidemiological features of COVID-19, SARS and MERS and AutoDock simulation of ACE2. Infect Dis Poverty. 2020;9(1):99.
2. Kubitschke H, Schnauss J, Nnetu KD, Warmt E, Stange R, Kaes J. Actin and microtubule networks contribute differently to cell response for small and large strains. New J Phys. 2017;19(9):093003.
3. Walsh D, Naghavi MH. Exploitation of cytoskeletal networks during early viral infection. Trends Microbiol. 2019;27(1):39–50.
4. Kłyszejko-Stefanowicz L. Cytobiochemia – biochemia niektórych struktur komórkowych. 3rd ed. Warsaw: PWN SA; 2015. p. 58–62.
5. Wen Z, Zhang Y, Lin Z, Shi K, Jiu Y. Cytoskeleton—a crucial key in host cell for coronavirus infection. Yao X, editor. J Mol Cell Biol. 2021;12(12):968–79.
6. Tiwari V, Koganti R, Russell G, Sharma A, Shukla D. Role of tunneling nanotubes in viral infection, neurodegenerative disease, and cancer. Front Immunol. 2021;12:680891.
7. Tardivel M, Bégard S, Bousset L, Dujardin S, Coens A, Melki R, et al. Tunneling nanotube (TNT)-mediated neuron-to neuron transfer of pathological Tau protein assemblies. Acta Neuropathol Commun. 2016;4(1):117.
8. Abounit S, Wu JW, Duff K, Victoria GS, Zurzolo C. Tunneling nanotubes: a possible highway in the spreading of tau and other prion-like proteins in neurodegenerative diseases. Prion. 2016;10(5):344–51.
9. Panasiuk M, Rychłowski M, Derewońko N, Bieńkowska-Szewczyk K. Tunneling nanotubes as a novel route of cell-to-cell spread of herpesviruses. Sandri-Goldin RM, editor. J Virol. 2018;92(10):e00090–18.
10. Desai A, Mitchison TJ. Microtubule polymerization dynamics. Annu Rev Cell Dev Biol. 1997;13(1):83–117.
11. Downing KH. Structural basis for the interaction of tubulin with proteins and drugs that affect microtubule dynamics. Annu Rev Cell Dev Biol. 2000;16(1):89–111.
12. Döhner K, Sodeik B. The role of the cytoskeleton during viral infection. In: Marsh M, editor. Membrane trafficking in viral replication. Berlin/Heidelberg: Springer-Verlag; 2005. p. 67–108. (Current Topics in Microbiology and Immunology; vol. 285). Available from: http://link.springer.com/10.1007/3-540-26764-6_3. Cited 2023 Feb 7.
13. Sanchez AD, Feldman JL. Microtubule-organizing centers: from the centrosome to non-centrosomal sites. Curr Opin Cell Biol. 2017;44:93–101.
14. Mohan R, John A. Microtubule-associated proteins as direct crosslinkers of actin filaments and microtubules: ROLE OF MAPs IN THE ACTIN-MICROTUBULE NETWORK. IUBMB Life. 2015;67(6):395–403.
15. Elliott G, O'Hare P. Herpes simplex virus type 1 tegument protein VP22 induces the stabilization and hyperacetylation of microtubules. J Virol. 1998;72(8):6448–55.
16. Diefenbach RJ, Davis A, Miranda-Saksena M, Fernandez MA, Kelly BJ, Jones CA, et al. The basic domain of herpes simplex virus 1 pUS9 recruits kinesin-1 to facilitate egress from neurons. Sandri-Goldin RM, editor. J Virol. 2016;90(4):2102–11.
17. Sathish N, Zhu FX, Yuan Y. Kaposi's sarcoma-associated herpesvirus ORF45 interacts with kinesin-2 transporting viral capsid-tegument complexes along microtubules. Farzan M, editor. PLoS Pathog. 2009;5(3):e1000332.
18. Glon D, Vilmen G, Perdiz D, Hernandez E, Beauclair G, Quignon F, et al. Essential role of hyperacetylated microtubules in innate immunity escape orchestrated by the EBV-encoded BHRF1 protein. Lin Z, editor. PLoS Pathog. 2022;18(3):e1010371.
19. Alonso C, Miskin J, Hernáez B, Fernandez-Zapatero P, Soto L, Cantó C, et al. African swine fever virus protein p54 interacts with the microtubular motor complex through direct binding to light-chain dynein. J Virol. 2001;75(20):9819–27.
20. Santos da Silva E, Shanmugapriya S, Malikov V, Gu F, Delaney MK, Naghavi MH. HIV -1 capsids mimic a microtubule regulator to coordinate early stages of infection. EMBO J. 2020;39(20). Available from: https://onlinelibrary.wiley.com/doi/10.15252/embj.2020104870. Cited 2023 Feb 7.
21. de Mareuil J, Carre M, Barbier P, Campbell GR, Lancelot S, Opi S, et al. HIV-1 Tat protein enhances microtubule polymerization. Retrovirology. 2005;2(1):5.
22. Cotton BT, Hyde JL, Sarvestani ST, Sosnovtsev SV, Green KY, White PA, et al. The norovirus NS3 protein is a dynamic lipid- and microtubule-associated protein involved in viral RNA replication. Dermody TS, editor. J Virol. 2017;91(3):e02138–16.
23. Kalicharran K, Dales S. Involvement of microtubules and the microtubule-associated protein TAU in trafficking of JHM virus and components within neurons. In: Talbot PJ, Levy GA, editors. Corona- and related viruses. Boston: Springer, US; 1995. p. 57–61. (Advances in Experimental Medicine and Biology; vol. 380). Available from: http://link.springer.com/10.1007/978-1-4615-1899-0_8. Cited 2023 Feb 7.

24. Ploubidou A, Way M. Viral transport and the cytoskeleton. Curr Opin Cell Biol. 2001;13(1):97–105.
25. McMurray CT. Neurodegeneration: diseases of the cytoskeleton? Cell Death Differ. 2000;7(10):861–5.
26. Cairns NJ, Lee VMY, Trojanowski JQ. The cytoskeleton in neurodegenerative diseases: cytoskeletal proteins in neurodegenerative diseases. J Pathol. 2004;204(4):438–49.
27. Eira J, Silva CS, Sousa MM, Liz MA. The cytoskeleton as a novel therapeutic target for old neurodegenerative disorders. Prog Neurobiol. 2016;141:61–82.
28. Whittaker A, Anson M, Harky A. Neurological manifestations of COVID-19: a systematic review and current update. Acta Neurol Scand. 2020;142(1):14–22.
29. Lingor P, Demleitner AF, Wolff AW, Feneberg E. SARS-CoV-2 and neurodegenerative diseases: what we know and what we don't. J Neural Transm. 2022;129(9):1155–67.
30. Hosking MP, Lane TE. The pathogenesis of murine coronavirus infection of the central nervous system. Crit Rev Immunol. 2010;30(2):119–30.
31. Douaud G, Lee S, Alfaro-Almagro F, Arthofer C, Wang C, McCarthy P, et al. SARS-CoV-2 is associated with changes in brain structure in UK Biobank. Nature. 2022;604(7907):697–707.
32. Khateb M, Bosak N, Muqary M. Coronaviruses and central nervous system manifestations. Front Neurol. 2020;11:715.
33. Morgello S. Coronaviruses and the central nervous system. J Neurovirol. 2020;26(4):459–73.
34. Körner R, Majjouti M, Alcazar M, Mahabir E. Of mice and men: the coronavirus MHV and mouse models as a translational approach to understand SARS-CoV-2. Viruses. 2020;12(8):880.
35. Fehr AR, Perlman S. Coronaviruses: an overview of their replication and pathogenesis. In: Maier HJ, Bickerton E, Britton P, editors. Coronaviruses. New York: Springer New York; 2015. p. 1–23. (Methods in Molecular Biology; vol. 1282). Available from: http://link.springer.com/10.1007/978-1-4939-2438-7_1. Cited 2023 Feb 7.
36. Weiss SR, Navas-Martin S. Coronavirus pathogenesis and the emerging pathogen severe acute respiratory syndrome coronavirus. Microbiol Mol Biol Rev. 2005;69(4):635–64.
37. Matthews A, Weiss S, Paterson Y. Murine hepatitis virus–a model for virus-induced CNS demyelination. J Neurovirol. 2002;8(2):76–85.
38. Weiss SR, Leibowitz JL. Coronavirus pathogenesis. In: Advances in virus research. Elsevier; 2011. p. 85–164. Available from: https://linkinghub.elsevier.com/retrieve/pii/B9780123858856000092. Cited 2023 Feb 7.
39. Cowley TJ, Long SY, Weiss SR. The murine coronavirus nucleocapsid gene is a determinant of virulence. J Virol. 2010;84(4):1752–63.
40. Cymerys J, Dzieciątkowski T, Słońska A, Bierła J, Tucholska A, Chmielewska A, et al. Equine herpesvirus type 1 (EHV-1) replication in primary murine neurons culture. Pol J Vet Sci. 2010;13(4). Available from: http://journals.pan.pl/dlibra/publication/121082/edition/105483/content. Cited 2023 Feb 7.
41. Kärber G. Beitrag zur kollektiven Behandlung pharmakologischer Reihenversuche. Naunyn-Schmiedebergs. Arch Für Exp Pathol Pharmakol. 1931;162(4):480–3.
42. Barlow AL, MacLeod A, Noppen S, Sanderson J, Guérin CJ. Colocalization analysis in fluorescence micrographs: verification of a more accurate calculation of Pearson's correlation coefficient. Microsc Microanal. 2010;16(6):710–24.
43. Naghavi MH, Walsh D. Microtubule regulation and function during virus infection. Glaunsinger BA, editor. J Virol. 2017;91(16):e00538–17.
44. Colombo J, Weintraub MI, Munoz R, Verma A, Ahmad G, Kaczmarski K, et al. Long COVID and the autonomic nervous system: the journey from dysautonomia to therapeutic neuro-modulation through the retrospective analysis of 152 patients. NeuroSci. 2022;3(2):300–10.
45. Spudich S, Nath A. Nervous system consequences of COVID-19. Science. 2022;375(6578):267–9.
46. Pasick J, Dales S. MHV-JHM infections of rodent neuronal cells: replication and trafficking of structural proteins and progeny virions. In: Laude H, Vautherot JF, editors. Coronaviruses. Boston: Springer US; 1994. p. 319–25. (Advances in Experimental Medicine and Biology; vol. 342). Available from: http://link.springer.com/10.1007/978-1-4615-2996-5_49. Cited 2023 Feb 7.
47. Rüdiger AT, Mayrhofer P, Ma-Lauer Y, Pohlentz G, Müthing J, von Brunn A, et al. Tubulins interact with porcine and human S proteins of the genus Alphacoronavirus and support successful assembly and release of infectious viral particles. Virology. 2016;497:185–97.
48. Biswas K, Das Sarma J. Effect of microtubule disruption on neuronal spread and replication of demyelinating and nondemyelinating strains of mouse hepatitis virus in vitro. Perlman S, editor. J Virol. 2014;88(5):3043–7.
49. Bender SJ, Weiss SR. Pathogenesis of murine coronavirus in the central nervous system. J Neuroimmune Pharmacol. 2010;5(3):336–54.
50. Sattentau QJ. The direct passage of animal viruses between cells. Curr Opin Virol. 2011;1(5):396–402.
51. Sattentau Q. Avoiding the void: cell-to-cell spread of human viruses. Nat Rev Microbiol. 2008;6(11):815–26.
52. Barbier P, Zejneli O, Martinho M, Lasorsa A, Belle V, Smet-Nocca C, et al. Role of tau as a microtubule-associated protein: structural and functional aspects. Front Aging Neurosci. 2019;11:204.
53. Sy M, Kitazawa M, Medeiros R, Whitman L, Cheng D, Lane TE, et al. Inflammation induced by infection potentiates tau pathological features in transgenic mice. Am J Pathol. 2011;178(6):2811–22.
54. Matthews JD, Morgan R, Sleigher C, Frey TK. Do viruses require the cytoskeleton? Virol J. 2013;10(1):121.
55. Lavi E, Gilden DH, Wroblewska Z, Rorke LB, Weiss SR. Experimental demyelination produced by the A59 strain of mouse hepatitis virus. Neurology. 1984;34(5):597–597.
56. Zhao S, Gao J, Zhu L, Yang Q. Transmissible gastroenteritis virus and porcine epidemic diarrhoea virus infection induces dramatic changes in the tight junctions and microfilaments of polarized IPEC-J2 cells. Virus Res. 2014;192:34–45.
57. Pepe A, Pietropaoli S, Vos M, Barba-Spaeth G, Zurzolo C. Tunneling nanotubes provide a route for SARS-CoV-2 spreading. Sci Adv. 2022;8(29):eabo0171.
58. Ng ML, Lee JWM, Leong MLN, Ling AE, Tan HC, Ooi EE. Topographic changes in SARS coronavirus–infected cells at late stages of infection. Emerg Infect Dis. 2004;10(11):1907–14.
59. Gov NS, Gopinathan A. Dynamics of membranes driven by actin polymerization. Biophys J. 2006;90(2):454–69.
60. Yeung ML, Teng JLL, Jia L, Zhang C, Huang C, Cai JP, et al. Soluble ACE2-mediated cell entry of SARS-CoV-2 via interaction with proteins related to the renin-angiotensin system. Cell. 2021;184(8):2212–2228.e12.

Publisher's Note

SZKOŁA GŁÓWNA
GOSPODARSTWA
WIEJSKIEGO

Warszawa, 20.05.2025

mgr inż. Michalina Bartak
Zakład Mikrobiologii
Katedra Nauk Przedklinicznych
Instytut Medycyny Weterynaryjnej
ul. Ciszewskiego 8, 02-786 Warszawa
michalina_bartak@sggw.edu.pl

Rada Dyscypliny Weterynaria

Szkoły Głównej Gospodarstwa Wiejskiego w Warszawie

Oświadczenie o współautorstwie

Niniejszym oświadczam, że w pracy:

Bartak, M., Bąska, P., Chodkowski, M., Tymińska, B., Bańbura, M. W., & Cymerys, J. (2024). Neurons cytoskeletal architecture remodeling during the replication cycle of mouse coronavirus MHV-JHM: a morphological in vitro study. BMC veterinary research, 20(1), 18.

Mój indywidualny udział w jej powstaniu polegał na opracowaniu koncepcji artykułu, zaprojektowaniu i przeprowadzeniu eksperymentów, analizie danych, wizualizacji danych, opracowaniu manuskryptu.
Indywidualny wkład pracy w publikację wynosił 70%.

.....

Podpis

SZKOŁA GŁÓWNA
GOSPODARSTWA
WIEJSKIEGO

Warszawa, 20.05.2025r

Dr hab. inż. Piotr Bąska, prof. SGGW
Zakład Toksykologii i Farmakologii
Katedra Nauk Przedklinicznych
Instytut Medycyny Weterynaryjnej
ul. Ciszewskiego 8, 02-786 Warszawa
piotr_bąska@sggw.edu.pl

Rada Dyscypliny Weterynaria

Szkoły Głównej Gospodarstwa
Wiejskiego w Warszawie

Oświadczenie o współautorstwie

Niniejszym oświadczam, że w pracy:

Bartak, M., Bąska, P., Chodkowski, M., Tymińska, B., Bańbura, M. W., & Cymerys, J. (2024). Neurons cytoskeletal architecture remodeling during the replication cycle of mouse coronavirus MHV-JHM: a morphological in vitro study. BMC veterinary research, 20(1), 18.

Mój indywidualny udział w jej powstaniu polegał na pomocy w przeprowadzeniu części eksperymentów, analizie danych oraz krytycznej edycji manuskryptu.
Indywidualny wkład pracy w publikację wynosił 5%.

Piotr Bąska
Podpis

SZKOŁA GŁÓWNA
GOSPODARSTWA
WIEJSKIEGO

Warszawa, 20.05.2025

Dr Marcin Chodkowski
Zakład Mikrobiologii Medycznej i Środowiskowej
Wojskowy Instytut Higieny i Epidemiologii
ul. Kozielska 4, 01-063 Warszawa
marcin.chodkowski@wihe.pl

Rada Dyscypliny Weterynaria

Szkoły Głównej Gospodarstwa Wiejskiego w Warszawie

Oświadczenie o współautorstwie

Niniejszym oświadczam, że w pracy:

Bartak, M., Bąska, P., Chodkowski, M., Tymińska, B., Bańbura, M. W., & Cymerys, J. (2024). Neurons cytoskeletal architecture remodeling during the replication cycle of mouse coronavirus MHV-JHM: a morphological in vitro study. BMC veterinary research, 20(1), 18.

Mój indywidualny udział w jej powstaniu polegał na pomocy w przeprowadzeniu części eksperymentów, użyczeniu sprzętu badawczego oraz krytycznej edycji manuskryptu.
Indywidualny wkład pracy w publikację wynosił 5%.

Chodkowski Marcin

Podpis

SZKOŁA GŁÓWNA
GOSPODARSTWA
WIEJSKIEGO

Warszawa, 20.05.2025

Dr hab. Joanna Cymerys-Bulenda prof. SGGW
Zakład Mikrobiologii
Katedra Nauk Przedklinicznych
Instytut Medycyny Weterynaryjnej
ul. Ciszewskiego 8, 02-786 Warszawa
joanna_cymerys@sggw.edu.pl

Rada Dyscypliny Weterynaria

Szkoły Głównej Gospodarstwa
Wiejskiego w Warszawie

Oświadczenie o współautorstwie

Niniejszym oświadczam, że w pracy:

Bartak, M., Bąska, P., Chodkowski, M., Tymińska, B., Bańbura, M. W., & Cymerys, J. (2024). Neurons cytoskeletal architecture remodeling during the replication cycle of mouse coronavirus MHV-JHM: a morphological in vitro study. BMC Veterinary Research, 20(1), 18.

Mój indywidualny udział w jej powstaniu polegał na pomocy w opiece nad projektem, zaprojektowaniu części eksperymentów, analizie danych, koncepcji artykułu oraz krytycznej edycji manuskryptu.
Indywidualny wkład pracy w publikację wynosił 18%.

J. Joanna Cymerys-Bulenda
Podpis

SZKOŁA GŁÓWNA
GOSPODARSTWA
WIEJSKIEGO

Warszawa, 20.05.2025r

Prof. Dr hab. Marcin W. Bańbura
Zakład Mikrobiologii
Katedra Nauk Przedklinicznych
Instytut Medycyny Weterynaryjnej
ul. Ciszewskiego 8, 02-786 Warszawa
marcin_banbura@sggw.edu.pl

Rada Dyscypliny Weterynaria

Szkoły Głównej Gospodarstwa
Wiejskiego w Warszawie

Oświadczenie o współautorstwie

Niniejszym oświadczam, że w pracy:

Bartak, M., Bąska, P., Chodkowski, M., Tymińska, B., Bańbura, M. W., & Cymerys, J. (2024). Neurons cytoskeletal architecture remodeling during the replication cycle of mouse coronavirus MHV-JHM: a morphological in vitro study. BMC veterinary research, 20(1), 18.

Mój indywidualny udział w jej powstaniu polegał na pomocy w analizie danych oraz krytycznej edycji manuskryptu.
Indywidualny wkład pracy w publikację wynosił 1%.

Podpis

International Journal of
Molecular Sciences

MDPI

Article

ATPase Valosin-Containing Protein (VCP) Is Involved During the Replication and Egress of Sialodacryoadenitis Virus (SDAV) in Neurons

Michalina Bartak [1,*], Weronika D. Krahel [1], Marcin Chodkowski [2], Hubert Grel [3], Jarosław Walczak [4], Adithya Pallepati [4,5], Michał Komorowski [4] and Joanna Cymerys [1,*]

1 Division of Microbiology, Department of Preclinical Sciences, Institute of Veterinary Medicine, Warsaw University of Life Sciences, Ciszewskiego 8 St., 02-786 Warsaw, Poland; weronika_krahel@sggw.edu.pl
2 Division of Medical and Environmental Microbiology, Military Institute of Hygiene and Epidemiology, Kozielska 4 St., 01-063 Warsaw, Poland; marcin.chodkowski@wihe.pl
3 Department of Physics and Biophysics, Institute of Biology, Warsaw University of Life Sciences, 02-787 Warsaw, Poland; hubert_grel@sggw.edu.pl
4 Department of Biosystems and Soft Matter, Institute of Fundamental Technological Research, Polish Academy of Sciences, Pawińskiego 5B St., 02-106 Warsaw, Poland; jwalczak@ippt.pan.pl (J.W.); apallepati@iimcb.gov.pl (A.P.); mkomor@ippt.pan.pl (M.K.)
5 Laboratory of Single-Molecule Biophysics, International Institute of Molecular and Cell Biology in Warsaw, Ks. Trojdena 4 St., 02-109 Warsaw, Poland
* Correspondence: michalina_bartak@sggw.edu.pl (M.B.); joanna_cymerys@sggw.edu.pl (J.C.)

Abstract: Sialodacryoadenitis virus (SDAV) has been identified as the etiological agent responsible for the respiratory system and salivary gland infections in rats. The existing literature on SDAV infections is insufficient to address the topic adequately, particularly in relation to the central nervous system. In order to ascertain how SDAV gains access to neuronal cells and subsequently exits, our attention was focused on the small molecule valosin-containing protein (VCP), which is an ATPase. VCP is acknowledged for its function in the ubiquitin-mediated proteasomal degradation of proteins, including those of viral origin. To ascertain the potential influence of VCP on SDAV replication and egress, high-content screening was employed to determine the viral titer and protein content. Western blot analysis was employed to ascertain the relative expression of VCP. Real-time imaging of SDAV-infected cells and confocal imaging for qualitative morphological analysis were conducted. The Eeyarestatin I (EerI) inhibitor was employed to disrupt VCP involvement in the endoplasmic reticulum-associated protein degradation pathway (ERAD) in both pre- and post-incubation systems, with concentrations of 5 µM/mL and 25 µM/mL, respectively. We demonstrated for the first time that SDAV productively replicates in cultured primary neurons. VCP expression is markedly elevated during SDAV infection. The application of 5 µM/mL EerI in the post-treatment system yielded a statistically significant inhibition of the SDAV yield. It is likely that this modulates the efficacy of virion assembly by arresting viral proteins in the submembrane area.

Keywords: SDAV; VCP; primary neurons; virion assembly; ERAD; eeyarestatin I

Citation: Bartak, M.; Krahel, W.D.; Chodkowski, M.; Grel, H.; Walczak, J.; Pallepati, A.; Komorowski, M.; Cymerys, J. ATPase Valosin-Containing Protein (VCP) Is Involved During the Replication and Egress of Sialodacryoadenitis Virus (SDAV) in Neurons. *Int. J. Mol. Sci.* **2024**, *25*, 11633. https://doi.org/10.3390/ijms252111633

Academic Editor: Alberto Cuesta

Received: 5 September 2024
Revised: 21 October 2024
Accepted: 28 October 2024
Published: 29 October 2024

1. Introduction

Rodents are the most diverse and most abundant order of mammals in the world; they account for about 43% of mammalian species. Belonging to rodents, rats mainly inhabit urban areas, which is associated with their frequent interaction with humans. These animals are reservoirs of viruses, including coronaviruses, and thus pose a potential threat of zoonotic transmission. To date, two human-infecting coronaviruses, HCoV-HKU1 and HCoV-OC43, have been reported that are likely derived from rodent coronaviruses [1,2]. Following the One Health approach, viruses that cause rat infections should be studied more to better understand the nature of coronaviruses that are potentially dangerous

to humans [3,4]. Sialodacryoadenitis virus (SDAV) is the aetiological agent of frequent respiratory infections in laboratory rats [5–7]. Clinical signs of infection include salivary and lacrimal gland inflammation and pharyngitis, photophobia, intermandibular edema, and, in some cases, reduced fertility. SDAV is antigenically related to the mouse hepatitis virus (MHV) serogroup [8] and can cause CNS infection and encephalopathies (documented only by in vivo studies) [9,10].

The viral replication cycle is a complex process in which the interactions of pathogen structures with host cell components are crucial. Identifying the proteins and other molecules present in cells that are important during viral entry, multiplication, and release are critical regarding potential zoonotic transfer. One protein that has been extensively studied in the context of viral infections due to its ubiquitous presence in cells and involvement in many cellular processes is valosin-containing protein (VCP). VCP belongs to the family of ATPases associated with diverse cellular activities (AAA+). It is expressed in different cells and is a highly conserved protein in all eukaryotes. It also occurs under other names—p97 in mammals, Cdc48 in yeast, CDC-48 in *Caenorhabditis elegans*, and Ter94 in *Drosophila melanogaster* [11–13]. It is mainly localized in the cytosol but is also present on the membranes of organelles such as endosomes, cell nucleus, endoplasmic reticulum, and Golgi apparatus [14]. VCP participates in numerous cellular processes, and the full range of VCP-related functions is still emerging [11]. VCP's segregase activity and role in targeting proteins for degradation are best characterized. Both processes make essential contributions to maintaining cellular homeostasis. Eliminating abnormal proteins, organelles, and granular compartments is crucial for the proper function of neurons [15–18]. VCP also participates in endoplasmic reticulum-associated degradation (ERAD) [19], ribosome-associated protein quality control (RQC) [20], and mitochondria-associated degradation (MAD) [21]. The VCP is a promising target for clinical research in cancer treatment [22,23]. Although further research is necessary, recent reports indicate that the VCP inhibitor Eeyarestatin I (EerI) has shown promising results in the treatment of multiple myeloma and acute myeloid leukemia. In particular, the EerI-derived compound CB-5083 has demonstrated favourable synergistic effects when combined with other anti-leukemia drugs, including cytarabine and venetoclax [24]. This targeted therapy may be primarily based on the induction of apoptosis in tumour cells and the unfolded protein replication (UPR) pathway [22,25]. Another compound, VP20, has been demonstrated to inhibit tumour progression by inhibiting the NF-κB signalling pathway in the context of malignant multiple myeloma [26]. Another finding proved that targeting VCP with EerI in non-small cell lung carcinoma (NSCLC) restored p53 and NFB levels and ameliorated the growth and tumorigenicity, improving clinical outcomes [27]. In the case of experimental treatment of idiopathic epilepsy, VCP inhibition by EerI without stress induction, together with folding enhancement, represents a new strategy to restore the proteostasis of misfolding-prone GABAA receptors [28].

Considering the numerous functions performed in the cell and the widespread occurrence of VCP, the involvement of this protein during viral infections has begun to be studied. VCP has been shown to be utilized by various families of viruses, both with genomes in the form of RNA and DNA, during entry, replication, and exit from cells [29–32]. The protein likely mediates endosomal vesicle fusion through interactions with early endosome antigen 1 (EEA1), clathrin, and syntaxin 5 [33–35]. It is also possible that VCP controls the multimerization state of viral proteins during entry into the host cell [29,36]. The way viruses likely utilize VCP during the initial stages of infection has been best described in the family *Flaviridae*, whose cell entry is mediated by clathrin- and dynamin-dependent endocytosis [37–40]. VCP was also shown to be involved in the release of gammacoronavirus Infectious Bronchitis virus (IBV) and Human alphacoronavirus 229E (HCoV-229E) from endosomes [41]. The application of VCP-specific siRNA resulted in the accumulation of these viruses in the early endosomes of infected cells. This suggests the involvement of VCP in the acidification of the environment for envelope–membrane fusion and in the reprocessing and degradation of the nucleocapsid protein, which may indicate an important role for VCP in the infection of all coronaviruses [29,42]. Another process in which VCP is involved

is the viral replication in cells. A disrupted replication process due to VCP inhibition has been observed in the case of infection with viruses of the *Togaviridae* family, including Chikunguya virus (CHIKV), Semliki Forest virus (SFV), and o'nyong'nyong virus (ONNV), or in case of flavivirus, Zika virus [40,43]. Studies indicate that VCP inhibition at different time points during infection with the human coronaviruses HCoV-229E and HCoV-OC43 resulted in reduced levels of RNA replication. In addition, these coronaviruses were found to affect proteins involved in the cell cycle through VCP [44]. Reduced replication levels were also observed when SARS-CoV-2-infected cells were treated with a VCP inhibitor [45]. The impact of VCP function in the late stage of infection during viral release was studied using the Rift Valley Fever virus (RVFV). RVFV has been found to utilize VCP, probably when moving viral glycoproteins into the Golgi apparatus and releasing virions from cells [46].

As mentioned above, VCP plays a role in the viral infection cycle at various stages, including receptor binding and entry, replication, and viral egress. This is primarily through its enzymatic activity. In addition, viruses can use VCP to exploit innate and adaptive immune responses, leading to chronic infections and virus-induced diseases [29]. The ubiquitous presence of VCP in cells, coupled with its involvement in the replication cycle of viruses from several families, including *Coronaviridae*, suggests that VCP may also be a critical factor during SDAV infection. It is essential to understand the molecular mechanisms underlying the potential proviral role of VCP, including the proteins that interact with SDAV, in order to develop effective therapies that target functions that inhibit the proviral action of VCP. The precise role of VCP during SDAV replication in cells, particularly in neurons, remains to be fully elucidated. In the research presented here, we have taken on this task.

2. Results

2.1. SDAV Cytopathic Effect in Cultured Neurons

An analysis of primary neuronal cultures of BALB/c mice showed that SDAV infection causes focal and diffuse cytopathic effects in the neurons, during which the cell shape changes and vacuolization and lysis occur, resulting in the formation of plaques. This gradual process is shown in Figure 1. What is worth mentioning is that the initial cytopathic effect (CPE) in primary neurons started to occur at 276 h post-infection (h p.i.) (Figure 1A, red arrow) by syncytium formation. After 454 h p.i. it was possible to distinguish two growing plaques, but the cell culture confluence was still 82% (97,66% before infection, Figure 1B). The progressive changes started to appear after 577 h p.i. when more plaques were formed (Figure 1A, red arrow), and cells' confluence decreased to 78,5% (Figure 1B). Within a few hours, there was visible cell degradation along with extensive plaque formation. These events resulted in decreasing cell confluence to 23,9% after 628 h p.i. (Figure 1B). It was notable that some neurons survived the infection (Figure 1A, orange arrow). Their activity was sustained until the end of the assay three days later.

The Determination of fluorescent focus units (FFU) in cultured primary neurons was performed using Array Scan XTI (ThermoFisher™, Waltham, MA, USA). Figure 2B shows images from individual wells of a 96-well plate where primary neurons infected with 10-fold dilutions of SDAV (10^0–10^{-5}) were cultured. SDAV titer was determined as log10 FFU/mL = 2.193 ± 0.15 (Figure 2A).

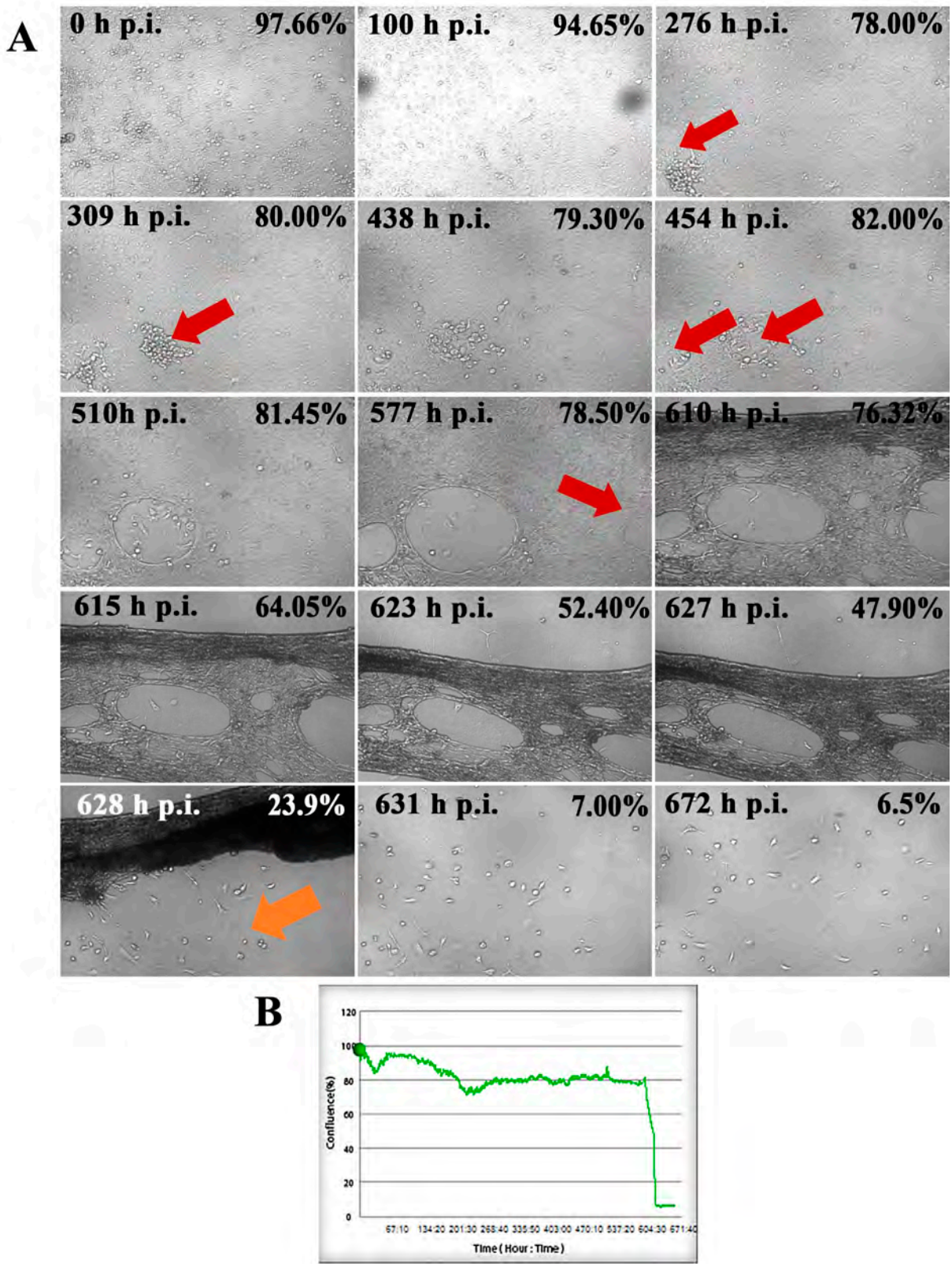

Figure 1. Real-time cell growth analysis of SDAV-infected primary murine neurons performed by live image movie analyzer JuLi™Br (NanoEnTek, Seoul, Republic of Korea). Cultures were observed for 672 h post-infection (h p.i.). Red arrows indicate the process of creating the cytopathic effect (CPE) in the form of plaques. The Orange arrow represents surviving neurons (**A**). The generated graph shows the percentage of cells' confluence level [%] during the whole analysis [hours]. Images were taken every 10 min and analyzed for monolayer confluence (**B**). Objective magnification ×40.

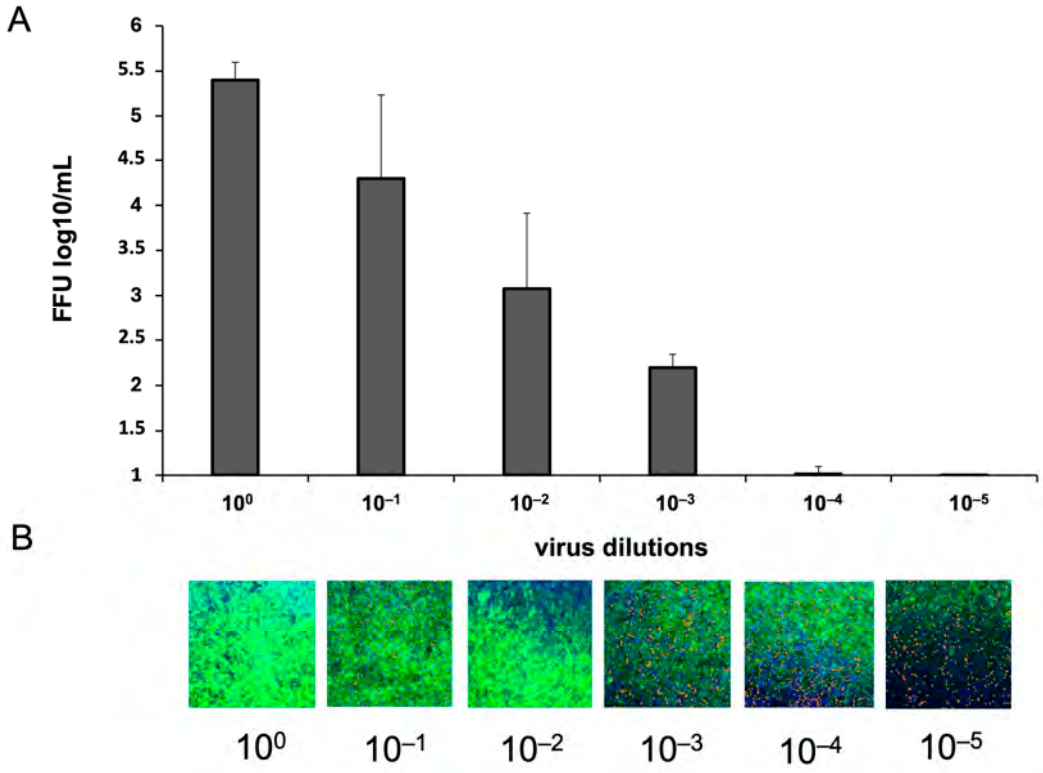

Figure 2. Virus titer is defined as log10 FFU/mL in neurons infected with 10-fold dilutions of SDAV stock solution (**A**). Representative images of individual wells of a 96-well plate seeded with primary neuron cells infected with 10-fold dilutions of SDAV. SDAV nucleocapsid protein (green), cell nuclei (blue) (**B**). Array Scan XTI (ThermoFisher™, Waltham, MA, USA), ×5 magnification.

2.2. Evaluation of SDAV Replication in Primary Murine Neurons

The visualization of SDAV nucleocapsid proteins and cellular structures in primary neuron cells made it possible to assess viral replication using high-content image analysis. An analysis of the images showed the presence of signals corresponding to the nucleocapsid protein inside infected cells (Figure 3A). No signal specific to the nucleocapsid protein was observed in control cultures. In images showing 0 h p.i., 0.5 h p.i., 2 h p.i., and 4 h p.i. cells, a similar intensity of green signal was observed. Images taken of 1 h p.i. and 18 h p.i. neurons showed higher levels of green fluorescence compared to the aforementioned post-infection times. The highest increase was observed in images showing 24 h p.i. cells (Figure 3A). A quantitative analysis was performed on an average of 400 cells per field of view. When comparing the mean fluorescence intensity corresponding to the SDAV nucleocapsid protein at different times after infection (0–24 h p.i.) to that of the negative control, a highly statistically significant increase in fluorescent intensity was detected at all tested times (Figure 3B, blue asterisk). The smallest increase was observed at 0 and 0.5 h p.i., while the largest increase was seen at 24 h p.i. Comparison to 0 h p.i. showed a statistically significant increase only at 18, 24 h p.i. (Figure 3B, black asterisks).

Analyzing the morphology of SDAV-infected neurons, virus antigens can be seen in the area of the cell's membrane and moving inside neurites after 24 h p.i. (Figure 4C(a)), white arrows). Furthermore, it is visible that the signal corresponding to the VCP antigen is in close affinity with the virus antigen (Figure 4C(b), yellow arrow, and white arrows).

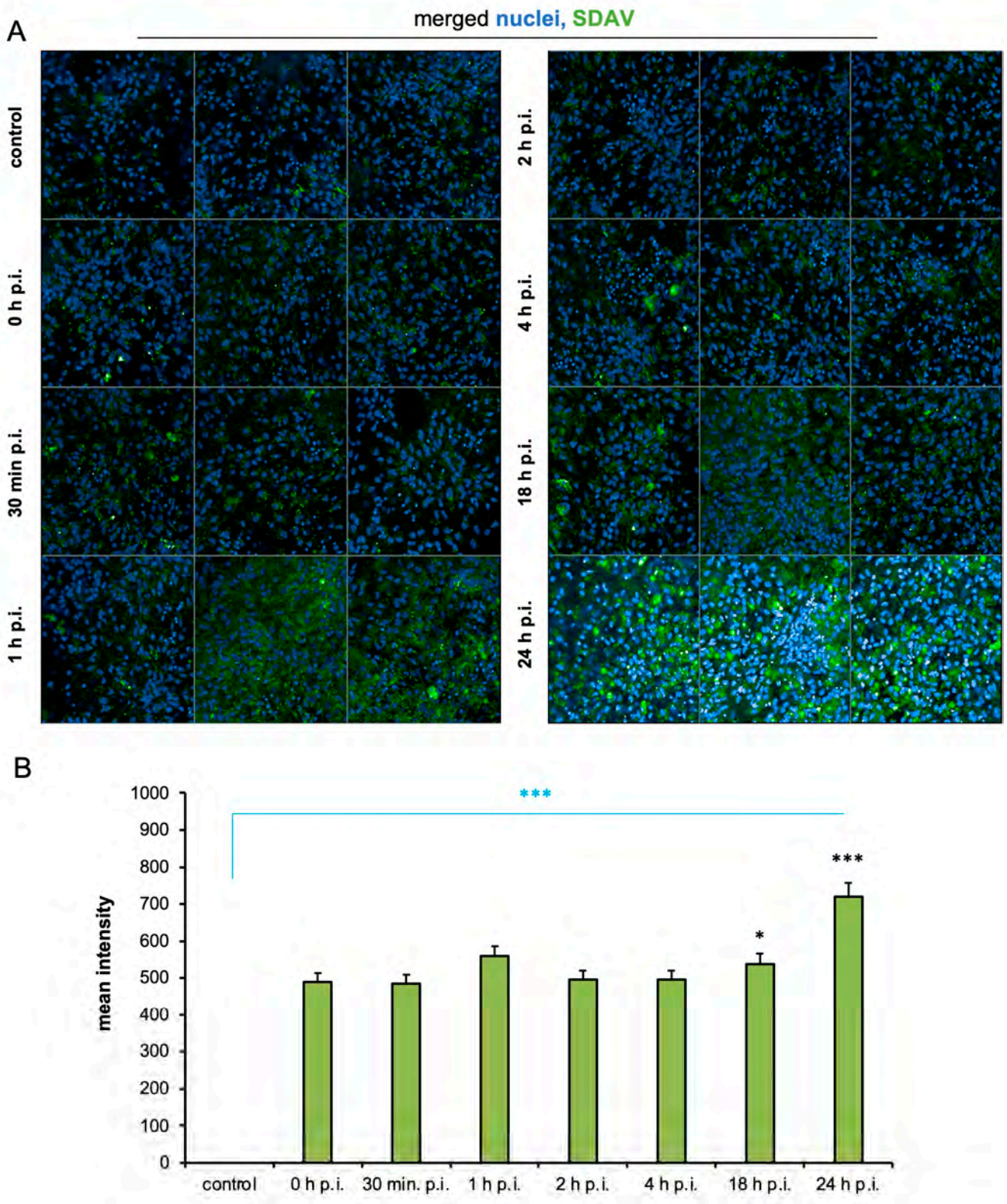

Figure 3. Representative images for each time point after SDAV infection (0–24 h). Cell nuclei (blue), SDAV antigen (green). Magnification x10 (**A**). Mean fluorescence intensity corresponding to virus protein as a function of time after infection of primary neuron cells (**B**). Negative control—uninfected cells. Data from three independent experiments are shown as mean ± SD. One-way ANOVA, * $p < 0.05$, *** $p \leq 0.001$. Blue asterisk—comparison to uninfected control; black asterisk—comparison to 0 h p.i.

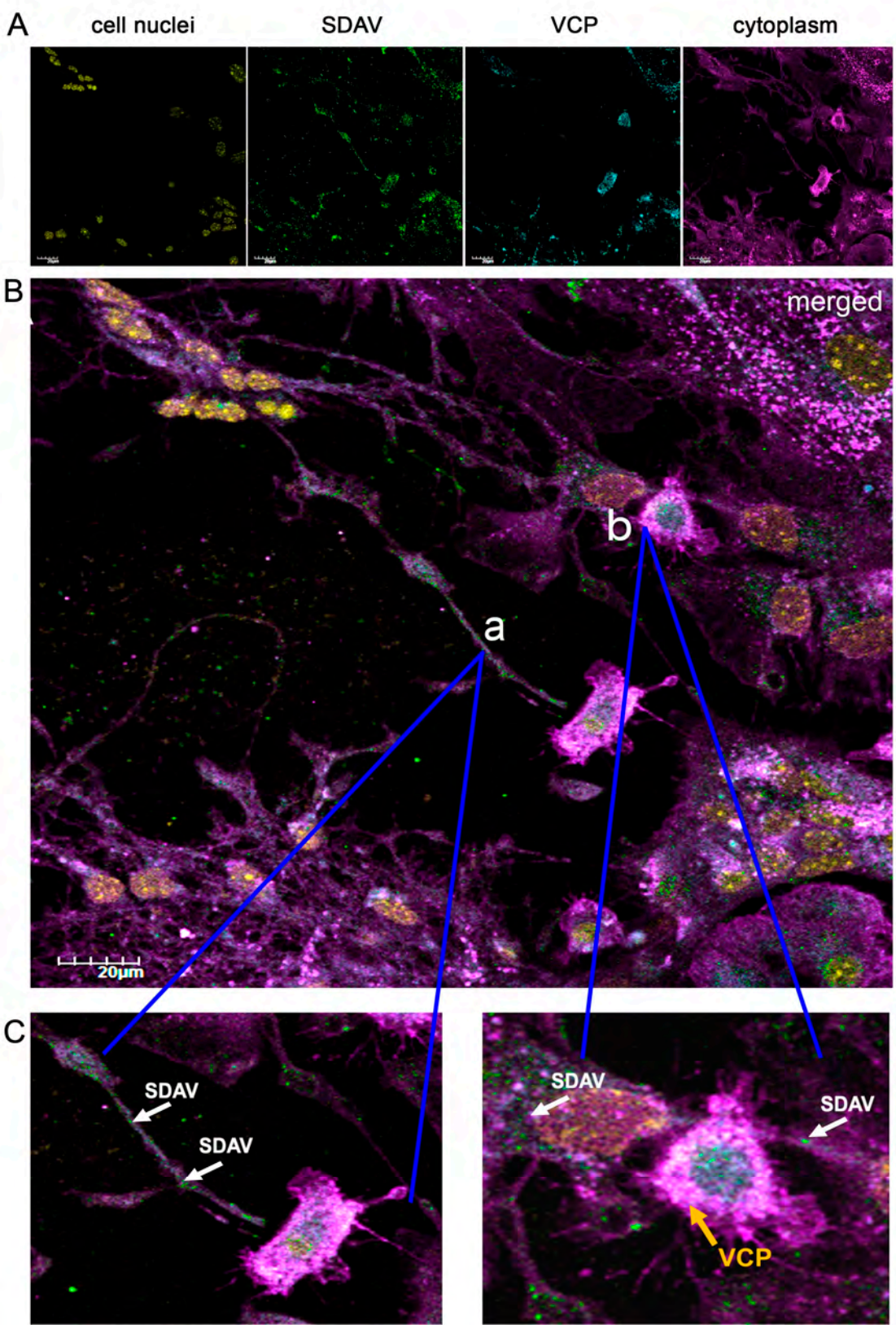

Figure 4. Representative confocal images of primary neurons morphology after infection with SDAV for 24 h (**A**). Merged image of SDAV antigen (green), VCP (blue), cell nuclei (yellow), cell membrane (magenta) (**B**). Closeup image of SDAV antigen moving inside cell protrusion (**C**(**a**)). Closeup of viral antigen in close affinity of cell nuclei and possible colocalization with VCP (whitish fluorescence) (**C**(**b**)). Magnification ×60, scale bar 20 µm. Olympus FV10i.

2.3. Levels of VCP in SDAV-Infected Neurons

Similarly, an HCS analysis of the mean fluorescence intensity signal of VCP antigen in the control and cells infected from 0 to 24 h showed interesting results. In the time from 0 to 18 h p.i., there was no significant increase in antigen levels compared to the uninfected control (Figure 5A,B). A rise in the mean intensity of the red fluorescence signal (VCP antigen) was observed in images taken 24 h p.i. A highly significant increase was detected in the quantitative analysis compared to the positive, uninfected control (Figure 5A). This was also observed in qualitative observation as a bright fluorescence signal of VCP antigen in the perinuclear area (Figure 4C, yellow arrows).

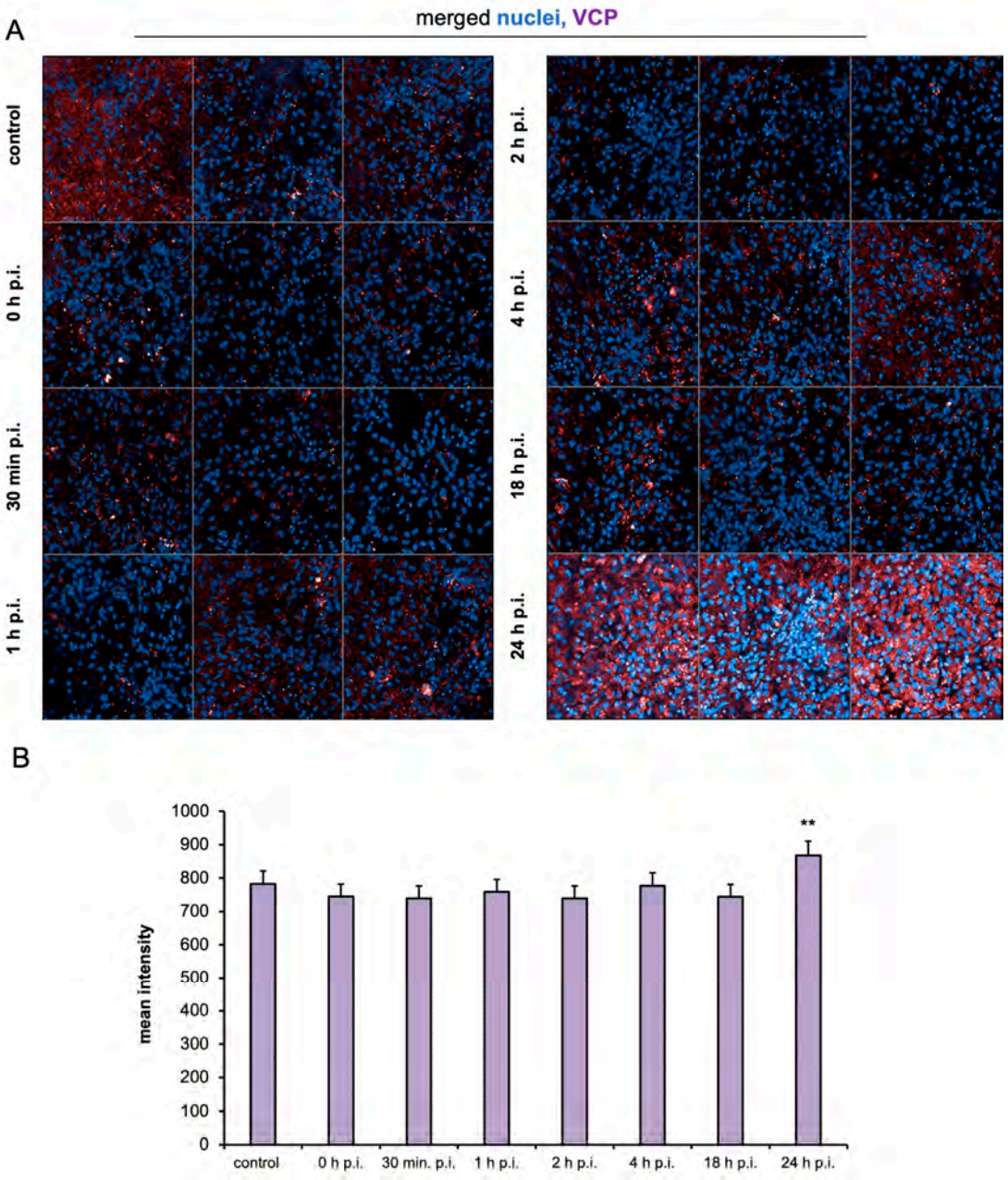

Figure 5. Representative images for each time point after SDAV infection (0–24 h). Cell nuclei (blue), VCP antigen (red). Magnification ×10 (**A**). Mean fluorescence intensity corresponding to VCP as a function of time after SDAV infection of primary neuron cells (**B**). Negative control—uninfected cells. Data from three independent experiments are shown as mean ± SD. One-way ANOVA, ** $p \leq 0.01$.

2.4. Evaluation of the Contribution of VCP to the SDAV Replication Cycle in Cultured Primary Neurons

The potential involvement of VCP in the SDAV replication cycle was assessed by visualizing infected cultures untreated (Figure 4B) or treated with EerI (Figures 6 and 7A,B) and by quantitative analysis of the spot count/cell of the VCP and N protein antigens in EerI-treated cultures compared to infected controls not treated with the inhibitor (Figure 8B,C).

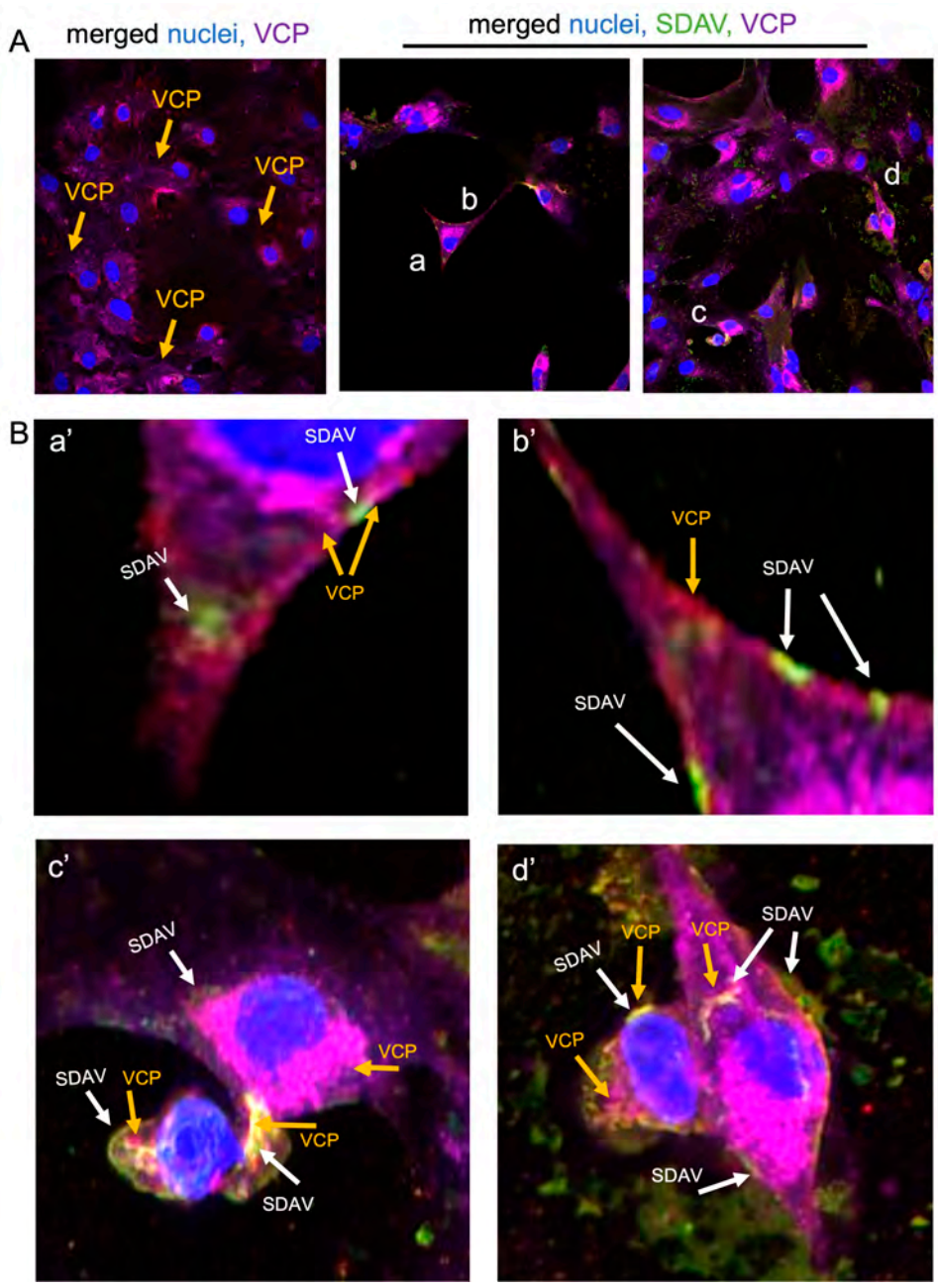

Figure 6. Representative confocal images of primary neurons morphology after infection with SDAV for 24 h treated with 5 µM/mL EerI and control nontreated. Merged image of SDAV antigen (green), VCP (orange), cell nuclei (blue), and cell membrane (magenta) (**A**,**B**; **a**–**d** are regions zoomed in and shown as **a′**–**d′**). Closeup image of SDAV antigen in the perinuclear area possibly correlating with VCP (whitish fluorescence) (**B**(**a′**,**c′**)). Closeup of viral antigen trapped in the submembrane region along with VCP (**B**(**b′**,**d′**)). Magnification ×60, scale bar 20 µm. Operetta CLS (Revvity™, Waltham, MA, USA).

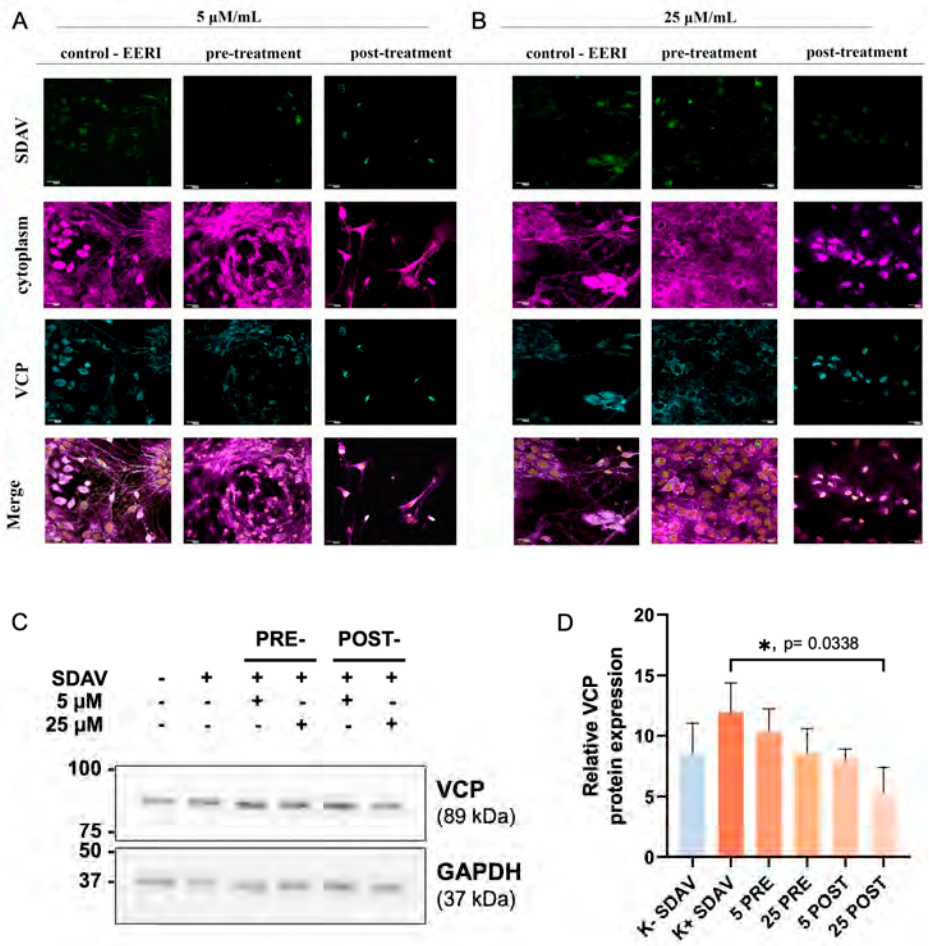

Figure 7. Representative images of neurons 24 h p.i. with SDAV. Cells were treated with 5 µM/mL and 25 µM/mL EerI in pre-incubation and post-incubation methods. Positive control—infected cells, untreated with EerI. Cytoplasm (magenta), VCP antigen (blue), SDAV nucleocapsid protein (green). FV10i (Olympus), magnification ×40, scale bar 20µm (**A**,**B**). Representative Western blot image for VCP followed by densitometric semi-quantification of relative VCP expression in infected neurons (SDAV+), pre- or post-incubated with VCP EerI inhibitor (5 µM/mL or 25 µM/mL separately), compared to non-infected control (SDAV−). Acquired in Image Lab™ Software v6.0.1 (Bio-Rad, Hercules, CA, USA) (**C**). Data from three independent experiments are presented as mean ± SD (**D**). Non-parametric, Friedman test, followed by post hoc group comparison test, * $p < 0.05$.

The SDAV antigen is located in the outer cell membrane region after incubation with 5 µM/mL EerI (Figure 6B(b′,d′); white arrows). Nevertheless, in non-treated cells, the virus antigen is detected moving in cell protrusions (Figure 4C(a), white arrows). Interestingly, there is a noticeable, possible colocalization of VCP with SDAV antigens seen as bright magenta fluorescence (Figure 6B(c′,d′), yellow and white arrows).

The analysis of morphological alterations in cells revealed no abnormalities after administering 5 µM/mL and 25 µM/mL EerI for 24 h p.i. However, notable alterations in the intensity of the viral antigen and VCP fluorescence signals were observed following the treatment with both inhibitor concentrations, particularly in the post-incubation method. The fewest changes were observed in cultures that had been pre-incubated with 25 µM/mL EerI. In these cultures, the intensity of the fluorescence of the viral antigen and VCP was found to be similar to that observed in the control cells that had not been treated (Figure 7A,B). Western blot analysis demonstrated a statistically significant ($p < 0.05$) increase in VCP expression 24 h p.i. (12 ± 1.1) in comparison to the uninfected control cells (9 ± 0.98) (Figure 7C,D). Following incubation with EerI, a statistically significant ($p < 0.05$) decrease in VCP expression was observed in both incubation methods when compared to

the positive infected control. Pre-incubation with 5 µM/mL (10 ± 1.1 vs. 12 ± 1.1), 25 µM (9 ± 0.95 vs. 12 ± 1.1), and post-incubation with 5 µM/mL (8.7 ± 0.4 vs. 12 ± 1.1), 25 µM (5 ± 1.0 vs. 12 ± 1.1) indicated a statistically significant ($p < 0.05$) drop in VCP expression. A decrease in VCP expression in comparison to the uninfected control was only observed for the post-incubation method at the 25 µM/mL concentration level (9 ± 0.98 vs. 5 ± 0.90).

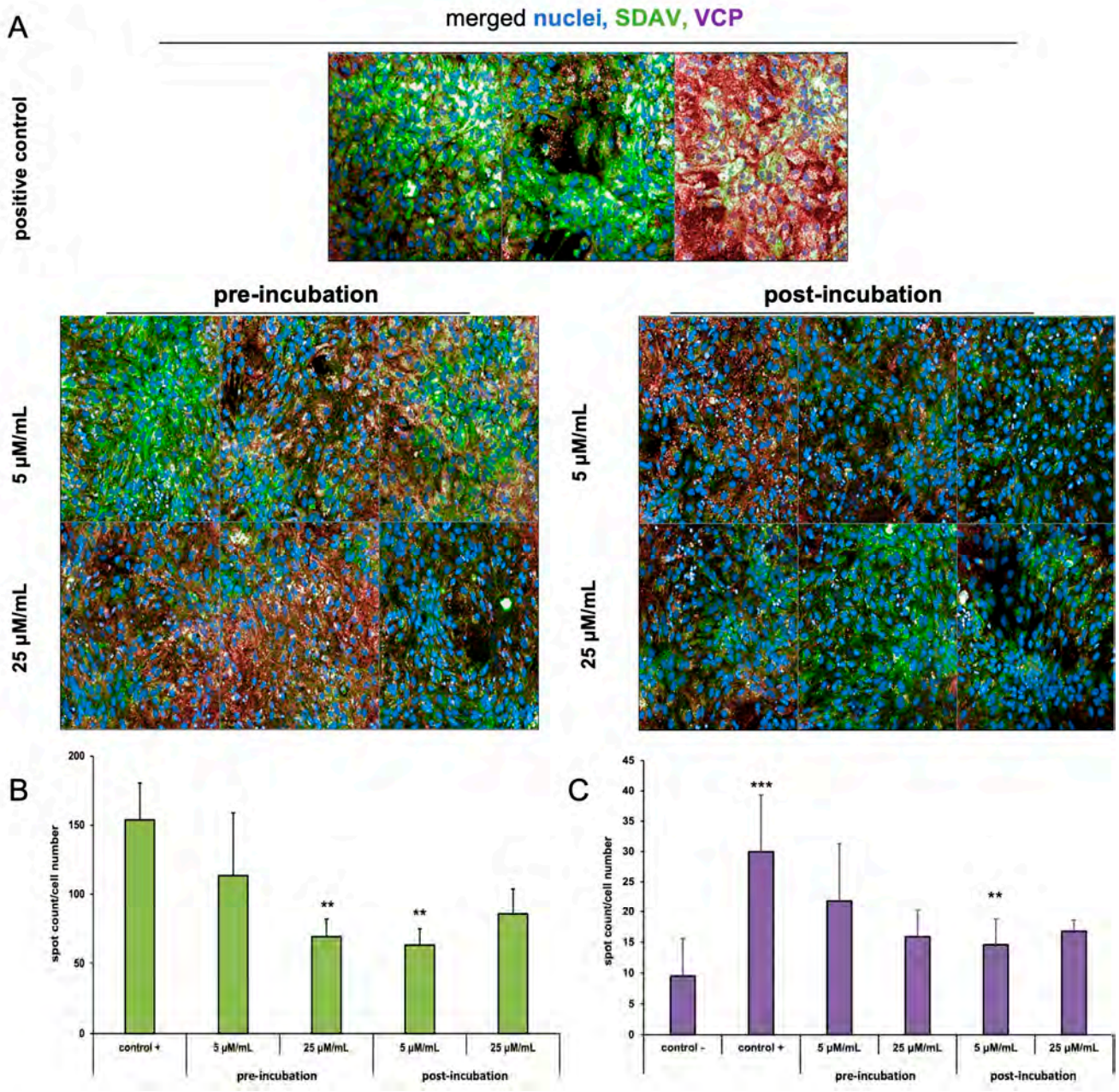

Figure 8. High-content imaging screening spot detection analysis of SDAV nucleocapsid and VCP antigen 24 h p.i in neurons. Representative images for infected untreated cells (positive control) and cells treated with EerI inhibitor at concentrations of 5 µM/mL and 25 µM/mL in the pre-incubation and post-incubation system. Cell nuclei (blue), viral antigen (green), VCP (red signal). Operetta® CLS™ (Revivity™, Waltham, MA, USA), ×40 magnification (**A**). Quantitative analysis corresponding to the nucleocapsid protein of SDAV (**B**) and VCP (**C**) depending on the incubation method and inhibitor concentration using Harmony™ 4.9 software (Revvity™, Waltham, MA, USA) spot detecting protocol. Negative control—non-infected cells, positive control—infected, untreated cells. Data from three independent experiments are presented as mean ± SD. Two-way ANOVA, ** $p \leq 0.01$ (to positive control) or *** $p \leq 0.001$ (to negative control).

The visualization of infected cultures treated with EerI along with quantitative analysis was performed using Operetta® CLS™ and Harmony™ (Revvity™, Waltham, MA, USA) (Figure 8A–C). A quantitative analysis was performed for approximately 400 cells present in the field of view. The spot count of AlexaFluor™ 488 (N protein) and AlexaFluor™ 647 (VCP) signals in EerI-treated cultures was compared to the infected, non-EerI-treated neurons (positive control) after 24 h p.i. Changes in spot count number per cell corresponding to the nucleocapsid protein were detected for both incubation methods (5 µM/mL or 25 µM/mL) compared to positive control (153.87 ± 26.7) (Figure 8B). A highly statistically significant (** $p \leq 0.01$) decrease in the spot count of N protein occurred in pre-incubated 25 µM/mL (69.07 ± 12.5) and post-incubated 5 µM/mL (63.17 ± 11.5) EerI-treated neurons (Figure 8B).

Interestingly the spot number of VCP increased extremely statistically significantly (*** $p \leq 0.001$) after SDAV infection (29.96 ± 9.35) compared to the uninfected, untreated control (9.52 ± 6.1) (Figure 8C). After treatment with EerI, a highly significant statistical decrease (** $p \leq 0.01$) in the spot count of VCP was observed only in the post-incubation method with 5 µM/mL EerI (14.61 ± 4.19). The decreasing trend of the VCP number was observed after SDAV infection compared to the positive control. The VCP number increased in all conditions when compared to the negative control (Figure 8C).

The changes in SDAV titer following treatment with EerI were evaluated using high-content analysis (HCA), with the results expressed as log10 FFU/mL. To evaluate the efficacy of the employed treatment, the SDAV was initially titrated with the EerI inhibitor at concentrations of 5 µM/mL and 25 µM/mL in a post-incubation system (chosen based on previous promising results) for 24 h p.i. (Figure 9A(c)). Subsequently, prior to analysis, the cell media was collected and utilized for a second titer analysis to ascertain whether EerI influenced SDAV egress from neurons (Figure 9A(d)).

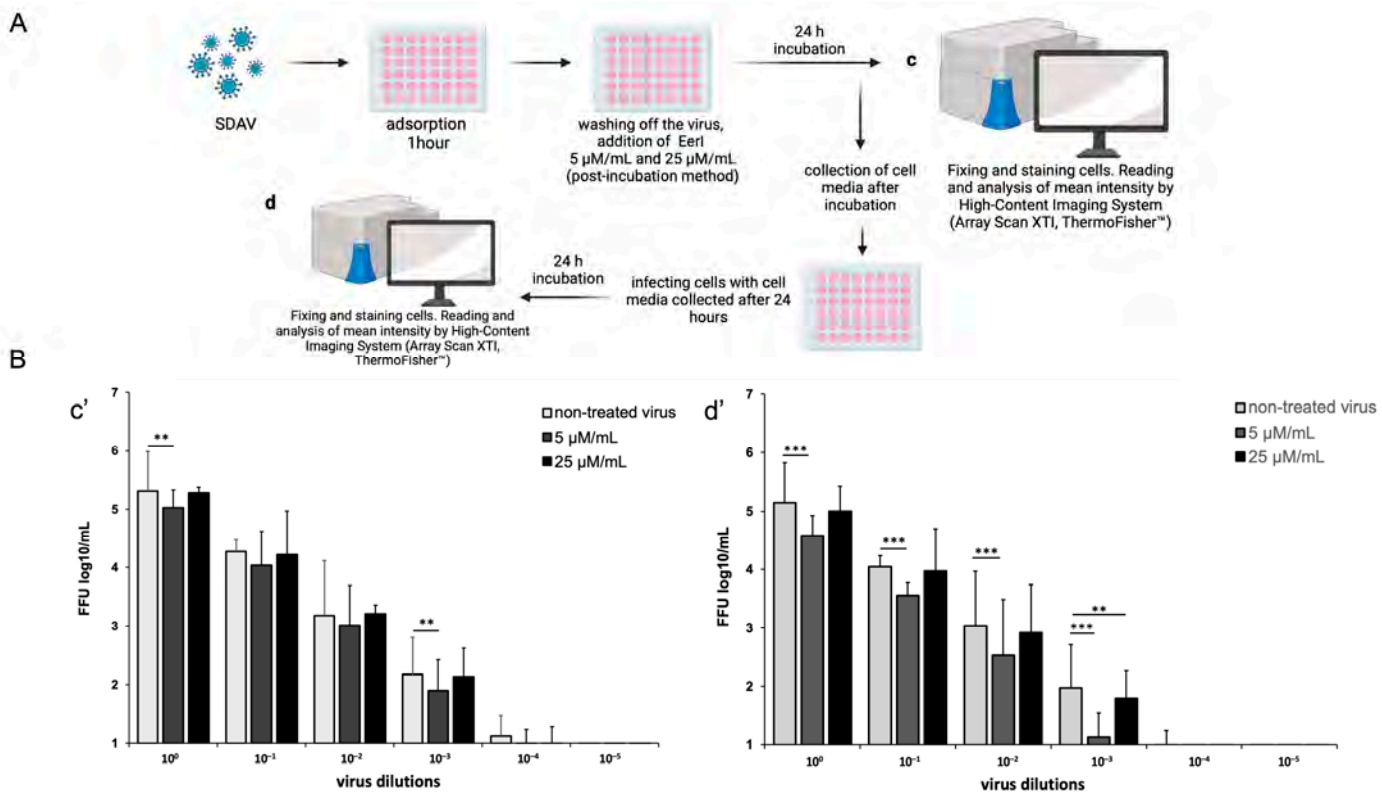

Figure 9. High-content analysis for SDAV nucleocapsid antigen after post-incubation with EerI at concentrations of 5 µM/mL and 25 µM/mL (HCS™ studio software v2.0 spot detector protocols, ThermoFisher®). Schematic representation of the procedure (**A**; **c**,**d** represent analysis steps with respective results shown in **c'**,**d'**). Mean fluorescent signal intensity of spots detected for virus antigen

in the function of 10-fold dilutions of SDAV stock solution (**B**(**c′**)). Mean fluorescent signal intensity of spots detected for virus antigen in the function of 10-fold dilutions of previously infected cell media to test the hindering effect of the EerI inhibitor on the release of SDAV progeny virions (**B**(**d′**)). Data from three independent experiments are presented as mean ± SD. Two-way ANOVA, ** $p \leq 0.01$, *** $p \leq 0.001$.

A highly statistically significant (** $p \leq 0.01$) decrease in log10 FFU/mL occurred in a concentration of 5 µM/mL EerI by 0.278 logarithms in dilution 10^0 and 0.270 logarithms in dilution 10^{-3} compared to the non-treated virus (dilution 10^0: 5.39 ± 0.81 non-treated vs. 5.03 ± 0.29 5 µM/mL treated and 10^{-3}: 2.19 ± 0.51 non-treated vs. 1.90 ± 0.51 5 µM/mL treated) (Figure 9B(c′)). Interestingly, an extremely significant decrease (*** $p \leq 0.001$) in log10 FFU/mL appeared in the second round of viral tittering with collected cell media (Figure 9B(d′)). Again, the best results were obtained after incubation with 5 µM/mL EerI, where a 0.840 logarithms drop in dilution 10^{-3} was observed (1.96 ± 0.53 non-treated vs. 1.12 ± 0.41 5 µM/mL treated).

To assess the morphology of cells and the potential manifestation of CPE following SDAV infection, a post-incubation method utilizing EerI at a concentration of 5 µM/mL was performed. This employed additional real-time growth analysis over a 672 h interval (Figure 10). During the course of the infection, the formation of small plaques was observed, though they did not evolve into larger plaques (Figure 10A, red arrows). The level of cell confluence remained above 94% throughout the entire recording span, indicating that EerI had a limiting effect on the egress of SDAV progeny virions (Figure 10B).

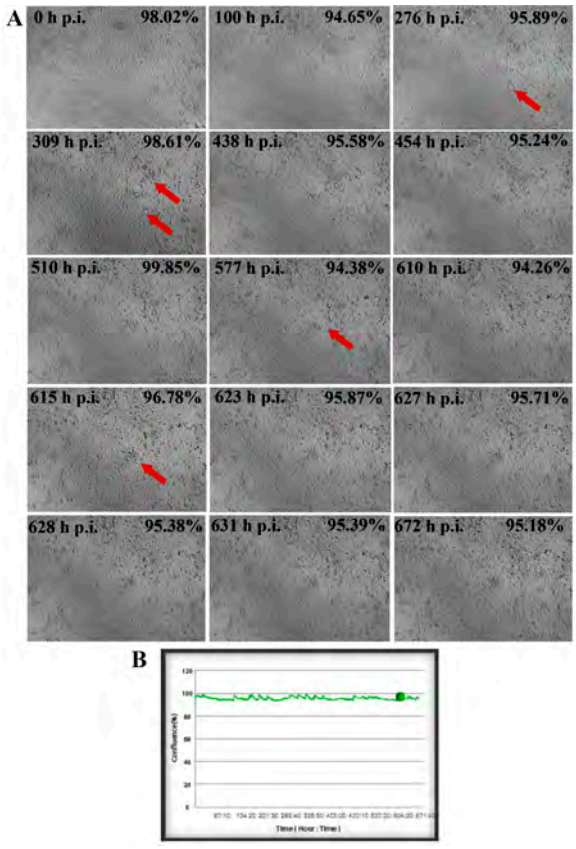

Figure 10. Real-time cell growth analysis of SDAV-infected primary murine neurons post-incubated with EerI at a concentration of 5 µM/mL performed by live image move analyzer JuLi™Br. Cultures were observed for 672 h p.i. Red arrows indicate the process of creating the CPE (**A**). The generated graph shows the percentage of cells' confluence level [%] during the whole analysis [hours]. Images were taken every 10 min and analyzed for cell confluence (**B**). Objective magnification ×40.

3. Discussion

The Sialodacryoadenitis virus, a highly infectious pathogen that causes infections in rats, poses a potential threat to humans and other animals due to possible interspecies transfer. Cases of mutation of the genome of various coronaviruses leading to the acquisition of the ability to infect new species have been documented [4]. It is now known that VCP can be a pro- or antiviral factor. Its effect has so far been verified for picornaviruses [32,46,47], flaviviruses [48–50], and coronaviruses (IBV, HCoV 229E, HCoV OC43) [41,43]. For this reason, the present study decided to carry out research to gain a better understanding of SDAV. We decided to target valosin-containing protein, knowing its crucial role in cell metabolism and viral replication. A successful in vitro multiplication of the Sialodacryoadenitis virus has so far been found in a few established lines (L2p, LBC) and a primary culture of rat kidney cells [5,51–53]. An attempt to multiply SDAV in mice brain cells' primary culture was unsuccessful [5], despite studies showing brain lesions in neonatal CD-1, CWF mice, and W1 Wistar rats infected with SDAV [10].

For the first time, we demonstrated SDAV replication in the primary neuron culture of BALB/c mice without previous adaptation. Focal and diffuse cytopathic effects were shown in primary neurons (Figure 1A, red arrows). The PFU = 10^6 and log10 FFU/mL = 2.193 $\pm$ 0.15 obtained in the study are comparable to those obtained by Gaertner et al. (1992) [54] (Figure 2). The onset of plaque formation was observed at 276 h p.i. (Figure 1A, red arrows), while in the case of the infected LBC established line, defined plaques were visible after 48 h p.i. [55]. This may be an indication of the movement of SDAV virions between neurons without cell destruction. An analysis of SDAV replication in primary neuron cells derived from BALB/c mice was carried out based on the Harmony (Revvity™, Waltham, MA, USA) algorithm's calculation of the average fluorescence intensity corresponding to the SDAV nucleocapsid protein (Figure 3). Compared to cells analyzed at 0 h p.i. (after cell entry), there was an extremely statistically significant (*** $p \leq 0.001$) increase in the mean fluorescence intensity at 24 h p.i., confirming the effective penetration of SDAV into mouse neurons and the completion of a full SDAV replication cycle. To explore the role of VCP in SDAV replication, we first examined VCP levels in uninfected and SDAV-infected primary neurons. We reported a highly statistically significant increase (** $p \leq 0.01$) in mean fluorescence intensity corresponding to VCP 24 h p.i., which may suggest increased production of this protein in neurons resulting from SDAV infection (Figure 5). Similar results were obtained from Western blot analysis, where there was a statistically significant (* $p \leq 0.05$) increase in relative VCP expression in infected cells (12 $\pm$ 1.1) in comparison to the uninfected control cells (9 $\pm$ 0.98) (Figure 7C,D).

The effect on VCP expression was studied before in the context of SARS-CoV and CoV-229E infection. It was shown that 24 h p.i. VCP expression in human monocytes for both coronaviruses decreased [56], contrary to our results. Coronaviruses require a suitable environment for replication to take place, which is created, among other things, by DMVs, which are thought to originate from EDEMosomes—vesicles that arise from the endoplasmic reticulum membrane and contain regulators of the ERAD pathway. It has been shown that during betacoronavirus infection, there is increased formation of EDEMosomes. This may be related to the prevention of the accumulation of viral proteins in the ER, as regulators contained in EDEMosomes may increase ERAD activity and thus affect the release of viral structural proteins [57–60]. It is possible that the increase in the mean fluorescence corresponding to VCP and protein relative expression, one of the components of ERAD, is related to the activation of ERAD by regulators contained in EDEMosomes (Figures 5 and 7C,D).

To further explore the role of VCP in SDAV replication, we used Eeyarestatin I (EerI), a VCP inhibitor, and checked its effect on SDAV-infected primary neurons. EerI is a substance that shows affinity for the endoplasmic reticulum due to its aromatic domain. EerI has been shown to interact with VCP located within the endoplasmic reticulum via a nitrofuran-containing group (NFC). The VCP present in this area is part of ERAD, a pathway associated with protein degradation [50,61]. In high-content screening analysis

(Operetta CLS, Revvity™, Waltham, MA, USA) of the spot count/cell of the VCP antibody signal, an extremely statistically significant (*** $p \leq 0.001$) increase in the infected, non-treated control was observed 24 h p.i. compared to uninfected neurons (29.96 ± 9.35 vs. 9.52 ± 6.1, respectively) (Figure 8C). The statistically significant decrease compared to the positive control occurred only in 5 µM/mL EerI post-treatment (29.96 ± 9.35 vs. 14.61 ± 4.19, respectively) (Figure 8C). No statistically significant changes were observed under other incubation conditions. This may be due to the action of EerI, its affinity for the endoplasmic reticulum, and its inability to interact with VCPs located in other organelles or in the cytoplasm [62]. In addition, an overall higher spot count/cell (Figure 8C) and a higher relative expression (Figure 7C,D) of VCP in infected neurons, both untreated and treated with EerI, suggest its important involvement in SDAV virion assembly. In the context of the SDAV N protein signal after EerI treatment, a highly statistically significant (** $p \leq 0.01$) decrease in the spot count/cell was observed for 25 µM/mL pre-incubation (69.07 ± 12.5) and 5 µM/mL post-incubation (63.17 ± 11.5) compared to the positive control (153.87 ± 26.7) (Figure 8B). This indicates the likely involvement of VCP at a later stage of replication, during the release of viral proteins from the endoplasmic reticulum. An interesting observation that confirms the VCP role at later stages of viral replication was the accumulation of the viral antigen signal in the submembrane areas of neurons after post-incubating with 5 µM/mL (Figure 6B(b',d'), white arrows). No presence was detected in cell protrusions like it was seen in the untreated infected control (Figure 4C, white arrows). Here, we can speculate that a similar phenomenon of "viral protein homeostasis" described by Tabata et al. (2022) [62] played a role by controlling the amount of each SDAV protein in virus-infected cells by the ERAD system modulated by the EerI inhibitor. Another study demonstrated that the administration of either Xanthohumol or Eeyarestatin I resulted in a reduction in Zika virus (ZIKV) and Usutu virus (USUV) titers in infected cells. This finding aligns with the crucial role of valosin-containing protein (VCP) during the intracellular stages of the viral replication cycle. Of particular interest, the research also revealed a previously unappreciated direct antiviral activity of Eeyarestatin I against virus infectivity (virucidal activity). However, this activity was exclusive to Eeyarestatin I, and not observed with Xanthohumol [63]. Concluding the results, we noticed a better effect in reducing virus yield by using the post-incubation method (Figures 6–9). To evaluate the efficiency of this treatment, the SDAV was initially tittered with the EerI inhibitor at concentrations of 5 µM/mL and 25 µM/mL and, again, using a collected cell medium (after 24 h course of infection) to ascertain whether VCP inhibition by EerI influenced SDAV egress from neurons (Figure 9A,B). The analysis confirmed our hypothesis, indicating that the second titer showed an extremely statistically significantly (*** $p \leq 0.001$) reduction in the virus titer.

The usage of 5 µM/mL decreased log10 FFU/mL by 0.840 logarithms in dilution 10^{-3} (1.96 ± 0.53 non-treated vs. 1.12 ± 0.41 5 µM/mL treated) (Figure 9B(d')). This outcome prompted the decision to conduct the final analysis using only a concentration of 5 µM/mL in the post-treatment system. The real-time observation of neuronal growth following treatment and infection with SDAV for 672 h demonstrated a minimal cytopathic effect and a sustained cell confluence of no less than 94% (Figure 10). A comparison of the results of the same analysis conducted without prior incubation with EerI confirmed the effect of VCP on the assembly and release of SDAV progeny virions. In cells that had not been treated and that had been infected for 672 h, the level of confluence dropped to an incomplete 6%, and a significant cytopathic effect was observed, manifesting as plaques and cell vacuolization (Figure 10).

4. Materials and Methods

4.1. Primary Neuronal Cell Culture

Balb/c ($H2^d$) mice were used to establish the primary culture of murine neurons using the method by Cymerys et al. (2010; 2016) [64,65]. Pregnant female mice (16–19 days post-mating) were sacrificed, and fetuses were removed and decapitated for brain collection. Then, isolated cerebral hemispheres from fetal brains were washed three times in cold HBSS solution (10x Hanks Buffer; Life Technologies Waltham, MA, USA) and treated with 2.5% EDTA-free trypsin solution at 37 °C in 5% CO_2 for 15 min. Again, after incubation, cells were washed three times in a warm HBSS solution and mechanically homogenized using a pipette. After suspending and counting, cells were plated onto poly-L-lysine-coated wells or poly-D-lysine with laminin-coated coverslips. Primary murine neurons were cultured in B-27 Neuron Plating Medium, consisting of the neurobasal medium, B-27 supplement, 200 mmol/L of glutamine, 10 mmol/L of glutamate, 1% penicillin/streptomycin antibiotics with 5% supplement of fetal bovine, and 5% horse serum (Gibco Life Technologies, Waltham, MA, USA). To avoid propagation of non-neural cells, cultures were maintained in growth medium supplemented with 10 µM cytosine β-D-arabinofuranoside (after 3 days for 24 h) (Sigma-Aldrich, Darmstadt, Germany). Subsequently, the medium was removed and replaced with Neuron Feeding Medium (B-27 Neuron Plating Medium without glutamate; Life Technologies Waltham, MA, USA). In such conditions, neurons were maintained for the next 8 days before analysis, infection, and incubation with inhibitor at 37 °C with 5% CO_2.

4.2. SDAV Infection and Calculation of Viral Antigen Signal Using High-Content Analysis

The virus used in the study, Sialodacryoadenitis virus strain 681, was provided courtesy of Professor Susan Compton, Yale University, USA. The strain was isolated in 1976 at Yale [66,67]. A rat L2 lung epithelial cell line (CCL-149™, ATCC®, Manassas, VA, USA) was used to multiply and determine the viral titer (PFU/mL = 10^6 using the method by Gaertner et al. (1993)) [54]. Viral titer in primary murine neurons was assessed by the fluorescent focus units (FFU). Cells were seeded in 96-well plates (at a density of 5×10^3 cells/well) and infected with 10-fold dilutions of the SDAV (from 10^0–10^{-5} in twelve replicates). After 1 h of incubation in 5% CO_2, 37 °C, the virus suspension was aspirated, and a fresh growth medium was added. At 24 h post-infection (h p.i.), cells were fixed in 3.7% paraformaldehyde (PFA) in PBS (ThermoFisher™, USA) for 15 min at room temperature (RT). Next, the cells were permeabilized with 0.5% Tween (Sigma-Aldrich) in PBS (15 min, RT) and blocked with 1% bovine serum albumin (BSA, Sigma-Aldrich) in PBS (30 min, RT) to prevent nonspecific binding. Next, SDAV nucleocapsid proteins were visualized by incubation with mouse-SARS/SARS-CoV-2 monoclonal primary antibody specific for N protein (ThermoFisher™) (1:250 dilution, 1 h, 37 °C) and AlexaFluor™ 488 Goat anti-Mouse IgG secondary antibody (ThermoFisher™) (1:500 dilution, 1 h, RT). Cell nuclei were visualized for cell localization with Hoechst 33,258 (ThermoFisher™) (2 µg/1 mL, 3 min, RT). The fluorescent signals were detected via high-content analysis (Array Scan XTI, ThermoFisher™, Waltham, MA, USA) at ×10 magnification. The number of infected cells in each well was automatically obtained from 9 images per well (approx. 10,000 cells) using HCS studio software version 2.0 spot detector protocols. How the algorithm worked is shown in Figure 11. Results were presented as the number of spots detected (AlexaFluor 488™) corresponding to virus antigen in log10 FFU/mL [68,69].

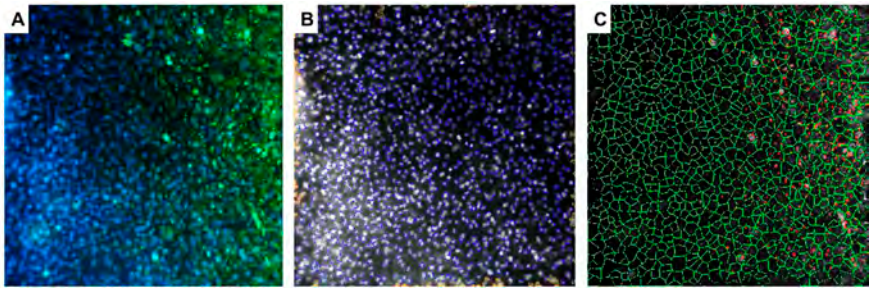

Figure 11. Representative images of SDAV-infected primary neurons presenting how the algorithm for detecting the spot-protein area of the SDAV nucleocapsid works. (**A**) Overlay of green signal (AlexaFluor™ 488, SDAV N protein) and blue signal (Hoechst 33258, cell nuclei), (**B**) non-blue signals (cell nuclei) from which the algorithm determines the cell area, (**C**) green lines represent cell areas, and red dots represent the detected viral antigen: Array Scan XTI (ThermoFisher™, USA), magnification ×5.

4.3. Real-Time Imaging of SDAV Cytopathic Effect in Primary Neurons

To determine the cellular growth and morphology of primary neurons infected with SDAV and incubated with VCP inhibitor, the JuLI^{TM}Br Live Cell-system for bright-field analysis (NanoEnTek, Seoul, Republic of Korea) was used [70]. When cultured neurons reached about 90% confluency, cells were infected with undiluted SDAV suspension (10^0), as previously described. Images were captured for 672 h with 10 min intervals. The results were obtained and analyzed using JuLi^{TM}Br PC v1.01. software. Uninfected cells were used as a negative control. All images were captured at ×40 magnification.

4.4. Cell Treatment with VCP-Interfering Inhibitor

Eeyarestatin I (EerI, Sigma-Aldrich®) was used to determine the potential use of VCP by SDAV in the replication cycle. It is a membrane-penetrating substance that preferentially localizes near the endoplasmic reticulum. EerI causes inhibition of the ERAD pathway through an irreversible interaction with VCP. Cell viability after EerI treatment was detected by XTT assay (data not shown) (The Cell Proliferation Kit II (XTT), Roche, Basel, Switzerland). EerI concentrations were chosen by XTT assay results and literature data [63,71,72]. The potential use of VCP by SDAV was investigated by treating primary neuron cultures with EerI before and after virus infection (pre-incubation and post-incubation, respectively). All analyses of EerI-treated cultures were performed in triplicates in a 96-well plate and Nunc™ systems. Positive controls were infected cells not treated with EerI. Noninfected cells were negative control. Pre-incubation consisted of adding EerI diluted in culture medium (5 µM/mL and 25 µM/mL, 1 h, 5% CO_2, 37 °C) to uninfected primary neuron cultures, aspiring the EerI media, adding the SDAV to the cell culture (1 h, 5% CO_2, 37 °C), and replacing inoculum with fresh medium. Post-incubation, on the other hand, consisted of infecting the primary neuron culture with the SDAV (1 h, 5% CO_2, 37 °C), washing of the SDAV, and adding EerI in growth medium (5 µM/mL and 25 µM/mL, 24 h, 5% CO_2, 37 °C). After 24 h, cultures were fixed and prepared for visualization as described above.

4.5. SDAV Titration After EerI Treatment Using High-Content Analysis

To determine the outcome of EerI treatment on viral titer, we repeated viral titration using focus forming assay. Primary neuron cultures were post-incubated with 5 µM/mL or 25 µM/mL EerI and fixed after 24 h of incubation (5% CO_2, 37 °C). As described above, fluorescence staining of N protein and cell nuclei and high-content screening were carried out. To evaluate the efficacy of the employed treatment, the SDAV was initially titrated with the EerI inhibitor at concentrations of 5 µM/mL and 25 µM/mL in a post-incubation system for 24 h p.i. Subsequently, prior to analysis, the cell media was collected and utilized for a second titer analysis to ascertain whether EerI influenced SDAV egress from neurons. A schematic representation is shown in Figure 9A, which was made with Biorender [73].

4.6. Immunofluorescence Staining for Morphology Analysis of SDAV Infected Neurons

The immunofluorescence method was used to visualize cell structures and viral antigens. After pre-incubation and post-incubation with 5 μM/mL or 25 μM/mL EerI, primary neuronal cell cultures were washed twice in PBS (Sigma-Aldrich, Darmstadt, Germany), then fixed in 4% PFA (Thermo Fisher, Waltham, MA, USA) for 10 min at 24 h p.i. After fixation, the cells were washed twice with PBS solution and incubated with 1% Tween/PBS solution for 5 min at room temperature. Cells were then washed twice with PBS solution. After blocking with 1% BSA/PBS for 15 min, the cells were incubated with a 1:250 dilution ratio of primary antibody specific for SARS-CoV-2 Nucleoprotein (N) (Mouse mAb) (Thermo Fisher Scientific, Waltham, MA, USA) overnight at 4 °C. The unbound antibody was removed by washing with PBS three times. Then, the Goat anti-Mouse IgG (H + L) Highly Cross-Adsorbed Secondary Antibody, Alexa Fluor 488 (Thermo Fisher Scientific, USA), was used at a 1:1000 dilution ratio for 1h at room temperature. VCP was visualized by incubation with rabbit anti-VCP primary monoclonal antibody (ThermoFisher™) (1:500 dilution, overnight, 4 °C) and Texas Red™-X secondary goat anti-rabbit IgG antibody (ThermoFisher™) (dilution 1:500, 1 h, RT). To stain the cell membranes, cells were incubated with wheat germ agglutinin (WGA) conjugate, AlexaFluor™ 647 (ThermoFisher™) (10 μg/mL, 1 h, RT). Additionally, cell nuclei were stained with Hoechst 33,258 (Thermo Fisher, Waltham, MA, USA) for 2 min, RT. Afterward, cover slips were mounted on microscope slides using ProLong Gold Antifade Mounting Medium (Thermo Fisher, Waltham, MA, USA). Images were acquired in a confocal microscope (Fluoview FV10i, Olympus, Japan), saved in 24-bit .tiff format, and analyzed using FV10i v4.1 software (Olympus), ImageJ2 (NIH Image, v1.53q, Bethesda, MD, USA), and Adobe Photoshop CS6 software (Adobe Systems Incorporated, v23.4.1, San Jose, CA, USA). During data processing to improve visualization of the structures, the fluorescence signals were changed to the following colours: Texas Red™—blue; AlexaFluor™ 647—purple; Hoechst™—yellow.

4.7. High-Content Imaging System for Quantitative SDAV Nucleoprotein and Valosin-Containing Protein (VCP) Detection

The high-content screening was performed on cells in the 96-well plate with two methods. First, screening was performed without treatment (uninfected and 0, 0.30, 1, 2, 4, 18, 24 h p.i.) to assess the level of proteins. Second, it was performed with pre-treatment and post-treatment (5 μM/mL or 25 μM/mL EerI, 24 h p.i.) in order to check the VCP involvement in SDAV replication. Fluorescent staining was carried out as described in the confocal imaging section.

The images were acquired using the Operetta CLS high-content imaging system (Revvity™, Waltham, MA, USA), equipped with an ×40 water objective lens. The exposure time for each channel was customized to optimize the signal-to-noise ratio, ensuring clear and accurate data capture. Illumination intensity was adjusted for optimal fluorescent signal capture, and at least 400 cells were analyzed per condition, providing a robust dataset for downstream analysis.

The analysis of cellular images was conducted using the Harmony 4.9 software (Revvity™, Waltham, MA, USA). This process involved a sequence of segmentation and feature extraction steps designed to quantify specific protein distributions within cells. The Hoechst channel was selected, and Harmony's built-in algorithm was used to perform automatic nuclei segmentation. Parameters were adjusted to accurately detect the nuclei, ensuring that objects of irregular shapes were recognized correctly. WGA conjugated to AlexaFluor™ 647 (ThermoFisher™) was used to stain the cell membrane and cytoplasm. Alexa647 channel was employed to detect cytoplasmic regions surrounding the nuclei. Noise reduction techniques, such as Gaussian filtering, were applied to enhance signal-to-background contrast. Using Harmony's segmentation algorithms, the cytoplasm was segmented by expanding outward from the previously segmented nuclei. Careful parameter tuning was conducted to prevent cytoplasmic overlap between adjacent cells. Objects touching the image boundary were excluded from further analysis to avoid artifacts from

incomplete cell structures. Spot detection algorithms in Harmony were utilized to locate distinct fluorescent spots corresponding to VCP and SDAV proteins. Parameters such as spot size, intensity threshold, and minimum distance between spots were optimized for precise detection. The total number of spots per cell was calculated.

4.8. VCP Expression Analysis by Western Blot

Murine primary neuron cells were cultured and treated accordingly (5 µM/mL or 25 µM/mL EerI post- and pre-treated for 24 h p.i.). Cell lysates were prepared with cell lysis buffer (N-PER™ Neuronal Protein Extraction Reagent, Thermo Scientific™, USA) and protease inhibitor (Halt™ Protease Inhibitor Cocktail, Thermo Scientific™, USA). Protein content was measured using Micro BCA™ Protein Assay Kit (Thermo Scientific™, USA), and protein samples were prepared using an equal amount of protein, 4× Laemmli Sample Buffer (Bio-Rad, USA) and 2-mercaptoethanol. Protein samples were heated at 95 °C for 10 min and equally loaded and separated on 12% polyacrylamide gels by electrophoresis (Mini-PROTEAN Tetra Cell, Bio-Rad, USA) in the following conditions: 80 V for 15 min, followed by 120 V for 85 min and then transferred to polyvinylidene difluoride (PVDF) 0.45 µm membranes (Immobilon® P Membrane, Merck Millipore, Burlington, MA, USA) using wet-blotting system (Bio-Rad, USA) and 330 mA for 1h in cooling conditions. Membranes were blocked after transfer for 30 min in 5% skim milk in TBS-Tween 20 (TBS-T) buffer at room temperature and incubated overnight with primary antibodies at 4 °C. The following day, membranes were washed 5 times for 5 min in TBS-T buffer and placed in secondary antibodies conjugated with horseradish peroxidase for 1 h at room temperature. After incubation, membranes were washed again using the same protocol, and proteins were visualized with an ECL kit (Clarity™, Bio-Rad, USA) using ChemiDoc Touch Imaging System (Bio-Rad, USA) using signal accumulation mode (SAM) with the same settings for each membrane (Bio-Rad, USA). Densitometry was performed using images acquired after the exact same time of exposure in Image Lab™ Software v6.0.1 (Bio-Rad, USA). Each target protein band intensity was compared to the intensity of the GAPDH protein band (loading control). Expression is presented as a relative protein expression (target protein/loading control). All antibodies used were diluted in blocking buffer, and the following dilutions were used: anti-VCP (1:1000, #MA3-004, Invitrogen, ThermoFisher, USA), anti-GAPDH (1:5000, #MA5-15738, Invitrogen, ThermoFisher, USA). Secondary HRP-conjugated antibodies were used, including anti-mouse (1:5000, #31450, Invitrogen, ThermoFisher, USA). Antibodies were freshly prepared and used once.

4.9. Statistical Analysis

The results were statistically evaluated by one-way or two-way analysis of variation (ANOVA) using Tukey's multiple comparisons test or multiple unpaired t-test using threshold *p*-value with the Šídák–Bonerroni multiple comparisons correction method. For Western blot analysis, the non-parametric Friedman test, followed by a post hoc group comparison test, was used. All experiments were performed at least in triplicate. These analyses were performed using GraphPad Prism™ version 9.4.0 (453) for macOS software (GraphPad Software Inc., San Diego, CA, USA). Statistical differences were interpreted as significant at $p \leq 0.05$, highly significant at $p \leq 0.01$, extremely significant at $p \leq 0.001$, and not significant at $p > 0.05$.

5. Conclusions

In addition to its multiple roles in regulating cellular homeostasis, particularly in nervous system cells, the ATPase valosin-containing protein is an important host factor in viral infections. It remains unclear in which critical replication points VCP is used by SDAV. However, the results of our study have provided insight into the important role of the VCP in the assembly and release of progeny virion. We have shown for the first time that SDAV infection in neurons enhances VCP expression, which explains the use of ATPase in the viral replication cycle. In addition, using an EerI inhibitor that targets the role of

VCP in the ERAD system results in an apparent reduction in viral titer. These changes are particularly evident in the second round of titers replicated from the cell medium after the first infection cycle. What is more, based on confocal image analysis, we can conclude that EerI influences the SDAV capability of viral protein assembly and egress from the cell by "trapping" the virions in the submembrane area.

Author Contributions: Conceptualization, M.B. and J.C.; validation, W.D.K.; methodology, M.B. and J.C.; formal analysis, M.B., J.W. and A.P.; investigation, M.B, W.D.K., M.C., J.W., H.G. and A.P.; resources, M.B., M.C., H.G., J.W., A.P. and M.K.; data curation, M.C.; writing—original draft preparation, M.B. and W.D.K.; writing—review and editing, J.C., M.C., H.G., J.W. and A.P.; visualization, M.B.; supervision, J.C.; project administration, M.B.; funding acquisition, M.B. All authors have read and agreed to the published version of the manuscript.

Funding: This research was funded by the National Science Centre (NCN) Poland, grant number 2021/41/N/NZ6/04383. The article APC was financed by the Science Development Foundation—Warsaw University of Life Sciences. The performance of analyses on Operetta CLS (Revvity™, Waltham, MA, USA) was possible by funding from National Science Centre (NCN) Poland, grant number 2020/39/B/NZ2/03259.

Institutional Review Board Statement: Not applicable.

Informed Consent Statement: Not applicable.

Data Availability Statement: The data used to support the findings of this study are included in the article.

Acknowledgments: Thanks to Susan Compton, Chief of Molecular and Serological Diagnostics Comparative Medicine at Yale University School of Medicine for providing the viral material.

Conflicts of Interest: The authors declare that there are no conflicts of interest regarding the publication of this paper.

References

1. Decaro, N.; Lorusso, A. Novel human coronavirus (SARS-CoV-2): A lesson from animal coronaviruses. *Vet. Microbiol.* **2020**, *244*, 108693. [CrossRef] [PubMed]
2. Lau, S.K.; Woo, P.C.; Li, K.S.; Tsang, A.K.; Fan, R.Y.; Luk, H.K.; Cai, J.P.; Chan, K.H.; Zheng, B.J.; Wang, M.; et al. Discovery of a novel coronavirus, China Rattus coronavirus HKU24, from Norway rats supports the murine origin of Betacoronavirus 1 and has implications for the ancestor of Betacoronavirus lineage A. *J. Virol.* **2015**, *89*, 3076–3092. [CrossRef]
3. Bartak, M.; Słońska, A.; Bańbura, M.W.; Cymerys, J. SDAV, the Rat Coronavirus-How Much Do We Know about It in the Light of Potential Zoonoses. *Viruses* **2021**, *13*, 1995. [CrossRef]
4. Bonilauri, P.; Rugna, G. Animal Coronaviruses and SARS-CoV-2 in Animals, What Do We Actually Know? *Life* **2021**, *11*, 123. [CrossRef]
5. Bhatt, P.N.; Percy, D.H.; Jonas, A.M. Characterization of the virus of sialodacryoadenitis of rats: A member of the coronavirus group. *J. Inf. Dis.* **1972**, *126*, 123–130. [CrossRef]
6. Parker, J.C.; Cross, S.S.; Rowe, W.P. Rat coronavirus (RCV): A prevalent, naturally occurring pneumotropic virus of rats. *Arch. Ges. Vir.* **1970**, *31*, 293–302. [CrossRef]
7. Utsumi, K.; Ishikawa, T.; Maeda, T.; Shimizu, S.; Tatsumi, H.; Fujiwara, K. Infectious sialodacryoadenitis and rat breeding. *Lab Anim.* **1980**, *14*, 303–307. [CrossRef]
8. Fauquet, C.M.; Fargette, D. International Committee on Taxonomy of Viruses and the 3142 unassigned species. *Virol. J.* **2005**, *2*, 64. [CrossRef]
9. Kojima, A.; Fujinami, F.; Doi, K.; Yasoshima, A.; Okaniwa, A. Isolation and properties of sialodacryoadenitis virus of rats. *Exp. Anim.* **1980**, *29*, 409–418. [CrossRef]
10. Percy, D.H.; Lynch, J.A.; Descôteaux, J.P. Central nervous system lesions in suckling mice and rats inoculated intranasally with sialodacryoadenitis virus. *Vet. Pathol.* **1986**, *23*, 42–49. [CrossRef]
11. Ahlstedt, B.A.; Ganji, R.; Raman, M. The functional importance of VCP to maintaining cellular protein homeostasis. *Biochem. Soc. Trans.* **2022**, *50*, 1457–1469. [CrossRef] [PubMed]
12. Meyer, H.; Weihl, C.C. The VCP/p97 system at a glance: Connecting cellular function to disease pathogenesis. *J. Cell Sci.* **2014**, *127*, 3877–3883. [CrossRef] [PubMed]
13. Erzberger, J.P.; Berger, J.M. Evolutionary relationships and structural mechanisms of AAA+ proteins. *Annu. Rev. Biophys. Biomol. Struct.* **2006**, *35*, 93–114. [CrossRef]

14. Ye, Y.; Tang, W.K.; Zhang, T.; Xia, D.A. Mighty "Protein Extractor" of the Cell: Structure and Function of the p97/CDC48 ATPase. *Front. Mol. Biosci.* **2017**, *4*, 39. [CrossRef]
15. Calabrese, G.; Molzahn, C.; Mayor, T. Protein interaction networks in neurodegenerative diseases: From physiological function to aggregation. *J. Biol. Chem.* **2022**, *298*, 102062. [CrossRef]
16. Mee Hayes, E.; Sirvio, L.; Ye, Y. A Potential Mechanism or Targeting Aggregates With Proteasomes and Disaggregases in Liquid Droplets. *Front. Aging Neurosci.* **2022**, *14*, 854380. [CrossRef]
17. Buchan, J.R.; Kolaitis, R.M.; Taylor, J.P.; Parker, R. Eukaryotic Stress Granules Are Cleared by Autophagy and Cdc48/VCP Function. *Cell* **2013**, *153*, 1461–1474. [CrossRef]
18. Papadopoulos, C.; Kravic, B.; Meyer, H. Repair or Lysophagy: Dealing with Damaged Lysosomes. *J. Mol. Biol.* **2020**, *432*, 231–239. [CrossRef]
19. Bhattacharya, A.; Qi, L. ER-associated degradation in health and disease—From substrate to organism. *J. Cell Sci.* **2019**, *132*, jcs232850. [CrossRef]
20. Joazeiro, C.A.P. Mechanisms and functions of ribosome-associated protein quality control. *Nat. Rev. Mol. Cell Biol.* **2019**, *20*, 368–383. [CrossRef]
21. Escobar-Henriques, M.; Anton, V. Mitochondrial Surveillance by Cdc48/ p97: MAD vs. Membrane Fusion. *Int. J. Mol. Sci.* **2020**, *21*, 6841. [CrossRef] [PubMed]
22. Kilgas, S.; Ramadan, K. Inhibitors of the ATPase p97/VCP: From basic research to clinical applications. *Cell Chem. Biol.* **2023**, *30*, 3–21. [CrossRef] [PubMed]
23. Chu, S.; Xie, X.; Payan, C.; Stochaj, U. Valosin containing protein (VCP): Initiator, modifier, and potential drug target for neurodegenerative diseases. *Mol. Neurodegeneration.* **2023**, *18*, 52. [CrossRef] [PubMed]
24. Szczęśniak, P.P.; Heidelberger, J.B.; Serve, H.; Beli, P.; Wagner, S.A. VCP inhibition induces an unfolded protein response and apoptosis in human acute myeloid leukemia cells. *PLoS ONE* **2022**, *17*, e0266478. [CrossRef] [PubMed]
25. Zhang, X.; Jiang, L.; Li, Y.; Feng, Q.; Sun, X.; Wang, Y.; Zhao, M. Discovery of novel benzylquinazoline molecules as p97/VCP inhibitors. *Front. Pharmacol.* **2023**, *14*, 1209060. [CrossRef]
26. Wei, R.; Cao, Y.; Wu, H.; Liu, X.; Jiang, M.; Luo, X.; Deng, Z.; Wang, Z.; Ke, M.; Zhu, Y.; et al. Inhibition of VCP modulates NF-κB signaling pathway to suppress multiple myeloma cell proliferation and osteoclast differentiation. *Aging* **2023**, *15*, 8220–8236. [CrossRef]
27. Valle, C.W.; Min, T.; Bodas, M.; Mazur, S.; Begum, S.; Tang, D.; Vij, N. Critical Role of VCP/p97 in the Pathogenesis and Progression of Non-Small Cell Lung Carcinoma. *PLoS ONE* **2011**, *6*, e29073. [CrossRef]
28. Han, D.Y.; Di, X.J.; Fu, Y.L.; Mu, T.W. Combining valosin-containing protein (VCP) inhibition and suberanilohydroxamic acid (SAHA) treatment additively enhances the folding, trafficking, and function of epilepsy-associated γ-aminobutyric acid, type A (GABAA) receptors. *J. Biol. Chem.* **2015**, *290*, 325–337. [CrossRef]
29. Das, P.; Dudley, J.P. How Viruses Use the VCP/p97 ATPase Molecular Machine. *Viruses* **2021**, *13*, 1881. [CrossRef]
30. Lin, Y.T.; Prendergast, J.; Grey, F. The Host Ubiquitin-Dependent Segregase VCP/P97 Is Required for the Onset of Human Cytomegalovirus Replication. *PLoS. Pathog.* **2017**, *13*, e1006329. [CrossRef]
31. Carissimo, G.; Chan, Y.H.; Utt, A.; Chua, T.K.; Bakar, F.A.; Merits, A.; Ng, L.F.P. VCP/P97 Is a Proviral Host Factor for Replication of Chikungunya Virus and Other Alphaviruses. *Front. Microbiol.* **2019**, *10*, 2236. [CrossRef] [PubMed]
32. Arita, M.; Wakita, T.; Shimizu, H. Valosin-Containing Protein (VCP/P97) Is Required for Poliovirus Replication and Is Involved in Cellular Protein Secretion Pathway in Poliovirus Infection. *J. Virol.* **2012**, *86*, 5541–5553. [CrossRef] [PubMed]
33. Pleasure, I.; Black, M.; Keen, J. Valosin-containing protein, VCP, is a ubiquitous clathrin-binding protein. *Nature* **1993**, *365*, 459–462. [CrossRef] [PubMed]
34. Roy, L.; Bergeron, J.J.; Lavoie, C.; Hendriks, R.; Gushue, J.; Fazel, A.; Pelletier, A.; Morré, D.J.; Subramaniam, V.N.; Hong, W.; et al. Role of p97 and syntaxin 5 in the assembly of transitional endoplasmic reticulum. *Mol. Biol. Cell.* **2000**, *11*, 2529–2542. [CrossRef]
35. Ramanathan, H.N.; Ye, Y. The p97 ATPase associates with EEA1 to regulate the size of early endosomes. *Cell Res.* **2012**, *22*, 346–359. [CrossRef]
36. Chu, J.J.; Ng, M.L. Interaction of West Nile virus with alpha v beta 3 integrin mediates virus entry into cells. *J. Biol. Chem.* **2004**, *279*, 54533–54541. [CrossRef]
37. Chu, J.J.H.; Ng, M.L. Infectious Entry of West Nile Virus Occurs through a Clathrin-Mediated Endocytic Pathway. *J. Virol.* **2004**, *78*, 10543–10555. [CrossRef]
38. Xu, Z.; Waeckerlin, R.; Urbanowski, M.D.; van Marle, G.; Hobman, T.C. West Nile virus infection causes endocytosis of a specific subset of tight junction membrane proteins. *PLoS ONE* **2012**, *7*, e37886. [CrossRef]
39. Ramanathan, H.N.; Zhang, S.; Douam, F.; Mar, K.B.; Chang, J.; Yang, P.L.; Schoggins, J.W.; Ploss, A.; Lindenbach, B.D. A Sensitive Yellow Fever Virus Entry Reporter Identifies Valosin-Containing Protein (VCP/p97) as an Essential Host Factor for Flavivirus Uncoating. *mBio* **2020**, *11*, e00467-20. [CrossRef]
40. Liu, D.X.; Liang, J.Q.; Fung, T.S. Human Coronavirus-229E, -OC43, -NL63, and -HKU1 (Coronaviridae). *Enc. Virol.* **2021**, 428–440. [CrossRef]
41. Wong, H.H.; Kumar, P.; Tay, F.P.; Moreau, D.; Liu, D.X.; Bard, F. Genome-Wide Screen Reveals Valosin-Containing Protein Requirement for Coronavirus Exit from Endosomes. *J. Virol.* **2015**, *8*, 11116–11128. [CrossRef] [PubMed]

42. Anton, A.; Mazeaud, C.; Freppel, W.; Gilbert, C.; Tremblay, N.; Sow, A.A.; Roy, M.; Rodrigue-Gervais, I.G.; Chatel-Chaix, L. Valosin-containing protein ATPase activity regulates the morphogenesis of Zika virus replication organelles and virus-induced cell death. *Cell. Microbiol.* **2021**, *23*, e13302. [CrossRef] [PubMed]
43. Cheng, K.W.; Li, S.; Wang, F.; Ruiz-Lopez, N.M.; Houerbi, N.; Chou, T.F. Impacts of p97 on Proteome Changes in Human Cells during Coronaviral Replication. *Cells* **2021**, *10*, 2953. [CrossRef] [PubMed]
44. Bojkova, D.; Klann, K.; Koch, B.; Widera, M.; Krause, D.; Ciesek, S.; Cinatl, J.; Münch, C. Proteomics of SARS-CoV-2-infected host cells reveals therapy targets. *Nature* **2020**, *583*, 469–472. [CrossRef] [PubMed]
45. Brahms, A.; Mudhasani, R.; Pinkham, C.; Kota, K.; Nasar, F.; Zamani, R.; Bavari, S.; Kehn-Hall, K. Sorafenib Impedes Rift Valley Fever Virus Egress by Inhibiting Valosin-Containing Protein Function in the Cellular Secretory Pathway. *J. Virol.* **2017**, *91*, e00968-17. [CrossRef]
46. Wu, K.X.; Phuektes, P.; Kumar, P.; Goh, G.Y.; Moreau, D.; Chow, V.T.; Chu, J.J.H. Human genome-wide RNAi screen reveals host factors required for enterovirus 71 replication. *Nat. Commun.* **2016**, *7*, 13150. [CrossRef]
47. Wang, T.; Wang, B.; Huang, H.; Zhang, C.; Zhu, Y.; Pei, B.; Cheng, C.; Sun, L.; Wang, J.; Jin, Q.; et al. Enterovirus 71 protease 2Apro and 3Cpro differentially inhibit the cellular endoplasmic reticulum-associated degradation (ERAD) pathway via distinct mechanisms, nd enterovirus 71 hijacks ERAD component p97 to promote its replication. *PLoS Pathog.* **2017**, *13*, e1006674. [CrossRef]
48. Yi, Z.; Fang, C.; Zou, J.; Xu, J.; Song, W.; Du, X.; Pan, T.; Lu, H.; Yuan, Z. Affinity purification of the hepatitis C virus replicase identifies valosin-containing protein, a member of the ATPases associated with diverse cellular activities family, as an active virus replication modulator. *J. Virol.* **2016**, *90*, 9953–9966. [CrossRef]
49. Phongphaew, W.; Kobayashi, S.; Sasaki, M.; Carr, M.; Hall, W.W.; Orba, Y.; Sawa, H. Valosin-containing protein (VCP/p97) plays a role in the replication of West Nile virus. *Vir. Res.* **2017**, *228*, 114–123. [CrossRef]
50. Yi, Z.; Yuan, Z. Aggregation of a hepatitis C virus replicase module induced by ablation of p97/VCP. *J. Gen. Virol.* **2017**, *98*, 1667–1678. [CrossRef]
51. Percy, D.; Bond, S.; MacInnes, J. Replication of sialodacryoadenitis virus in mouse L-2 cells. *Arch. Virol.* **1989**, *104*, 323–333. [CrossRef] [PubMed]
52. Hirano, N.; Takamaru, H.; Ono, K.; Murakami, T.; Fujiwara, K. Replication of sialodacryoadenitis virus of rat in LBC cell culture. Brief report. *Arch. Virol.* **1986**, *88*, 121–125. [CrossRef] [PubMed]
53. Hirano, N.; Suzuki, Y.; Ono, K.; Murakami, T.; Fujiwara, K. Growth of rat sialodacryoadenitis viruses in LBC cell culture. *Jpn. J. Vet. Sci.* **1986**, *48*, 193–195. [CrossRef]
54. Gaertner, D.J.; Winograd, D.F.; Compton, S.R.; Paturzo, F.X.; Smith, A.L. Development and optimization of plaque assays for rat coronaviruses. *J. Virol. Methods* **1993**, *43*, 53–64. [CrossRef]
55. Hirano, N. Plaque assay and propagation in rat cell line LBC cells of rat coronavirus and 5 strains of sialodacryoadenitis virus. *J. Vet. Med. Ser. B* **1990**, *37*, 91–96. [CrossRef]
56. Hu, W.; Yen, Y.T.; Singh, S.; Kao, C.L.; Wu-Hsieh, B.A. SARS-CoV regulates immune function-related gene expression in human monocytic cells. *Viral Immunol.* **2012**, *25*, 277–288. [CrossRef]
57. Movaqar, A.; Yaghoubi, A.; Rezaee, S.R.; Jamehdar, S.A.; Soleimanpour, S. Coronaviruses construct an interconnection way with ERAD and autophagy. *Future Microbiol.* **2021**, *16*, 1135–1151. [CrossRef]
58. Noack, J.; Bernasconi, R.; Molinari, M. How viruses hijack the ERAD tuning machinery. *J. Virol.* **2014**, *88*, 10272–10275. [CrossRef]
59. Reggiori, F.; Monastyrska, I.; Verheije, M.H.; Calì, T.; Ulasli, M.; Bianchi, S.; Bernasconi, R.; de Haan, C.A.; Molinari, M. Coronaviruses Hijack the LC3-I-positive EDEMosomes, ER-derived vesicles exporting short-lived ERAD regulators, for replication. *Cell Host Microbe* **2010**, *7*, 500–508. [CrossRef]
60. Reggiori, F.; de Haan, C.A.; Molinari, M. Unconventional use of LC3 by coronaviruses through the alleged subversion of the ERAD tuning pathway. *Viruses* **2011**, *3*, 1610–1623. [CrossRef]
61. Wang, Q.; Shinkre, B.A.; Lee, J.G.; Weniger, M.A.; Liu, Y.; Chen, W.; Wiestner, A.; Trenkle, W.C.; Ye, Y. The ERAD inhibitor Eeyarestatin I is a bifunctional compound with a membrane-binding domain and a p97/VCP inhibitory group. *PLoS ONE* **2010**, *5*, 15479. [CrossRef] [PubMed]
62. Tabata, K.; Arakawa, M.; Ishida, K.; Kobayashi, M.; Nara, A.; Sugimoto, T.; Okada, T.; Mori, K.; Morita, E. Endoplasmic Reticulum-Associated Degradation Controls Virus Protein Homeostasis, Which Is Required for Flavivirus Propagation. *J. Virol.* **2021**, *95*, 0223420. [CrossRef]
63. Rodrigo, I.; Ballesta, C.; Nunes, E.B.; Pérez, P.; García-Arriaza, J.; Arias, A. Eeyarestatin I, an inhibitor of the valosin-containing protein, exhibits potent virucidal activity against the flaviviruses. *Antivir. Res.* **2022**, *207*, 105416. [CrossRef]
64. Cymerys, J.; Dzieciątkowski, T.; Słońska, A.; Bierła, J.; Tucholska, A.; Chmielewska, A.; Bańbura, M. Equine herpesvirus type 1(EHV-1) replication in primary murine neurons culture. *Pol. J. Vet. Sci.* **2010**, *13*, 701–708. [CrossRef]
65. Cymerys, J.; Słońska, A.; Skwarska, J.; Bańbura, M.W. Function of myosin during entry and egress of equid herpesvirus type 1 in primary murine neurons. *Acta Virol.* **2016**, *60*, 410–416. [CrossRef]
66. Bihun, C.G.; Percy, D.H. Coronavirus infections in the laboratory rat: Degree of cross protection following immunization with a heterologous strain. *Can. J. Vet. Res.* **1994**, *58*, 224–229.
67. Zeiss, C.J.; Asher, J.L.; Vander Wyk, B.; Allore, H.G.; Compton, S.R. Modeling SARS-CoV-2 propagation using rat coronavirus-associated shedding and transmission. *PLoS ONE* **2021**, *16*, 0260038. [CrossRef]

68. Rak, A.; Matyushenko, V.; Prokopenko, P.; Kostromitina, A.; Polyakov, D.; Sokolov, A.; Rudenko, L.; Isakova-Sivak, I. A novel immunofluorescent test system for SARS-CoV-2 detection in infected cells. *PLoS ONE* **2024**, *19*, 0304534. [CrossRef]
69. Amarilla, A.A.; Modhiran, N.; Setoh, Y.X.; Peng, N.Y.G.; Sng, J.D.J.; Liang, B.; McMillan, C.L.D.; Freney, M.E.; Cheung, S.T.M.; Chappell, K.J.; et al. An Optimized High-Throughput Immuno-Plaque Assay for SARS-CoV-2. *Front. Microbiol.* **2021**, *12*, 625136. [CrossRef]
70. NanoEnTek Inc., Korea. 2015. Available online: http://www.nanoentek.com (accessed on 8 August 2024).
71. Cross, B.C.; McKibbin, C.; Callan, A.C.; Roboti, P.; Piacenti, M.; Rabu, C.; Wilson, C.M.; Whitehead, R.; Flitsch, S.L.; Pool, M.R.; et al. Eeyarestatin I inhibits Sec61-mediated protein translocation at the endoplasmic reticulum. *J. Cell Sci.* **2009**, *122*, 4393–4400. [CrossRef]
72. Wang, Q.; Li, L.; Ye, Y. Inhibition of p97-dependent protein degradation by Eeyarestatin I. *J. Biol. Chem.* **2008**, *283*, 7445–7454. [CrossRef] [PubMed]
73. Bartak, M. Created in BioRender. 2024. Available online: http://BioRender.com/g65u531 (accessed on 28 July 2024).

SZKOŁA GŁÓWNA
GOSPODARSTWA
WIEJSKIEGO

Warszawa, 20.05.2025

mgr inż. Michalina Bartak
Zakład Mikrobiologii
Katedra Nauk Przedklinicznych
Instytut Medycyny Weterynaryjnej
ul. Ciszewskiego 8, 02-786 Warszawa
michalina_bartak@sggw.edu.pl

Rada Dyscypliny Weterynaria

Szkoły Głównej Gospodarstwa Wiejskiego w Warszawie

Oświadczenie o współautorstwie

Niniejszym oświadczam, że w pracy:

Bartak, M., Krahel, W. D., Chodkowski, M., Grel, H., Walczak, J., Pallepati, A., Komorowski, M., & Cymerys, J. (2024). ATPase Valosin-Containing Protein (VCP) Is Involved During the Replication and Egress of Sialodacryoadenitis Virus (SDAV) in Neurons. *International journal of molecular sciences*, *25*(21), 11633.

Mój indywidualny udział w jej powstaniu polegał na opracowaniu koncepcji artykułu, zaprojektowaniu i przeprowadzeniu eksperymentów, analizie danych, wizualizacji danych, opracowaniu manuskryptu.
Indywidualny wkład pracy w publikację wynosił 65%.

Podpis

SZKOŁA GŁÓWNA
GOSPODARSTWA
WIEJSKIEGO

Warszawa, 20.05.2025

Mgr inż. Weronika Daria Krahel
Zakład Mikrobiologii
Katedra Nauk Przedklinicznych
Instytut Medycyny Weterynaryjnej
ul. Ciszewskiego 8, 02-786 Warszawa
weronika_krahel@sggw.edu.pl

Rada Dyscypliny Weterynaria

Szkoły Głównej Gospodarstwa Wiejskiego w Warszawie

Oświadczenie o współautorstwie

Niniejszym oświadczam, że w pracy:

Bartak, M., Krahel, W. D., Chodkowski, M., Grel, H., Walczak, J., Pallepati, A., Komorowski, M., & Cymerys, J. (2024). ATPase Valosin-Containing Protein (VCP) Is Involved During the Replication and Egress of Sialodacryoadenitis Virus (SDAV) in Neurons. *International journal of molecular sciences*, *25*(21), 11633.

Mój indywidualny udział w jej powstaniu polegał na pomocy w przeprowadzeniu części eksperymentów oraz krytycznej edycji manuskryptu.
Indywidualny wkład pracy w publikację wynosił 5%.

Weronika Daria Krahel
.....
Podpis

SZKOŁA GŁÓWNA
GOSPODARSTWA
WIEJSKIEGO

Warszawa, 20.05.2025

Dr Marcin Chodkowski
Zakład Mikrobiologii Medycznej i Środowiskowej
Wojskowy Instytut Higieny i Epidemiologii
ul. Kozielska 4, 01-063 Warszawa
marcin.chodkowski@wihe.pl

Rada Dyscypliny Weterynaria

Szkoły Głównej Gospodarstwa Wiejskiego w Warszawie

Oświadczenie o współautorstwie

Niniejszym oświadczam, że w pracy:

Bartak, M., Krahel, W. D., Chodkowski, M., Grel, H., Walczak, J., Pallepati, A., Komorowski, M., & Cymerys, J. (2024). ATPase Valosin-Containing Protein (VCP) Is Involved During the Replication and Egress of Sialodacryoadenitis Virus (SDAV) in Neurons. *International journal of molecular sciences*, *25*(21), 11633.

Mój indywidualny udział w jej powstaniu polegał na pomocy w przeprowadzeniu części eksperymentów, użyczeniu sprzętu badawczego oraz krytycznej edycji manuskryptu.
Indywidualny wkład pracy w publikację wynosił 5%.

Podpis

SZKOŁA GŁÓWNA
GOSPODARSTWA
WIEJSKIEGO

Warszawa, 28.05.2025

Mgr inż. Hubert Grel
Katedra Fizyki i Biofizyki
Instytut Biologii
ul. Nowoursynowska 159, 02-776 Warszawa
hubert_grel@sggw.edu.pl

Rada Dyscypliny Weterynaria

Szkoły Głównej Gospodarstwa
Wiejskiego w Warszawie

Oświadczenie o współautorstwie

Niniejszym oświadczam, że w pracy:

Bartak, M., Krahel, W. D., Chodkowski, M., Grel, H., Walczak, J., Pallepati, A., Komorowski, M., & Cymerys, J. (2024). ATPase Valosin-Containing Protein (VCP) Is Involved During the Replication and Egress of Sialodacryoadenitis Virus (SDAV) in Neurons. *International journal of molecular sciences*, *25*(21), 11633.

Mój indywidualny udział w jej powstaniu polegał na pomocy w przeprowadzeniu części eksperymentów oraz analizy danych.
Indywidualny wkład pracy w publikację wynosił 5%.

Podpisane elektronicznie przez Hubert Grzegorz Grel (Certyfikat kwalifikowany) w dniu 2025-05-28.

.....

Podpis

SZKOŁA GŁÓWNA
GOSPODARSTWA
WIEJSKIEGO

Warszawa, 20.05.2025

Dr hab. Joanna Cymerys-Bulenda prof. SGGW
Zakład Mikrobiologii
Katedra Nauk Przedklinicznych
Instytut Medycyny Weterynaryjnej
ul. Ciszewskiego 8, 02-786 Warszawa
joanna_cymerys@sggw.edu.pl

Rada Dyscypliny Weterynaria

Szkoły Głównej Gospodarstwa
Wiejskiego w Warszawie

Oświadczenie o współautorstwie

Niniejszym oświadczam, że w pracy:

Bartak, M., Krahel, W. D., Chodkowski, M., Grel, H., Walczak, J., Pallepati, A., Komorowski, M., & Cymerys, J. (2024). ATPase Valosin-Containing Protein (VCP) Is Involved During the Replication and Egress of Sialodacryoadenitis Virus (SDAV) in Neurons. *International journal of molecular sciences*, *25*(21), 11633.

Mój indywidualny udział w jej powstaniu polegał na pomocy w opiece nad projektem, zaprojektowaniu części eksperymentów, analizie danych, koncepcji artykułu oraz krytycznej edycji manuskryptu.
Indywidualny wkład pracy w publikację wynosił 10%.

Joanna Cymerys-Bulenda

Podpis

cells

MDPI

Article

Cytokine Profile Analysis During Sialodacryoadenitis Virus and Mouse Hepatitis Virus JHM Strain Infection in Primary Mixed Microglia and Astrocyte Culture—Preliminary Research

Michalina Bartak [1,*], Weronika D. Krahel [1], Karolina Gregorczyk-Zboroch [1], Marcin Chodkowski [2], Adrian Valentin Potârniche [3,4], Ewa Długosz [1], Małgorzata Krzyżowska [2] and Joanna Cymerys [1,*]

[1] Division of Microbiology, Department of Preclinical Sciences, Institute of Veterinary Medicine, Warsaw University of Life Sciences, 02-786 Warsaw, Poland; weronika_krahel@sggw.edu.pl (W.D.K.)
[2] Division of Medical and Environmental Microbiology, Military Institute of Hygiene and Epidemiology, 01-063 Warsaw, Poland
[3] Department of Infectious Diseases and Preventive Medicine, Faculty of Veterinary Medicine, University of Agricultural Sciences and Veterinary Medicine Cluj-Napoca, 400372 Cluj-Napoca, Romania
[4] Division of Veterinary Epidemiology and Economics, Institute of Veterinary Medicine, Warsaw University of Life Sciences-SGGW, 02-776 Warsaw, Poland
* Correspondence: michalina_bartak@sggw.edu.pl (M.B.); joanna_cymerys@sggw.edu.pl (J.C.)

Abstract: The Coronaviridae family has again demonstrated the potential for significant neurological complications in humans during the recent pandemic. In patients, these symptoms persist throughout the infection, often lasting for months. The consequences of most of these post-infection symptoms might be linked with abnormal cytokine production and reactive oxygen species (ROS) expression, resulting in neuron damage. We investigated the effect of infection with the Mouse Hepatitis Virus (MHV) JHM strain and Sialodacryoadenitis Virus (SDAV) on a primary microglia and astrocyte culture by analysing ROS production, cytokine and chemokine expression, and cell death during one month post infection. For this purpose, confocal microscopy, flow cytometry, and a high-throughput Luminex ProcartaPlex immunopanel for 48 cytokines and chemokines were utilised. The replication of MHV-JHM and SDAV in microglia and astrocytes has increased the production of pro-inflammatory cytokines and inhibited the production of anti-inflammatory cytokines. The cytokine expression induced by the two viruses differed, as did their detection after infection. SDAV infection resulted in a much broader cytokine response compared to that of MHV-JHM. Both viruses significantly increased ROS levels and induced apoptosis in a small percentage of the cells, but without necrosis.

Keywords: SDAV; MHV-JHM; microglia; astrocytes; ROS; apoptosis; cytokine release syndrome

Academic Editor: Hakan Aldskogius

Received: 28 February 2025
Revised: 14 April 2025
Accepted: 20 April 2025
Published: 25 April 2025

Citation: Bartak, M.; Krahel, W.D.; Gregorczyk-Zboroch, K.; Chodkowski, M.; Potârniche, A.V.; Długosz, E.; Krzyżowska, M.; Cymerys, J. Cytokine Profile Analysis During Sialodacryoadenitis Virus and Mouse Hepatitis Virus JHM Strain Infection in Primary Mixed Microglia and Astrocyte Culture—Preliminary Research. *Cells* **2025**, *14*, 637. https://doi.org/10.3390/cells14090637

1. Introduction

The havoc that the *Coronaviridae* family has once again presented in the form of a historically catastrophic pandemic can still be observed in humans in the form of intractable and critical neurological complications. A multitude of neuropsychiatric symptoms was observed, i.e., impaired cognition, altered attention, reduced consciousness, seizures, and abnormal movements [1]. Patients experience persistent or new symptoms after a 4-week acute phase, often lasting many months [2–4]. These events have led to deterioration in patients with neurodegenerative diseases such as Alzheimer's disease (AD) or Parkinson's

disease (PD) [5,6]. However, information on the connection between infection and amyotrophic lateral sclerosis (ALS), frontotemporal dementia (FTD), or Huntington's disease (HD) is still limited [4,5,7–9]. The rationale for long-term COVID-19 lies in the course of infection and the immune response. The events in glial cells, particularly microglia and astrocytes, are critical to the subsequent development of neuropathy [10–12]. Significant cytokine output is a particular and important consequence of most COVID-19 infections. This phenomenon is referred to as cytokine release syndrome (CRS), a systemic inflammatory response triggered by infections, drugs, antibody-based immunotherapies, chemotherapeutic agents, and graft-vs.-host disease. The description of CRS provides a more balanced presentation of symptoms in patients with elevated cytokine production and clinical manifestations [13,14].

During an emergency state such as a viral infection, crosstalk between microglia cells and central nervous system (CNS) resident cells, including neurons, astrocytes, and oligodendrocytes, comes into action as a specific anti-pathogen barricade. Microglia and astrocytes are especially able to recognise invading pathogens by cellularly sensing pathogen-associated molecular patterns (PAMPs) using pattern recognition receptors (PRRs) [13,15]. In turn, they react by producing an array of inflammatory factors, including cytokines, resulting in oxidative stress, which triggers neuroinflammation [16,17]. The recognition of viruses by microglia via toll-like receptors (TLRs), RIG-I-like receptors (RLRs), and cGAS-STING pathways triggers the rapid production of interleukin 6 (IL-6), tumour nercosis factor alpha (TNF alpha), IL-1 beta, and interferon gamma (IFN gamma), which in turn activate astrocytes through direct viral detection or damage-associated molecular patterns (DAMPs) such as high mobility group box 1 protein (HMGB1) [12,18–21].

Among many cytokines, the most crucial ones in terms of viral infection are IFNs, IL-8, IL-6, IL-1, granulocyte and macrophage colony-stimulating factor (GM-CSF), TNF alpha, IL-18, IL-12, IL-2, and IL-23. Furthermore, these cytokines are involved in the induction of an immune response-type Th1/TCL with the purpose of eliminating infected cells and extracellular viruses, while cytokines such as IL-4, IL-10, IL-13, IL-37, and transforming growth factor beta (TGF beta) modulate the immune response to a Th2 and Th17 phenotype, which produce immunomodulatory and anti-inflammatory actions [22]. Moreover, in the infection course, various cytokines are produced by innate and adaptive cells that can be infected or activated. In filovirus infection, IL-1 beta, IL-5, IL-8, and IL-18, as well as various chemokines like macrophage inflammatory protein-1 alpha (MIP-1 alpha) and MIP-1 beta, monocyte chemoattractant protein 1 (MCP-1), and IFN gamma-inducible protein 10 (IP10), among others, are produced [23]. In influenza virus infection, TNF alpha, IL-1 alpha and beta, and IL-6 and IL-8 are produced [24–26], and hepatitis C virus can promote the expression of IL-6, IL-8, MIP-1 alpha, MIP-1 beta, and IL-1 [27], while rotavirus can induce the production of IFN, IL-8, IL-6, IL-1, TNF alpha, IL-18, IL-12, IL-2, and IL-23 [28–30]. Murine Hepatitis Virus strain A59 (MHV-A59) brain infection elevates five proinflammatory cytokines: TNF alpha, IL-1 beta, IL-6, IL-12p40, and IL-15 [31,32]. The cytokine signature differs when coronavirus infects the brain compared to when the virus stays outside the central nervous system [33].

The glia consists of microglia (immune cells), oligodendrocytes and astrocytes (of neural origin). These cells differ in their activity and the role they play in the homeostasis of CNS [34]. Microglia are the resident mononuclear phagocytes of the CNS that originated from yolk-sack, accounting for 5–12% of cells in the adult mouse brain [35] and 0.5–16.6% of cells in the adult human brain [36]. The activation of microglia in the CNS is heterogenous, with two opposite phenotypes—pro-inflammatory M1 and anti-inflammatory M2 [37]. Polarisation towards the M1 phenotype occurs upon exposure to brain-invading pathogens, cellular debris, and pro-inflammatory cytokines (IFN gamma and TNF alpha). This leads

to the production of pro-inflammatory cytokines (TNF alpha, IL-1 beta, IL-6, and IL-2), chemokines, nitric oxide (NO), reactive oxygen species (ROS), reactive nitrogen species (RNS), and superoxide. The induction of M2 phenotype is caused by anti-inflammatory cytokines (IL-4 and IL-13), leading to the production of anti-inflammatory IL-10, TGF beta, insulin-like growth factor 1 (IGF-1), fibroblast growth factor (FGF), and colony-stimulating factor 1 (CSF-1) [38–42]. The M1 phenotype can be switched to the M2 phenotype by many factors [43]. Similarly to microglia, astrocytes, supporting cells of the CNS, can also be polarised into a pro-inflammatory, neurotoxic A1 type and neuroprotective A2 type [44,45]. Crosstalk between astrocytes, microglia, and neurons, based on neuro-immune communication, is fundamental to brain homeostasis [46–48].

In the present study, we investigated the effect of two animal batacoronaviruses—Mouse Hepatitis Virus (MHV) and rat Sialodacryoadenitis Virus (SDAV) on a mixed primary culture of microglia and astrocytes in vitro, with a particular focus on analysing the expression levels of cytokines secreted in response to infection. MHV strain JHM (MHV-JHM) is neuropathogenic, and SDAV possesses high zoonotic and neurotropic potential. To date, SDAV research has not considered the importance of CNS infections. Few publications confirmed the possibility of brain infection by SDAV [49], but no molecular pathway has been researched yet. MHV-JHM, on the other hand, is a well-known reference model for neuropathogenic diseases. The demyelination observed in MHV-JHM infection is also considered immune-mediated. While microglia are crucial for initiating the immune response, their continued activation can lead to excessive inflammation that damages not only virus-infected cells but also uninfected oligodendrocytes and neuronal cells [32,50–53].

2. Materials and Methods

2.1. Primary Mixed Microglia and Astrocyte Culture

Mixed microglia and astrocyte cell cultures were obtained from the whole brains of neonatal BALB/c mice. The blood vessels and meninges were carefully removed from the brain. Then, the whole mice brains were pooled together, washed with cold phosphate-buffered saline (PBS), and digested with a 2.5% trypsin EDTA-free solution for 15 min at 37 °C. Again, after incubation, the cells were washed five times in a warm PBS solution and mechanically homogenised using a pipette. Subsequently, the homogenate was filtered through a 70 µM cell strainer (BD Biosciences, Franklin Lakes, NJ, USA) into a 50 mL conical tube. After suspending in cell medium and counting, the cells were plated onto poly-D-lysine-coated flasks (at a density of 3×10^4 cells/25 cm^2 flask). The mixture was then cultured in Dulbecco's modified Eagle's/F12 medium with GlutaMAX (DMEM/F12), supplemented with 10% FBS, 10,000 units/mL penicillin–streptomycin mix (ThermoFisher™, Waltham, MA, USA). The cell culture was incubated at 37 °C with 5% CO_2. The medium was replaced after one day and supplemented with 5 ng/mL murine recombinant granulocyte and macrophage colony-stimulating factor (GM-CSF) (Sigma-Aldrich, St. Louis, MO, USA). Next, the cells were utilised for experimentation after two weeks of culture, consisting of 40% CD11b+ cells and 60% GFAP+ cells [54].

The growth of the cell cultures was monitored using a CKX53 inverted microscope (Olympus™, Warsaw, Poland). To determine the phenotype of the cells, the cells were stained during their culture (days 7 and 14 of incubation) using specific markers appropriately selected for each population analysed. The following antibodies were used: mouse anti-CD11b APC-conjugated (for microglia; ThermoFisher™), mouse anti-GFAP, Alexa Fluor 488-conjugated (for astrocytes; ThermoFisher™, Waltham, MA, USA), mouse anti-CNP (for oligodendrocytes; ThermoFisher™, Waltham, MA, USA), and mouse anti-NeuN (for neurons; ThermoFisher™, Waltham, MA, USA). The samples were analysed by

confocal microscopy (FluoView FV10i and FV10-ASW 3.0 Viewer software, Olympus™, Warsaw, Poland).

2.2. Viruses

The mouse coronavirus (MHV, Mouse Hepatitis Virus) neuropathological strain MHV-JHM [VR-76513™, ATCC®, Manassas, VA, USA] was propagated in a mouse hepatocyte cell line [NCTC, CCL-9.1™, ATCC®, Manassas, VA, USA]. The median tissue culture infectious dose ($TCID_{50}$) was calculated using the Spearman–Kärber method [55]. Aliquots were stored at −80 °C. All studies were conducted with the virus stock at the second passage level and a titre of $10^{7.8}$ $TCID_{50}$/mL.

Sialodacryoadenitis Virus strain 682 (SDAV, courtesy of Prof. Susan Compton, Yale University, New Haven, CT, USA) was propagated in rat lung epithelium [L-2, CCL-149™, ATCC®, Manassas, VA, USA]. The plaque-forming units (PFU) were established via plaque assay [56]. All studies were conducted with the virus stock at the third passage level and a titre of $10^{6.8}$ PFU/mL.

MHV-JHM or SDAV stock was added to the cell culture and incubated for 1 h (37 °C with 5% CO_2). The virus suspension was aspirated, and a fresh growth medium was added. Infected cultures were incubated for 224, 48, 72, 96, 168, and 672 h at 37 °C with 5% CO_2 according to the experimental needs. In the case of 672 h of infection (1 month), cell media were added if needed to maintain the culture (about 0.5 mL for a 6-well plate and 50 µL for a 96-well plate to keep the medium level at 2 mL and 200 µL appropriately).

2.3. Immune Response Profiling

Conditioned cell media from mixed glial cell cultures (collected at 2, 24, 48, 72, 96, 168, and 672 (1 month) hours post infection (h p.i.)) infected with MHV and SDAV were analysed for their production of 48 cytokines, chemokines, growth factors/regulators, and soluble receptors (presented in Table 1) simultaneously for efficient immune response profiling using Luminex xMAP technology (ProcartaPlex™ Mouse Immune Monitoring Panel, 48plex, ThermoFisher™, Waltham, MA, USA). All samples were incubated in a 96-well Solid Polystyrene Microplate (Corning®, New York, NY, USA), and during the washing process, a magnetic 96-well separator (Ambion™ 96-well Magnetic-Ring Stand, ThermoFisher™, Waltham, MA, USA) was used following the manufacturer's instructions.

Table 1. List of the soluble immune factors included in this study.

Type	Target List
Cytokines:	BAFF, G-CSF (CSF-3), GM-CSF, IFN alpha, IFN gamma, IL-1 alpha, IL-1 beta, IL-2, IL-3, IL-4, IL-5, IL-6, IL-7, IL-9, IL-10, IL-12p70, IL-13, IL-15/IL-15R, IL-17A (CTLA-8), IL-18, IL-19, IL-22, IL-23, IL-25 (IL-17E), IL-27, IL-28, IL-31, IL-33, LIF18, M-CSF, RANKL, TNF alpha
Chemokines:	ENA-78 (CXCL5), Eotaxin (CCL11), GRO alpha (CXCL1), IP-10 (CXCL10), MCP-1 (CCL2), MCP-3 (CCL7), MIP-1 alpha (CCL3), MIP-1 beta (CCL4), MIP-2, RANTES (CCL5)
Growth factors/regulators:	Betacellulin (BTC), Leptin, VEGF-A
Soluble receptors:	IL-2R, IL-7R alpha, IL-33R (ST2)

This system contains bead set markers with varying ratios of two different fluorophores coupled to monoclonal antibodies directed against various cytokines, chemokines, growth/regulatory factors, and soluble receptors. The protein of interest was bound to a monoclonal antibody on a bead (after 24 h incubation), and a secondary detection antibody

specific to the molecule of interest was added (2 h incubation). The colour-coded beads were read on a MAGPIX® system (Luminex Corporation, New York, NY, USA) using two lasers. One laser is used to identify the bead and thus the protein of interest, while the other is used to detect the amount of detection agent on the bead and thus the amount of soluble protein of interest. In addition, a standard curve in duplicate has been provided by the manufacturer for each experiment. A five-parameter logistic curve was then generated, and the standard recovery was calculated using the following equation: (observed concentration/expected concentration) × 100. A desired recovery range was between 70% and 130%. Any sample outside this range was considered impure. A sample was considered positive if it exceeded the limits of detection as defined by the manufacturer's specifications. Data acquisition was performed using the MAGPIX® instrument and xMAP® component software v. 4.2. A data analysis was performed using xPONENT® software ver. 4.3 for Luminex instruments.

2.4. ELISA

An immunoenzymatic ELISA (Mouse DuoSet®, R&D Systems, Minneapolis, MN, USA) was used to analyse the cytokines expressed in the primary mixed glia culture infected with SDAV and MHV-JHM for 2, 24, 48, 72, 96, and 168 h. The expression levels of IL-4, IL-5, IL-6, IL-10, IL-17, and TNF alpha were analysed according to the procedure outlined by the manufacturer. Briefly, monoclonal antibodies for the tested cytokines were diluted to yield concentrations of 4 µg/mL for IL-4 and IL-10, 2 µg/mL for IL-6 and IL-17, 1 µg/mL for IL-5, and 800 ng/mL for TNF alpha. To prepare the standards, seven 2-fold serial dilutions were performed at concentrations of 1000–15.6 pg/mL for IL-4, IL-6, and IL-17 and at concentrations of 2000–31.2 pg/mL for TNF alpha, IL-5, and IL-10. Previously prepared test samples—mixed glia cells cultured in 6-well plates (uninfected cells—control and infected cells)—were transferred into 1.5 mL tubes and centrifuged for 5 min at 1200 rpm. Then, 50 µL of the supernatant (test samples) and standards was applied to 96-well plates previously coated with antibodies. The plates were incubated overnight at 4 °C. After incubation, the plates were washed with 0.05% Tween/PBS (3×). Secondary antibodies were prepared and diluted in 1% BSA/PBS to give concentrations of 250 ng/mL for IL-4 and IL-10, 75 ng/mL for IL-6, 50 ng/mL for IL-5 and IL-17, and 37.5 ng/mL for TNF alpha. Then, 50 µL of II-antibodies was applied per well and incubated for 2 h at room temperature. After this time, they were washed in 0.05% Tween/PBS (3×). In the next step, 50 µL of the streptavidin-HRP conjugate (diluted 1:40 in 1% BSA/PBS) was applied and incubated in the dark for 20 min at room temperature. After incubation with the conjugate, the plates were washed again with 0.05% Tween/PBS (3×). Then, 50 µL of a 1:1 H_2O_2/TMB solution was applied and incubated for 20 min at room temperature. After incubation, 50 µL of 2 M H_2SO_4 was applied to stop the reaction. Optical density readings at 450 nm and 570 nm were measured using a Synergy H1 plate reader (BioTek Instruments™, Winooski, VT, USA).

2.5. Confocal Microscopy Analysis of SDAV and MHV-JHM Infection

Control and SDAV- or MHV-JHM-infected cells (2, 24. 48, 72, 96, 168, and 672 (1 month) h p.i.) were washed with PBS and fixed with 3.7% PFA for 15 min at room temperature. After washing with PBS, the cells were incubated at room temperature with 0.1% Tween/PBS for 15 min. Next, the cells were washed twice with PBS and then incubated with BSA/PBS for 30 min at RT. For phenotyping, the following antibodies were used: mouse anti-GFAP, Alexa Fluor 488-conjugated (astrocytes, diluted 1:100 in BSA/PBS); mouse anti-CD11b APC-conjugated (microglia; diluted 1:100 in BSA/PBS); mouse anti-CNP mAb (oligodendrocytes; diluted 1:100 in BSA/PBS); and mouse anti-NeuN mAb (neurons; diluted 1:100

in BSA/PBS). Following 1 h of incubation, secondary antibody Alexa Fluor 647 (goat anti-mouse; diluted 1:250 in BSA/PBS) was added. The viral antigen was visualised by mouse anti-SARS/SARS-CoV-2 mAb specific for N protein (diluted 1:200 in BSA/PBS) and incubated for 1 h at 37 °C. After this time, the cells were washed twice in PBS, and secondary antibody AlexaFluor™ 488 (goat anti-mouse; diluted 1:500) or TexasRed (goat anti-mouse; diluted 1:1000) was added (1 h, in the dark, RT). Next, the cells were washed twice with PBS, followed by staining with phalloidin/TRITC solution (500 ng/mL) for 1h in the dark at RT to visualise the actin filaments. After incubation, the cultures were washed twice with PBS. An amount of 1 µg/mL of Bisbenzimidine/Hoechst 33258 dye was used to visualise the cell nuclei (2–3 min, RT). All the antibodies and fluorochromes were purchased from ThermoFisher™ (Waltham, MA, USA). Then, the slides were rinsed twice with PBS and once with deionised water. The slides were mounted using Prolong Gold Antifade Reagent (ThermoFisher™, Waltham, MA, USA). Image acquisition was performed with a FluoView FV10i confocal microscope (Olympus™, Warsaw, Poland), equipped with a 60× water-immersion objective. The images were processed using the FV10-ASW 3.0 Viewer software (Olympus™, Warsaw, Poland) and then converted to 24-bit TIFF files.

2.6. ROS Detection

The ROS levels in the mixed glial cell culture were assessed from 2, 24, 48, 72, 96, and 168 h to 1 month post-infection with SDAV and MHV-JHM. The negative control was uninfected cells, while the positive control was 1 mM H_2O_2-treated cells (1 min, RT). The cells were incubated in culture fluid supplemented with fluorogenic probe CellROX® Green Reagent (5 µM/mL, 30 min, 37 °C; ThermoFisher™, Waltham, MA, USA), measuring oxidative stress in live cells [57]. Then, the cells were washed with PBS, stained with Hoechst 33542, and fixed with 3.7% PFA/PBS for 15 min in RT. After fixation, the cells were washed twice with PBS and mounted with Prolong Gold Antifade Reagent. The slides were analysed using a FluoView FV10i confocal microscope (Olympus™, Warsaw, Poland) equipped with a 60× water-immersion objective. The images were processed using the FV10-ASW 3.0 Viewer software (Olympus™, Poland) and then converted to 24-bit TIFF files.

The Image J/Fiji (ver. 2.14.0/1.54p, NIH Image, Bethesda, MD, USA) tool was used to quantify ROS expression. TIFF files were converted to 16-bit greyscale images. Then, the region of interest (ROI) was selected using the polygon tool for each cell, and a scale from pixels to µm was set up. This was followed by measuring the ROI of each cell to obtain specific parameters, such as the area, mean, integrated density, and raw integrated intensity. Additionally, independent blinded counts were performed around each cell ROI for manual quantitation. The obtained parameters were used to calculate Corrected Total Cell Fluorescence (CTCF) = Integrated Density − (Area of selected cell × Mean fluorescence of background readings).

2.7. Flow Cytometry

Flow cytometry was used to measure apoptosis/necrosis and the ROS rate in mixed glial cells after infection with MHV-JHM and SDAV (2, 24, 48, 72, 96, 168 h, and 1 month p.i.) using Dead Cell Apoptosis Kits with Annexin V for Flow Cytometry (ThermoFisher™, Waltham, MA, USA) and the CellROX™ Green Flow Cytometry Assay Kit (ThermoFisher™, Waltham, MA, USA). Infected cells (10^4 cells/mL) and proper controls were stained according to the manufacturer's protocols. Samples were analysed by Cytoflex LX cytometer (BD Biosciences, Franklin Lakes, NJ, USA) to specify the proportion of necrotic cells (Annexin V-FITC−/PI+), early apoptotic cells (Annexin FITC+/PI−), late apoptotic cells (Annexin V-FITC+/PI+), and non-apoptotic cells (Annexin V-FITC−/PI−), and the presence of ROS+

cells. Calculations were performed with CellQuest Pro™ analysis software ver. 5.2.1 (BD Biosciences, Franklin Lakes, NJ, USA). The experiments were performed in triplicate.

2.8. Statistical Analysis

The results were statistically evaluated by two-way or one-way analysis of variation (ANOVA) using the Dunnet or Tukey multiple comparison test. The non-parametric variables were assessed using the Kruskal–Wallis test with the post hoc Dunn test. All experiments were performed at least in triplicate. These analyses were performed using GraphPad Prism™ version 9.4.0 (453) for macOS software (GraphPad Software Inc., San Diego, CA, USA). Statistical differences were interpreted as significant at $p \leq 0.05$ (*), very significant at $p \leq 0.01$ (**), highly significant at $p \leq 0.001$ (***), and not significant at $p > 0.05$.

3. Results

3.1. SDAV Infection of Primary Mixed Microglia and Astrocyte Cells

To carry out the planned analyses, we first optimised the primary culture of astrocytes and microglia so that, after 14 days of growth, the cell ratio reached 40% microglia to 60% astrocytes (Figure 1A). The cells were infected with SDAV to check the possibility of infection of astrocytes and microglia. Observation of the 72 h infection using confocal microscopy showed that the viral antigen (red fluorescence) was initially present in astrocyte cells labelled with GFAP antibody (green fluorescence) (Figure 1(Be), white arrows). The viral antigen (green fluorescence) was detected travelling along the filopodia to reach nearby microglial cells labelled with CD11b (dark blue fluorescence) (Figure 1(Bf), white arrows). The viral antigen was present in large numbers and with high fluorescence in both cell types. We also infected mixed microglia and astrocytes with MHV-JHM as a better-known model to compare the effect of SDAV infection. After 72 h post-infection (h p.i.) the MHV-JHM antigen was visible at the cell membrane side of GFAP-labelled astrocytes (Figure 1(Bg); white arrows). In the CD11b-labelled microglia cells, the MHV antigen was located in the perinuclear region (Figure 1(Bh); white arrows). A cytopathic effect in the form of syncytium was visible (Figure 1(Bh), white rectangle).

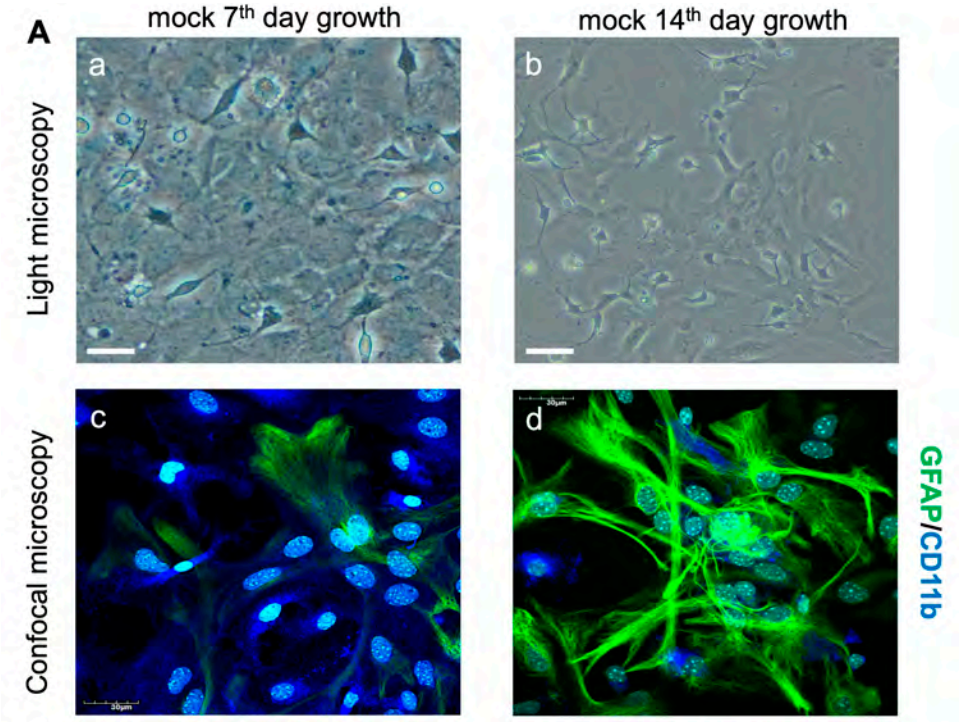

Figure 1. *Cont.*

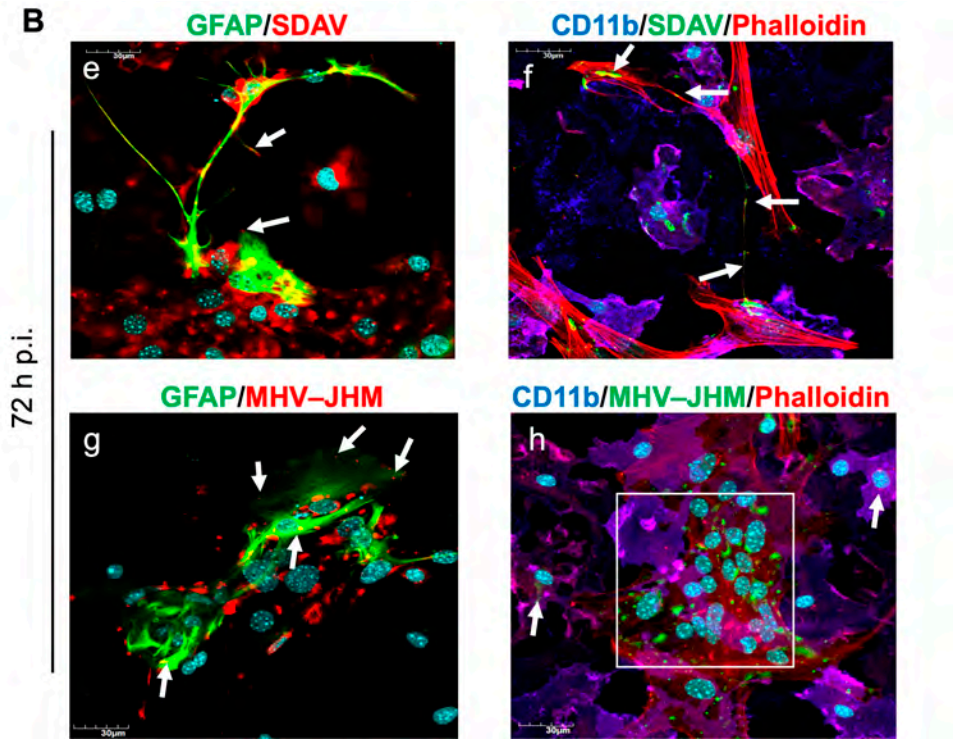

Figure 1. Representative images of primary astrocytes and microglia cells, uninfected (**A**) and infected with SDAV and MHV-JHM for 72 h (**B**). Cells were cultured for 14 days before each experiment. Microglia were more abundant than astrocytes during the first 7 days (**a**,**c**). After stimulation with GM-CSF, the ratio of microglia to astrocytes on the 14th day of growth was 40% to 60%, respectively (**b**,**d**). These changes were captured by a light microscope (**a**,**b**) and confocal microscope (**c**,**d**; green—GFAP (astrocytes), dark blue—CD11b (microglia), light blue—cell nuclei). After 14 days of growth, the primary mixed glial culture was infected with SDAV and MHV-JHM for 72 h and labelled using immunofluorescence (**B**). A signal corresponding to SDAV and MHV-JHM was found both in the astrocytes (**e**,**g**; green—GFAP (astrocytes), red—SDAV, MHV-JHM, light blue—cell nuclei) and microglia (**f**,**h**; dark blue—CD11b (microglia), green—SDAV, MHV-JHM, red—F-actin, light blue—cell nuclei). The white arrows show the placement of SDAV (**e**,**f**) or MHV-JHM (**g**,**h**) in the cells. The white rectangle shows syncytium formation (**h**). Microscope CKX53 (**a**,**b**) and FluoView FV10i (**c**,**d**,**B**) (Olympus™, Poland). Scale bar: 30µm.

3.2. FACS Analysis of Cell Death

Annexin V-FITC and PI FACS analyses were performed for the differentiation and quantitative determination of the percentage of necrotic, viable, and apoptotic cells (early and late types) after infection with MHV-JHM and SDAV (Figure 2). MHV-JHM induced apoptosis in the mixed microglia and astrocytes culture within the first 2 h p.i. and persisted until 672 h p.i. (1 month). The percentage of early apoptotic cells increased significantly highly (*** $p \leq 0.001$) from 2.75% in the uninfected control to 41.20% at 2 h p.i. and remained at a similar level until one month post infection. The late apoptotic cells increased non significantly from 3.43% in the control to 10.7% 2 h p.i. and stayed at a similar level until 168 h p.i. At 672 h p.i., late apoptosis reached 27.6% (*** $p \leq 0.001$). Signs of cell necrosis appear the highest after 1 month of infection with MHV-JHM, reaching 4.43%, compared to the uninfected control, with 1.88% of necrotic cells (Figure 2A). However, this increase was not statistically significant. After infection with the SDAV strain, we observed a similar trend of inducing cell apoptosis. The level of early apoptotic cells increased highly significantly (*** $p \leq 0.001$) from 2.75% in the uninfected control cells to 37.8% after 2 h p.i. and remained high until 1 month post-infection, reaching 74.9% (*** $p \leq 0.001$) (Figure 2B). The percentage of late apoptotic cells increased statistically significantly only

after 48 and 168 h p.i. (11.8% and 12.4%, respectively) compared to that in the uninfected control (3.43%). Necrosis did not occur in the case of SDAV infection in the primary mixed microglia and astrocyte cultures. A high % of viable cells remained unaffected from 2 to 168 h p.i. (55.1–48.2%); however, a high statistical decrease (*** $p \leq 0.001$) was observed after 1 month post-infection (22.1%) compared to that in the uninfected control (91.95%) (Figure 2B).

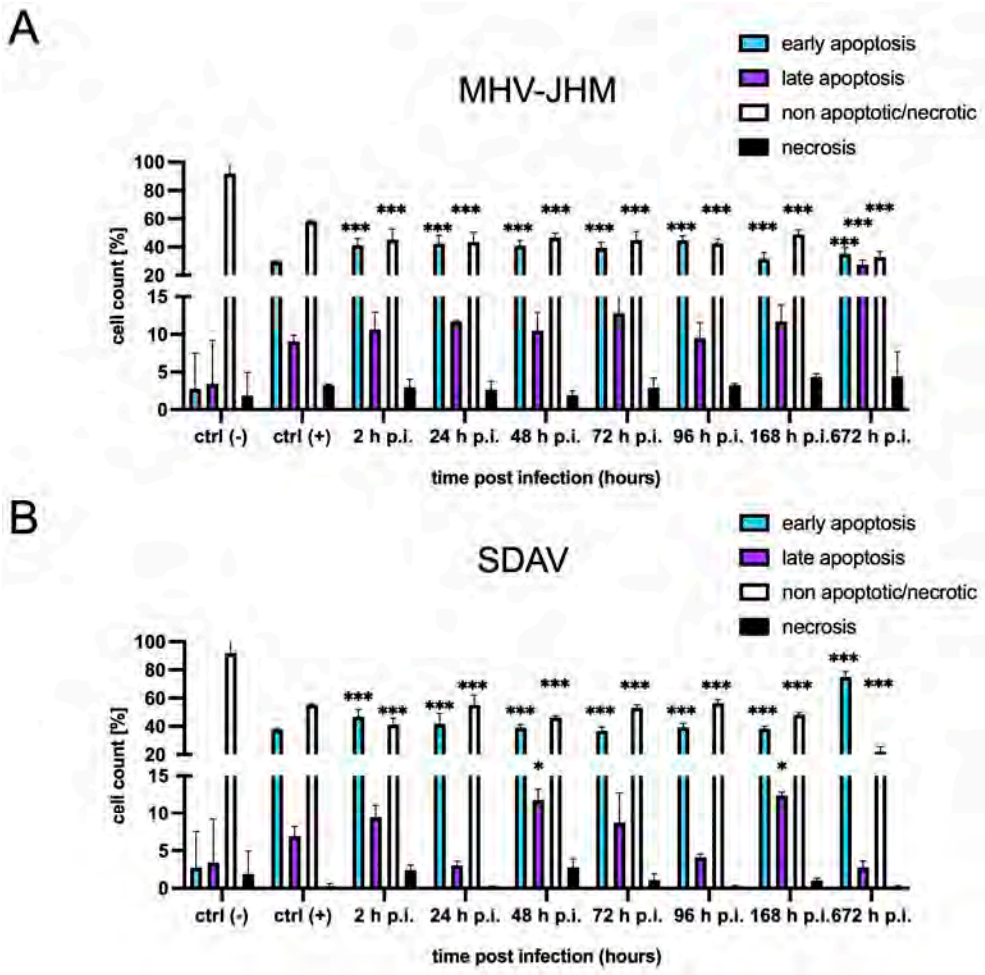

Figure 2. The percentage (mean ± SD) of early apoptotic, late apoptotic, necrotic, and non-apoptotic cells in a mixed primary microglia and astrocyte culture from 2 to 672 h p.i. with MHV-JHM (**A**) and SDAV (**B**) from three independent experiments (ANOVA, * $p \leq 0.05$, *** $p \leq 0.001$).

3.3. ROS Expression

We performed two experiments to investigate reactive oxygen species (ROS) release in primary mixed microglia and astrocyte cells after infection with MHV-JHM and SDAV (Figures 3A,B and 4A,B). A quantitative flow cytometry analysis (% of ROS) was followed by a semi-quantitative examination of confocal microscopy imaging using corrected total cell fluorescence (CTCF). A flow cytometry analysis revealed a rapid, highly statistically significant increase in reactive oxygen species 2 h p.i. in cells infected with MHV-JHM (26.48% ± 5.12%, *** $p \leq 0.001$) compared to the uninfected control (10.55% ± 0.61%) (Figure 3B). The highest observed ROS value was after 24 h p.i. (31.47% ± 0.46%,*** $p \leq 0.001$) compared to that in the uninfected control (10.55% ± 0.61%) (Figure 3B). Gradually, the ROS levels decreased but were still significantly higher than the uninfected control levels, and the values were as follows: after 48 h p.i. with MHV-JHM, 26.99% ± 4.11% (*** $p \leq 0.001$); 72 h p.i., 20.68% ± 3.84% (** $p = 0.004$); 96 h p.i., 18.68% ± 1.68% (* $p = 0.019$); 168 h p.i., 22.48% ± 5.22% (*** $p \leq 0.001$) compared to the

uninfected control (10.55% ± 0.61%) (Figure 3B). The lowest value was noted after 672 h p.i., where the ROS level decreased insignificantly to 5.34% ± 0.22% (p = 0.363) compared to that for the control uninfected cells (10.55% ± 0.61%) (Figure 3B).

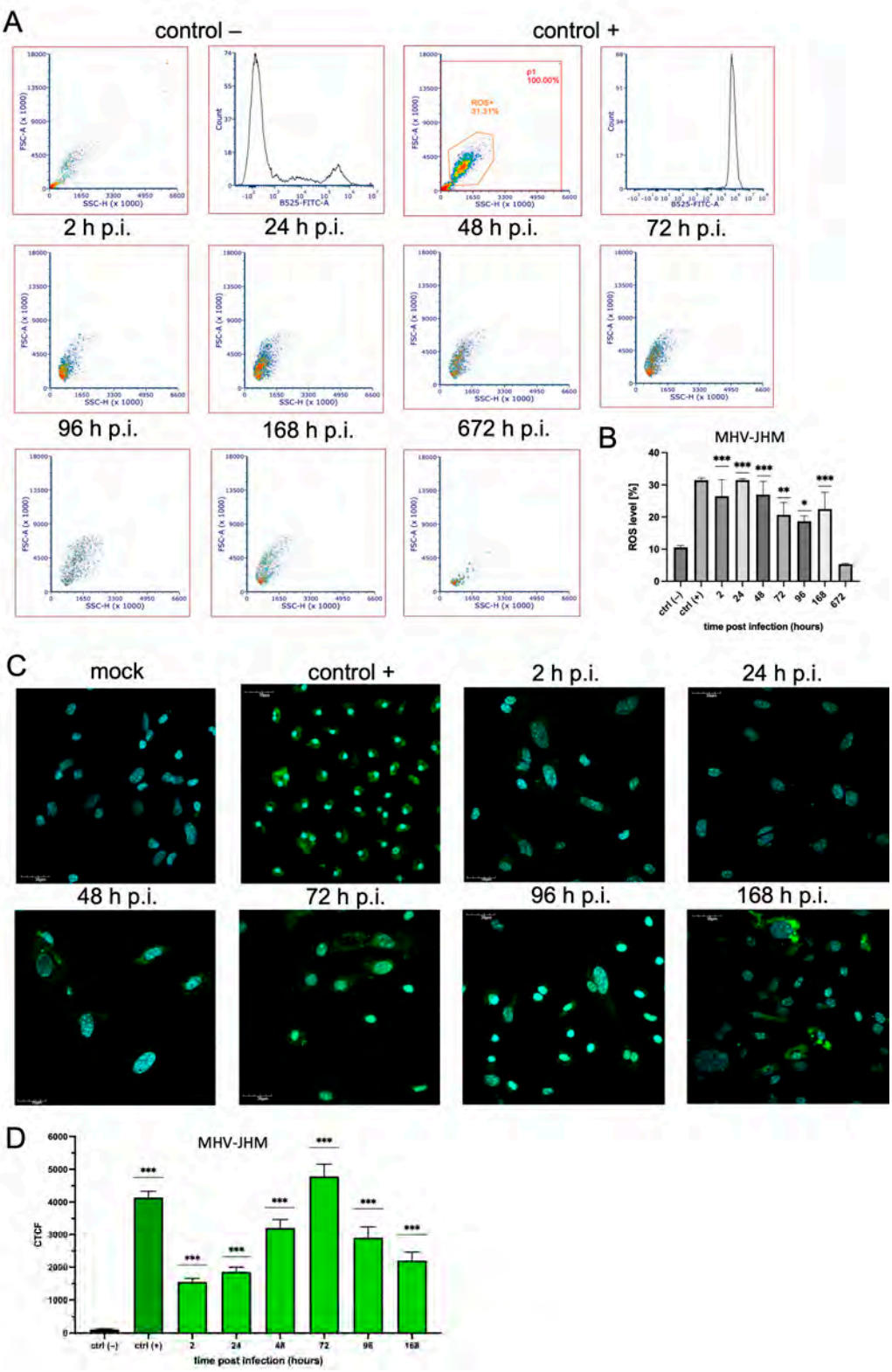

Figure 3. ROS production in mixed primary culture of microglia and astrocyte cells in mock and MHV-JHM-infected cells for 2–672 h. ROS levels were obtained from flow cytometry analysis using CellROX Green (ThermoFisher™) staining (**A**,**B**). Representative histograms and dot plots of ROS levels in uninfected labelled control −, uninfected labelled control + (treated with H_2O_2), and infected cells (**A**). The mean fluorescence intensity (MFI) of ROS-positive cells after MHV-JHM infection for

2–672 h is presented as mean ± SD (n = 10,000 cells) from three independent experiments. ANOVA; * $p \leq 0.05$, ** $p \leq 0.01$, *** $p \leq 0.001$ (**B**). ROS levels were obtained from confocal microscopy analysis using CellROX Green (ThermoFisher™) staining (**C**,**D**). Representative confocal microscopy images of MHV-JHM-infected primary mixed microglia and astrocyte cells for 2–168 h. Negative control—uninfected cells; positive control—cells treated with H_2O_2. Cell nuclei (blue), ROS (green). Scale bar: 30 µm (**C**). Analysis of ROS fluorescence intensities performed with Fiji software (ver. 2.14.0/1.54p) described as cell total corrected fluorescence (CTCF), presented as mean ± SEM (n = 100 cells), ANOVA; *** $p \leq 0.001$ (**D**).

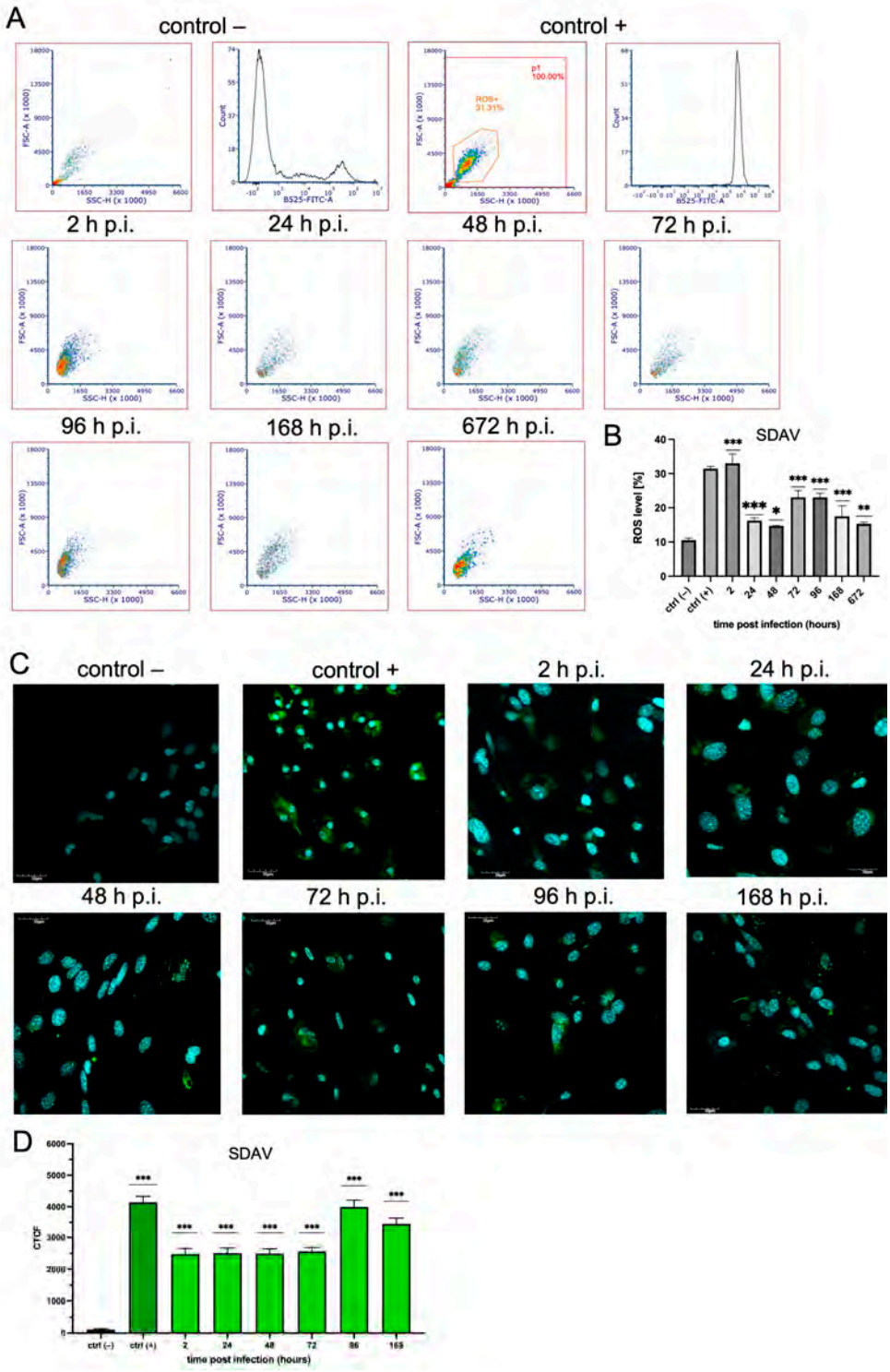

Figure 4. ROS production in mixed primary culture of microglia and astrocyte cells in mock and

SDAV-infected cells for 2–672 h. ROS levels were obtained from flow cytometry analysis using CellROX Green (ThermoFisher™) staining (**A**,**B**). Representative histograms and dot plots of ROS levels in uninfected labelled control −, uninfected labelled control + (treated with H_2O_2), and infected cells (**A**). The mean fluorescence intensity (MFI) of ROS-positive cells after SDAV infection for 2–672 h is presented as mean ± SD (n = 10,000 cells) from three independent experiments. ANOVA; * $p \leq 0.05$, ** $p \leq 0.01$, *** $p \leq 0.001$ (**B**). ROS levels were obtained from confocal microscopy analysis using a CellROX Green (ThermoFisher™) staining (**C**,**D**). Representative confocal microscopy images of SDAV-infected primary mixed microglia and astrocyte cells for 2–168 h. Negative control—uninfected cells; positive control—cells treated with H_2O_2. Cell nuclei (blue), ROS (green). Scale bar: 30 µm (**C**). Analysis of ROS fluorescence intensities performed with Fiji software (ver. 2.14.0/1.54p) described as cell total corrected fluorescence (CTCF), presented as mean ± SEM (n = 100 cells), ANOVA; *** $p \leq 0.001$ (**D**).

Cells infected with SDAV presented the highest abundance of ROS levels after 2 h p.i. The level of ROS increased highly statistically significantly (33.03% ± 2.72%, *** $p \leq 0.001$) compared to that of the uninfected control (10.55% ± 0.61%) (Figure 4B). The values at 24 h p.i. (16.25 ± 0.85, *** $p \leq 0.001$) and 48 h p.i. (14.71 ± 0.08, * $p = 0.012$) slightly decreased but were still statistically significantly higher than that for the control uninfected cells (10.55% ± 0.61%) (Figure 4B). After 72 h p.i. and 96 h p.i., a highly statistically significant increase occurred at a constant level of 23.08% ± 1.96% and 23.06% ± 1.22% (*** $p \leq 0.001$), respectively, compared to that for the uninfected control (10.55% ± 0.61%) (Figure 4B). Then, after 168 h p.i. and 672 h p.i., the ROS levels slightly decreased to 17.53 ± 3.06 (*** $p \leq 0.001$) and 15.31 ± 0.45 (** $p \leq 0.005$), respectively, compared to previous time points but remained statistically significantly higher than those for the uninfected control (10.55% ± 0.61%) (Figure 4B).

An analysis of the confocal images stained with a fluorogenic probe showed an evenly distributed signal of ROS in the cells after infection with both viruses (Figures 3C,D and 4C,D). In the case of MHV-JHM, ROS were uniformly present throughout the cell from 2 h p.i. to 168 h p.i. (Figure 3C). After a detailed data analysis, we determined the quantitative value of the probe corresponding to the number of ROS in the form of corrected total cell fluorescence (CTCF) (Figure 3D). MHV-JHM infection triggered ROS production from 115.4 ± 216.0 in the uninfected control cells to 1547.0 ± 1091 (*** $p \leq 0.001$), after 2 h p.i. This value remained similar until 48 h p.i., where the values highly statistically significantly increased to 3212.0 ± 2574.0 (*** $p \leq 0.001$) compared to the uninfected control (115.4 ± 216.0). The highest rate was observed after 72 h p.i. (4784.0 ± 3700.0) compared to the uninfected control (115.4 ± 216.0).

The ROS distribution after SDAV infection of mixed microglia and astrocytes was visible on confocal images during all times post-infection. The brightest fluorescence was present after 96 and 168 h p.i. (Figure 4C). A data analysis revealed that the CTCF values were nearly similar after 2, 24, 48, and 72 h p.i. (2474.0 ± 1776.0, 2505.0 ± 1604.0, 2492.0 ± 1486.0, 2560.0 ± 1216.0; *** $p \leq 0.001$, respectively) with SDAV, with a highly statistically significant increase compared to those for the uninfected control (115.4 ± 216.0) (Figure 4D). The highest values were recorded after 96 h p.i. (3452.0 ± 216.0) and 168 h p.i. (3991.0 ± 2177.0) compared to the uninfected control cells (115.4 ± 216.0).

3.4. Cytokine and Chemokine Expression

The levels of expressed cytokines and chemokines, as well as growth factors and soluble receptors, were measured after infection with MHV-JHM and SDAV in primary mixed microglia and astrocyte cells using multiplex technology (Luminex xMAP), analysing 48 proteins crucial for immunomodelling. The results showed changes in both viruses over the course of the one-month infection period, as visualised by a heat map. In the case of

MHV-JHM infection, changes in expression (from 0% to 100%) were visible in IL-6, IL-18, IL-33, ENA-78 (CXCL5), GRO alpha (CXCL1), IP-10 (CXCL10), MCP-1 (CCL2), MIP-1 beta (CCL4), MIP-2 alpha (CXCL2), RANTES (CCL5), and TNF alpha (Figure 5A). However, SDAV infection increased the protein expression of IL-1 alpha, IL-6, IL-10, IL-18, IL-19, IL-23, IL-28, IL-33, ENA-78 (CXCL5), GRO alpha (CXCL1), IP-10 (CXCL10), MCP-1(CCL2), MCP-3(CCL3), MIP-1 alpha (CCL3), MIP-1 beta (CCL4), MIP-2 alpha (CXCL2), RANTES (CCL5), TNF alpha, and Leptin (Figure 5B).

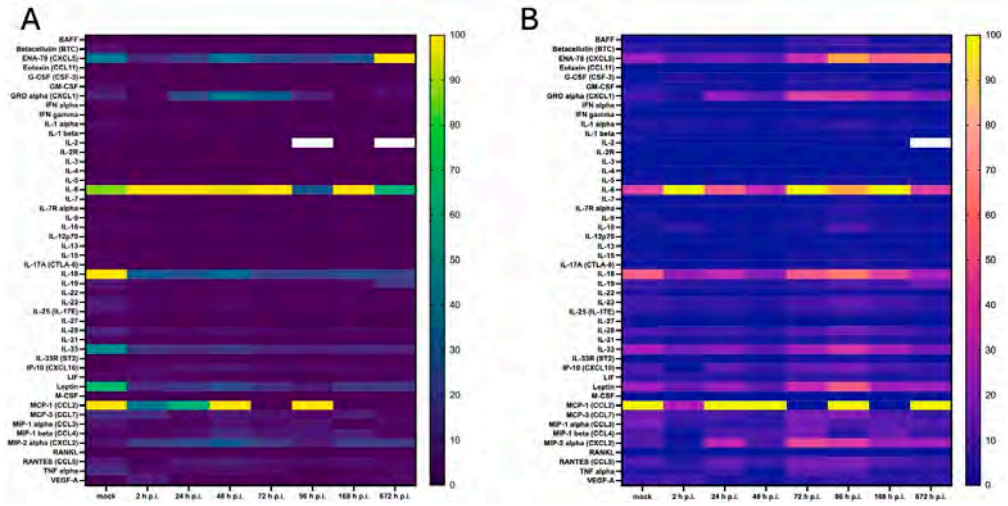

Figure 5. Heat map showing the cytokine concentrations secreted by primary mixed microglia and astrocyte cells after infection with MHV-JHM (**A**) and SDAV (**B**) from 2 to 672 h. Colours are assigned according to the relative, normalised scale of expression. The scale ranges from 0 to 100% (lowest to highest concentration in a row).

More detailed changes in expression pattern post-infection, shown as concentration [pg/mL], were revealed by statistical analysis of the obtained protein concentration compared to the mock. After 2 h p.i. with MHV-JHM, a statistically highly significant increase compared to the mock (*** $p \leq 0.001$) was observed for G-CSF (196.0 ± 17.73; 9.54 ± 4.65), IL-2R (23.09 ± 0.4; 3.15 ± 0.65), IL-33R (121.8 ± 14.32; 0.0), LIF (465.5 ± 194.1; 60.55 ± 21.77), and RANKL (39.88 ± 20.98; 8.35 ± 2.35). Statistically very significant (** $p \leq 0.01$) and statistically significant (* $p \leq 0.05$) results were obtained for BAFF (109.9 ± 32.71; 17.63 ± 4.62), IL-1 beta (57.74 ± 17.27; 23.19 ± 8.07), IL-7 (43.42 ± 9.6; 7.12 ± 3.18), IL-23 (476.3 ± 58.99; 152.2 ± 51.47), IL-28 (522.5 ± 183.3; 182 ± 63.01), IL-31 (152.4 ± 17.71; 71.12 ± 22.24), and VEGF-A (832.10 ± 93.61; 15.92 ± 2.80) (Figure 6A). At 24 h p.i., most cytokines, chemokines, and growth factors remained at the same level as at 2 h p.i., but new statistically highly significant increases were observed for IL-12 (53.41 ± 8.66; 13.77 ± 2.3), IP-10 (801.3; 80.02 ± 14.71), and RANTES (860.2; 127.0 ± 59.98). Statistically very significant (** $p \leq 0.01$) and statistically significant (* $p \leq 0.05$) results were obtained for GM-CSF (122.5 ± 5.96; 69.73 ± 13.45), GRO alpha (2606.0 ± 631.1; 131.6 ± 17.85), IFN gamma (4.806 ± 0.71; 1.69 ± 0.49), IL-1 alpha (327.5 ± 37.48; 87.74 ± 45.21), IL-1 beta (46.50 ± 3.75; 23.19 ± 8.07), IL-3 (3.52 ± 0.42; 1.39 ± 0.38), IL-6 (11,168.0 ± 1806.0; 912.2 ± 83.72), IL-12 (53.41 ± 8.66; 13.77 ± 2.30), Il-13 (28.25 ± 1.29; 10.29 ± 3.77), IL-15 (88.71 ± 5.97; 35.04 ± 10.80), IL-17A (65.94 ± 5.63; 27.59 ± 4.19), IL-18 (2936 ± 204.7; 1465.0 ± 456.5), IL-22 (75.52 ± 7.47; 46.10 ± 10.59), IL-27 (12.49 ± 1.36; 4.5 ± 1.11), IL-28 (544.9 ± 62.92; 182.9 ± 63.01), IL-31 (147.9 ± 12.58; 71.12 ± 22.24), IL-33 (1642.0 ± 252.6; 718.7 ± 490.9), MIP-2 alpha (2527.0 ± 416.4; 112.2 ± 48.98), and TNF alpha (608.0 ± 47.51; 221.2 ± 65.15) (Figure 6B). At 48 h p.i. MHV-JHM significantly increased the protein expression for only Eotaxin (3.4 ± 3.01; 0.0), IL-5 (61.63 ± 11.45; 25.69 ± 6.74), IL-17A (63.06 ± 6.3; 27.59 ± 35.29), IP-10 (583.3 ± 63.34;

14.71 ± 4.52), MIP-1 beta (987.3 ± 128.8; 59.89 ± 28.34), MIP-2 alpha (1892.0 ± 366.6; 112.2 ± 48.98), and RANTES (718.6 ± 23.37; 127.0 ± 59.62) (Figure 6C). However, highly significant (*** $p \leq 0.001$) and very significant (** $p \leq 0.01$) statistical increases were observed for almost all proteins after 72 h p.i. The highest increase in concentration was observed for ENA-78 (3661.0 ± 642.9; 621 ± 177.6), GRO-alpha (7253.0 ± 286.8; 131.6. ± 17.85), IFN-gamma (4.784 ± 0.61; 1.69 ± 0.49), IL-1 beta (48.35 ± 3.09; 23.19 ± 8.07), IL-3 (3.94 ± 0.92; 1.39 ± 0.38), IL-6 (13,941.0 ± 959.60; 912.2 ± 83.72), IL-12 (56.27 ± 7.85; 13.77 ± 2.30), IL-15 (86.99 ± 9.83; 35.04 ± 10.80), IL-18 (2866.0 ± 239.6; 1465.0 ± 456.5), IL-19 (329.0 ± 43.38; 118.7 ± 19.69), IL-23 (497.50 ± 60.68; 152.2 ± 51.47), IL-33 (1778.0 ± 405.4; 718.7 ± 490.9), LIF (205.6 ± 8.23; 60.55 ± 21.77), MCP-3 (205.6 ± 8.23; 223.5 ± 33.83), MIP-1 beta (1046.0 ± 552.80; 59.89 ± 28.34), MIP-2 alpha (2553.0 ± 366.6; 112.2 ± 48.98), and TNF alpha (559.3 ± 61.83; 221.2 ± 65.15) (Figure 6D). After 96 h p.i. with MHV-JHM, statistically very significant (** $p \leq 0.01$) and statistically significant (* $p \leq 0.05$) results were obtained only for MIP-1alpha (1095.0.0 ± 346.40; 246.9 ± 65.28) and MIP-1 beta (1095 ± 346.40; 59.89 ± 28.34) (Figure 6E). At 168 h p.i., protein expression was similar to that at 72 h p.i., with almost all proteins being highly significant (*** $p \leq 0.001$), very significant (** $p \leq 0.01$) or (* $p \leq 0.05$) upregulated. The most significant changes in expression were observed for BAFF (109.9 ± 32.71; 17.63 ± 4.62), ENA-78 (2185.0 ± 253.7; 621 ± 177.6), IFN alpha (53.50 ± 3.38; 17.82 ± 7.19), Leptin (2135 ± 460.6; 1022 ± 1632.1), MCP-1 alpha (1095.0.0 ± 346.40; 246.9 ± 65.28), MCP-3 (1164.0 ± 164.90; 223.5 ± 33.83), MIP-1 beta (1532 ± 967.40; 59.89 ± 28.34), MIP-2 alpha (2163 ± 366.6; 112.2 ± 48.98), RANKL (205.4 ± 207.10; 8.35 ± 2.35), and VEGF-A (273.20 ± 45.16; 15.92 ± 2.80) (Figure 6F). Finally, after one month p.i. with MHV-JHM, all of the cytokines, chemokines, and growth factors were still significantly increased compared to the mock. The greatest changes were observed for ENA-78 (3237.0 ± 1024.0; 621 ± 177.6), G-CSF (156.20 ± 26.38; 9.54 ± 4.65), GM-CSF (616.50 ± 66.73; 69.73 ± 13.55), IL-6 (13,941.0 ± 83.72; 15,590 ± 4491), IL-33 (1827.0 ± 262.5; 718.7 ± 490.9), MIP-2 alpha (3361 ± 378.81; 112.20 ± 48.98), and VEGF-A (695.00 ± 516.20; 15.92 ± 2.80) (Figure 6G).

SDAV infection of primary microglia and astrocytes revealed slightly different protein expression. After 2 h p.i., a statistically highly significant increase compared to mock (*** $p \leq 0.001$) was observed for betacellulin (224.90 ± 35.99; 85.02 ± 7.39), G-CSF (402.8 ± 275.90; 2.81 ± 1.39), IFN alpha (59.54 ± 6.21; 18.33 ± 3.44), IFN gamma (4.58 ± 0.58; 1.30 ± 0.08), IL-1 alpha (245.5 ± 6.81; 44.02 ± 6.81), IL-1 beta (93.39 ± 34.13; 23.92 ± 3.87), IL-3 (3.78 ± 0.49; 0.99 ± 0.14), IL-6 (13,400.00 ± 3749; 912.20 ± 83.72), IL-7 (62.24 ± 17.92; 10.55 ± 2.37), IL-10 (460.5 ± 183.40; 26.15 ± 1.92), IL-13 (33.79 ± 3.08; 7.41 ± 0.72), IL-15 (86.93 ± 9.84; 26.82 ± 0.87), IL-23 (476.30 ± 58.99; 129.90 ± 9.56), IL-28 (604.80 ± 48.53; 155.40 ± 41.10), IL-33 (1794.00 ± 256.00; 529.40 ± 97.05), Leptin (1453.00 ± 348.10; 468.40 ± 41.09), MCP-3, (1030 ± 254.10; 277.80 ± 32.41), RANKL (41.35 ± 5.99; 6.68 ± 0.68), and VEGF-A (817.60 ± 366.0; 101.00 ± 5.11). Statistically very significant (** $p \leq 0.01$) and statistically significant (* $p \leq 0.05$) results were obtained for BAFF (136.60 ± 29.64; 17.80 ± 2.72), IL-4 (8.51 ± 0.75; 3.48 ± 0.22), IL-12 (28.56 ± 3.76; 7.54 ± 1.14), IL-18 (2659 ± 285.70; 1148 ± 111.7), IL-19 (477.6 ± 66.11; 126.4 ± 32.87), IL-27 (13.26 ± 1.55; 4.43 ± 0.66), IL-31 (152.40 ± 17.71; 46.57 ± 1.76), M-CSF (15.99 ± 4.04; 3.40 ± 0.46), and TNF alpha (340.30 ± 106.70; 38.23 ± 4.62) (Figure 7A). At 24 h p.i. with SDAV, the concentration of most cytokines, chemokines, and growth factors decreased, but only a few remained significantly elevated: Eotaxin (1.39 ± 0.70; 0.00 ± 0.00, (* $p \leq 0.05$)), IL-6 (4509.00 ± 2010.00; 912.20 ± 83.72, (*** $p \leq 0.001$)), IP-10 (780.5 ± 173.78; 16.34 ± 3.96, (** $p \leq 0.01$)), RANTES (810.10 ± 131.30; 170.10 ± 70.05, (** $p \leq 0.01$)), and TNF alpha (423.10 ± 110.20; 38.23 ± 4.62, (** $p \leq 0.01$)) (Figure 7B).After 48 h p.i. with SDAV, only IL-17A (59.87 ± 6.83; 15.20 ± 1.61), MIP-1 beta (982.2 ± 310.20; 58.72 ± 9.73), and RANTES

(748.9 ± 39.83; 170.10 ± 70.05, (** $p \leq 0.01$) showed significant increases in protein expression (Figure 7C). Interestingly, highly significant (*** $p \leq 0.001$) and very significant (** $p \leq 0.01$) statistical increases were observed for almost all proteins after 72 h p.i. The greatest change in concentration was observed for BAFF (208.80 ± 28.49; 17.80 ± 2.72), Eotaxin (5.69 ± 1.05; 0.00 ± 0.00), G-CSF (97.67 ± 8.80; 2.81 ± 1.39), GRO alpha (4060 ± 955.50; 131.60 ± 17.85), IFN gamma (4.03 ± 0.34; 1.30 ± 0.08), IL-6 (6126.00 ± 1062.00; 912.2 ± 83.72), IL-12 (28.43 ± 2.71; 7.54 ± 1.14), IL-15 (79.38 ± 5.77; 26.82 ± 1.95), IL-17A (61.66 ± 3.50; 15.20 ± 1.61), IL-18 (2966.00 ± 221.00; 1148 ± 111.70), IL-22 (75.92 ± 8.65; 33.11 ± 4.46), IP-10 (661.90 ± 64.25; 16.34 ± 3.96), Leptin (1940.00 ± 169.20; 468.40 ± 41.09), MCP-3 (922.5.50 ± 303.30; 277.80 ± 32.41), MIP-1 beta (1131.0 ± 386.40; 58.72 ± 9.73), MIP-2 alpha (2627.00 ± 164.70; 172.2 ± 79.46), RANTES (815.20 ± 105.80; 170.10 ± 70.05), and TNF alpha (577.80 ± 45.75; 38.23 ± 4.62). Statistically significant changes in expression were also observed for IL-3 (3.26 ± 0.55; 0.99 ± 0.14), IL-9 (43.28 ± 2.39; 29.70 ± 2.48), IL-10 (117.3 ± 16.85; 26.15 ± 1.92), IL-23 (391.70 ± 26.09; 129.9 ± 9.56), IL-28 (491.80 ± 12.62; 155.40 ± 41.10), and LIF (220.30 ± 17.15; 81.76 ± 10.92) (Figure 7D). After 96 h p.i. with SDAV, the protein expression pattern remained similar to that at 72 h p.i., but only a few proteins changed. Statistically highly significant (*** $p \leq 0.001$) increases were observed only for BAFF (305.20 ± 153.50; 17.80 ± 2.72), IL-7 (60.98 ± 23.70; 10.55 ± 2.37), IL-9 (72.36 ± 34.69; 29.70 ± 2.48), IL-10 (298.70 ± 151.00; 26.15 ± 1.92), IL-13 (36.03 ± 12.18; 7.41 ± 0.72), and Il-17A (70.36 ± 11.91; 15.20 ± 1.61). Other cytokines and chemokines with very significant increases (** $p \leq 0.01$) were ENA-78 (3385.00 ± 562.70; 469.00 ± 67.43), Eotaxin (2.52 ± 1.63; 0.00 ± 0.00), IFN gamma (4.03 ± 0.34; 1.30 ± 0.08), IL-1β (63.32 ± 22.31; 23.92 ± 3. 87), IL-4 (12.34 ± 7.12; 3.48 ± 0.22), IL-12 (32.58 ± 10.96; 7.54 ± 1.14), IL-28 (599.30 ± 240.50; 155.40 ± 41. 10), IL-31 (159.50 ± 27.89; 46.57 ± 1.76), leptin (2202.00 ± 641.40; 468.40 ± 41.09), and MCP-3 (770.60 ± 229.90; 277.80 ± 32.41). Finally, other proteins were elevated statistically significantly (* $p \leq 0.05$): IFN alpha (55.02 ± 13.29; 18.33 ± 3.44), IL-5 (78.99 ± 24.36; 19.70 ± 2.57), IL-18 (2673 ± 222.80; 1148 ± 111.7), IL-19 (317.1 ± 55.83; 126.4 ± 32.87), Il-23 (463.60 ± 226.10; 129.9 ± 9.56), IL-33 (1652.00 ± 448.70; 529.40 ± 97.05), IP-10 (605.70 ± 141.80; 16.34 ± 3.96), RANKL (41.35 ± 5.99; 6.68 ± 0.68), and TNF alpha (371.10 ± 195.70; 38.23 ± 4.62) (Figure 7E). At 168 h p.i., protein expression was only very significantly increased (** $p \leq 0.01$) or significantly increased (* $p \leq 0.05$) for a few datasets. The most significant change in expression was found for BAFF (52.69 ± 6.21; 17.80 ± 2.72), ENA-78 (3410.00 ± 484.40; 469.00 ± 67.43), GM-CSF (109.80 ± 8.622; 6.51 ± 4.46), GRO alpha (2232 ± 751.60; 131.60 ± 17.85), IFN alpha (51.57 ± 8.68; 18.33 ± 3.44), IL-1 alpha (123.70 ± 36.74; 44.02 ± 6.81), IL-5 (70.87 ± 13.67; 19.70 ± 2.57), IL-15 (86.93 ± 9.84; 26.82 ± 1.95), IL-17A (59.93 ± 5.85; 15.20 ± 1.61), IL-19 (391.30 ± 59.78; 126.4 ± 32.87), IL-23 (381.60 ± 49.21; 129.9 ± 9.56), IL-27 (11.96 ± 3.37; 4.43 ± 0.66), IL-33 (1579.00 ± 317.60; 529.40 ± 97.05), MIP-1 beta (696.50 ± 142.60; 58.72 ± 9.73), and RANTES (572.30 ± 31.60; 670.6 ± 70.05) (Figure 7F). Finally, after one month p.i. with SDAV, most of the cytokines, chemokines, and growth factors were significantly increased compared to the mock. The greatest highly significant (*** $p \leq 0.001$) changes were observed for ENA-78 (6467.00 ± 1908.00; 469.00 ± 67.43), IL-4 (3.48 ± 0.22; 10.41 ± 1.88), IL-12 (35.38 ± 6.38, 7.54 ± 1.14), IL-19 (1456.00 ± 69.00; 126.40 ± 32.87), IL-27 (14.77 ± 1.49; 4.43 ± 0.66), Leptin (2426 ± 216.1; 468.4 ± 41.09), MIP-2 alpha (2645.00 ± 404.4; 172.2 ± 79.46), RANKL (21.84 ± 1.39; 6.68 ± 0.68), and VEGF (396.6 ± 106.40; 101.00 ± 5.11) (Figure 7G).

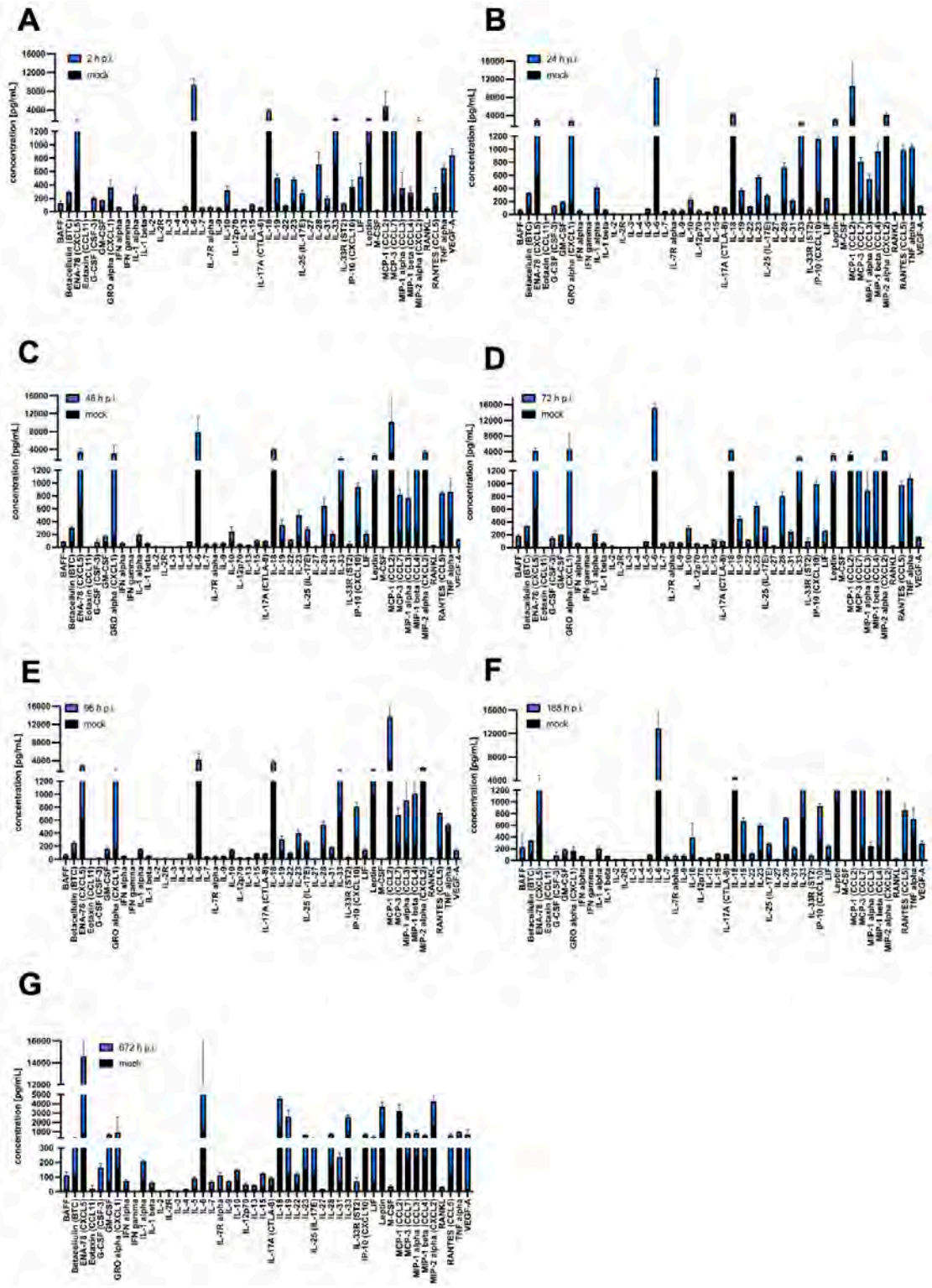

Figure 6. MHV-induced cytokine, chemokine, and growth factor expression [pg/mL] in infected (2–672 h) primary microglia and astrocyte cells. Bar plots indicate the concentration change of expressed 48 protein markers in a single biological replicate (n = 6 for each group), shown as mean ± SD (**A**–**G**). Statistical data are shown in Supplementary File S1.

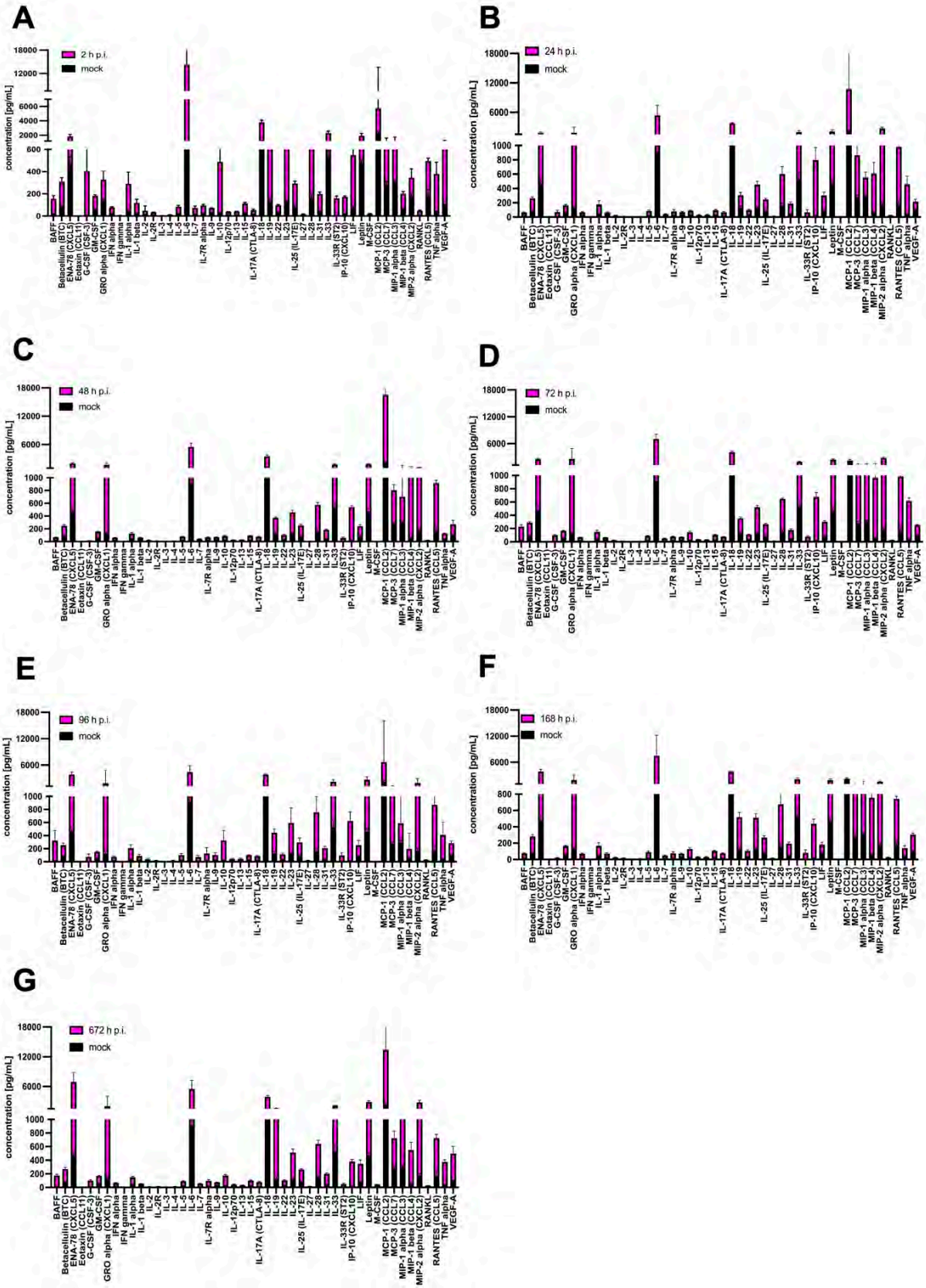

Figure 7. SDAV-induced cytokine, chemokine, and growth factor expression [pg/mL] in infected (2–672 h) primary microglia and astrocyte cells. Bar plots indicate a concentration change in expressed 48 protein markers in a single biological replicate (n = 6 for each group), shown as mean ± SD (**A**–**G**). Statistical data are shown in Supplementary File S1.

The next step was performing a classical ELISA for representative cytokines important for viral infection—IL-4, IL-5, IL-6, IL-10, IL-17, and TNF alpha. The anti-inflammatory cytokine IL-4 levels were significantly decreased in SDAV during all time points compared to the control (11.42 ± 1.28, * $p \leq 0.05$). For MHV-JHM, a significant decrease was observed for 24 h p.i. (7.23 ± 0.55, * $p \leq 0.05$) and 48 h p.i.; (2.89 ± 0.51, ** $p \leq 0.01$) compared to the control (14.43 ± 0.17). A nonsignificant increase was only noted at 168 h p.i. with MHV-JHM (15.39 ± 0.55) compared to the control (14.43 ± 0.17). In the case of the pro-inflammatory cytokine IL-5, MHV-JHM induced a statistically significant increase compared to the uninfected cells at all time points. The highest value was observed at 96 h p.i. (29.36 ± 6.91, *** $p \leq 0.001$) and 168 h p.i. (23.93 ± 3.39, *** $p \leq 0.001$) compared to the control (0.00 ± 0.00). After infection with SDAV, the increase in cytokine concentrations was visible after 24, 48, 72, and 168 h, but the results were not statistically significant compared to those of the control cells. (Figure 8B). The level of pro-inflammatory cytokine IL-6 changed after infection with both viruses compared to the mock. A statistically significant increase was observed after 48 h p.i. (1035.92 ± 3.64, * $p \leq 0.05$) and 72 h p.i. (1017.92 ± 1.80, * $p \leq 0.05$) after infection with SDAV compared to the control (701.62 ± 77.37). After infection with MHV-JHM, a statistically significant increase was observed after 2 h p.i. (624.24 ± 8.18; * $p \leq 0.05$) compared to the control (564.98 ± 1.54) (Figure 8C). The anti-inflammatory cytokine IL-10 was statistically highly significant after 96 h p.i. (1748.76 ± 398.05, *** $p \leq 0.001$) with SDAV and after 72 h p.i. (687.33 ± 214.67, *** $p \leq 0.001$) with MHV-JHM (Figure 8D) in comparison to both controls (199.97 ± 14.77, 184.91 ± 32.58, respectively). The pro-inflammatory cytokine IL-17 levels were statistically increased at all time points after SDAV infection. The highest levels were observed at 2 h p.i. (0.71 ± 0.09, * $p \leq 0.05$), 48 h p.i. (0.71 ± 0.02, *** $p \leq 0.001$), and 168 h p.i. (0.81 ± 0.012, *** $p \leq 0.001$) compared to the control (0.14 ± 0.003). MHV-JHM infection induced a significant change in expression after 2 h p.i. (0.89 ± 0.11, * $p \leq 0.05$), 24 h p.i. (0.04 ± 0.01, * $p \leq 0.05$), and 72 h p.i. (0.13 ± 0.01, * $p \leq 0.05$) compared to the control (0.26 ± 0.05) (Figure 8E). During SDAV infection, an increase in TNF alpha expression was observed, but it was not statistically significant compared to the control (71.42 ± 36.38). A statistically highly significant increase was observed after 2 h p.i. (731.33 ± 40.74, *** $p \leq 0.001$), 24 h p.i. (495.08 ± 36.58, *** $p \leq 0.001$), and 72 h p.i. (440.51 ± 44.23, *** $p \leq 0.001$) with MHV-JHM compared to the control (119.62 ± 26.20) (Figure 8F).

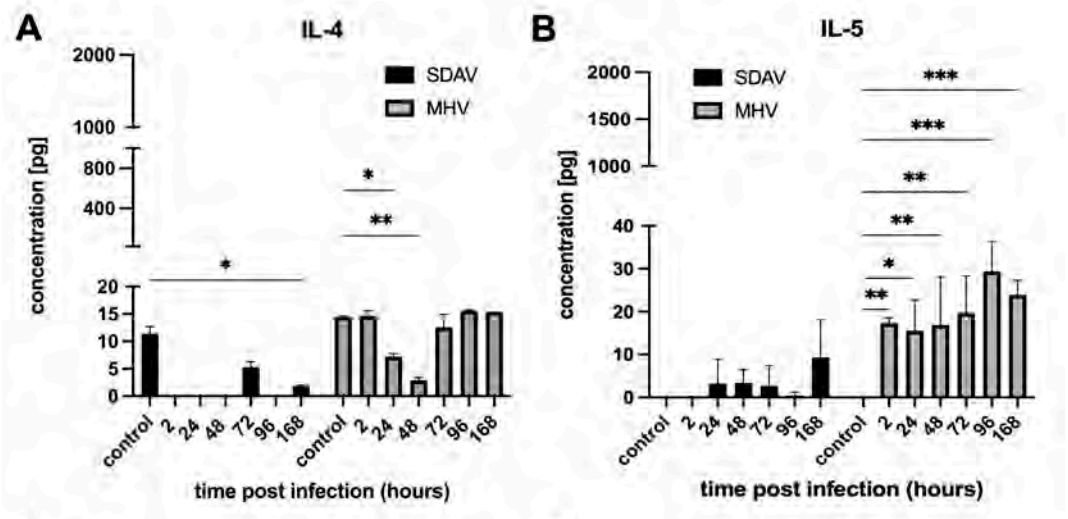

Figure 8. *Cont.*

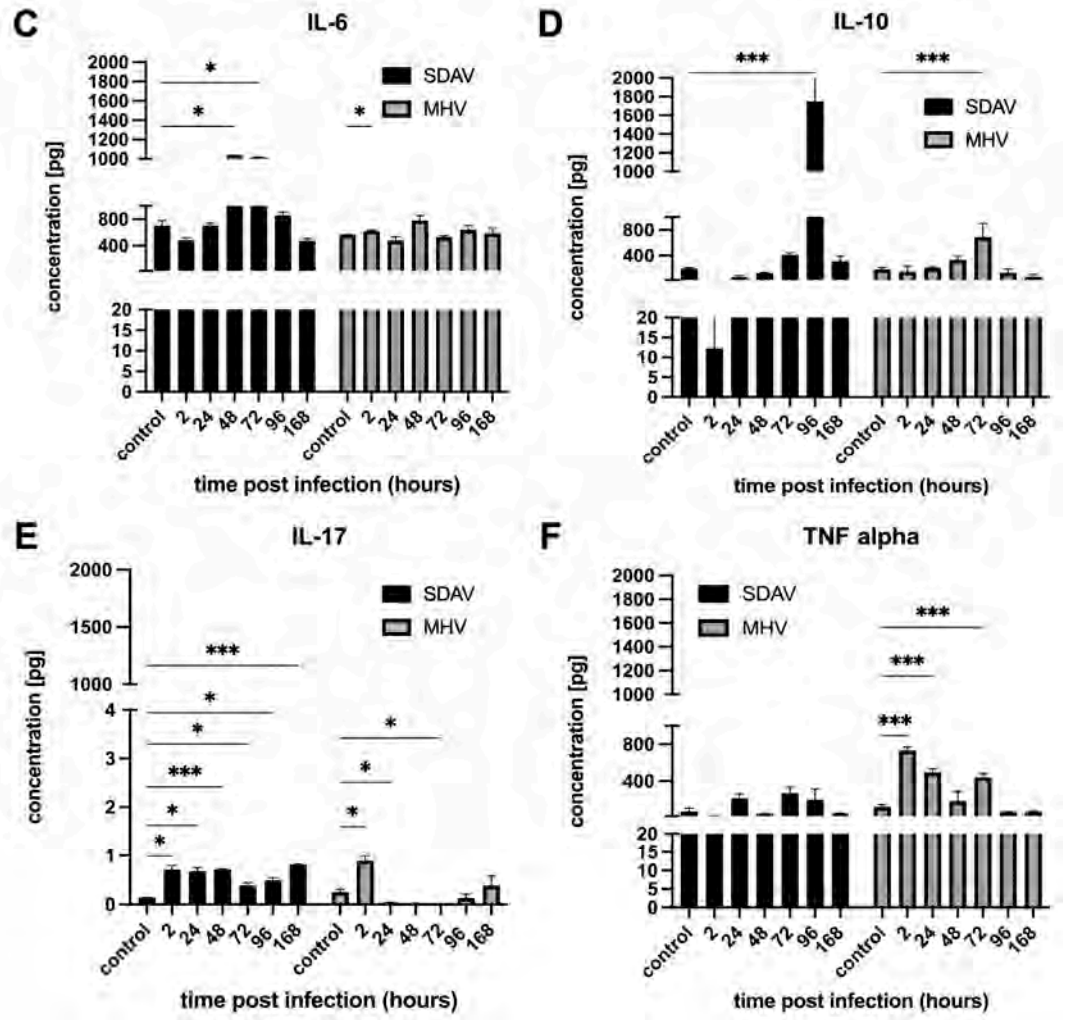

Figure 8. Concentration of selected cytokines produced by primary mixed microglia and astrocytes during SDAV and MHV-JHM (2–168 h) infection, analysed by ELISA. Control cells were not infected. Results are presented as the mean of calculated concentration [pg/mL] ± SD. Statistics were determined using ANOVA, * $p \leq 0.05$, ** $p \leq 0.01$, *** $p \leq 0.001$, (**A**–**F**).

4. Discussion

There are many studies concerning coronaviral infection outcomes in the brain conducted on patients suffering from long-COVID syndrome. However, we still seek answers to the underlying molecular reasoning behind serious health complications [58–61]. More and more research is focused on analysing the immune reaction, seeing abnormalities in cytokine/chemokine release as a main cause [62]. It is established that several viruses can induce cytokine storm syndrome/cytokine release syndrome, including, but not limited to, SARS-CoV-2, Human Immunodeficiency Virus (HIV) (including both AIDS infection and secondary infection-induced infections/malignancies), Epstein–Barr Virus (EBV), Human Herpesvirus 6 (HHV-6), Cytomegalovirus (CMV), various haemorrhagic fever viruses, and influenza viruses [63–65]. Studying how viruses affect glial cell function to trigger specific immune responses is important for creating targeted therapeutic strategies. Understanding the importance of further research on this topic, we have analysed two animal coronavirus models—MHV-JHM and SDAV—to answer the unknown molecular mechanism of long-COVID syndrome. Both viruses can infect rodents' central nervous system (CNS) [50,66] and cause neurodegeneration [49,50,53,67]. However, little is known about their infection effect on microglia and astrocytes. Most research has been conducted on the MHV-A59 strain [31,68–70]. Some recent studies on MHV-JHM presented the roles for microglia in

both demyelination and remyelination in vivo [71–74]. However, there are no data regarding SDAV. Considering this, MHV-JHM and SDAV constitute a good model that we used to investigate the effects of infection on primary mixed microglia and astrocyte cultures. We focused on characterising the type of cell death, reactive oxygen species (ROS) production, and cytokine/chemokine expression in response to infection with each virus. It is worth underlining that such research was conduct for the first time to reveal the effect of infection on glial cells and enrich the knowledge about SDAV infection in the CNS.

As mentioned, MHV-JHM was proven to infect microglia in vitro and in vivo [31,68–70]. However, any data considering SDAV replication in this kind of cell have not yet been described. We demonstrated that SDAV could effectively infect primary mixed microglia and astrocyte cultures. The results showed that viral antigens were present in both cell types (Figure 1(Be)). Confocal microscopy revealed that the viral antigens were initially present in the astrocytes and later detected in the microglial cells (Figure 1(Bf), white arrows).

Both MHV-JHM and SDAV induced apoptosis in the mixed glial cultures, as evidenced by Annexin V-FITC and PI FACS analyses. MHV-JHM triggered early apoptosis within 2 h p.i., sustaining increased levels throughout the one-month infection (Figure 2A). Cells infected with SDAV displayed a similar early apoptotic response, significantly increasing late apoptosis at 48 and 168 h p.i. (Figure 2B). Notably, necrosis was minimal in the SDAV-infected cells, contrasting with a slight increase observed after one month p.i. with MHV-JHM (Figure 2A,B). In comparison, previous studies confirmed that MHV-JHM induces caspase-mediated apoptosis in oligodendrocytes and the damage of myelin sheath in the CNS. This suggests one of the underlying mechanisms for the pathogenesis of MHV-induced demyelinating diseases in animals, along with the activation of the Fas signalling pathway [75,76]. On the other hand, SARS-CoV-2 infection in microglia (HMC3 cell line) induced the gene expression of antiviral immune and ER stress responses in the early phase of infection and apoptosis in the late phase of infection by intrinsic and death receptor (DR)-mediated apoptosis [77]. Data concerning SDAV apoptosis patterns have not been described so far.

A possible link to the high early apoptosis percentage after infection with MHV-JHM and SDAV can be due to ROS production by microglia and astrocytes as cell defensive mechanisms. As Villalpando-Rodriguez and Gibson (2021) suggested, the level and the type of ROS determine the ability of cells to undergo cell death [78]. Our study demonstrated a rapid and significant increase in ROS production in response to both MHV-JHM and SDAV infection, confirmed by flow cytometry and a data analysis of confocal images (Figures 3 and 4). Infection with MHV-JHM induced a significant increase in ROS production levels at 2 h p.i., remaining significantly higher than uninfected control cells until one week of infection (Figure 3A,B). SDAV infection induced ROS production as early as 2 h p.i. and maintained elevated levels throughout the infection (up to 1 month) compared to the control (Figure 4A,B). The confocal microscopic analysis demonstrated the expression of ROS in the infected cells, and a data analysis revealed a highly significant increase in CTCF levels. After infection with MHV-JHM, the highest ROS fluorescence was observed at 72 h p.i., whereas for SDAV, it was observed at 96 h p.i. (Figures 3C,D and 4C,D). The levels of ROS fluorescence in the cells infected with MHV-JHM at 72 h p.i. and with SDAV at 96 h p.i. and 168 h p.i. were nearly as high or higher than in uninfected positive control cells treated with H_2O_2 (Figures 3D and 4D). The constant ROS production observed in our study suggests a prolonged state of oxidative stress in the infected mixed primary microglia and astrocyte cells, potentially exacerbating neuroinflammation and contributing to encephalitis, mimicking long-COVID effect.

A high-throughput Luminex analysis revealed crosstalk of cytokine and chemokine signalling following MHV-JHM and SDAV infection of mixed primary microglia and

astrocytes (Figures 5–8). At the early stages of infection, at 2 h p.i., SDAV infection induced a much broader and more pronounced cytokine response compared to MHV-JHM (Figures 6A and 7A). We have shown that SDAV infection triggers statistically significant increases in the expression levels of betacellulin, G-CSF, IFN alpha, IFN gamma, IL-1 alpha, IL-1 beta, IL-3, IL-6, IL-7, IL-10, IL-13, IL-15, IL-23, IL-28, IL-33, Leptin, MCP-3, RANKL, and VEGF-A. At the later replication phase (from 72 h p.i.), both viruses caused a broad increase in cytokine and chemokine expression; however, SDAV generally maintained a higher overall level of cytokine expression compared to MHV-JHM (Figures 6D–G and 7D–G). By one-month p.i., the most significant increases for MHV-JHM were observed for ENA-78, G-CSF, GM-CSF, IL-6, IL-33, MIP-2 alpha, and VEGF-A (Figure 6G). Notably, SDAV uniquely induced cytokines like IL-1 alpha, IL-10, IL-19, IL-23, and IL-28, which were not significantly elevated in MHV-JHM infection (Figure 7G).

Both viruses induced the expression of cytokines like IL-6, IP-10, and TNF alpha, but the temporal dynamics of their expression varied. MHV-JHM exhibited a more sustained increase in certain cytokines, such as IL-6 and IL-33, throughout the one-month period. SDAV presented a more transient response, showing a decrease in most cytokines at 24 h p.i. (Eotaxin, IL-6, IP-10, RANTES, and TNF alpha), followed by a resurgence at later time points. Recent studies on SARS-CoV-2 revealed that COVID-19-associated cytokine storms (CSs) show elevated levels of IL-1 beta, IL-6, CXCL10, TNF alpha, IFN gamma, MIP 1 alpha, and 1 beta, as well as MCP-1, GM-CSF, VEGF, and IL-10 [79–81]. A comparison of the present study's findings with those of related research involving MHV-A59 reveals the upregulation of several cytokines in type I astrocytes, including IL-1 alpha, IL-1 beta, IL-2, IL-15, IL-13, IL-17, all three interferons, and TNF. The absence of induction of anti-inflammatory cytokines, such as IL-4 and IL-10, due to coronavirus infection may provide a potential explanation for the heightened inflammatory response observed during a "cytokine storm" [31]. The same pattern of increased pro-inflammatory cytokine secretion and depletion of anti-inflammatory cytokines was seen in our results, both in the case of MHV-JHM and SDAV. Consequently, there is a high probability of the occurrence of cytokine release syndrome (CRS) in mixed primary microglia and astrocyte cells. It is known that reactive astrocytes and microglia (pathogen-induced) can express and secrete crucial cytokines such as IL-1 beta, IL-6, TNF alpha, IL-18, TGF beta, and IL-10 after acute tissue injury [21,82]. Karki et al. (2021) established a new paradigm for defining the mechanism of cell death through "PANoptosis" induced by cytokine-mediated inflammation. Their research proved that increased TNF alpha and IFN gamma levels resulted in cytokine shock in mice and mirrored cytokine storm syndrome in COVID-19 patients [83]. The increased expression of these cytokines in our study can also be associated with this mechanism, but in our case, the triggering agent is a viral infection.

Both viruses induced a significant increase in key chemokines. These included IP-10, RANTES, MIP-2 alpha, ENA-78, MCP-1 alpha, and RANKL for MHV-JHM and Eotaxin, ENA-78, Gro alpha, IP-10, RANTES, RANKL, MCP-3, and MIP-1 alpha for SDAV. In comparison, the study by Miura et al. (2007) showed that alveolar type I cells infected with RCoV-P (Parkers Rat Coronavirus) or SDAV induced the expression of chemokines, CINC-2 (GRO), CINC-3 (MIP-2), LIX (ENA-78), MIP-3 alpha, and fractalkine at both 6 h and 24 h after inoculation [84]. In a separate study by Funk et al. (2009), the levels of inflammatory cytokines IL-1 alpha, IL-1 beta, TNF alpha, IFN gamma, and IL-6 in bronchoalveolar lavage fluid (BALF) did not increase significantly following SDAV infection. However, chemokines that were upregulated following SDAV infection of the airway and alveolar epithelial cells for 12 days were identified. The chemokines that were found to be significant in this study were MCP-1, LIX (ENA-78), and IP-10 [85]. Chemokines can have multiple functions in the CNS, from crucial ones like modulation of the activity of microglia and astrocytes to

maintaining the health of neurons or being involved in common response mechanisms to viral infection. Elevated levels of these chemokines are often correlated with more severe disease outcomes. For instance, higher levels of IP-10 and MIP-2 alpha have been associated with increased disease severity in COVID-19 patients [86,87]. Notably, IP-10 expression can regulate the synthesis of other biomolecules. These include MCP-3, MCP-1, MIP1 alpha, RANTES, MIP-2 alpha, GRO alpha, IL-7, IL-6, and IFN gamma [88–93]. This correlation has been observed in our results for SDAV at all time points and for MHV-JHM at 24, 48, 72, and 168 h p.i. (Figures 6 and 7). Similarly, persisting ENA-78 and MIP-2 alpha levels throughout the infection of both viruses may indicate amplification of innate immunity by microglia through the recruitment of neutrophils and monocytes [18,94].

The high level of IL-6 probably induced IL-10 and VEGF-A expression for possible tissue repair at the initial and late stages of infection (Figures 6–8). On the other hand, we observed at 2, 96, and 672 h p.i. with SDAV an IL-4 synergy with IL-5 to possibly dampen neurotoxic Th1/Th17 responses (Figure 7) [18,21]. Significantly high levels of betacellulin and RANKL expression after one month of infection with SDAV and MHV-JHM may contribute to astrocyte-mediated repair and T-cell regulation (Figures 6 and 7) [18,21]. Constantly elevated TNF-alpha, IL-1 beta, IL-1 alpha, IFN gamma, and IL-6 levels throughout infection with both viruses (Figures 6–8) might be linked to sustained apoptosis (Figure 2). As described before, microglial-derived TNF alpha and IL-1 beta secretion activated astrocytes via NF-κB and MAPK pathways, inducing nitric oxide (NO) production through inducible nitric oxide synthase (iNOS), which may trigger astrocyte apoptosis [11,95,96]. Additionally, persisting IL-1 alpha levels promoted possible reactive astrogliosis via high ROS generation (Figures 3B,D and 4B,D), as was also confirmed by others [11,96].

In studies conducted on COVID-19 patients, proinflammatory cytokines like IFN gamma, IL-1, 2, 6, 10, IP-10, (MCP-1), and (GM-CSF) were elevated [97]. The mechanism behind the excessive production of cytokines is that a deregulated immune system causes vascular leakage, leading to an increase in the permeability of the BBB, allowing the virus to enter the CNS, causing neurotoxicity, neuroinflammation, and neurodegeneration by apoptosis, cell lysis, or disrupting transcriptional pathways [98]. Additionally, the phenotype of glial cells can change due to viral infection into activated astrocytes and microglial cells, which can be neurotoxic (A1 phenotype and M1 phenotype of microglial cells) or neuroprotective (A2 phenotype and M2 phenotype of microglial cells) [99]. Moreover, it has been shown that the presence of reactive proinflammatory microglia secreting IL-1 alpha, IL-1 beta, IL-6, and TNF alpha or exposure to PAMP/DAMP can induce the expression of proinflammatory genes in astrocytes that trigger neuroinflammation and neurodegeneration. Moreover, A1 astrocytes secrete CCL-2, CX3CL1, CXCL10, GM-CSF, and IL-1, activating pro-inflammatory microglia [44,99–102].

5. Conclusions

This study demonstrated, for the first time, that SDAV can effectively infect primary murine microglia and astrocyte cells. Both viruses induced a rapid and significant increase in ROS production, with MHV-JHM causing an initial rise, followed by a gradual decrease. At the same time, SDAV maintained elevated levels throughout the infection. This prolonged oxidative stress may suggest a contribution to neuroinflammation and might mimic long-COVID effects. SDAV infection induced a broader and more pronounced early cytokine response than MHV-JHM. Both viruses caused a broad increase in cytokine and chemokine expression at later stages, with SDAV generally maintaining higher levels. Our study thus provides novel insights into the effects of MHV-JHM and SDAV infection on primary mixed microglia and astrocyte cultures, offering potential molecular explanations for cytokine release syndrome (CRS). It is also important to recognise that even mild

inflammation of the cells that act as a protective coating for neurons can interfere with proper functioning of the central nervous system.

Supplementary Materials: The following supporting information can be downloaded at https://www.mdpi.com/article/10.3390/cells14090637/s1; Figures S1 and S2: Statistical analysis of cytokine profile for Figures 6 and 7. Figure S1. MHV-induced cytokine, chemokine, receptor and growth factor expression [pg/mL] in infected (2–672 h) primary microglia and astrocyte cells. Each dot plot represents the concentration of one protein from ProcartaPlex™ Mouse Immune Monitoring Panel, 48plex. Results are shown as mean ± SD, (n = 6 for each time point). Statistics were determined using a Kruskal—Wallis Test with a Dunn Test post hoc, * $p \leq 0.05$, ** $p \leq 0.01$, *** $p \leq 0.001$. Figure S2. SDAV-induced cytokine, chemokine, receptor and growth factor expression [pg/mL] in infected (2–672 h) primary microglia and astrocyte cells. Each dot plot represents the concentration of one protein from ProcartaPlex™ Mouse Immune Monitoring Panel, 48plex. Results are shown as mean ± SD, (n = 6 for each time point). Statistics were determined using a Kruskal—Wallis Test with a Dunn Test post hoc, * $p \leq 0.05$, ** $p \leq 0.01$, *** $p \leq 0.001$.

Author Contributions: Conceptualisation, M.B. and J.C.; methodology, M.B. and J.C.; validation, J.C.; formal analysis, J.C.; investigation, M.B., W.D.K., K.G.-Z., M.C. and J.C.; resources, K.G.-Z., A.V.P., E.D., M.K. and J.C.; data curation, M.B.; writing—original draft preparation, M.B.; writing—review and editing, J.C., W.D.K., K.G.-Z., M.C., E.D. and A.V.P.; visualisation, M.B.; supervision, J.C.; project administration, M.B.; funding acquisition, M.B. and A.V.P. All authors have read and agreed to the published version of the manuscript.

Funding: This study was financed by a grant from the Ministry of Science and Higher Education of the Republic of Poland (decision No. 2021/41/N/NZ6/04383). The APC was financed by the Science Development Fund of the Warsaw University of Life Sciences—SGGW.

Institutional Review Board Statement: Not applicable.

Informed Consent Statement: Not applicable.

Data Availability Statement: All original contributions presented in this study are included in this article and its Supplementary Materials. Further inquiries can be directed to the corresponding authors.

Acknowledgments: This study was partially financed by grants from the Ministry of Science and Higher Education of the Republic of Poland (decision No. 9506/E-385/R/2018 and 16/491568/SPUB/SP/2021). The grants provided financial support for modernisation and maintenance laboratories in which some procedures for this study were performed. Adrian-Valentin Potârniche thanks the Polish National Agency for Academic Exchange (decision No. BPN/ULM/2022/1/00087/U/00001) for the support. The authors acknowledge using Perplexity AI (Perplexity AI Inc., San Francisco, CA, USA; https://www.perplexity.ai (accessed on 20 February 2025)) to enhance the clarity and coherence of the English language in this article.

Conflicts of Interest: The authors declare no conflicts of interest.

References

1. Davis, H.E.; McCorkell, L.; Vogel, J.M.; Topol, E.J. Long COVID: Major Findings, Mechanisms and Recommendations. *Nat. Rev. Microbiol.* **2023**, *21*, 133–146. [CrossRef]
2. Krahel, W.D.; Bartak, M.; Cymerys, J. Acute and Long-Term SARS-CoV-2 Infection and Neurodegeneration Processes—Circulus Vitiosus. *Acta Virol.* **2024**, *68*, 12765. [CrossRef]
3. Mielcarska, M.B.; Rouse, B.T. Viruses and the Brain—A Relationship Prone to Trouble. *Viruses* **2025**, *17*, 203. [CrossRef]
4. Lopez-Leon, S.; Wegman-Ostrosky, T.; Perelman, C.; Sepulveda, R.; Rebolledo, P.A.; Cuapio, A.; Villapol, S. More than 50 Long-Term Effects of COVID-19: A Systematic Review and Meta-Analysis. *Sci. Rep.* **2021**, *11*, 16144. [CrossRef]
5. Hu, C.; Chen, C.; Dong, X.-P. Impact of COVID-19 Pandemic on Patients With Neurodegenerative Diseases. *Front. Aging Neurosci.* **2021**, *13*, 664965. [CrossRef]
6. Que, Y.; Hu, C.; Wan, K.; Hu, P.; Wang, R.; Luo, J.; Li, T.; Ping, R.; Hu, Q.; Sun, Y.; et al. Cytokine Release Syndrome in COVID-19: A Major Mechanism of Morbidity and Mortality. *Int. Rev. Immunol.* **2022**, *41*, 217–230. [CrossRef]

7. De Marchi, F.; Gallo, C.; Sarnelli, M.F.; De Marchi, I.; Saraceno, M.; Cantello, R.; Mazzini, L. Accelerated Early Progression of Amyotrophic Lateral Sclerosis over the COVID-19 Pandemic. *Brain Sci.* **2021**, *11*, 1291. [CrossRef]
8. Musson, L.S.; Collins, A.; Opie-Martin, S.; Bredin, A.; Hobson, E.V.; Barkhouse, E.; Coulson, M.C.; Stavroulakis, T.; Gould, R.L.; Al-Chalabi, A.; et al. Impact of the Covid-19 Pandemic on Amyotrophic Lateral Sclerosis Care in the UK. *Amyotroph. Lateral Scler. Front. Degener.* **2023**, *24*, 91–99. [CrossRef]
9. Sfera, A.; Rahman, L.; Zapata-Martín del Campo, C.M.; Kozlakidis, Z. Long COVID as a Tauopathy: Of "Brain Fog" and "Fusogen Storms". *Int. J. Mol. Sci.* **2023**, *24*, 12648. [CrossRef] [PubMed]
10. Jorgačevski, J.; Potokar, M. Immune Functions of Astrocytes in Viral Neuroinfections. *Int. J. Mol. Sci.* **2023**, *24*, 3514. [CrossRef]
11. Liu, L.; Liu, J.; Bao, J.; Bai, Q.; Wang, G. Interaction of Microglia and Astrocytes in the Neurovascular Unit. *Front. Immunol.* **2020**, *11*, 1024. [CrossRef]
12. Sun, M.; You, H.; Hu, X.; Luo, Y.; Zhang, Z.; Song, Y.; An, J.; Lu, H. Microglia–Astrocyte Interaction in Neural Development and Neural Pathogenesis. *Cells* **2023**, *12*, 1942. [CrossRef]
13. Low, R.N.; Low, R.J.; Akrami, A. A Review of Cytokine-Based Pathophysiology of Long COVID Symptoms. *Front. Med.* **2023**, *10*, 1011936. [CrossRef]
14. Shimabukuro-Vornhagen, A.; Gödel, P.; Subklewe, M.; Stemmler, H.J.; Schlößer, H.A.; Schlaak, M.; Kochanek, M.; Böll, B.; Von Bergwelt-Baildon, M.S. Cytokine Release Syndrome. *J. Immunother. Cancer* **2018**, *6*, 56. [CrossRef]
15. Klein, R.S.; Garber, C.; Funk, K.E.; Salimi, H.; Soung, A.; Kanmogne, M.; Manivasagam, S.; Agner, S.; Cain, M. Neuroinflammation During RNA Viral Infections. *Annu. Rev. Immunol.* **2019**, *37*, 73–95. [CrossRef]
16. Galán, M.; Vigón, L.; Fuertes, D.; Murciano-Antón, M.A.; Casado-Fernández, G.; Domínguez-Mateos, S.; Mateos, E.; Ramos-Martín, F.; Planelles, V.; Torres, M.; et al. Persistent Overactive Cytotoxic Immune Response in a Spanish Cohort of Individuals With Long-COVID: Identification of Diagnostic Biomarkers. *Front. Immunol.* **2022**, *13*, 848886. [CrossRef]
17. Shabab, T.; Khanabdali, R.; Moghadamtousi, S.Z.; Kadir, H.A.; Mohan, G. Neuroinflammation Pathways: A General Review. *Int. J. Neurosci.* **2017**, *127*, 624–633. [CrossRef]
18. Ismail, F.S.; Faustmann, T.J.; Faustmann, P.M.; Corvace, F. Microglia as Potential Key Regulators in Viral-Induced Neuroinflammation. *Front. Cell. Neurosci.* **2024**, *18*, 1426079. [CrossRef]
19. Xu, P.; Yu, Y.; Wu, P. Role of Microglia in Brain Development after Viral Infection. *Front. Cell Dev. Biol.* **2024**, *12*, 1340308. [CrossRef]
20. Chhatbar, C.; Prinz, M. The Roles of Microglia in Viral Encephalitis: From Sensome to Therapeutic Targeting. *Cell. Mol. Immunol.* **2021**, *18*, 250–258. [CrossRef]
21. Gao, C.; Jiang, J.; Tan, Y.; Chen, S. Microglia in Neurodegenerative Diseases: Mechanism and Potential Therapeutic Targets. *Signal Transduct. Target. Ther.* **2023**, *8*, 359. [CrossRef]
22. Muñoz-Carrillo, J.L.; Contreras, J.; Gutierrez-Coronado, O.; Villalobos-Gutiérrez, P.; Ramos Gracia, L.G.; Hernández-Reyes, V. *Cytokine Profiling Plays a Crucial Role in Activating Immune System to Clear Infectious Pathogens*; IntechOpen: London, UK, 2018; ISBN 978-1-78985-151-9.
23. Bixler, S.L.; Goff, A.J. The Role of Cytokines and Chemokines in Filovirus Infection. *Viruses* **2015**, *7*, 5489–5507. [CrossRef]
24. Düsedau, H.P.; Steffen, J.; Figueiredo, C.A.; Boehme, J.D.; Schultz, K.; Erck, C.; Korte, M.; Faber-Zuschratter, H.; Smalla, K.-H.; Dieterich, D.; et al. Influenza A Virus (H1N1) Infection Induces Microglial Activation and Temporal Dysbalance in Glutamatergic Synaptic Transmission. *mBio* **2021**, *12*, e01776-21. [CrossRef]
25. Hosseini, S.; Wilk, E.; Michaelsen-Preusse, K.; Gerhauser, I.; Baumgärtner, W.; Geffers, R.; Schughart, K.; Korte, M. Long-Term Neuroinflammation Induced by Influenza A Virus Infection and the Impact on Hippocampal Neuron Morphology and Function. *J. Neurosci.* **2018**, *38*, 3060–3080. [CrossRef]
26. Jiang, H.; Zhang, Z. Immune Response in Influenza Virus Infection and Modulation of Immune Injury by Viral Neuraminidase. *Virol. J.* **2023**, *20*, 193. [CrossRef]
27. Radkowski, M.; Grabarczyk, P.; Kryczka, T.; Caraballo Cortès, K.; Kubicka-Russel, D.; Janiak, M.; Osuch, S.; Perlejewski, K.; Laskus, T. Cytokine Profile and Viral Diversity in the Early Seronegative Stage of Community-Acquired Hepatitis C Virus (HCV) Infection. *Sci. Rep.* **2023**, *13*, 20045. [CrossRef]
28. Casola, A.; Estes, M.K.; Crawford, S.E.; Ogra, P.L.; Ernst, P.B.; Garofalo, R.P.; Crowe, S.E. Rotavirus Infection of Cultured Intestinal Epithelial Cells Induces Secretion of CXC and CC Chemokines. *Gastroenterology* **1998**, *114*, 947–955. [CrossRef]
29. Holloway, G.; Coulson, B.S. Innate Cellular Responses to Rotavirus Infection. *J. Gen. Virol.* **2013**, *94*, 1151–1160. [CrossRef]
30. Malamba-Banda, C.; Mhango, C.; Benedicto-Matambo, P.; Mandolo, J.J.; Chinyama, E.; Kumwenda, O.; Barnes, K.G.; Cunliffe, N.A.; Iturriza-Gomara, M.; Jambo, K.C.; et al. Acute Rotavirus Infection Is Associated with the Induction of Circulating Memory CD4+ T Cell Subsets. *Sci. Rep.* **2023**, *13*, 9001. [CrossRef]
31. Lavi, E.; Cong, L. Type I Astrocytes and Microglia Induce a Cytokine Response in an Encephalitic Murine Coronavirus Infection. *Exp. Mol. Pathol.* **2020**, *115*, 104474. [CrossRef]

32. Rajayer, S.R.; Smith, S.M. Neurovirulent Cytokines Increase Neuronal Excitability in a Model of Coronavirus-Induced Neuroinflammation. *Intensive Care Med. Exp.* **2023**, *11*, 71. [CrossRef]
33. Li, Y.; Fu, L.; Gonzales, D.M.; Lavi, E. Coronavirus Neurovirulence Correlates with the Ability of the Virus to Induce Proinflammatory Cytokine Signals from Astrocytes and Microglia. *J. Virol.* **2004**, *78*, 3398–3406. [CrossRef]
34. Domingues, H.S.; Portugal, C.C.; Socodato, R.; Relvas, J.B. Corrigendum: Oligodendrocyte, Astrocyte and Microglia Crosstalk in Myelin Development, Damage, and Repair. *Front. Cell Dev. Biol.* **2016**, *4*, 79. [CrossRef]
35. Lawson, L.J.; Perry, V.H.; Dri, P.; Gordon, S. Heterogeneity in the Distribution and Morphology of Microglia in the Normal Adult Mouse Brain. *Neuroscience* **1990**, *39*, 151–170. [CrossRef]
36. Mittelbronn, M.; Dietz, K.; Schluesener, H.J.; Meyermann, R. Local Distribution of Microglia in the Normal Adult Human Central Nervous System Differs by up to One Order of Magnitude. *Acta Neuropathol.* **2001**, *101*, 249–255. [CrossRef]
37. Tang, Y.; Le, W. Differential Roles of M1 and M2 Microglia in Neurodegenerative Diseases. *Mol. Neurobiol.* **2016**, *53*, 1181–1194. [CrossRef]
38. Colton, C.A. Heterogeneity of Microglial Activation in the Innate Immune Response in the Brain. *J. Neuroimmune Pharmacol.* **2009**, *4*, 399–418. [CrossRef]
39. Orihuela, R.; McPherson, C.A.; Harry, G.J. Microglial M1/M2 Polarization and Metabolic States. *Br. J. Pharmacol.* **2016**, *173*, 649–665. [CrossRef]
40. Colonna, M.; Butovsky, O. Microglia Function in the Central Nervous System During Health and Neurodegeneration. *Annu. Rev. Immunol.* **2017**, *35*, 441–468. [CrossRef]
41. Guo, S.; Wang, H.; Yin, Y. Microglia Polarization From M1 to M2 in Neurodegenerative Diseases. *Front. Aging Neurosci.* **2022**, *14*, 815347. [CrossRef]
42. Patrycy, M.; Chodkowski, M.; Krzyzowska, M. Role of Microglia in Herpesvirus-Related Neuroinflammation and Neurodegeneration. *Pathogens* **2022**, *11*, 809. [CrossRef]
43. Wang, J.; Xing, H.; Wan, L.; Jiang, X.; Wang, C.; Wu, Y. Treatment Targets for M2 Microglia Polarization in Ischemic Stroke. *Biomed. Pharmacother.* **2018**, *105*, 518–525. [CrossRef]
44. Liddelow, S.A.; Guttenplan, K.A.; Clarke, L.E.; Bennett, F.C.; Bohlen, C.J.; Schirmer, L.; Bennett, M.L.; Münch, A.E.; Chung, W.-S.; Peterson, T.C.; et al. Neurotoxic Reactive Astrocytes Are Induced by Activated Microglia. *Nature* **2017**, *541*, 481–487. [CrossRef]
45. Giovannoni, F.; Quintana, F.J. The Role of Astrocytes in CNS Inflammation. *Trends Immunol.* **2020**, *41*, 805–819. [CrossRef]
46. Macht, V.A. Neuro-Immune Interactions across Development: A Look at Glutamate in the Prefrontal Cortex. *Neurosci. Biobehav. Rev.* **2016**, *71*, 267–280. [CrossRef]
47. Matejuk, A.; Ransohoff, R.M. Crosstalk Between Astrocytes and Microglia: An Overview. *Front. Immunol.* **2020**, *11*, 1416. [CrossRef]
48. Passaro, A.P.; Lebos, A.L.; Yao, Y.; Stice, S.L. Immune Response in Neurological Pathology: Emerging Role of Central and Peripheral Immune Crosstalk. *Front. Immunol.* **2021**, *12*, 676621. [CrossRef]
49. Bartak, M.; Krahel, W.D.; Chodkowski, M.; Grel, H.; Walczak, J.; Pallepati, A.; Komorowski, M.; Cymerys, J. ATPase Valosin-Containing Protein (VCP) Is Involved During the Replication and Egress of Sialodacryoadenitis Virus (SDAV) in Neurons. *Int. J. Mol. Sci.* **2024**, *25*, 11633. [CrossRef]
50. Bender, S.J.; Weiss, S.R. Pathogenesis of Murine Coronavirus in the Central Nervous System. *J. Neuroimmune Pharmacol.* **2010**, *5*, 336–354. [CrossRef]
51. Bergmann, C.C.; Lane, T.E.; Stohlman, S.A. Coronavirus Infection of the Central Nervous System: Host-Virus Stand-Off. *Nat. Rev. Microbiol.* **2006**, *4*, 121–132. [CrossRef]
52. Nakagaki, K.; Nakagaki, K.; Taguchi, F. Receptor-Independent Spread of a Highly Neurotropic Murine Coronavirus JHMV Strain from Initially Infected Microglial Cells in Mixed Neural Cultures. *J. Virol.* **2005**, *79*, 6102–6110. [CrossRef]
53. Pasick, J.; Dales, S. MHV-JHM Infections of Rodent Neuronal Cells: Replication and Trafficking of Structural Proteins and Progeny Virions. In *Coronaviruses*; Laude, H., Vautherot, J.-F., Eds.; Advances in Experimental Medicine and Biology; Springer: Boston, MA, USA, 1994; Volume 342, pp. 319–325. ISBN 978-1-4613-6305-7.
54. Cymerys, J.; Kowalczyk, A.; Mikołajewicz, K.; Słońska, A.; Krzyżowska, M. Nitric Oxide Influences HSV-1-Induced Neuroinflammation. *Oxid. Med. Cell. Longev.* **2019**, *2019*, e2302835. [CrossRef]
55. Kärber, G. Beitrag zur kollektiven Behandlung pharmakologischer Reihenversuche. *Naunyn-Schmiedebergs Arch. Für Exp. Pathol. Pharmakol.* **1931**, *162*, 480–483. [CrossRef]
56. Gaertner, D.J.; Winograd, D.F.; Compton, S.R.; Paturzo, F.X.; Smith, A.L. Development and Optimization of Plaque Assays for Rat Coronaviruses. *J. Virol. Methods* **1993**, *43*, 53–64. [CrossRef]
57. Cymerys, J.; Chodkowski, M.; Słońska, A.; Krzyżowska, M.; Bańbura, M.W. Disturbances of Mitochondrial Dynamics in Cultured Neurons Infected with Human Herpesvirus Type 1 and Type 2. *J. Neurovirol.* **2019**, *25*, 765. [CrossRef]
58. Boes, M.; Falter-Braun, P. Long-COVID-19: The Persisting Imprint of SARS-CoV-2 Infections on the Innate Immune System. *Signal Transduct. Target. Ther.* **2023**, *8*, 460. [CrossRef]

59. Gulyaeva, N.V. Brain Mechanisms Involved in Post COVID Syndrome: A Narrative Review. *Neurochem. J.* **2024**, *18*, 397–405. [CrossRef]
60. Prosperini, L.; Tortorella, C.; Haggiag, S.; Ruggieri, S.; Galgani, S.; Gasperini, C. Determinants of COVID-19-Related Lethality in Multiple Sclerosis: A Meta-Regression of Observational Studies. *J. Neurol.* **2022**, *269*, 2275–2285. [CrossRef]
61. Tate, W.; Walker, M.; Sweetman, E.; Helliwell, A.; Peppercorn, K.; Edgar, C.; Blair, A.; Chatterjee, A. Molecular Mechanisms of Neuroinflammation in ME/CFS and Long COVID to Sustain Disease and Promote Relapses. *Front. Neurol.* **2022**, *13*, 877772. [CrossRef]
62. Almulla, A.F.; Thipakorn, Y.; Zhou, B.; Vojdani, A.; Maes, M. Immune Activation and Immune-Associated Neurotoxicity in Long-COVID: A Systematic Review and *Meta*-Analysis of 103 Studies Comprising 58 Cytokines/Chemokines/Growth Factors. *Brain. Behav. Immun.* **2024**, *122*, 75–94. [CrossRef]
63. Cron, R.Q.; Goyal, G.; Chatham, W.W. Cytokine Storm Syndrome. *Annu. Rev. Med.* **2023**, *74*, 321–337. [CrossRef]
64. Gu, Y.; Zuo, X.; Zhang, S.; Ouyang, Z.; Jiang, S.; Wang, F.; Wang, G. The Mechanism behind Influenza Virus Cytokine Storm. *Viruses* **2021**, *13*, 1362. [CrossRef] [PubMed]
65. Ombrello, M.J.; Schulert, G.S. COVID-19 and Cytokine Storm Syndrome: Are There Lessons from Macrophage Activation Syndrome? *Transl. Res. J. Lab. Clin. Med.* **2021**, *232*, 1–12. [CrossRef]
66. Percy, D.H.; Lynch, J.A.; Descôteaux, J.-P. Central Nervous System Lesions in Suckling Mice and Rats Inoculated Intranasally with Sialodacryoadenitis Virus. *Vet. Pathol.* **1986**, *23*, 42–49. [CrossRef]
67. Bartak, M.; Bąska, P.; Chodkowski, M.; Tymińska, B.; Bańbura, M.W.; Cymerys, J. Neurons Cytoskeletal Architecture Remodeling during the Replication Cycle of Mouse Coronavirus MHV-JHM: A Morphological in Vitro Study. *BMC Vet. Res.* **2024**, *20*, 18. [CrossRef] [PubMed]
68. Das Sarma, J. Microglia-Mediated Neuroinflammation Is an Amplifier of Virus-Induced Neuropathology. *J. Neurovirol.* **2014**, *20*, 122–136. [CrossRef] [PubMed]
69. Savarin, C.; Bergmann, C.C. Fine Tuning the Cytokine Storm by IFN and IL-10 Following Neurotropic Coronavirus Encephalomyelitis. *Front. Immunol.* **2018**, *9*, 3022. [CrossRef]
70. Verma, A.K.; Zheng, J.; Mack, M.; Ginhoux, F.; Perlman, S. Differential Effects of Prostaglandin D2 Signaling on Macrophages and Microglia in Murine Coronavirus Encephalomyelitis. *mBio* **2021**, *12*, e0196921. [CrossRef]
71. Wheeler, D.L.; Sariol, A.; Meyerholz, D.K.; Perlman, S. Microglia Are Required for Protection against Lethal Coronavirus Encephalitis in Mice. *J. Clin. Investig.* **2018**, *128*, 931–943. [CrossRef]
72. Mangale, V.; Syage, A.R.; Ekiz, H.A.; Skinner, D.D.; Cheng, Y.; Stone, C.L.; Brown, R.M.; O'Connell, R.M.; Green, K.N.; Lane, T.E. Microglia Influence Host Defense, Disease, and Repair Following Murine Coronavirus Infection of the Central Nervous System. *Glia* **2020**, *68*, 2345–2360. [CrossRef]
73. Sariol, A.; Mackin, S.; Allred, M.-G.; Ma, C.; Zhou, Y.; Zhang, Q.; Zou, X.; Abrahante, J.E.; Meyerholz, D.K.; Perlman, S. Microglia Depletion Exacerbates Demyelination and Impairs Remyelination in a Neurotropic Coronavirus Infection. *Proc. Natl. Acad. Sci. USA* **2020**, *117*, 24464–24474. [CrossRef]
74. Syage, A.; Pachow, C.; Cheng, Y.; Mangale, V.; Green, K.N.; Lane, T.E. Microglia Influence Immune Responses and Restrict Neurologic Disease in Response to Central Nervous System Infection by a Neurotropic Murine Coronavirus. *Front. Cell. Neurosci.* **2023**, *17*, 1291255. [CrossRef]
75. Liu, Y.; Cai, Y.; Zhang, X. Induction of Caspase-Dependent Apoptosis in Cultured Rat Oligodendrocytes by Murine Coronavirus Is Mediated during Cell Entry and Does Not Require Virus Replication. *J. Virol.* **2003**, *77*, 11952–11963. [CrossRef]
76. Liu, Y.; Zhang, X. Murine Coronavirus-Induced Oligodendrocyte Apoptosis Is Mediated through the Activation of the Fas Signaling Pathway. *Virology* **2007**, *360*, 364–375. [CrossRef]
77. Jeong, G.U.; Lyu, J.; Kim, K.-D.; Chung, Y.C.; Yoon, G.Y.; Lee, S.; Hwang, I.; Shin, W.-H.; Ko, J.; Lee, J.-Y.; et al. SARS-CoV-2 Infection of Microglia Elicits Proinflammatory Activation and Apoptotic Cell Death. *Microbiol. Spectr.* **2022**, *10*, e01091-22. [CrossRef]
78. Villalpando-Rodriguez, G.E.; Gibson, S.B. Reactive Oxygen Species (ROS) Regulates Different Types of Cell Death by Acting as a Rheostat. *Oxid. Med. Cell. Longev.* **2021**, *2021*, 9912436. [CrossRef]
79. Dharra, R.; Kumar Sharma, A.; Datta, S. Emerging Aspects of Cytokine Storm in COVID-19: The Role of Proinflammatory Cytokines and Therapeutic Prospects. *Cytokine* **2023**, *169*, 156287. [CrossRef]
80. Fajgenbaum, D.C.; June, C.H. Cytokine Storm. *N. Engl. J. Med.* **2020**, *383*, 2255–2273. [CrossRef]
81. Wang, J.; Jiang, M.; Chen, X.; Montaner, L.J. Cytokine Storm and Leukocyte Changes in Mild versus Severe SARS-CoV-2 Infection: Review of 3939 COVID-19 Patients in China and Emerging Pathogenesis and Therapy Concepts. *J. Leukoc. Biol.* **2020**, *108*, 17–41. [CrossRef]
82. Gao, Z.; Zhu, Q.; Zhang, Y.; Zhao, Y.; Cai, L.; Shields, C.B.; Cai, J. Reciprocal Modulation Between Microglia and Astrocyte in Reactive Gliosis Following the CNS Injury. *Mol. Neurobiol.* **2013**, *48*, 690–701. [CrossRef]

83. Karki, R.; Sharma, B.R.; Tuladhar, S.; Williams, E.P.; Zalduondo, L.; Samir, P.; Zheng, M.; Sundaram, B.; Banoth, B.; Malireddi, R.K.S.; et al. Synergism of TNF-α and IFN-γ Triggers Inflammatory Cell Death, Tissue Damage, and Mortality in SARS-CoV-2 Infection and Cytokine Shock Syndromes. *Cell* **2021**, *184*, 149–168.e17. [CrossRef] [PubMed]
84. Miura, T.A.; Wang, J.; Holmes, K.V.; Mason, R.J. Rat Coronaviruses Infect Rat Alveolar Type I Epithelial Cells and Induce Expression of CXC Chemokines. *Virology* **2007**, *369*, 288–298. [CrossRef] [PubMed]
85. Funk, C.J.; Manzer, R.; Miura, T.A.; Groshong, S.D.; Ito, Y.; Travanty, E.A.; Leete, J.; Holmes, K.V.; Mason, R.J. Rat Respiratory Coronavirus Infection: Replication in Airway and Alveolar Epithelial Cells and the Innate Immune Response. *J. Gen. Virol.* **2009**, *90*, 2956–2964. [CrossRef]
86. Olivarria, G.; Lane, T.E. Evaluating the Role of Chemokines and Chemokine Receptors Involved in Coronavirus Infection. *Expert Rev. Clin. Immunol.* **2022**, *18*, 57–66. [CrossRef]
87. Khalil, B.A.; Elemam, N.M.; Maghazachi, A.A. Chemokines and Chemokine Receptors during COVID-19 Infection. *Comput. Struct. Biotechnol. J.* **2021**, *19*, 976–988. [CrossRef] [PubMed]
88. Gudowska-Sawczuk, M.; Mroczko, B. What Is Currently Known about the Role of CXCL10 in SARS-CoV-2 Infection? *Int. J. Mol. Sci.* **2022**, *23*, 3673. [CrossRef]
89. Chen, Y.; Wang, J.; Liu, C.; Su, L.; Zhang, D.; Fan, J.; Yang, Y.; Xiao, M.; Xie, J.; Xu, Y.; et al. IP-10 and MCP-1 as Biomarkers Associated with Disease Severity of COVID-19. *Mol. Med.* **2020**, *26*, 97. [CrossRef]
90. Yang, Y.; Shen, C.; Li, J.; Yuan, J.; Wei, J.; Huang, F.; Wang, F.; Li, G.; Li, Y.; Xing, L.; et al. Plasma IP-10 and MCP-3 Levels Are Highly Associated with Disease Severity and Predict the Progression of COVID-19. *J. Allergy Clin. Immunol.* **2020**, *146*, 119–127.e4. [CrossRef]
91. Tegethoff, S.A.; Danziger, G.; Kühn, D.; Kimmer, C.; Adams, T.; Heintz, L.; Metz, C.; Reifenrath, K.; Angresius, R.; Mang, S.; et al. TNF-Related Apoptosis-Inducing Ligand, Interferon Gamma-Induced Protein 10, and C-Reactive Protein in Predicting the Progression of SARS-CoV-2 Infection: A Prospective Cohort Study. *Int. J. Infect. Dis.* **2022**, *122*, 178–187. [CrossRef]
92. Lu, Q.; Zhu, Z.; Tan, C.; Zhou, H.; Hu, Y.; Shen, G.; Zhu, P.; Yang, G.; Xie, X. Changes of Serum IL-10, IL-1β, IL-6, MCP-1, TNF-α, IP-10 and IL-4 in COVID-19 Patients. *Int. J. Clin. Pract.* **2021**, *75*, e14462. [CrossRef]
93. Madhurantakam, S.; Lee, Z.J.; Naqvi, A.; Prasad, S. Importance of IP-10 as a Biomarker of Host Immune Response: Critical Perspective as a Target for Biosensing. *Curr. Res. Biotechnol.* **2023**, *5*, 100130. [CrossRef]
94. Rodríguez, A.M.; Rodríguez, J.; Giambartolomei, G.H. Microglia at the Crossroads of Pathogen-Induced Neuroinflammation. *ASN Neuro* **2022**, *14*, 17590914221104566. [CrossRef]
95. Van Everbroeck, B.; Dewulf, E.; Pals, P.; Lübke, U.; Martin, J.-J.; Cras, P. The Role of Cytokines, Astrocytes, Microglia and Apoptosis in Creutzfeldt-Jakob Disease. *Neurobiol. Aging* **2002**, *23*, 59–64. [CrossRef]
96. Smith, J.A.; Das, A.; Ray, S.K.; Banik, N.L. Role of Pro-Inflammatory Cytokines Released from Microglia in Neurodegenerative Diseases. *Brain Res. Bull.* **2012**, *87*, 10–20. [CrossRef]
97. Darif, D.; Hammi, I.; Kihel, A.; El Idrissi Saik, I.; Guessous, F.; Akarid, K. The Pro-Inflammatory Cytokines in COVID-19 Pathogenesis: What Goes Wrong? *Microb. Pathog.* **2021**, *153*, 104799. [CrossRef]
98. Kujawska, M.; Mostafavi, E.; Kaushik, A. SARS-CoV-2 Getting into the Brain; Neurological Phenotype of COVID-19, and Management by Nano-Biotechnology. *Neural Regen. Res.* **2023**, *18*, 519. [CrossRef]
99. Kwon, H.S.; Koh, S.-H. Neuroinflammation in Neurodegenerative Disorders: The Roles of Microglia and Astrocytes. *Transl. Neurodegener.* **2020**, *9*, 42. [CrossRef]
100. Price, B.R.; Johnson, L.A.; Norris, C.M. Reactive Astrocytes: The Nexus of Pathological and Clinical Hallmarks of Alzheimer's Disease. *Ageing Res. Rev.* **2021**, *68*, 101335. [CrossRef]
101. Rosciszewski, G.; Cadena, V.; Murta, V.; Lukin, J.; Villarreal, A.; Roger, T.; Ramos, A.J. Toll-Like Receptor 4 (TLR4) and Triggering Receptor Expressed on Myeloid Cells-2 (TREM-2) Activation Balance Astrocyte Polarization into a Proinflammatory Phenotype. *Mol. Neurobiol.* **2018**, *55*, 3875–3888. [CrossRef] [PubMed]
102. Rosciszewski, G.; Cadena, V.; Auzmendi, J.; Cieri, M.B.; Lukin, J.; Rossi, A.R.; Murta, V.; Villarreal, A.; Reinés, A.; Gomes, F.C.A.; et al. Detrimental Effects of HMGB-1 Require Microglial-Astroglial Interaction: Implications for the Status Epilepticus -Induced Neuroinflammation. *Front. Cell. Neurosci.* **2019**, *13*, 380. [CrossRef] [PubMed]

SZKOŁA GŁÓWNA
GOSPODARSTWA
WIEJSKIEGO

Warszawa, 20.05.2025r

mgr inż. Michalina Bartak
Zakład Mikrobiologii
Katedra Nauk Przedklinicznych
Instytut Medycyny Weterynaryjnej
ul. Ciszewskiego 8, 02-786 Warszawa
michalina_bartak@sggw.edu.pl

Rada Dyscypliny Weterynaria

Szkoły Głównej Gospodarstwa Wiejskiego w Warszawie

Oświadczenie o współautorstwie

Niniejszym oświadczam, że w pracy:

Bartak, M., Krahel, W. D., Gregorczyk-Zboroch, K., Chodkowski, M., Potârniche, A. V., Długosz, E., Krzyżowska, M., & Cymerys, J. (2025). Cytokine Profile Analysis During Sialodacryoadenitis Virus and Mouse Hepatitis Virus JHM Strain Infection in Primary Mixed Microglia and Astrocyte Culture-Preliminary Research. *Cells*, *14*(9), 637.

Mój indywidualny udział w jej powstaniu polegał na opracowaniu koncepcji artykułu, finasowaniu, zaprojektowaniu i przeprowadzeniu eksperymentów, analizie danych, wizualizacji danych, opracowaniu manuskryptu.
Indywidualny wkład pracy w publikację wynosił 70%.

.....
Podpis

SZKOŁA GŁÓWNA
GOSPODARSTWA
WIEJSKIEGO

Warszawa, 20.05.2025

Mgr inż. Weronika Daria Krahel
Zakład Mikrobiologii
Katedra Nauk Przedklinicznych
Instytut Medycyny Weterynaryjnej
ul. Ciszewskiego 8, 02-786 Warszawa
weronika_krahel@sggw.edu.pl

Rada Dyscypliny Weterynaria

Szkoły Głównej Gospodarstwa Wiejskiego w Warszawie

Oświadczenie o współautorstwie

Niniejszym oświadczam, że w pracy:

Bartak, M., Krahel, W. D., Gregorczyk-Zboroch, K., Chodkowski, M., Potârniche, A. V., Długosz, E., Krzyżowska, M., & Cymerys, J. (2025). Cytokine Profile Analysis During Sialodacryoadenitis Virus and Mouse Hepatitis Virus JHM Strain Infection in Primary Mixed Microglia and Astrocyte Culture-Preliminary Research. *Cells*, *14*(9), 637.

Mój indywidualny udział w jej powstaniu polegał na pomocy w przeprowadzeniu części eksperymentów oraz krytycznej edycji manuskryptu.

Indywidualny wkład pracy w publikację wynosił 5%.

Weronika Daria Krahel

Podpis

SZKOŁA GŁÓWNA
GOSPODARSTWA
WIEJSKIEGO

Warszawa, 20.05.2025

dr Karolina Gregorczyk-Zboroch
Zakład Immunologii
Katedra Nauk Przedklinicznych
Instytut Medycyny Weterynaryjnej
ul. Ciszewskiego 8, 02-786 Warszawa
karolina_gregorczyk_zboroch@sggw.edu.pl

Rada Dyscypliny Weterynaria

Szkoły Głównej Gospodarstwa
Wiejskiego w Warszawie

Oświadczenie o współautorstwie

Niniejszym oświadczam, że w pracy:

Bartak, M., Krahel, W. D., Gregorczyk-Zboroch, K., Chodkowski, M., Potârniche, A. V., Długosz, E., Krzyżowska, M., & Cymerys, J. (2025). Cytokine Profile Analysis During Sialodacryoadenitis Virus and Mouse Hepatitis Virus JHM Strain Infection in Primary Mixed Microglia and Astrocyte Culture-Preliminary Research. *Cells, 14*(9), 637.

Mój indywidualny udział w jej powstaniu polegał na pomocy w przeprowadzeniu części eksperymentów, użyczeniu sprzętu oraz krytycznej edycji manuskryptu.
Indywidualny wkład pracy w publikację wynosił 3%.

K. Gregorczyk-Zboroch

Podpis

SZKOŁA GŁÓWNA
GOSPODARSTWA
WIEJSKIEGO

Warszawa, 20.05.2025

Dr Marcin Chodkowski
Zakład Mikrobiologii Medycznej i Środowiskowej
Wojskowy Instytut Higieny i Epidemiologii
ul. Kozielska 4, 01-063 Warszawa
marcin.chodkowski@wihe.pl

Rada Dyscypliny Weterynaria

Szkoły Głównej Gospodarstwa Wiejskiego w Warszawie

Oświadczenie o współautorstwie

Niniejszym oświadczam, że w pracy:

Bartak, M., Krahel, W. D., Gregorczyk-Zboroch, K., Chodkowski, M., Potârniche, A. V., Długosz, E., Krzyżowska, M., & Cymerys, J. (2025). Cytokine Profile Analysis During Sialodacryoadenitis Virus and Mouse Hepatitis Virus JHM Strain Infection in Primary Mixed Microglia and Astrocyte Culture-Preliminary Research. *Cells*, *14*(9), 637.

Mój indywidualny udział w jej powstaniu polegał na pomocy w przeprowadzeniu części eksperymentów oraz krytycznej edycji manuskryptu.
Indywidualny wkład pracy w publikację wynosił 5%.

Podpis

SZKOŁA GŁÓWNA
GOSPODARSTWA
WIEJSKIEGO

Warszawa, 20.05.2025

Dr hab. Joanna Cymerys-Bulenda prof. SGGW
Zakład Mikrobiologii
Katedra Nauk Przedklinicznych
Instytut Medycyny Weterynaryjnej
ul. Ciszewskiego 8, 02-786 Warszawa
joanna_cymerys@sggw.edu.pl

Rada Dyscypliny Weterynaria

Szkoły Głównej Gospodarstwa
Wiejskiego w Warszawie

Oświadczenie o współautorstwie

Niniejszym oświadczam, że w pracy:

Bartak, M., Krahel, W. D., Gregorczyk-Zboroch, K., Chodkowski, M., Potârniche, A. V., Długosz, E., Krzyżowska, M., & Cymerys, J. (2025). Cytokine Profile Analysis During Sialodacryoadenitis Virus and Mouse Hepatitis Virus JHM Strain Infection in Primary Mixed Microglia and Astrocyte Culture-Preliminary Research. *Cells*, *14*(9), 637.

Mój indywidualny udział w jej powstaniu polegał na pomocy w opiece nad projektem, zaprojektowaniu części eksperymentów, analizie danych, koncepcji artykułu oraz krytycznej edycji manuskryptu.
Indywidualny wkład pracy w publikację wynosił 10%.

Joanna Cymerys-Bulenda

Podpis